UNIVERSITAT POLITÈCNICA DE CATALUNYA BARCELONATECH

Surface modification of zirconia-based bioceramics for orthopedic and dental applications

Quentin Flamant

Surface modification of zirconia-based bioceramics for orthopedic and dental applications

A dissertation submitted in partial fulfillment of the requirements
for the degree of Doctor of Philosophy by

Quentin Flamant

Department of Materials Science and Metallurgical Engineering
Doctoral Program in Materials Science and Engineering
Universitat Politècnica de Catalunya - BarcelonaTech

Supervisor: Prof. Marc Anglada

UNIVERSITAT POLITÈCNICA DE CATALUNYA
BARCELONATECH
Departament de Ciència dels Materials
i Enginyeria Metal·lúrgica

Barcelona, June 2016

To John Gall Speed

Abstract

Due to their outstanding mechanical properties and excellent biocompatibility, the use of zirconia-based ceramics in dental and orthopedic applications has grown rapidly over the last decades. However, both alumina and zirconia are bioinert, which hampers their implantation in direct contact with bone. Furthermore, infections remain one of the leading causes of implant failure. To address both issues, an improved surface design is required: in particular, an adequate topography can promote osseointegration and limit bacterial adhesion.

On the other hand, long-term reliability is a major concern for load-bearing implants, and zirconia-containing ceramics require special attention. As for other ceramics, surface alterations can impair their mechanical properties. Besides, the tetragonal to monoclinic phase transformation, which accounts for their exceptional toughness, can occur spontaneously in the presence of water, potentially deteriorating the material properties. The kinetics of this phenomenon, known as hydrothermal ageing, are highly sensitive to processing changes. Any surface modification of zirconia-containing ceramics should thus be accompanied by a careful assessment of its impact on implant reliability.

Based on these observations, the objective of this thesis was to develop processes to modify the surface of zirconia-based implants, in particular the topography, without compromising their mechanical properties and hydrothermal stability. The research effort focused on two materials of particular interest: yttria-stabilized zirconia (3Y-TZP), which is increasingly used for prosthodontic applications (e.g., crowns, implants), and zirconia toughened alumina (ZTA), which is the current gold standard in orthopedics for the fabrication of load-bearing ceramic components. Accordingly, this work can be divided into two main parts.

In the first part, an extensive study of the hydrofluoric acid (HF) etching of zirconia was carried out. It was shown that monitoring etching time allows controlling the roughness and fractal dimension of the surface. Furthermore, the results indicated suitable processing conditions for a fast and uniform roughening of zirconia components, without compromising substantially their strength and ageing resistance. Based on these findings, zirconia samples with roughness gradients were obtained by immersing specimens into an etching solution with a controlled

speed. Thanks to this method, which drastically reduces the efforts and resources necessary to study cell-surface interactions, a rapid screening of the influence of HF-induced micro- and nano-topography on mesenchymal stem cell morphology was conducted. Correlations between roughness parameters and cell morphology were evidenced, highlighting the importance of multiscale optimization of topography to induce the desired cell response.

In the second part, an integrated strategy was developed to provide both osseointegrative and antibacterial properties to ZTA surfaces. The micro-topography was controlled by injection molding. Meanwhile a novel process involving the selective dissolution of zirconia by HF (selective etching) was used to produce nano-roughness and interconnected surface nanoporosity. Potential utilization of the porosity for delivery of antibiotic molecules was demonstrated, and it was shown that liposomal encapsulation could improve drug loading. Furthermore, the impact of selective etching on mechanical properties and hydrothermal stability was shown to be limited. The combination of injection molding and selective etching appears thus promising for fabricating a new generation of ZTA components implantable in direct contact with bone.

Keywords: zirconia, zirconia-toughened alumina, surface modification, chemical etching, dental and orthopedic materials, topography, roughness, drug delivery, strength, ageing

Acknowledgements

Finishing this PhD thesis and finally writing the acknowledgements section after 1353 days makes me feel kind of weird: something between relief, happiness and nostalgia. Relief because 1353 days is quite a long time and fortunately I did not lose my hair yet (I was really afraid, since some of my colleagues were not as a lucky as I am). Happiness because I'm almost a doctor and ready for holid… oops, I mean the next step of a successful career that will hopefully lead me to the Ig Nobel prize. Nostalgia because it has been a great experience, in great places, with great people.

So, firstly, I would like to thank everyone from UPC, in particular: my supervisor, Marc Anglada for his help, support and confidence from the beginning to the end of this project; people from my office for supporting me for so long, even when I was singing very loud: Erik (for singing with me), Yassine (for singing too), Jose Maria (for suggesting lyrics), Erica (for listening), Joanna (for the chocolate and sweets), Daniela (for her "ta tranquilo, ta favoravel" attitude), Monica (for not killing me even when she was extremely busy), Latifa (idem), Zhi Tong (idem) and all the others; people from the office upstairs: Jing (for the Chinese and Kung Fu lessons), Miquel (for the coffee breaks and his valuable movie recommendations), Ina (for almost lighting a fire inside a house to celebrate Christmas), Newsha (for the good mood) and I'm sure that I forget someone; people from the nano-center office: Roberta ("no seu quadrado"), Romain and his best friend John Gall Speed, Mireia (for being available at least one Wednesday a month, and believe me, in her case, it's not that easy), Giuseppe (for the good stories); Super-Trifon and Montse for their help and patience; people from the CIEFMA group (in particular Emilio, Fernando and Joan Josep for their help to my work); people from the office next door: Elia (for staying with me until 22:00 when everybody left), Anna, Jordi, Meritxell, Montse, Cristina, Edgar, David and the others; Maria Angeles for cheering us up every day (and cleaning our mess, that's not an easy task); the staff from the department; and I'm sure that I still forget many !

Secondly, I would like to thank everyone from INSA Lyon, in particular Jérôme, for his confidence and support and giving me the opportunity to participate to this project; Sylvain, for

his availability and his help during my secondment and after (without forgetting the good mood); Laurent, for his help and useful advice; Helen, for her help and support finding this PhD position; and all the others (secretaries, staff and PhD students), for their warm welcome.

Next, I would like to thank people from Imperial College London, in particular Rona, for her support, patience and availability every time that I needed help; Chris and Inge for their collaboration to my work; and the entire Stevens group for their welcome (they know that they are too many to be cited).

Then, I would like to thank all the Biobone network, in particular: Eduardo, for being the most entertaining project coordinator ever; Abel, Ana-Maria, Carlos, Claudio, Elena, Gil, Katia, Marcel, Marta, Martin, Preethi, Francesca, Valentina and Yann for being the funniest PhD/postdoc team; Alan and Meinhard from CeramTec (thanks for the samples!); Marianna and Mauro from the AO Foundation (thanks for the cell cultures!); and all the others!

Last but not least, I would like to acknowledge the European Commission funding under the 7th Framework Programme (Marie Curie Initial Training Networks; grant number: 289958, Bioceramics for bone repair) for financing my research, workshops, conferences, lunches, dinners, coffees, late-night taxis, week-ends, vacations and many other things. I would also like to thank the Spanish state for being so slow to deliver the NIE (someone knows why).

Thanks to my family and friends, thanks to those I forget, thanks everyone!

Preface

This dissertation is submitted for the degree of Doctor of Philosophy at the Universitat Politècnica de Catalunya – BarcelonaTech. The research described in this thesis was carried out by the author between 2012 and 2016 under the supervision of Prof. Marc Anglada within the framework of the Marie Curie Initial Training Network "Biobone" (Bioceramics for bone repair). The experimental work was realized at three different places: the Department of Materials Science and Metallurgical Engineering of the Universitat Politècnica de Catalunya, the Laboratory "Matériaux, Ingénierie et Science" (MATEIS) of the National Institute of Applied Sciences of Lyon (INSA Lyon, France) and the Department of Materials of Imperial College London (UK). It also involved collaborations with the AO Foundation (Davos, Switzerland) for stem cell cultures and with the ceramic manufacturer CeramTec GmbH (Plochingen, Germany) for the fabrication of the zirconia-toughened alumina samples.

This thesis is presented as a collection of papers, which are listed in the next section. Chapter 1 is a review about the state of the art of zirconia-based bioceramics, their applications in orthopedics and dentistry and the existing methods for modifying their surface. The aims and scope of the thesis are presented in Chapter 2. The experimental details can be found in each article and related supplementary information (if present). The main findings are summarized in Chapter 3. General conclusions and perspectives are presented in Chapter 4. The full articles are appended at the end of the manuscript.

List of works

This dissertation is based on the publications listed below. IF = impact factor; Q = quartile.

Article I. Hydrofluoric acid etching of dental zirconia. Part 1: etching mechanism and surface characterization.

Authors: **Flamant, Q.**, García Marro, F., Rovira, J. J. R. & Anglada, M.

Published in: Journal of the European Ceramic Society (2016), 36(1), 121-134. doi: 10.1016/j.jeurceramsoc.2015.09.021. IF: 2.947, Q1, ranked 1/26 in the category "Materials Science, Ceramics".

Author's contribution**:** Design and realization of all the experiments, except for the preliminary study to which other co-authors participated, and for the XPS and ESI-FTMS measurements, which were performed by a technician. Analysis of the data and writing of the manuscript.

Article II. Hydrofluoric acid etching of dental zirconia. Part 2: effect on flexural strength and ageing behavior.

Authors**: Flamant Q.** & Anglada, M.

Published in: Journal of the European Ceramic Society (2016), 36(1), 135-145. doi:10.1016/j.jeurceramsoc.2015.09.022. IF: 2.947, Q1, ranked 1/26 in the category "Materials Science, Ceramics".

Author's contribution**:** Design and realization of all the experiments. Analysis of the data and writing of the manuscript.

Article III. Roughness gradients on zirconia for rapid screening of cell-surface interactions: fabrication, characterization and application.

Authors**: Flamant Q.**, Stanciuc A., Pavailler H., Sprecher C.M., Alini M., Peroglio M. & Anglada, M.

Published in: Journal of Biomedical Materials Research Part A (2016). doi: 10.1002/jbm.a.35791. IF: 3.369, Q1, ranked 13/76 in the category "Engineering, Biomedical".

Author's contribution**:** Design of all the experiments except for the stem cell cultures. Collaborative work with one of the co-authors for the fabrication of the samples and the surface measurements. Analysis of the data and writing of the manuscript.

Additionally, the work on zirconia-toughend alumina is described in Annex A.

Annex A. Selective etching of injection molded zirconia-toughened alumina: towards osseointegrated and antibacterial ceramic implants.

This work results from collaboration between UPC BarcelonaTech (Quentin Flamant, Marc Anglada), INSA Lyon (Carlos Caravaca, Sylvain Meille, Laurent Gremillard, Jérôme Chevalier), Imperial College London (Rona Chandrawati, Christopher D. Spicer, Inge K. Herrmann, Molly M. Stevens) and CeramTec GmbH (Katia Biotteau-Deheuvels, Meinhard Kuntz).

Author's contribution**:** Design and realization of all the experiments except for the fabrication of the injected samples, the strength and hydrothermal degradation testing and the FACS measurements. Analysis of the data and writing of the manuscript.

Other contributions

Related, not included publications

Camposilvan, E., **Flamant, Q.** & Anglada, M. (2015). *Surface roughened zirconia: towards hydrothermal stability.* Journal of the mechanical behavior of biomedical materials, 47, 95-106. doi:10.1016/j.jmbbm.2015.03.017.

Stanciuc A., **Flamant Q.**, Alini M., Anglada, M. & Peroglio M. *Femtosecond laser micro-patterning of zirconia for screening of cell-surface interactions.* Journal of the European Ceramic Society (special issue in preparation).

Caravaca C., **Flamant Q.**, Anglada M., Gremillard L. & Chevalier J. *Impact of sandblasting on the mechanical properties and aging resistance of alumina and zirconia-based ceramics.* Journal of the European Ceramic Society (special issue in preparation).

Patents

Flamant, Q. & Anglada M., inventors; Universitat Politècnica de Catalunya, assignee. *Método para decapado selectivo de circona situada en la superficie de un material cerámico que comprende una matriz de Al2O3*. Spanish patent: P201530813, application filed on June 10th, 2015.

Organization of scientific events

Main organizer of the workshop "Surface mechanical characterization of ceramic-based materials" within the framework of the "Biobone" Marie Curie Initial Training Network, 23rd - 24th April 2015, Barcelona, Spain.

Poster and oral presentations

García Marro, F., **Flamant, Q.**, Londiche, B. & Anglada, M. *Surface treatments on zirconia ceramics: a comparative study*. 7th EEIGM conference on Advanced Materials Research, 21st - 22nd March 2013, Luleå, Sweden. Poster presentation.

García Marro, F., **Flamant, Q.**, Londiche, B. & Anglada, M. *Surface characterization of zirconia: acid etching and sandblasting*. 13th International Conference of the European Ceramic Society, 23rd to 27th June 2013, Limoges, France. Poster presentation.

Flamant, Q., Pavailler H. & Anglada, M. *Fabrication of zirconia surfaces with a roughness gradient by chemical etching*. CIEC14 - European Inter-Regional Conference on Ceramics, 8th - 10th September 2014, Stuttgart, Germany. Oral presentation.

Flamant, Q., Camposilvan E. & Anglada, M. *Assessment of the ageing sensitivity of surface modified acid-etched zirconia for increased osseointegration*. Fall-meeting of the European Materials Research Society (E-MRS), 15th - 18th September 2014, Warsaw, Poland. Oral presentation.

Flamant, Q., García Marro, F., Roa Rovira, J.J. & Anglada, M. *Surface modification of zirconia by acid etching.* BIOCERAMICS 2014, 26th Symposium and Annual Meeting of the International Society for Ceramics in Medicine, 6th - 8th November 2014, Barcelona, Spain. Oral presentation.

Flamant Q., Chandrawati R., Herrmann I.K., Spicer C.D., Stevens M.M., Biotteau-Deheuvels K. & Anglada, M. *Surface modification of a structural bioceramic for drug delivery*. 8th EEIGM conference on Advanced Materials Research, 11th - 12th June 2015, Valencia, Spain. Oral presentation.

Flamant Q., Caravaca C., Meille S., Gremillard L., Chevalier J., Biotteau-Deheuvels K., Kuntz M., Chandrawati R., Herrmann I.K., Spicer C.D., Stevens M.M. & Anglada, M. *Surface modification of Zirconia Platelet Toughened Alumina for the fabrication of drug-releasing implants*. 14th International Conference of the European Ceramic Society, 21st - 25th June 2015, Toledo, Spain. Oral presentation.

Flamant Q., Caravaca C., Meille S., Gremillard L., Chevalier J., Biotteau-Deheuvels K., Kuntz M., Chandrawati R., Herrmann I.K., Spicer C.D., Stevens M.M. & Anglada, M. *Selective chemical etching of injection-molded zirconia platelet toughened alumina: a novel process for the fabrication of nano-rough implants with drug-releasing ability*. European Congress and Exhibition on Advanced Materials and Processes (EUROMAT), 20th - 24th September 2015, Warsaw, Poland. Oral presentation.

Flamant Q., Camposilvan, E., Caravaca C., Meille S., Gremillard L., Chevalier J., Biotteau-Deheuvels K., Kuntz M., Chandrawati R., Herrmann I.K., Spicer C.D., Stevens M.M. & Anglada, M. *Surface modifications of zirconia and zirconia-toughened alumina ceramics for dental and orthopedic applications.* Biobone symposium, 13th – 15th October 2015, Santiago de Compostela, Spain. Oral presentation.

Contents

List of figures and tables

Figures

Tables

List of abbreviations

3Y-TZP: 3 mol. % Y-TZP

AFM: Atomic Force Microscopy

Ce-TZP: Ceria-stabilized TZP

DI water: Deionized Water

DPPC: 1,2-dipalmitoyl-*sn*-glycero-3-phosphocholine

EDS: Energy Dispersive X-ray Spectroscopy

ESI-FTMS: Electrospray Ionization Fourier Transform Mass Spectrometry

FE: Finite Elements

FIB: Focused Ion Beam

HCl: Hydrochloric Acid

HF: Hydrofluoric Acid

hMSC: Human Bone Marrow Mesenchymal Stem Cell

LTD: Low Temperature Degradation

OPA: *o*-phtaldialdehyde

PBS: Phosphate Buffered Saline

SEM: Scanning Electron Microscopy

TCP: Tricalcium Phosphate

SRC: Smooth-Rough Crossover

TEM: Transmission Electron Microscopy

TZP: Tetragonal Zirconia Polycrystal

WLI: White Light Interferometry

XPS: X-Ray Photoelectron Spectroscopy

XRD: X-Ray Diffraction

Y-TZP: Yttria-stabilized TZP

ZTA: Zirconia-Toughened Alumina

Chapter 1. Introduction

1.1. Ceramics in orthopedics and dentistry

1.1.1. A brief history

The concept of bioceramic, which designates a ceramic material used for the repair and reconstruction of diseased or damaged parts of the body [1], is much older than one might think: in 1972, Amadeo Bobbio discovered 4000 year old Mayan skulls in which missing teeth had been replaced by nacre substitutes [2]. However, it was no until the end of the eighteenth century that the modern use of ceramics as biomaterials started with the first successful fabrication and implantation of porcelain dentures by the Parisian apothecary Alexis Duchateau and the dentist Nicholas Dubois de Chemant [3], while the diversification of materials and applications, as well as the industrial production, took place during the twentieth century (Figure 1.1).

In 1920, tricalcium phosphate (TCP) was proposed as potential filler for bone gaps. Nevertheless, its weak mechanical strength discarded its utilization for bearing purposes. The first to consider ceramics as replacement materials for joints was Rock, who received a German patent for alumina ceramics in 1930, but at that time performances were hampered by the poor quality of pre-war alumina [4]. More than three decades later, in 1965, Sandhaus proposed and patented an alumina material for hip joints, which can be considered as the first "high-tech" ceramic designed for orthopedics [4].

In the 1970s, hydroxyapatite, which is bio-stable and has a bone-like crystal structure, was introduced for the coating of dental implants and metallic hip joints [4], while the discovery of bioactive glass, which directly binds to bones, brought a new generation of bone tissue replacement products to the market [5]. Since then, the development of bone substitutes, fillers, and cements, which are bioresorbable, have been the focus of considerable interest.

Regarding structural applications, the revolution came from the discovery in 1975 of the transformation toughening phenomenon occurring in zirconia [6], which led to the development of tetragonal zirconia polycrystals (TZP). Two decades later, yttria-stabilized zirconia (Y-TZP)

ceramics became a popular alternative to alumina thanks to their outstanding fracture toughness and higher strength [4,7]. Nevertheless, issues related to the phenomenon of ageing, also known as hydrothermal degradation or low temperature degradation (LTD), that will be discussed later, were at the origin of the early failure of Prozyr® zirconia femoral heads in 2002 [8]. Even if the cause of this unfortunate event was process related and clearly identified, Y-TZP suffered from bad publicity in the orthopedic community and the development of other materials such as ceria-stabilized TZP (Ce-TZP) and zirconia-alumina composites was encouraged. In particular, zirconia-toughened alumina (ZTA) has become the gold standard for the fabrication of ceramic load-bearing components for joint replacements. Meanwhile, the use of Y-TZP as a bioceramic has not been abandoned: in particular, the utilization of Y-TZP for the fabrication of dental components such as crowns, bridges, abutments or implants has been growing fast in the last decade.

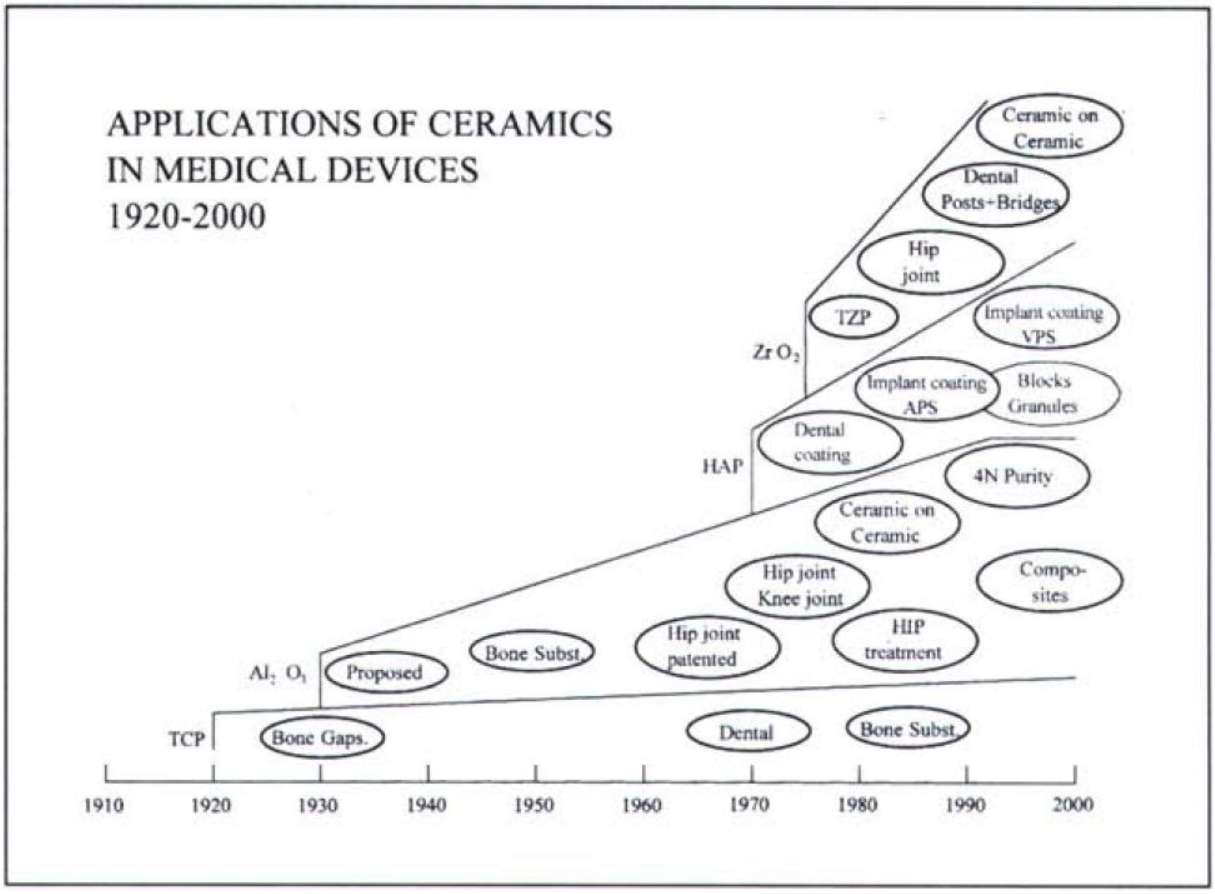

Figure 1.1. Application of ceramics in medical devices from 1920 to 2000 (reproduced from [4]).

1.1.2. Bioinert and bioactive ceramics

Bioceramics can be classified into two families depending on the type of peri-implant tissue response:

- Ceramics for which no direct bone-material interface is created are referred to as "bioinert" (although a material should never be considered as totally inert). Alumina, zirconia and their composites belong to this category.
- Ceramics that attach directly by chemical bonding to the bone are referred to as "bioactive" [1]. This is the case of bioactive glass and calcium phosphates.

This classification can be refined by considering the porosity and the resorbability of the material (see Table 1.1).

Table 1.1. Tissue attachment and bioceramic classification (reproduced from [1]).

Table II. Types of Bioceramics –Tissue Attachment and Bioceramic Classification

Type of bioceramic	Type of attachment	Example
1	Dense, nonporous, nearly inert ceramics attach by bone growth into surface irregularities by cementing the device into the tissues, or by press fitting into a defect (termed morphological fixation).	Al_2O_3 (single crystal and polycrystalline)
2	For porous inert implants bone ingrowth occurs, which mechanically attaches the bone to the material (termed biological fixation).	Al_2O_3 (porous polycrystalline) Hydroxyapatite-coated porous metals
3	Dense, nonporous, surface-reactive ceramics, glasses, and glass-ceramics attach directly by chemical bonding with the bone (termed bioactive fixation).	Bioactive glasses Bioactive glass-ceramics Hydroxyapatite
4	Dense, nonporous (or porous), resorbable ceramics are designed to be slowly replaced by bone.	Calcium sulfate (plaster of Paris) Tricalcium phosphate Calcium phosphate salts

In the case of bioinert ceramics, a soft tissue interlayer always shields the bone from the implant. This unfortunately leads to mechanical stress shielding of the bone, known to promote micro-motion and subsequent aseptic implant loosening. On the other hand, the poor mechanical properties of bioactive ceramics impair their use for structural applications [7]. Overall, so far, no tough and strong ceramic is able to create a good interface with bone. Hence, there is much interest in developing surface modification processes that improve bone anchorage of bioinert ceramics.

1.2. Alumina and zirconia based ceramics for biomedical applications

Alumina, zirconia and their composites are tough and strong ceramics (see Table 1.2), biocompatible and chemically resistant [9]. Besides, they exhibit a very low wear rate and release negligible quantities of metallic ions. This excellent combination of properties makes them an interesting alternative to metals for structural biomedical applications [10,11]. They have become materials of choice in orthopedics: in the last three decades, more than 3.5 million alumina, 600 thousand zirconia and 6 million ZTA components (e.g., femoral heads, inserts…) have been implanted worldwide [7,12]. Furthermore, their white color gives them a clear esthetical advantage for dental applications, in which the use of zirconia-based ceramics is growing fast [13,14].

Table 1.2. Mechanical properties of different bioceramics (reproduced from [7]).

Material	Toughness (K_{IC}, MPa m$^{1/2}$)	Threshold (K_{I0}, MPa m$^{1/2}$)	Strength (MPa)	Vickers hardness
Alumina	4.2	2.4	400–600	1800–2000
Zirconia	5.4	3.5	1000	1200–1300
A10Z0Y	5.8	4	700–900	1800
Hydroxyapatite	0.9	0.6	50–60	500
Tricalcium phosphate	1.3	0.8	50–60	900
Mg-PSZ	8	6	600	1000
12Ce-TZP	7.8	5.1	700	1000–1100
Micro-nano-alumina–zirconia	6	5	600	1800
Nano-nano-Ce-TZP–alumina	8.4	4.6	900	1300
Silicon nitride	10*	?	1000*	2500

Toughness (K_{IC}) and threshold stress intensity factor (K_{I0}) were measured by the Double Torsion method (except for values with *, extracted from Ref. 23) and strength by four point bending.

1.2.1. Alumina as a bioceramic

Most of alumina biomedical devices consist of polycrystalline α-Al_2O_3 produced by pressing and sintering at temperatures ranging from 1600 °C to 1800 °C [15]. A small amount of additives such as magnesium oxide (<0.5%), associated sometimes to zirconium oxide, is generally used as a grain growth inhibitor, and is essential to achieve a fully dense microstructure with fine grains. Strength, fatigue resistance and fracture toughness are a function of density, grain size and purity [15,16]. As mentioned above, alumina was the first ceramic to be used in total hip replacements (THR). In the 1980s, the progresses in powder processing, which enabled grain size reduction of the sintered alumina ceramics from 10 µm down to 2 µm, improved significantly their performances [17]. Alumina exhibits a very high hardness, and a satisfying flexural strength but a rather low fracture toughness and high sensitivity to surface flaws, which increase the risk of failure and limit design flexibility (see Table 1.2).

1.2.2. Zirconia as a bioceramic

Zirconia is a well-known polymorph that occurs in three forms: monoclinic (m), cubic (c) and tetragonal (t) (Figure 1.2). Pure zirconia is monoclinic at room temperature but the tetragonal phase can be stabilized by alloying with other oxides [18,19]. In 1975, Garvie *et al.* discovered the phenomenon of phase transformation toughening: under tensile stress, the metastable tetragonal phase can transform into monoclinic. This t-m phase transformation implies a volume expansion of about 3-4 %. The consequent grain expansion under matrix constraint is the origin of a compressive stress field that operates inversely to the tensile stress that leads the crack. The result is that the phase transition "stops the crack", and the fracture toughness of the material is increased (Figure 1.3) [6,20].

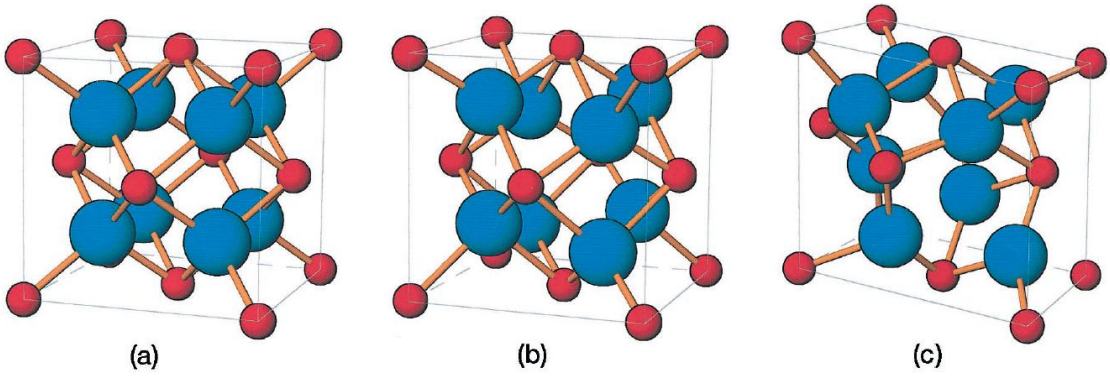

Figure 1.2. Schematic representation of the three polymorphs of ZrO_2: (a) cubic, (b) tetragonal, and (c) monoclinic (reproduced from [20]).

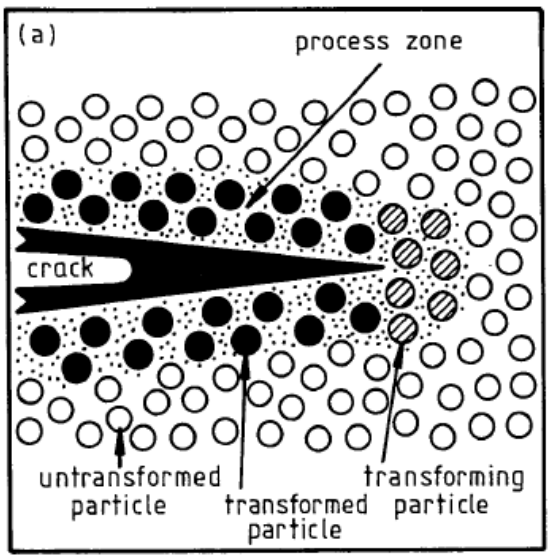

Figure 1.3. Representation of stress-induced transformation toughening process. Energy of the advancing crack is dissipated in phase transformation and in overcoming the matrix constraint by transforming grains (reproduced from [21]).

Thanks to phase transformation toughening, zirconia exhibits the best mechanical properties of single-phase oxide ceramics: a high bending strength, high fracture toughness and fairly high hardness (see Table 1.2 and Table 1.3). These properties made it a good candidate to replace alumina for biomedical applications [8]. Historically, several solid solutions, such as ZrO_2-MgO, ZrO_2-CaO and ZrO_2-Y_2O_3 were tested for this purpose, but rapidly research efforts focused on yttria-stabilized zirconia. Indeed, thanks to their fine grained microstructures, Y-TZP have the best mechanical properties of TZP ceramics (see Figure 1.4) [18]. In particular, 3 mol. % Y-TZP (3Y-TZP) exhibit the best combination of strength, toughness and hardness [20].

Table 1.3. Alumina vs. zirconia bioceramics comparative assessment (reproduced from [4]).

Comparable properties	Advantages ZrO_2	Advantages Al_2O_3
Biocompatibility	Strength	Historical experience
Geometry (surface, sphericity)	Young's modulus	Price
Chemical and corrosion resistance	Burst strength	Hardness
Life expectancy of implant	Fracture toughness	
Hard-hart articulation	Safety	

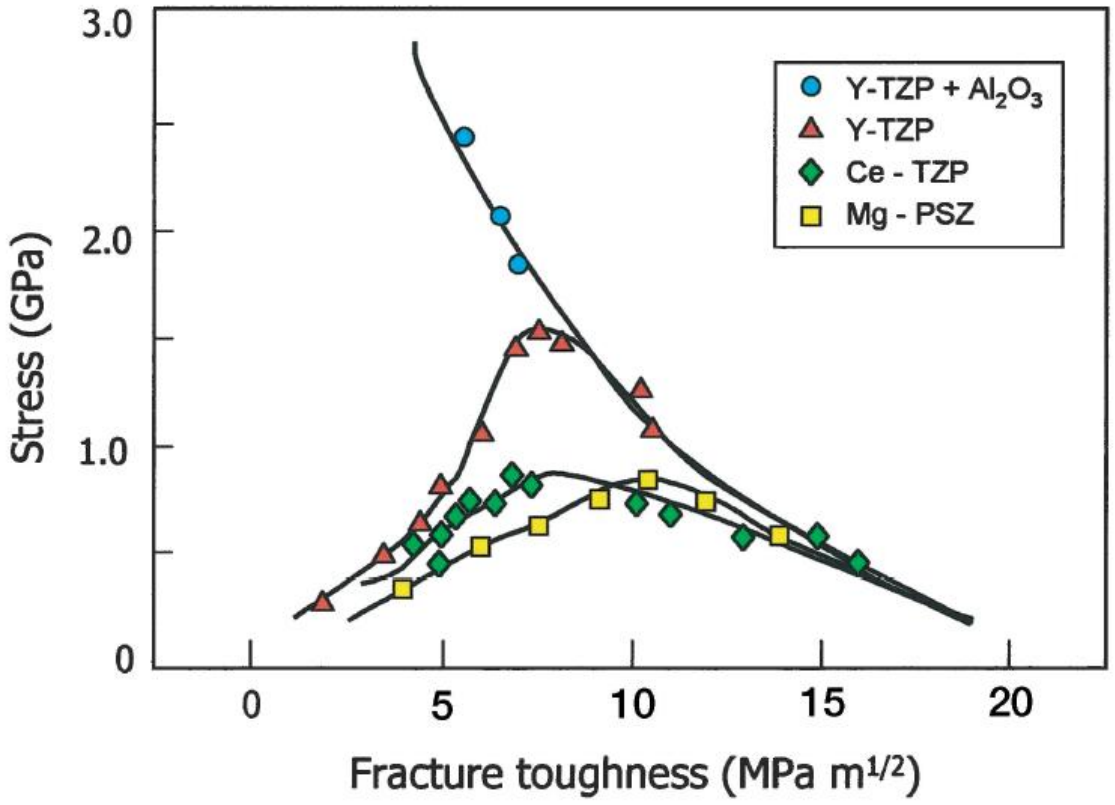

Figure 1.4. Strength versus fracture toughness for a selection of ZrO_2-toughened engineering ceramics. Maximums in the curves indicate a transition from flaw-size control of strength to transformation limited strength (reproduced from [20]).

Unfortunately, because of the metastability of the tetragonal phase, TZP ceramics are prone to ageing [22]. Ageing occurs by a water-assisted phase transformation, which propagates at the surface by a nucleation-and-growth mechanism and then invades the bulk (Figure 1.5). It results in roughening and microcracking, which in the case of femoral heads induces wear and the release of wear debris in the body. In the worst cases, it leads to failure of the component [23].

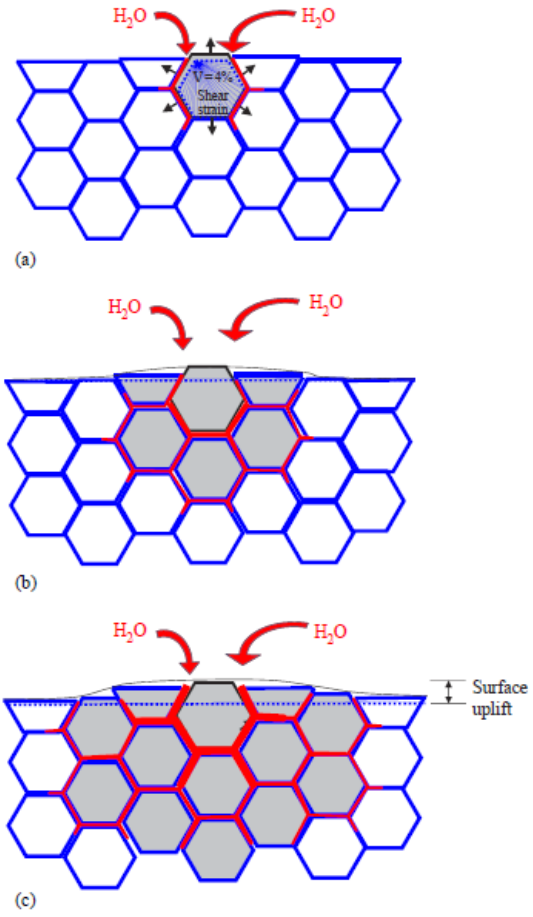

Figure 1.5. Scheme of the ageing process occurring in a cross section, showing the transformation from neighbor to neighbor. (a) Nucleation on a particular grain at the surface, leading to microcracking and stresses to the neighbors. (b) Growth of the transformed zone, leading to extensive microcracking and surface roughening. Transformed grains are gray. Red path represents the penetration of water due to microcracking around the transformed grains (reproduced from [8]).

The ageing phenomenon is complex and not fully understood at the moment. It is influenced by the presence of oxygen vacancies, which, in the case of Y-TZP, are induced by the difference of valence between yttrium and zirconium ions. Ageing behavior also depends on several parameters such as grain size, sintering conditions, residual stresses and porosity and is

thus very sensitive to processing changes, which explains the unexpected failure of Prozyr® femoral heads mentioned previously [23–25]. However, since this event, improved techniques have been developed to monitor and predict ageing behavior, which helps design safer implants [23]. Besides, it has been shown that adding small amounts of Al_2O_3 and incorporating the stabilizer by yttria coating of the ZrO_2 starting powder had a pronounced effect on retarding the degradation without compromising on the transformation induced fracture toughness [26]. In parallel, a lot of research efforts have been done to find an alternative to Y-TZP by using other dopants. The best example is the development of Ce-TZP: since cerium and zirconium ions have the same valence, cerium does not induce oxygen vacancies in the crystalline structure, which drastically reduces their ageing sensitivity.

1.2.3. Zirconia-toughened alumina as a bioceramic

As discussed above, despite their good properties, both alumina and zirconia present limitations for biomedical applications: alumina is very hard, but not tough and strong enough while zirconia is tough and strong but not as hard and suffer from ageing (Table 1.3). Therefore the idea of fabricating composites to obtain a material that combines the assets of both ceramics without their drawbacks is appealing. Zirconia-alumina composites can be divided into two main categories, depending on which oxide constitutes the main phase: alumina-toughened zirconia ceramics (ATZ) and zirconia-toughened alumina ceramics (ZTA). Although ATZ exhibit some interesting properties, in particular a lower susceptibility to ageing as compared to 3Y-TZP [27], the present manuscript will focus on ZTA, which is currently the gold standard for the fabrication of orthopedic load-bearing components.

ZTA is an alumina matrix composite ceramic, in which alumina is the primary or continuous phase and zirconia is the secondary phase (Figure 1.6). Under the condition that most of the zirconia is retained in the tetragonal phase, the addition of zirconia to alumina results in higher strength and fracture toughness (Figure 1.7) with little reduction in hardness and elastic modulus as compared to monolithic alumina ceramics. Additionally, the excellent wear characteristics and low susceptibility to stress-assisted degradation of alumina ceramics are preserved [28].

ZTA ceramics exhibit two main toughening mechanisms: phase transformation toughening, which is similar to the phenomenon observed in monolithic zirconia, and microcrack toughening. Microcrack toughening occurs as follows: some zirconia particles transform to the monoclinic phase during cooling, and tangential stresses are generated around the transformed monoclinic ZrO_2 particles. These, in turn, induce microcracks at the boundaries between the

inclusions and the matrix. The microcracks, by their ability to open in the stress field of a propagating crack, or deflect the propagating crack, can then absorb fracture energy [29].

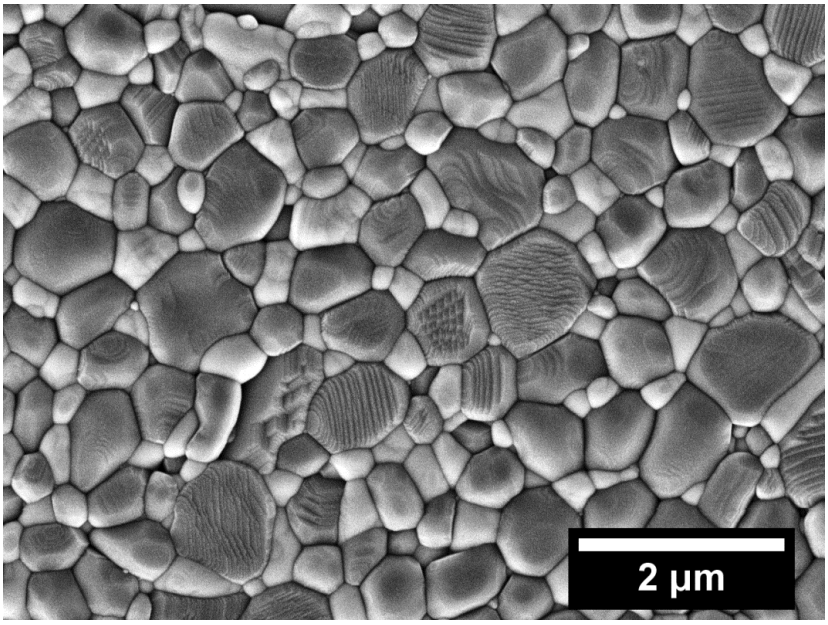

Figure 1.6. Microstructure of a zirconia-toughened alumina composite with 17 vol.% zirconia content. Alumina grains appear darker than zirconia grains.

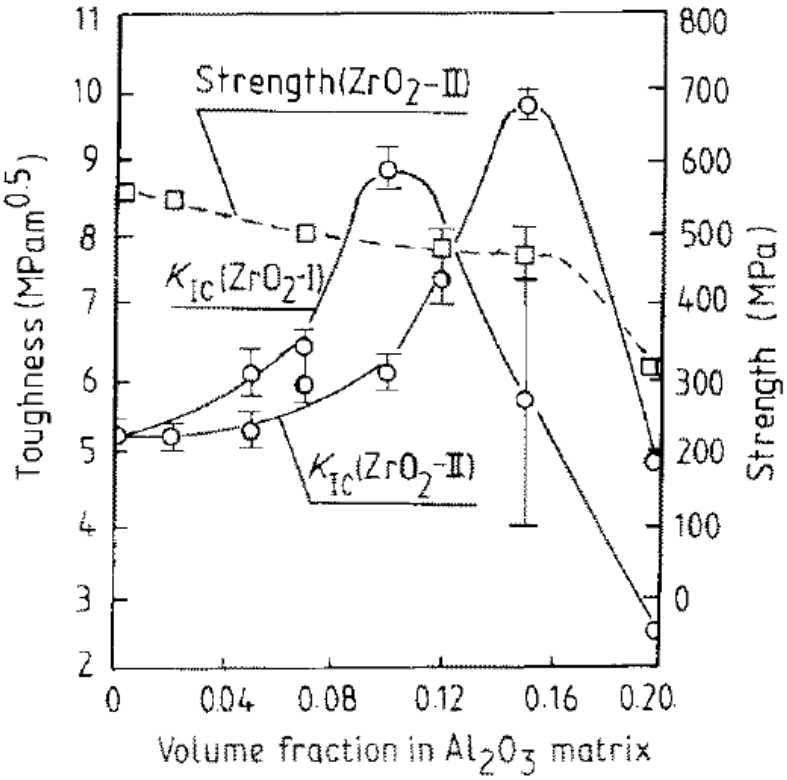

Figure 1.7. Fracture toughness and strength of alumina matrix containing unstabilized zirconia particles as a function of the zirconia volume fraction (reproduced from [29]).

The zirconia phase which is added to alumina can be either pure ZrO_2 (in this case there is a partial stabilization of the tetragonal phase by residual compressive stresses due to the alumina matrix) or TZP (e.g., Y-TZP or Ce-TZP). The main difference between these two forms of ZTA lies in the primary toughening mechanism: microcrack toughening in the former, transformation toughening in the latter [20].

Regarding hydrothermal stability, if the zirconia secondary phase is stabilized with yttria, ageing is possible but much slower than with monolithic zirconia, and can be avoided if the zirconia volume fraction is chosen below the percolation point [30,31]. In the case that the zirconia secondary phase is not stabilized, ageing seems to be occurring by water diffusion within the cracks created during cooling. If the zirconia volume fraction is kept low enough, those microcracks are not percolated, thus water is not able to diffuse and the material shows no evidence of ageing [31].

1.3. Biological response to implant materials

1.3.1. Osteoinduction, osteoconduction and osseointegration

Osteoinduction, osteoconduction and osseointegration are three key concepts related to bone response when implanting a device, but their definition can change depending on the authors. We report here the definitions proposed by Albrektsson and Johansson in ref. [32].

- Osteoinduction: this term means that primitive, undifferentiated and pluripotent cells are somehow stimulated to develop into the bone-forming cell lineage. One proposed definition is the process by which osteogenesis is induced. It is a phenomenon regularly seen in any type of bone healing process. Osteoinduction implies the recruitment of immature cells and the stimulation of these cells to develop into preosteoblasts. In a bone healing situation such as a fracture, the majority of bone healing is dependent on osteoinduction.
- Osteoconduction: this term means that bone grows on a surface. An osteoconductive surface is one that permits bone growth on its surface or down into pores, channels or pipes.
- Osseointegration: the term was first defined as direct contact (at the light microscope level) between living bone and implant. Osseointegration is also histologically defined as the direct anchorage of an implant by the formation of bony tissue around the implant without the growth of fibrous tissue at the bone-implant interface (see Figure 1.8). Since the histological definitions have some shortcomings, mainly that

they have a limited clinical application, another more biomechanically oriented definition of osseointegration has been suggested: "a process whereby clinically asymptomatic rigid fixation of alloplastic materials is achieved, and maintained, in bone during functional loading".

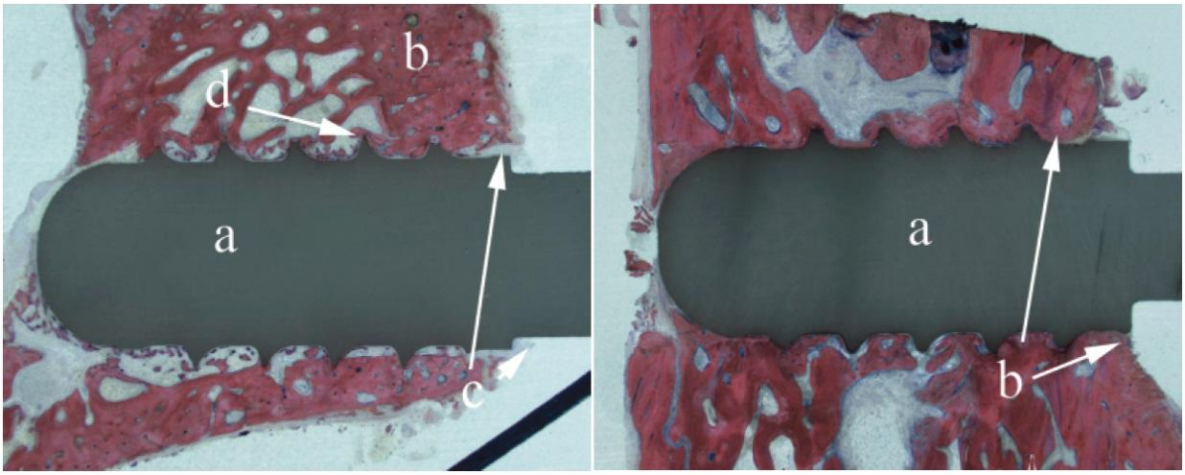

Figure 1.8. Left: zirconia machined implant showing a low degree of bone-to-implant contact after 12 weeks of healing: (a) implant; (b) bone; (c) tissue at the neck of the implant; (d) peaked threads. Right: zirconia sandblasted implant showing a high degree of bone to implant contact after 12 weeks of healing: (a) implant; (b) arrows showing mineralized bone at the neck of the implant (reproduced from [33]).

Osteoinduction, osteoconduction and osseointegration are interrelated, but not identical phenomena. Osteoinduction is part of normal bone healing and is responsible for the majority of newly formed bone. The implant itself may be osteoinductive, but this is not a prerequisite for bone induction. Osteoconduction and osseointegration both depend not only on biological factors, but also on the response to a foreign material [32].

Both zirconia and alumina have been shown to be osteoconductive [9,34,35]. Nevertheless, the osteoconductive response may be rather short lived, contrary to successful osseointegration, which maintains bone anchorage over a long period [32]. As will be discussed in the next sections, surface design is one of the keys to achieve it, which shows the need for developing surface modification processes able to promote osseointegration of zirconia-based ceramic implants.

1.3.2. Influence of surface properties on bone tissue response

Numerous factors affect bone tissue response: implant material, implant design, surface conditions (Figure 1.9), porosity, status of the bone, surgical technique and implant loading

conditions [36]. Nevertheless, considering the scope this thesis, this section will focus on the influence of surface properties.

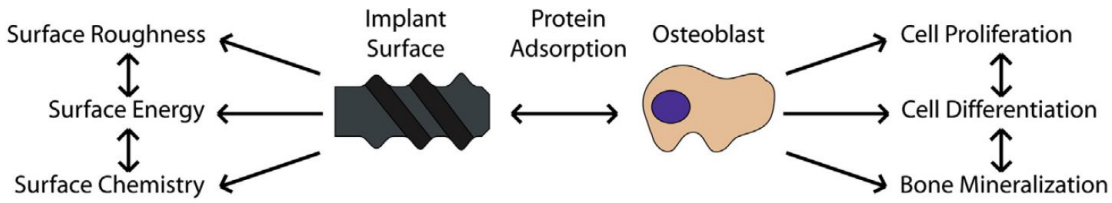

Figure 1.9. Diagram showing the direct and indirect interactions between surface properties (e.g. surface roughness, surface energy, surface chemistry) and biological events, such as protein adsorption and osteoblast response (e.g. proliferation, differentiation, bone mineralization). Reproduced from [37].

The surface characteristics of an implant that influence the speed and quality of osseointegration are numerous: they include surface chemistry, topography, wettability, charge, surface energy, crystal structure and crystallinity, roughness, chemical potential, the presence of impurities... [36,37] Wettability and free surface energy, which is directly related to roughness, play an important role. It has been demonstrated that osteoblast adhesion is related to the degree of roughness and the hydrophobicity / hydrophilicity of a surface [38]. Hydrophilic surfaces are better for blood coagulation than hydrophobic surfaces [36] and hydrophilic treatments on zirconia seem to enhance initial attachment of osteoblast-like cells [39]. Besides, it has been suggested that increased hydrophilicity could accelerate dental implant osseointegration [40]. However, whether or not hydrophilicity has a beneficial effect on implant anchorage is still questioned [41].

Roughness is a scale-dependent measurement and usually authors distinguish micro-roughness (roughness at the micrometer scale) from nano-roughness (roughness at the nanometer scale). Each topographical scale influence tissue response at a different level (Figure 1.10).

On the one hand, implant micro-roughness has been shown to strongly influence bone response [37,41–43]. On surfaces with rough micro-topographies, osteoblasts secrete factors that enhance osteoblast differentiation and decrease osteoclast formation and activity [44]. Besides, it has been demonstrated experimentally that osseointegration can be improved and accelerated through various roughening procedures and that there exists an optimal range in the micrometer scale [43]. The so-called moderately micro-roughened implant surfaces have been proven to present improved osseointegration in several experimental and clinical studies [42,45].

On the other hand, implant nano-roughness can influence osteoblast and stem cell behavior [41–43]. The positive effect of surfaces presenting nanoscale features on the adhesion, spreading, motility, proliferation, adhesion selectivity, and differentiation has been reported

[37,46–51], evidencing that certain cellular phenomena can be triggered through nanometer length-scale modification. Furthermore, it has been suggested that the combination of both micro- and nano-roughness can have synergistic effects [52]. Nevertheless, little is known beyond data from *in vitro* experiments, and further research is needed to validate the clinical relevance of these observations [41,43].

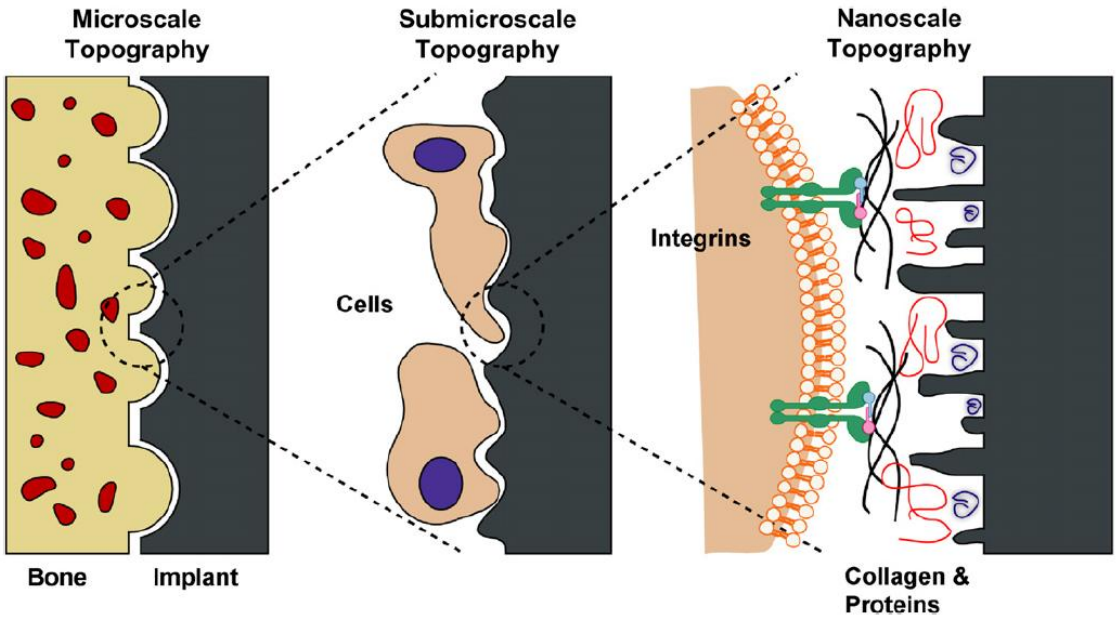

Figure 1.10. Schematic of the interactions between bone and the implant surface at different topographical scales (reproduced from [37]).

Finally, the degree of organization of a surface might play an important role: Anselme *et al.* showed that fractal parameters have an influence on cell behavior [53], whereas Dalby *et al.* evidenced that nanoscale disorder was able to stimulate human mesenchymal stem cell (hMSC) production of bone mineral *in vitro*, in the absence of osteogenic supplements [54].

Despite a huge number of studies, there is currently no consensus on the optimal surface topography required to promote osseointegration [55]. One of the reasons for this lack of knowledge is that the majority of published papers present an inadequate or insufficient surface characterization [42]. Another reason is that there is a strong interdependence between surface properties, which makes difficult to isolate the effect of a single parameter. In any case, there is a need for further research including more in-depth surface characterization.

1.3.3. Bacterial adhesion versus tissue integration: the race for the surface

It is well known that biomedical implants provide a substrate for the adhesion of bacteria, which can proliferate and form biofilms, dramatically increasing the resistance to therapeutic

agents [56]. The so-called "race for the surface" between bacteria and host cells makes it therefore critical to eliminate or contain pathogens as early as possible [57,58] and there is a strong interest in developing surfaces that can prevent infections, which have become the leading cause for arthroplasty revision [59–61]. Osseointegration and infection prophylaxis are often treated as separated issues. However, they are intimately related and should be addressed simultaneously [58,61]. As for host cells, surface properties such as topography and chemistry have a strong influence on bacterial adhesion (Figure 1.11) and growth [62,63]. Hence, one of the main issues faced when designing an implant is that a surface that promotes tissue integration may also favor biofilm formation. Ideally, surfaces with multiple functionalities that reliably select host cells over pathogens should thus be created. To do so, numerous surface engineering strategies have been explored (Figure 1.12). A lot of them involve the use of coatings, either to prevent bacterial adhesion thanks to a specific surface chemistry/topography or to the release of antibacterial agents [58,61].

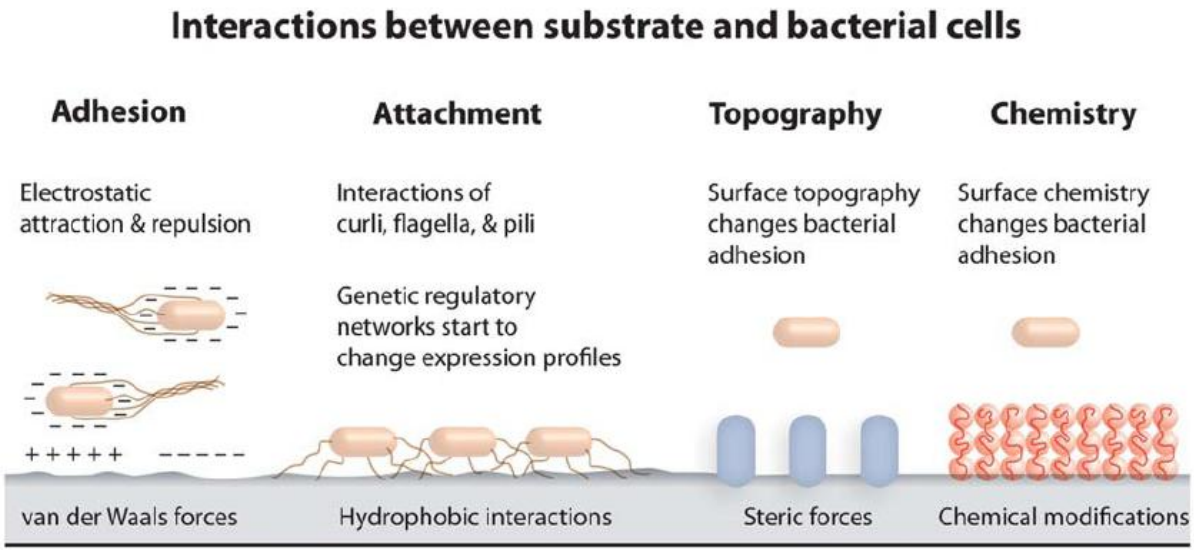

Figure 1.11. Properties of the surface such as charge, hydrophobicity, topography, and the identity of the exposed chemical groups interact with physico-chemical properties of bacterial cells and influence attachment (reproduced from [62]).

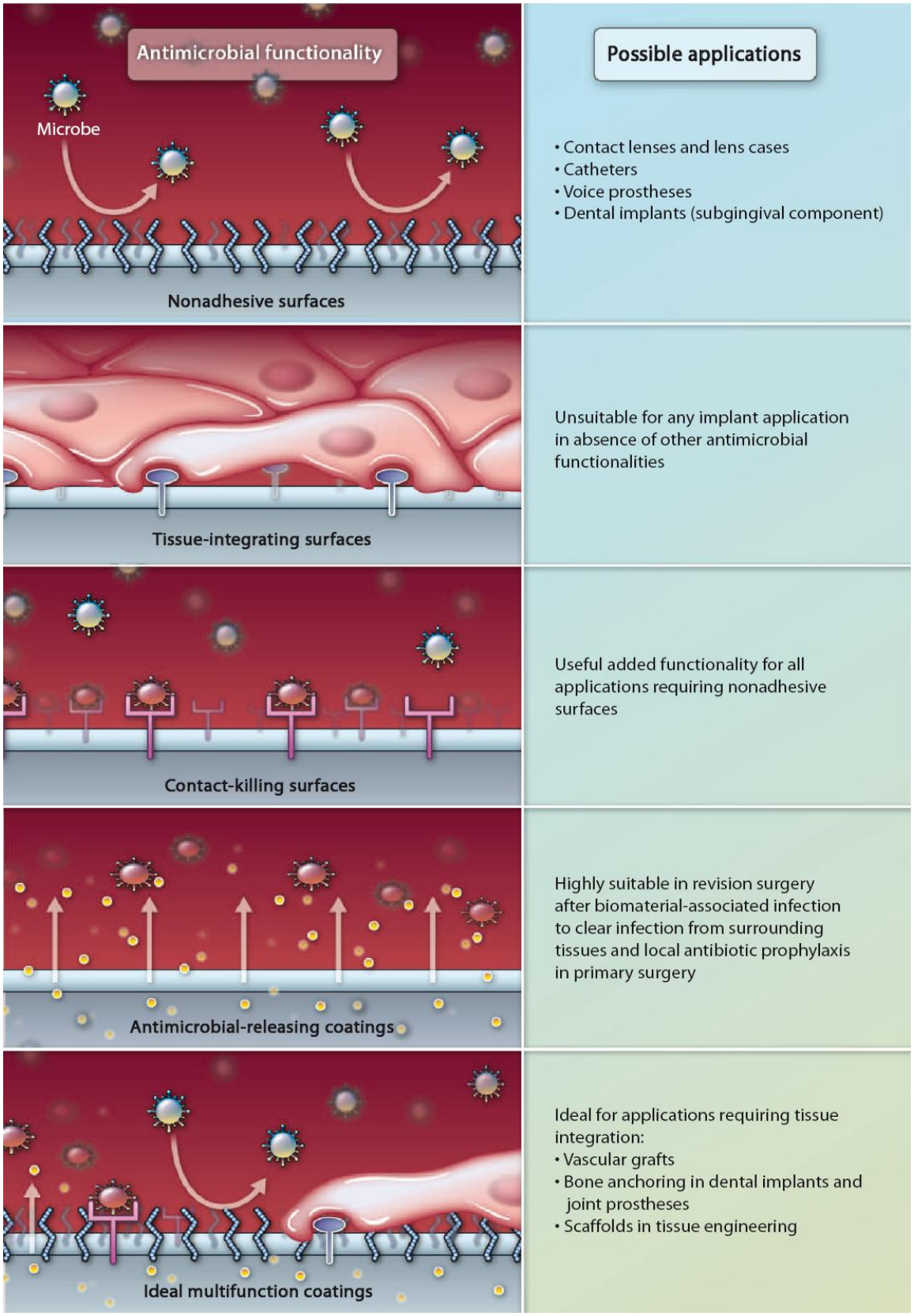

Figure 1.12. Function requirements to biomaterials and coatings in different clinical applications. A schematic presentation of different antimicrobial functionalities that can be added to the surface of a biomaterial implant or device, together with their possible application (reproduced from [58]).

1.4. Surface modifications of zirconia-based ceramics and their impact on reliability

As discussed in the previous section, surface properties have a strong influence on bone response and biofilm formation. Hence, numerous processes have been proposed to modify the surface of ceramic implants, with the purpose of improving osseointegration and limiting infections. Nevertheless, ceramics are sensitive to surface alterations. In particular surface defects have a strong influence on their strength [64]. Furthermore, as discussed previously, in the case of zirconia-containing ceramics, the ageing sensitivity should be assessed with a special care after any change in the fabrication route. Accordingly, the present section gives an overview of the processes that have been proposed to modify the surface of zirconia-based ceramic implants and of their impact on reliability (when documented). Considering the scope of this thesis, a special emphasis is given to the processes aiming to modify the topography.

1.4.1. Machining and grinding

Machining and grinding are part of the typical processing route of implants. By monitoring the processing conditions, it is possible to control the topography to some extent [65]. Nevertheless, these conditions also have a strong influence on the mechanical properties. Kosmač *et al.* found that dental grinding of Y-TZP at a high rotation speed leads to substantial strength degradation: it lowers the mean strength under static loading and the survival rate under cyclic loading [66,67]. By contrast, Muñoz-Tabarez *et al.* evidenced that the compressive residual stresses induced by grinding of Y-TZP could lead to an increase in strength [68]. Similarly, Xu *et al.* found that the strength of ZTA could decrease or not depending on grinding conditions [69]. Optimizing the balance residual stress / damage is thus critical to ensure implant reliability.

1.4.2. Sandblasting

Sandblasting on bioceramics is typically performed with alumina particles and results in a micro-rough surface. By varying parameters such as particle size, pressure or impact angle, it is possible to tailor the topography obtained [70]. Besides, it has been found that sandblasting performed on zirconia ground implants could improve osseointegration (Figure 1.8) [33]. Regarding mechanical properties, with adequate parameters the compressive residual stresses induced by the process can lead to an increase in flexural strength and higher survival rate under cyclic loading [66,67]. However, as for grinding, these parameters should be chosen carefully to avoid excessive damage [70–72].

1.4.3. Chemical etching

Chemical etching can induce a fine roughness, down to the nanoscale, which is why it is often combined to micro-roughening treatments (e.g., sandblasting) [73,74]. The most promising etchant for zirconia is hydrofluoric acid (HF). Although other chemicals, such as hypophosphorous acid or an equimolar mixture of potassium hydroxide and sodium hydroxide, have been reported to successfully etch Y-TZP [75,76], HF presents the advantage to be a fast etchant at room temperature. Besides, the incorporation of fluoride at the surface could enhance osteoblastic differentiation and interfacial bone formation and inhibit bacterial growth, as it does for titanium [77,78]. Furthermore, Gahlert *et al.* evidenced that HF etching of zirconia implants enhances bone apposition resulting in high removal torque values [79]. Finally, Ito *et al.* showed that the combination of sandblasting with HF etching leads to an increase in the proliferation rate and expression of ALP activity of osteoblast-like cells (MC3T3-E1) [73], Bergemann *et al.* found that it enhanced the human primary osteoblast maturation [80] and Saulacic et *al.* showed that acid etching of sandblasted zirconia increased bone-to-implant contact, which was not the case of alkaline etching [81].

1.4.4. Coating

Several coating strategies have been developed to improve an implant's ability to bond to bone. A first possibility is to deposit a coating of the same material as the substrate with a porosity that promotes osseointegration or even allows bone in-growth [24,82]. Nevertheless, in the absence of a careful control of the processing, porosity can impair mechanical properties and ageing resistance [24]. A second approach is to coat the implant with bioactive materials able to promote cell attachment, differentiation, and bone formation such as hydroxyapatite [83,84]. However, as discussed previously, these materials have poor mechanical properties, which may compromise long-term reliability. Additionally, a general issue related to coatings is the lack of adherence to the substrate and the associated residual stresses that may provoke delamination.

Regarding antibacterial coatings, literature is scarce for zirconia-based ceramics. An interesting approach is that implemented by Liu *et al.*, who showed that a polydopamine coating could reduce substantially bacterial activity [85]. Furthermore, numerous strategies have been developed for other materials and could be transposed to zirconia-based ceramics, such as the deposition of silver-releasing coatings, antibiotic-releasing coatings, polymer-brush coatings or chitosan coatings [61].

1.4.5. Other techniques

The processes detailed above are the most commonly reported but the list is far from exhaustive. Numerous other techniques have been proposed to modify the surface of ceramic implants. For instance, lasers can be used to modify topography: it has been shown that a YAG laser can efficiently increase surface roughness of zirconia [86]. Furthermore, thanks to its precision and the minimal damage induced in the processing area, it has been suggested that femtosecond laser microstructuring could offer an interesting alternative to conventional roughening treatments [87]. Regarding the modifications of surface physico-chemistry, several techniques have been experimented such as oxygen plasma, CO_2 laser, ultraviolet light or hydrogen peroxide treatment, which can increase the surface wettability [39,88,89]. Concerning infections, antibacterial strategies similar to those developed for titanium such as antibiotic immobilization or silver implantation might be successfully transposed to zirconia-based ceramics [61]. Finally, one of the most promising approach might be surface functionalization to immobilize biological agents, which have the potential to promote osteoinduction and osseointegration and limit biofilm formation: for instance Schickle *et al.* managed to immobilize proteins on inert alumina surface [90] and Fernandez-Garcia *et al.* succeeded to immobilize peptides on zirconia surface [91].

Chapter 2.

Aims and scope of the work

As has been shown in Chapter 1, zirconia-based bioceramics are bioinert, which hampers their implantation in direct contact with bone. On the other hand, infections are a major cause of failure for implants. One of the keys to address both issues is an optimized surface design, which can improve osseointegration and limit infections. There is thus a strong interest in developing processes to tailor surface properties. On the other hand, surface modifications can have a negative impact on implant reliability, which should thus be carefully assessed.

Based on these observations, the main objective of this thesis was to develop processes to modify the surface of zirconia-based implants, in particular the topography, without compromising their mechanical properties and hydrothermal stability. The research effort focused on two materials of particular interest, which were described in details in Chapter 1: yttria-stabilized zirconia (3Y-TZP), which is increasingly used for prosthodontic applications, and zirconia toughened alumina (ZTA), which is the current gold standard in orthopedics for the fabrication of load-bearing ceramic components. Accordingly, this work can be divided into two main parts.

2.1. Surface modification of zirconia by hydrofluoric acid etching

As reported in numerous studies (see Chapter 1), hydrofluoric acid (HF) etching can be used to induce roughness on zirconia with the purpose of improving osseointegration. Nevertheless, even if acid etched dental implants are already on the market (CeraRoot with ICE surface®), little is known about this process. The first part of this work was thus dedicated to the understanding, development and optimization of the HF etching of zirconia.

2.1.1. Understanding the etching mechanism and finding suitable processing conditions

Addressed in: **Article I**

The first objective of this thesis was to understand the HF etching mechanism through the study of the etching solution and the etching products, and to establish suitable conditions for a fast and uniform roughening of the zirconia surface.

2.1.2. Correlating processing conditions and surface properties

Addressed in: **Article I**

As discussed in Chapter 1, most of the studies about surface modification of implants present an improper or incomplete surface characterization. Hence, the second objective of this thesis was to perform an in-depth chemical, microstructural and topographical analysis of the zirconia surface after HF etching, and to establish correlations between the surface properties, in particular the topographical parameters, and the etching conditions.

2.1.3. Evaluating the impact of HF etching on reliability

Addressed in: **Article II**

As discussed in 1.2, minor changes in the fabrication of zirconia components may affect their resistance to hydrothermal degradation. Besides, as for other ceramics, surface alterations can have a strong impact on their mechanical properties. In spite of the common use of acid etching on zirconia, to the best of the knowledge of the author, no assessment of the effects of this process on implant reliability had been reported. The third objective of this work was thus to evaluate the impact of HF etching on surface integrity, strength and resistance to ageing of zirconia.

2.1.4. Fabrication of roughness gradients for rapid screening of cell-surface interactions

Addressed in: **Article III**

Cell-surface interactions are still poorly understood. One factor that explains this lack of knowledge is the large amount of time and resources required in classical cell studies. To address this issue, the fourth objective of this thesis was to develop a method to induce roughness gradients at the surface of zirconia by HF etching. To get an insight of the influence of topography on the early response of human bone marrow derived mesenchymal stem cells (hMSCs) and to validate the method, hMSCs were cultured on the gradient samples, and potential correlations between topographical parameters and cell morphology were systematically investigated.

2.2. Surface modification of zirconia-toughened alumina

As discussed in Chapter 1, ZTA is bioinert, which hampers its implantation in direct contact with bone. Furthermore, periprosthetic joint infections are now the leading cause of failure for joint arthroplasty prostheses. To address both issues, in the second part of this thesis

we developed an integrated strategy aiming to provide both osseointegrative and antibacterial properties to ZTA surfaces.

2.2.1. Tailoring the micro-topography by injection molding

Addressed in: **Annex A**

As discussed in 1.3.2, surface micro-roughness has a strong influence on bone response. The first objective of this second part was thus to produce ZTA specimens with a tailored micro-topography. Among the diverse surface micro-structuring techniques existing for ceramics, injection molding was selected as the most promising. In contrast to grinding or sandblasting for instance, it does not induce additional surface defects. Besides, it provides a high flexibility since it is theoretically possible to obtain any kind of micro-topography. Finally, it enables the mass production of complex components, which is an advantage from an industrial point of view.

2.2.2. Inducing nano-roughness and surface porosity by selective etching

Addressed in: **Annex A**

As discussed in 1.3.2, surface nano-roughness influences osteoblast and stem cell behavior. Furthermore, porosity can be used to load therapeutic agents. Accordingly, the second objective was to induce nano-roughness and porosity at the surface of ZTA, without affecting the micro-topography obtained by injection molding. To do so, a novel process involving the selective dissolution of zirconia by HF (selective etching) was developed.

2.2.3. Using surface porosity for drug delivery

Addressed in: **Annex A**

The third objective was to prove that the surface porosity obtained by selective etching can be used to load and deliver antibiotics in order to provide antibacterial properties to the surface. Different loading methods were experimented and *in vitro* drug release experiments and bacteria cultures were carried out to demonstrate the concept.

2.2.4. Evaluation of the impact of selective etching on reliability

Addressed in: **Annex A**

Porosity can have a strong impact on ceramic mechanical properties. Besides, as discussed in 1.2, any surface modification of zirconia-based ceramics should be followed by an assessment of its effect on mechanical properties and resistance to hydrothermal degradation. The last objective of this work was thus to evaluate the impact of selective etching on surface mechanical properties, strength and hydrothermal stability.

Chapter 3.

Summary of the results

3.1. Surface modification of zirconia by hydrofluoric acid etching

3.1.1. Determination of suitable etching conditions

Among the different concentrations tested, 40 wt.% seems to be the most suitable for the HF solution because it leads to the fastest and most homogeneous roughening of the surface (**Article I**). Regarding etching time, it appears that it should be kept below one hour, since a longer duration induces substantial damage and decrease in strength (**Article II**).

3.1.2. Etching mechanism

The following etching mechanism was suggested by the analysis of the etching products and the etching solution (**Article I**):

- HF dissolves zirconium oxide and yttrium oxide. Fluoride, oxide, and hydroxide complexes are formed. Etching is slightly preferential at the grain border, but also occurs inside the grains.
- Yttrium complexes have very low solubility. From the beginning of the etching process, yttrium trifluoride (YF_3) octahedral crystals precipitate on the surface.
- Zirconium complexes are partially soluble. After a certain time, an “adhered layer” composed of yttrium, zirconium and fluorine precipitates, probably because the saturation threshold for zirconium fluoride complexes is reached.

Furthermore, the exponential relationship between mass loss and concentration suggested the existence of a phenomenon of auto-catalysis.

3.1.3. Tailoring surface properties by monitoring etching time

The characterization of surface topography evidenced that it is possible to control roughness and fractal parameters by monitoring etching time (**Article I**, **Article III**). HF etching also induces an increase in the fluorine content of the surface but it is not correlated to the duration of the treatment (**Article I**).

3.1.4. Impact of etching on reliability

HF etching induces a sub-superficial damage, an increase in monoclinic phase content and a decrease in the biaxial flexural strength. In both cases, these changes do not exceed 15 % for etching durations below one hour. Besides, HF etched zirconia does not seem to exhibit an increased sensitivity to low temperature degradation. The strength of etched specimens can even increase with ageing, which could be explained in terms of crack tip blunting by phase transformation (**Article II**).

3.1.5. Fabrication of roughness gradients and rapid screening of hMSC morphology

Roughness gradients have been successfully produced at the surface of zirconia by controlling the speed of immersion of specimens into HF. The variation of topography influenced hMSC morphology, with significant changes in cell area, aspect ratio and solidity. Nano-topographical parameters were linearly correlated to cell solidity, while micro-topographical parameters appeared to be non-linearly correlated to cell area, which highlights the importance of multiscale optimization of implant topography (**Article III**).

3.2. Surface modification of zirconia-toughened alumina

3.2.1. Tailoring micro-topography by injection molding

Injection molding was shown to be a versatile process for surface micro-structuring, with a large possible range of values for roughness parameters such as the average roughness (S_a) and the developed interfacial area ratio (S_{dr}) (**Annex A**).

3.2.2. Inducing nano-roughness and surface porosity by selective etching

Selective etching is a novel process for ZTA, which can be used for two purposes (**Annex A**):

- With a short etching time, it allows superposing of a substantial nano-roughness to a pre-existing micro-topography such as that produced by injection molding, without affecting the bulk of the material. According to the literature, this combination of micro- and nano-roughness should be favorable in terms of osseointegration. Besides, the process induces an increase in the fluorine content of the surface that could enhance osteoblastic differentiation and interfacial bone formation as it does for titanium. Finally, bacteria cultures suggested that the selectively etched surface could reduce bacterial adhesion.

- With a longer etching time, it allows the production of an interconnected nanoporous alumina layer with a controlled thickness. This layer can be used for the loading of therapeutic agents (see next section).

3.2.3. Using surface porosity for drug delivery

In vitro release experiments demonstrated that the porous layer induced by selective etching has the potential to be used as a carrier for drug delivery, providing antibacterial properties to the surface. Furthermore, the proposed liposomal encapsulation technique improves antibiotic loading. Since liposomes can be loaded with both hydrophobic and hydrophilic molecules, the method is flexible. Nevertheless, the quantities loaded which represent about 0.5%-1% of the total porous volume available still appear small and there is thus room for optimization: in particular it should be possible to increase the quantity of drug loaded and the sustainability of the release by tuning liposome size (**Annex A**).

3.2.4. Evaluation of the impact of selective etching on reliability

The main benefit of selective etching when compared to other existing processes to produce nanoporous alumina on implants is that the layer obtained is not a coating. There is no interface with the bulk, which is highly beneficial in terms of reliability since it avoids any problem related to lack of adhesion or delamination. Furthermore, spherical nanoindentation testing evidenced that the contact behavior of the porous layer obtained is quasi-plastic (no cracks were observed under indentations), and the elastic modulus ($E \approx 275\ GPa$), the yield stress ($\sigma_y \approx 3300\ MPa$) and the indentation hardness (plateau at 8 GPa) are maintained at high values. Besides, it was shown that the presence of a ~10 µm thick porous layer does not impair flexural strength: the decrease in average strength, which was moderate, was compensated by an increase in Weibull modulus and the minimum strength was not affected. Finally, regarding phase transformation, the influence of selective etching is limited to a small increase in the initial volume of monoclinic phase content, without any impact on LTD kinetics. The excellent resistance to ageing of ZTA is thus not compromised by the treatment (**Annex A**).

Chapter 4. Conclusions and perspectives

4.1. Surface modification of zirconia by hydrofluoric acid etching

HF etching is a straightforward process that allows tailoring zirconia surface topography by monitoring the etching time. It results from a complex phenomenon involving the dissolution of zirconium and yttrium oxides and the precipitation of fluoride crystals, which is reported for the first time in this thesis. Etching has some impact on reliability, especially for long durations: it induces sub-superficial damage, an increase in monoclinic phase content and a decrease in the biaxial flexural strength. Nevertheless, HF etched zirconia does not seem to exhibit an increased sensitivity to low temperature degradation and the strength of etched specimens can even increase with ageing. Besides, as has been shown in another work from the author (not included in this thesis, see ref. [92]), reliability concerns can be addressed: the surface integrity and the resistance to ageing of etched specimens can be dramatically improved by a cerium salt infiltration and diffusion treatment.

Furthermore, roughness gradients can be fabricated by immersing specimens into HF with a controlled speed. A rapid screening of hMSC morphology on the gradients was carried out and evidenced correlations between cell morphology and micro- and nano-topography, which highlights the importance of multiscale optimization of implant surfaces. The gradient method has the potential to be transposed to other type of surfaces and cell-surface interaction studies, drastically reducing the amount of samples and resources required. The main shortcoming of this approach, however, lies in the intrinsic limitations of *in vitro* studies: while *in vitro* models allow a precise control of the culture conditions, they lack to reproduce the complex environment encountered by the implant inside the human body. Gradients should thus be used for screening purpose before moving to further *in vivo* evaluation of the most promising surfaces.

4.2. Surface modification of zirconia-toughened alumina

The combination of injection molding and selective etching, a novel process developed in this thesis, allows the manufacture of ZTA samples with a substantial nano-roughness superposed to a controlled micro-topography. Selective etching also enables the formation of an interconnected porous alumina layer, which can be used as a carrier for drug delivery. Furthermore, the liposomal encapsulation technique proposed in this work improves drug loading and provides a high flexibility regarding the choice of the therapeutic agent.

The main benefit of selective etching when compared to other existing processes to produce nanoporous alumina on implants is that the porous layer obtained is not a coating. There is no interface with the bulk, which is highly beneficial in terms of reliability. Moreover, the contact behavior of the layer is quasi-plastic and the elastic modulus, the yield stress and the hardness are maintained at high values. Finally, it was shown that the presence of a ~10 µm thick layer does not impair flexural strength and that the excellent resistance to ageing of ZTA is not compromised by the treatment.

An on-going cooperation with the AO Foundation (Davos, Switzerland) aims to study the influence of injection molding and selective etching on osteoblast behavior, and should give an insight into the potential held by these processes to improve osseointegration. Future studies should also aim to optimize drug loading and evaluate the impact of the porous layer thickness on mechanical properties.

References

[1] L.L. Hench, Bioceramics: From Concept to Clinic, J. Am. Ceram. Soc. 74 (1991) 1487–1510. doi:10.1111/j.1151-2916.1991.tb07132.x.

[2] A. Bobbio, The first endosseous alloplastic implant in the history of man., Bull. Hist. Dent. 20 (1972) 1–6.

[3] J.R. Kelly, I. Nishimura, S.D. Campbell, Ceramics in dentistry: historical roots and current perspectives., J. Prosthet. Dent. 75 (1996) 18–32.

[4] W. Rieger, Ceramics in orthopedics–30 years of evolution and experience, World Tribol. Forum Arthroplast. C. Rieker, S. …. (2001).

[5] J.R. Jones, Review of bioactive glass: From Hench to hybrids, Acta Biomater. 9 (2013) 4457–4486. doi:10.1016/j.actbio.2012.08.023.

[6] R.C. Garvie, R.H. Hannink, R.T. Pascoe, Ceramic steel?, Nature. 258 (1975) 703–704. doi:10.1038/258703a0.

[7] J. Chevalier, L. Gremillard, Ceramics for medical applications: A picture for the next 20 years, J. Eur. Ceram. Soc. 29 (2009) 1245–1255. doi:10.1016/j.jeurceramsoc.2008.08.025.

[8] J. Chevalier, What future for zirconia as a biomaterial?, Biomaterials. 27 (2006) 535–543. doi:10.1016/j.biomaterials.2005.07.034.

[9] Y. Josset, Z. Oum'Hamed, A. Zarrinpour, M. Lorenzato, J.J. Adnet, D. Laurent-Maquin, In vitro reactions of human osteoblasts in culture with zirconia and alumina ceramics., J. Biomed. Mater. Res. 47 (1999) 481–93. doi:10.1002/(SICI)1097-4636(19991215)47:4<481::AID-JBM4>3.0.CO;2-Y.

[10] L. Savarino, M. Greco, E. Cenni, L. Cavasinni, R. Rotini, N. Baldini, et al., Differences in ion release after ceramic-on-ceramic and metal-on-metal total hip replacement. Medium-term follow-up., J. Bone Joint Surg. Br. 88 (2006) 472–6. doi:10.1302/0301-620X.88B4.17333.

[11] A. Sargeant, T. Goswami, Hip implants – Paper VI – Ion concentrations, Mater. Des. 28

(2007) 155–171. doi:10.1016/j.matdes.2005.05.018.

[12] CeramTec, (2016). https://www.ceramtec.com/ceramic-materials/biolox/delta/ (accessed May 9, 2016).

[13] I. Denry, J. a. Holloway, Ceramics for Dental Applications: A Review, Materials (Basel). 3 (2010) 351–368. doi:10.3390/ma3010351.

[14] I. Denry, J.R. Kelly, Emerging Ceramic-based Materials for Dentistry, J. Dent. Res. 93 (2014) 1235–1242. doi:10.1177/0022034514553627.

[15] L.L.L. Hench, J. Wilson, An introduction to bioceramics, 1993.

[16] V. V. Lashneva, Y.N. Kryuchkov, S. V. Sokhan, Bioceramics based on aluminum oxide, Glas. Ceram. 55 (1998) 357–359. doi:10.1007/BF02694271.

[17] J. Li, G.W. Hastings, Oxide bioceramics: inert ceramic materials in medicine and dentistry, in: J.H.G. Black (Ed.), Handb. Biomater. Prop., Springer US, Boston, MA, 1998: pp. 340–354. doi:10.1007/978-1-4615-5801-9_21.

[18] C. Piconi, G. Maccauro, Zirconia as a ceramic biomaterial., Biomaterials. 20 (1999) 1–25.

[19] J. Chevalier, L. Gremillard, A. V. Virkar, D.R. Clarke, The Tetragonal-Monoclinic Transformation in Zirconia: Lessons Learned and Future Trends, J. Am. Ceram. Soc. 92 (2009) 1901–1920. doi:10.1111/j.1551-2916.2009.03278.x.

[20] A.H. Heuer, Transformation Toughening in ZrO2-Containing Ceramics, J. Am. Ceram. Soc. 70 (1987) 689–698. doi:10.1111/j.1151-2916.1987.tb04865.x.

[21] E.P. Butler, Transformation-toughened zirconia ceramics, Mater. Sci. Technol. 1 (1985) 417–432. doi:10.1179/mst.1985.1.6.417.

[22] S. Lawson, Environmental degradation of zirconia ceramics, J. Eur. Ceram. Soc. 15 (1995) 485–502. doi:10.1016/0955-2219(95)00035-S.

[23] J. Chevalier, L. Gremillard, S. Deville, Low-Temperature Degradation of Zirconia and Implications for Biomedical Implants, Annu. Rev. Mater. Res. 37 (2007) 1–32. doi:10.1146/annurev.matsci.37.052506.084250.

[24] J. Chevalier, J. Loh, L. Gremillard, S. Meille, E. Adolfson, Low-temperature degradation in zirconia with a porous surface, Acta Biomater. 7 (2011) 2986–2993. doi:10.1016/j.actbio.2011.03.006.

[25] M. Inokoshi, F. Zhang, J. De Munck, S. Minakuchi, I. Naert, J. Vleugels, et al., Influence of sintering conditions on low-temperature degradation of dental zirconia, Dent. Mater. 30 (2014) 669–678. doi:10.1016/j.dental.2014.03.005.

[26] F. Zhang, K. Vanmeensel, M. Inokoshi, M. Batuk, J. Hadermann, B. Van Meerbeek, et al., 3Y-TZP ceramics with improved hydrothermal degradation resistance and fracture toughness, J. Eur. Ceram. Soc. 34 (2014) 2453–2463. doi:10.1016/j.jeurceramsoc.2014.02.026.

[27] P. Kohorst, L. Borchers, J. Strempel, M. Stiesch, T. Hassel, F.W. Bach, et al., Low-temperature degradation of different zirconia ceramics for dental applications, Acta Biomater. 8 (2012) 1213–1220. doi:10.1016/j.actbio.2011.11.016.

[28] S.M. Kurtz, S. Kocagöz, C. Arnholt, R. Huet, M. Ueno, W.L. Walter, Advances in zirconia toughened alumina biomaterials for total joint replacement, J. Mech. Behav. Biomed. Mater. 31 (2014) 107–116. doi:10.1016/j.jmbbm.2013.03.022.

[29] J. Wang, R. Stevens, Zirconia-toughened alumina (ZTA) ceramics, J. Mater. Sci. 24 (1989) 3421–3440. doi:10.1007/BF02385721.

[30] G. Pezzotti, K. Yamada, A.A. Porporati, M. Kuntz, K. Yamamoto, Fracture toughness analysis of advanced ceramic composite for hip prosthesis, J. Am. Ceram. Soc. 92 (2009) 1817–1822. doi:10.1111/j.1551-2916.2009.03114.x.

[31] S. Deville, J. Chevalier, G. Fantozzi, J.F. Bartolomé, J. Requena, J.S. Moya, et al., Low-temperature ageing of zirconia-toughened alumina ceramics and its implication in biomedical implants, J. Eur. Ceram. Soc. 23 (2003) 2975–2982. doi:10.1016/S0955-2219(03)00313-3.

[32] T. Albrektsson, C. Johansson, Osteoinduction, osteoconduction and osseointegration, Eur. Spine J. 10 (2001) S96–S101. doi:10.1007/s005860100282.

[33] M. Gahlert, T. Gudehus, S. Eichhorn, E. Steinhauser, H. Kniha, W. Erhardt, Biomechanical and histomorphometric comparison between zirconia implants with varying surface textures and a titanium implant in the maxilla of miniature pigs., Clin. Oral Implants Res. 18 (2007) 662–8. doi:10.1111/j.1600-0501.2007.01401.x.

[34] M. Hisbergues, S. Vendeville, P. Vendeville, Zirconia: Established facts and perspectives for a biomaterial in dental implantology., J. Biomed. Mater. Res. B. Appl. Biomater. 88 (2009) 519–29. doi:10.1002/jbm.b.31147.

[35] A.K. Pandey, F. Pati, D. Mandal, S. Dhara, K. Biswas, In vitro evaluation of osteoconductivity and cellular response of zirconia and alumina based ceramics., Mater. Sci. Eng. C. Mater. Biol. Appl. 33 (2013) 3923–30. doi:10.1016/j.msec.2013.05.032.

[36] S. Anil, P.S. Anand, H. Alghamdi, J.A. Janse, Dental Implant Surface Enhancement and

Osseointegration, in: Implant Dent. - A Rapidly Evol. Pract., InTech, 2011: pp. 83–108. doi:10.5772/16475.

[37] R. a Gittens, R. Olivares-Navarrete, Z. Schwartz, B.D. Boyan, Implant osseointegration and the role of microroughness and nanostructures: Lessons for spine implants., Acta Biomater. 10 (2014) 3363–3371. doi:10.1016/j.actbio.2014.03.037.

[38] K. Anselme, Osteoblast adhesion on biomaterials., Biomaterials. 21 (2000) 667–81.

[39] H. Watanabe, K. Saito, K. Kokubun, H. Sasaki, M. Yoshinari, Change in surface properties of zirconia and initial attachment of osteoblastlike cells with hydrophilic treatment, Dent. Mater. J. 31 (2012) 806–814. doi:10.4012/dmj.2012-069.

[40] M. a Alfarsi, S.M. Hamlet, S. Ivanovski, Titanium surface hydrophilicity modulates the human macrophage inflammatory cytokine response., J. Biomed. Mater. Res. A. (2013) 60–67. doi:10.1002/jbm.a.34666.

[41] A. Wennerberg, T. Albrektsson, On implant surfaces: a review of current knowledge and opinions., Int. J. Oral Maxillofac. Implants. 25 (2009) 63–74. doi:10.1111/j.1600-051X.2008.01321.x.

[42] A. Wennerberg, T. Albrektsson, Effects of titanium surface topography on bone integration: a systematic review., Clin. Oral Implants Res. 20 Suppl 4 (2009) 172–84. doi:10.1111/j.1600-0501.2009.01775.x.

[43] P.G. Coelho, R. Jimbo, N. Tovar, E. a Bonfante, Osseointegration: hierarchical designing encompassing the macrometer, micrometer, and nanometer length scales., Dent. Mater. 31 (2015) 37–52. doi:10.1016/j.dental.2014.10.007.

[44] S. Lossdörfer, Z. Schwartz, L. Wang, C.H. Lohmann, J.D. Turner, M. Wieland, et al., Microrough implant surface topographies increase osteogenesis by reducing osteoclast formation and activity., J. Biomed. Mater. Res. A. 70 (2004) 361–369. doi:10.1002/jbm.a.30025.

[45] T. Albrektsson, A. Wennerberg, Oral implant surfaces: Part 1--review focusing on topographic and chemical properties of different surfaces and in vivo responses to them., Int. J. Prosthodont. 17 (2004) 536–43.

[46] R. a. Gittens, T. McLachlan, R. Olivares-Navarrete, Y. Cai, S. Berner, R. Tannenbaum, et al., The effects of combined micron-/submicron-scale surface roughness and nanoscale features on cell proliferation and differentiation, Biomaterials. 32 (2011) 3395–3403. doi:10.1016/j.biomaterials.2011.01.029.

[47] M.J. Dalby, N. Gadegaard, R.O.C. Oreffo, Harnessing nanotopography and integrin-matrix interactions to influence stem cell fate., Nat. Mater. 13 (2014) 558–69. doi:10.1038/nmat3980.

[48] M.J.P. Biggs, R.G. Richards, N. Gadegaard, R.J. McMurray, S. Affrossman, C.D.W. Wilkinson, et al., Interactions with nanoscale topography: Adhesion quantification and signal transduction in cells of osteogenic and multipotent lineage, J. Biomed. Mater. Res. - Part A. 91 (2009) 195–208. doi:10.1002/jbm.a.32196.

[49] M.J. Dalby, D. McCloy, M. Robertson, C.D.W. Wilkinson, R.O.C. Oreffo, Osteoprogenitor response to defined topographies with nanoscale depths, Biomaterials. 27 (2006) 1306–1315. doi:10.1016/j.biomaterials.2005.08.028.

[50] T.J. Webster, R.W. Siegel, R. Bizios, Osteoblast adhesion on nanophase ceramics., Biomaterials. 20 (1999) 1221–7.

[51] T.J. Webster, C. Ergun, R.H. Doremus, R.W. Siegel, R. Bizios, Enhanced functions of osteoblasts on nanophase ceramics., Biomaterials. 21 (2000) 1803–10.

[52] C. Zink, H. Hall, D.M. Brunette, N.D. Spencer, Orthogonal nanometer-micrometer roughness gradients probe morphological influences on cell behavior., Biomaterials. 33 (2012) 8055–61. doi:10.1016/j.biomaterials.2012.07.037.

[53] K. Anselme, M. Bigerelle, B. Noel, E. Dufresne, D. Judas, A. Iost, et al., Qualitative and quantitative study of human osteoblast adhesion on materials with various surface roughnesses, J. Biomed. Mater. Res. 49 (2000) 155–166. doi:10.1002/(SICI)1097-4636(200002)49:2<155::AID-JBM2>3.0.CO;2-J.

[54] M.J. Dalby, N. Gadegaard, R. Tare, A. Andar, M.O. Riehle, P. Herzyk, et al., The control of human mesenchymal cell differentiation using nanoscale symmetry and disorder., Nat. Mater. 6 (2007) 997–1003. doi:10.1038/nmat2013.

[55] T. Bernal, I. D. M. O., Risa, I., Hiroki, K., Ken-Ichiro, T., Naoko, Y., Toshi-Ichiro, Dental Implant Surface Roughness and Topography : A Review of the Literature, J. Gifu Dent. Soc. 35 (2009) 89–95.

[56] J.W. Costerton, Bacterial Biofilms: A Common Cause of Persistent Infections, Science (80-.). 284 (1999) 1318–1322. doi:10.1126/science.284.5418.1318.

[57] A.G. Gristina, P. Naylor, Q. Myrvik, Infections from biomaterials and implants: a race for the surface., Med. Prog. Technol. 14 (1987) 205–224.

[58] H.J. Busscher, H.C. van der Mei, G. Subbiahdoss, P.C. Jutte, J.J. a. M. van den Dungen,

S. a. J. Zaat, et al., Biomaterial-Associated Infection: Locating the Finish Line in the Race for the Surface, Sci. Transl. Med. 4 (2012) 153rv10–153rv10. doi:10.1126/scitranslmed.3004528.

[59] K.J. Bozic, S.M. Kurtz, E. Lau, K. Ong, T.P. Vail, D.J. Berry, The Epidemiology of Revision Total Hip Arthroplasty in the United States, J. Bone Jt. Surg. 91 (2009) 128–133. doi:10.2106/JBJS.H.00155.

[60] K.J. Bozic, S.M. Kurtz, E. Lau, K. Ong, V. Chiu, T.P. Vail, et al., The epidemiology of revision total knee arthroplasty in the united states, in: Clin. Orthop. Relat. Res., 2010: pp. 45–51. doi:10.1007/s11999-009-0945-0.

[61] J. Raphel, M. Holodniy, S.B. Goodman, S.C. Heilshorn, Multifunctional Coatings to Simultaneously Promote Osseointegration and Prevent Infection of Orthopaedic Implants, Elsevier Ltd, 2016. doi:10.1016/j.biomaterials.2016.01.016.

[62] H.H. Tuson, D.B. Weibel, Bacteria–surface interactions, Soft Matter. 9 (2013) 4368. doi:10.1039/c3sm27705d.

[63] L.C. Hsu, J. Fang, D. a. Borca-Tasciuc, R.W. Worobo, C.I. Moraru, Effect of micro- and nanoscale topography on the adhesion of bacterial cells to solid surfaces, Appl. Environ. Microbiol. 79 (2013) 2703–2712. doi:10.1128/AEM.03436-12.

[64] S. Usami, H. Kimoto, I. Takahashi, S. Shida, Strength of ceramic materials containing small flaws, Eng. Fract. Mech. 23 (1986) 745–761. doi:10.1016/0013-7944(86)90120-7.

[65] R.L. Hecker, S.Y. Liang, Predictive modeling of surface roughness in grinding, Int. J. Mach. Tools Manuf. 43 (2003) 755–761. doi:10.1016/S0890-6955(03)00055-5.

[66] T. Kosmač, Č. Oblak, L. Marion, The effects of dental grinding and sandblasting on ageing and fatigue behavior of dental zirconia (Y-TZP) ceramics, J. Eur. Ceram. Soc. 28 (2008) 1085–1090. doi:10.1016/j.jeurceramsoc.2007.09.013.

[67] T. Kosmač, C. Oblak, P. Jevnikar, N. Funduk, L. Marion, The effect of surface grinding and sandblasting on flexural strength and reliability of Y-TZP zirconia ceramic, Dent. Mater. 15 (1999) 426–433. doi:10.1016/S0109-5641(99)00070-6.

[68] J. a. Muñoz-Tabares, E. Jiménez-Piqué, J. Reyes-Gasga, M. Anglada, Microstructural changes in ground 3Y-TZP and their effect on mechanical properties, Acta Mater. 59 (2011) 6670–6683. doi:10.1016/j.actamat.2011.07.024.

[69] H.H.K. Xu, S. Jahanmir, L.K. Ives, Effect of grinding on strength of tetragonal zirconia and zirconia-toughened alumina, Mach. Sci. Technol. 1 (1997) 49–66.

doi:10.1080/10940349708945637.

[70] R.K. Chintapalli, A. Mestra Rodriguez, F. Garcia Marro, M. Anglada, Effect of sandblasting and residual stress on strength of zirconia for restorative dentistry applications., J. Mech. Behav. Biomed. Mater. 29 (2014) 126–37. doi:10.1016/j.jmbbm.2013.09.004.

[71] R.O.A. Souza, L.F. Valandro, R.M. Melo, J.P.B. Machado, M.A. Bottino, M. Özcan, Air–particle abrasion on zirconia ceramic using different protocols: Effects on biaxial flexural strength after cyclic loading, phase transformation and surface topography, J. Mech. Behav. Biomed. Mater. 26 (2013) 155–163. doi:10.1016/j.jmbbm.2013.04.018.

[72] R.K. Chintapalli, F.G. Marro, E. Jimenez-Pique, M. Anglada, Phase transformation and subsurface damage in 3Y-TZP after sandblasting., Dent. Mater. 29 (2013) 566–72. doi:10.1016/j.dental.2013.03.005.

[73] H. Ito, H. Sasaki, K. Saito, S. Honma, Y. Yajima, M. Yoshinari, Response of osteoblast-like cells to zirconia with different surface topography, Dent. Mater. J. 32 (2013) 122–129. doi:10.4012/dmj.2012-208.

[74] J. Fischer, A. Schott, S. Märtin, Surface micro-structuring of zirconia dental implants, Clin. Oral Implants Res. 27 (2016) 162–166. doi:10.1111/clr.12553.

[75] A. Casucci, C. Mazzitelli, F. Monticelli, M. Toledano, R. Osorio, E. Osorio, et al., Morphological analysis of three zirconium oxide ceramics: Effect of surface treatments., Dent. Mater. 26 (2010) 751–60. doi:10.1016/j.dental.2010.03.020.

[76] R. Gruber, E. Hedbom, D. D. Bosshardt, R. Heuberger, D. Buser, Acid and alkali etching of grit blasted zirconia: Impact on adhesion and osteogenic differentiation of MG63 cells in vitro, Dent. Mater. J. 31 (2012) 1097–1102. doi:10.4012/dmj.2012-107.

[77] L. Cooper, Y. Zhou, J. Takebe, J. Guo, A. Abron, A. Holmen, et al., Fluoride modification effects on osteoblast behavior and bone formation at TiO grit-blasted c.p. titanium endosseous implants, Biomaterials. 27 (2006) 926–936. doi:10.1016/j.biomaterials.2005.07.009.

[78] M. Yoshinari, Y. Oda, T. Kato, K. Okuda, Influence of surface modifications to titanium on antibacterial activity in vitro, Biomaterials. 22 (2001) 2043–2048. doi:10.1016/S0142-9612(00)00392-6.

[79] M. Gahlert, S. Röhling, M. Wieland, S. Eichhorn, H. Küchenhoff, H. Kniha, A comparison study of the osseointegration of zirconia and titanium dental implants. A

biomechanical evaluation in the maxilla of pigs., Clin. Implant Dent. Relat. Res. 12 (2010) 297–305. doi:10.1111/j.1708-8208.2009.00168.x.

[80] C. Bergemann, K. Duske, J.B. Nebe, A. Schöne, U. Bulnheim, H. Seitz, et al., Microstructured zirconia surfaces modulate osteogenic marker genes in human primary osteoblasts., J. Mater. Sci. Mater. Med. (2015). doi:10.1007/s10856-014-5350-x.

[81] N. Saulacic, R. Erdösi, D.D. Bosshardt, R. Gruber, D. Buser, Acid and Alkaline Etching of Sandblasted Zirconia Implants: A Histomorphometric Study in Miniature Pigs, Clin. Implant Dent. Relat. Res. 16 (2014) 313–322. doi:10.1111/cid.12070.

[82] R.J. Kohal, M. Bächle, A. Renz, F. Butz, Evaluation of alumina toughened zirconia implants with a sintered, moderately rough surface: An experiment in the rat, Dent. Mater. 32 (2016) 65–72. doi:10.1016/j.dental.2015.10.008.

[83] Y. Cho, J. Hong, H. Ryoo, D. Kim, J. Park, J. Han, Osteogenic responses to zirconia with hydroxyapatite coating by aerosol deposition., J. Dent. Res. 94 (2015) 491–499. doi:10.1177/0022034514566432.

[84] I. Rocchietta, F. Fontana, A. Addis, P. Schupbach, M. Simion, Surface-modified zirconia implants: Tissue response in rabbits, Clin. Oral Implants Res. 20 (2009) 844–850. doi:10.1111/j.1600-0501.2009.01727.x.

[85] M. Liu, J. Zhou, Y. Yang, M. Zheng, J. Yang, J. Tan, Surface modification of zirconia with polydopamine to enhance fibroblast response and decrease bacterial activity in vitro: A potential technique for soft tissue engineering applications, Colloids Surfaces B Biointerfaces. 136 (2015) 74–83. doi:10.1016/j.colsurfb.2015.06.047.

[86] K. Kakura, K. Yasuno, Y. Taniguchi, K. Yamamoto, T. Sakai, A. Irie, et al., Original Zirconia Implant with Rough Surface Produced by YAG Laser Treatment: Evaluation of Histomorphology and Strength of Osseointegration, J. Hard Tissue Biol. 23 (2014) 77–82.

[87] R. a Delgado-Ruíz, J.L. Calvo-Guirado, P. Moreno, J. Guardia, G. Gomez-Moreno, J.E. Mate-Sánchez, et al., Femtosecond laser microstructuring of zirconia dental implants., J. Biomed. Mater. Res. B. Appl. Biomater. 96 (2011) 91–100. doi:10.1002/jbm.b.31743.

[88] A. Noro, M. Kaneko, I. Murata, M. Yoshinari, Influence of surface topography and surface physicochemistry on wettability of zirconia (tetragonal zirconia polycrystal)., J. Biomed. Mater. Res. B. Appl. Biomater. 101 (2013) 355–63. doi:10.1002/jbm.b.32846.

[89] L. Hao, D.R. Ma, J. Lawrence, X. Zhu, Enhancing osteoblast functions on a magnesia partially stabilised zirconia bioceramic by means of laser irradiation, Mater. Sci. Eng. C.

25 (2005) 496–502. doi:10.1016/j.msec.2005.03.003.

[90] K. Schickle, A. Korsten, M. Weber, C. Bergmann, S. Neuss, H. Fischer, Towards osseointegration of bioinert ceramics: Can biological agents be immobilized on alumina substrates using self-assembled monolayer technique?, J. Eur. Ceram. Soc. 33 (2013) 2705–2713. doi:10.1016/j.jeurceramsoc.2013.03.032.

[91] E. Fernandez-Garcia, X. Chen, C.F. Gutierrez-Gonzalez, A. Fernandez, S. Lopez-Esteban, C. Aparicio, Peptide-functionalized zirconia and new zirconia/titanium biocermets for dental applications, J. Dent. 43 (2015) 1162–1174. doi:10.1016/j.jdent.2015.06.002.

[92] E. Camposilvan, Q. Flamant, M. Anglada, Surface roughened zirconia: Towards hydrothermal stability, J. Mech. Behav. Biomed. Mater. 47 (2015) 95–106. doi:10.1016/j.jmbbm.2015.03.017.

Appended articles

Article I.

Hydrofluoric acid etching of dental zirconia. Part 1: etching mechanism and surface characterization.

Journal of the European Ceramic Society 36 (2016) 121–134

Contents lists available at www.sciencedirect.com

Journal of the European Ceramic Society

journal homepage: www.elsevier.com/locate/jeurceramsoc

Hydrofluoric acid etching of dental zirconia. Part 1: etching mechanism and surface characterization

Quentin Flamant[a,b,*], Fernando García Marro[a,b], Joan Josep Roa Rovira[a,b], Marc Anglada[a,b,*]

[a] Department of Materials Science and Metallurgical Engineering, Universitat Politècnica de Catalunya, Av. Diagonal 647, Barcelona 08028, Spain
[b] Center for Research in Nano-Engineering, CRNE, Universitat Politecnica de Catalunya, C. Pascual i Vila, 15, Barcelona 08028, Spain

ARTICLE INFO

Article history:
Received 9 July 2015
Received in revised form
14 September 2015
Accepted 15 September 2015
Available online 3 October 2015

Keywords:
Zirconia
Hydrofluoric
Etching
Dental
Roughness

ABSTRACT

Rough surfaces have been shown to promote osseointegration, which is one of the keys for a successful dental implantation. Among the diverse treatments proposed to roughen zirconia, hydrofluoric acid (HF) etching appears to be a good candidate, however little is known about this process. In this work, the effect of HF concentration and etching time on the surface topography and chemistry of yttria-stabilized zirconia was assessed. Besides, to understand the etching mechanism, the reaction products present in solution and on the surface were characterized. The results indicate suitable parameters for a fast and uniform roughening of zirconia. The formation of adhered fluoride precipitates on the surface is reported for the first time and highlights the importance of cleaning after etching. Finally, it is shown that monitoring the time allows controlling the surface roughness, smooth–rough transition and fractal dimension, which should make possible the fabrication of implants with an optimal topography.

1. Introduction

Yttria-stabilized tetragonal zirconia polycrystals (Y-TZP, short: zirconia) are biocompatible and exhibit the best combination of strength and toughness of single-phase oxide ceramics. They were introduced as biomaterials in the end of the 1980s to overcome the limitations of alumina in the field of orthopedics [1]. While monolithic zirconia has been almost abandoned for orthopedic applications, in the last decade its use in restorative dentistry has been growing fast [2]. In particular, its good esthetics, high resistance to corrosion and the absence of allergic reaction make zirconia a good candidate to replace titanium for the fabrication of dental implants [3]. However, some authors reported a higher failure rate and a higher marginal bone loss when comparing zirconia to titanium. According to them, the use of zirconia implants does not appear recommendable at the moment except for specific cases (e.g. allergy to titanium), and there is a need for further research before generalizing their clinical use [4,5].

The key to solve the problem of bone loss mentioned above is to achieve a good osseointegration, which depends on numerous parameters such as surface topography and chemistry [6]. In particular it has been shown that rough surfaces exhibit a better bone response than smooth ones, and that the combination of micro- and nano-scale roughness could have synergistic effects [7–9]. Nevertheless, what is the optimal roughness for a dental implant remains unclear [8,9]. On the other hand, a complementary approach to the classical roughness parameters calculation is to perform a fractal analysis. It has been demonstrated that osteoblastic cells proliferation and adhesion is strongly correlated to fractal parameters [10]. There is therefore a strong interest in developing processes which allow controlling the roughness and the fractal dimension of a surface.

Among the different surface chemical treatments already experimented in the literature to achieve this purpose, hydrofluoric acid (HF) etching appears to be a good candidate. Although other chemicals, such as hypophosphorous acid or an equimolar mixture of potassium hydroxide and sodium hydroxide, have been reported to successfully etch Y-TZP [11,12], HF presents the advantage to be a fast etchant at room temperature. More importantly, Gahlert et al. evidenced that HF etching of zirconia implants enhances

Abbreviations: AFM, atomic force microscopy; DI water, deionized water; EDS, energy dispersive spectrometry; ESI-FTMS, electrospray ionization Fourier transform mass spectrometry; HF, hydrofluoric acid; SEM, scanning electron microscopy; SRC, smooth–rough crossover; TEM, Transmission electron microscopy; WLI, white light interferometry; XPS, X-ray photoelectron spectroscopy; Y-TZP, Yttria-stabilized tetragonal zirconia polycrystals; 3Y-TZP, 3 mol% Y-TZP.

* Corresponding authors. Fax: +34 934016706.
E-mail addresses: quentin.flamant@upc.edu (Q. Flamant), marc.j.anglada@upc.edu (M. Anglada).

http://dx.doi.org/10.1016/j.jeurceramsoc.2015.09.021
0955-2219/

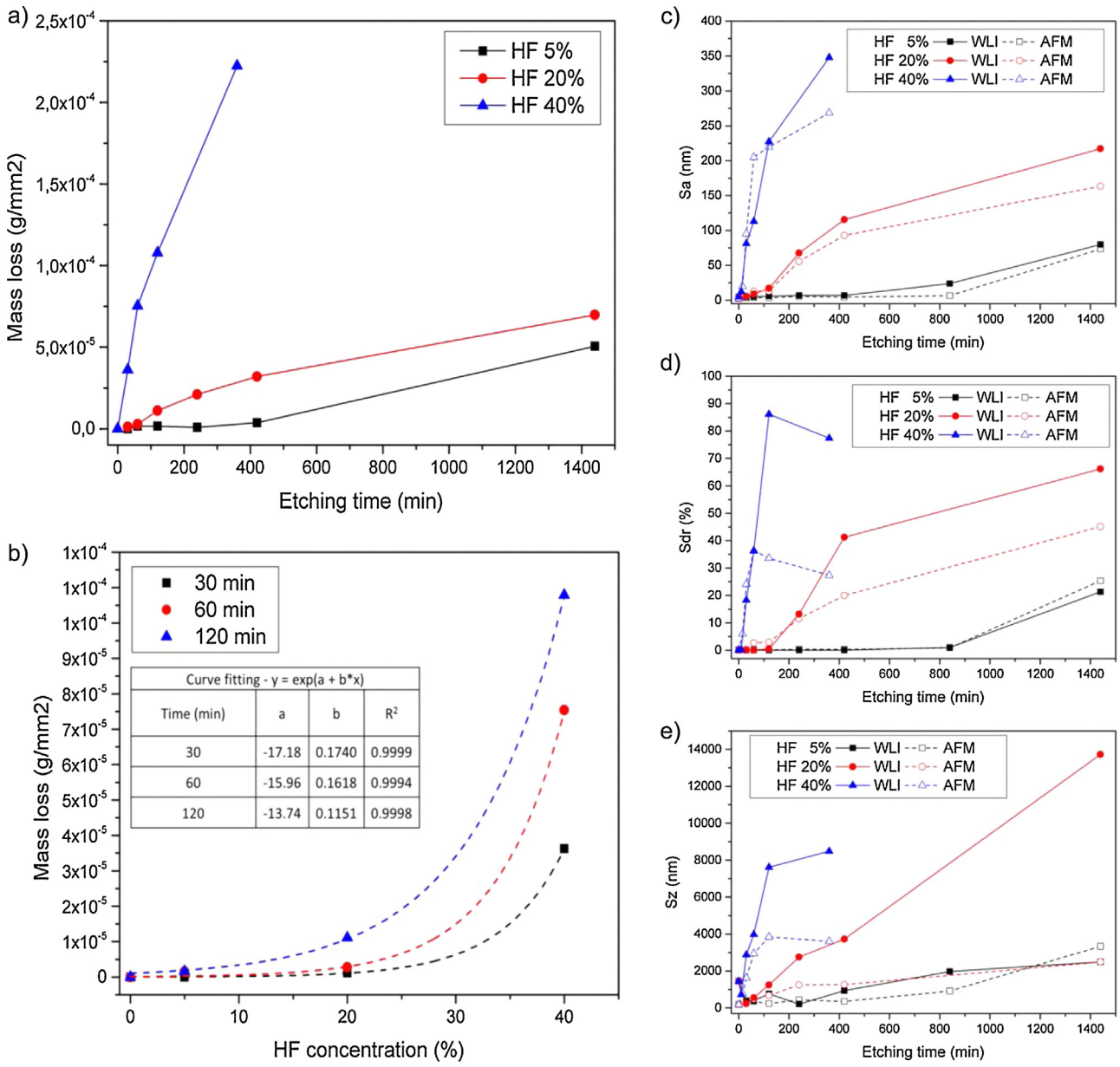

Fig. 1. Left: mass loss per initial sample external area as a function of (a) etching time for different HF concentrations, (b) HF concentration for different etching times. Right: (c) Sa, (d) Sdr and (e) Sz parameters determined from AFM and WLI data as a function of etching time for different HF concentrations. For all graphs each data point corresponds to a distinct specimen.

bone apposition resulting in high removal torque values [13]. Besides, HF etching can be successfully associated to sandblasting. Ito et al. showed that the combination of both treatments leads to an increase in the proliferation rate and expression of ALP activity of osteoblast-like cells (MC3T3-E1) [14] and Bergemann et al. found recently that it enhanced the human primary osteoblast maturation [15]. Additionally, the incorporation of fluoride at the surface could enhance osteoblastic differentiation and interfacial bone formation, as it does for titanium [16]. Finally, zirconia dental implants with acid etched surface are already commercialized (CeraRoot implants with ICE^{TM} surface) and apparently have shown a similar or higher success rate as compared to titanium implants after five years of follow-up [17].

Despite of numerous studies in which HF has been used for the etching of Y-TZP, to the best of the knowledge of the authors, very little is known about the chemical reaction involved. Besides, the influence of parameters such as time and concentration is not documented. The objectives of the present work are therefore to determine suitable conditions for a fast and uniform roughening of dental zirconia, to provide a complete surface characterization with a special emphasis on topography and to contribute to the understanding of the etching mechanism. Questions related to the influence of etching on the mechanical properties and long-term reliability are treated in a second article [18].

2. Materials and methods

2.1. Zirconia disks preparation

Commercial 3Y-TZP powder (TZ-3YSB-E Tosoh Co., Japan) was cold isostatically compacted under pressure of 200 MPa in a cylindrical mold for producing a green body, and then sintered in an alumina tube furnace at 1450 °C for two hours (3 °C/min heating and cooling rates), as described in previous work [19]. The sin-

Table 1
Applied restrictions for the calculation of molecular formulas from ESI-FTMS spectra.

Isotope	Minimum number	Maximum number
^{16}O	0	15
^{12}C	0	5
^{1}H	0	30
^{14}N	0	5
^{89}Y	0	10
^{90}Zr	0	10
^{19}F	0	10

tered ceramic cylinders were cut into specimens in the form of disks (2 mm thick, 9 mm diameter), which were ground and polished down to a 3 μm diamond suspension. The samples were then successively cleaned for five minutes with acetone, ethanol and deionized water (DI water) in an ultrasonic bath in order to remove contaminants. The polishing step, which is not likely to be part of the processing for a commercial implant, was introduced in order to facilitate the surface characterization. It was assumed that the effects of etching on a machined and annealed surface or on a sintered surface would be comparable.

2.2. Chemical etching

Concentrated HF (Hydrofluoric Acid 40% QP Panreac, Spain) was used to prepare aqueous solutions with respective mass concentrations of 5%, 20% and 40%. Etching was performed at room temperature on zirconia disks in high-density polyethylene flasks. The volume of acid was 1 mL by sample. The disks were placed with the polished side upwards. Just after being removed from HF, they were rinsed with DI water in order to stop the reaction. Unless otherwise specified, after etching samples were cleaned twice ten minutes with fresh DI water in an ultrasonic bath in order to remove any remaining product of the reaction from the surface.

2.3. Preliminary study: determination of adequate etching conditions

A preliminary study was carried out to determine which combinations of concentration and time were more suitable to achieve rapidly an appropriate roughness on the zirconia surface. One ultrasonically cleaned sample was used for each condition. Atomic Force Microscopy (AFM Veeco Dimension 3100) in tapping mode and White Light Interferometry (WLI, Veeco Wyko 9300NT) were used in order to characterize the topography at different scales. AFM measurements were performed on 50 μm × 50 μm areas (resolution: 512 × 512 pixels) and WLI measurements were performed on 150 μm × 150 μm areas (stitching of 4 images acquired at magnification 50×, resolution: 758 × 758 pixels). The roughness analysis of the data from AFM and WLI was performed using Veeco's Vision® software. Tilt was corrected and a robust short wavelength pass Gaussian filter (cut-off wavelength: 10 μm) was applied to the data in order to separate waviness from roughness. Then the 3D roughness parameters S_a, S_z and S_{dr} were determined (for definitions, see Table 2).

The mass loss per initial external sample area and the roughness parameters were determined as a function of concentration and etching time. Based on this preliminary study the main part of this work was focused on the etching with HF 40% for times between zero and two hours. The reasons for this choice will be discussed later.

2.4. Analysis of the etching solution

In order to identify the soluble products of the reaction, 1 mL of the solution resulting from the etching of a zirconia disk with HF 40% was evaporated. The dry residue was dissolved in 1 mL of DI water with 0.1% of formic acid (HCOOH). Electrospray ionization Fourier transform mass spectrometry (ESI-FTMS) of the resulting solution was carried out on a LTQ Orbitrap™ Velos mass spectrometer coupled with a Thermo Scientific Accela™ High-Performance Liquid Chromatography system. The solution was introduced by the flow injection analysis method (flow rate: 100 μL/min, mobile phase: H_2O/CH_3CN (1:1) with 0.1% of formic acid, injected volume: 5 μL). Mass spectra were acquired in both positive and negative mode. For the calculation of molecular formulas the restrictions detailed in Table 1 were applied.

2.5. Analysis of the etching products

To understand the etching mechanism and to identify the precipitates which formed during the treatment, zirconia disks were immersed for different times in HF 40%. To avoid removing the reaction products from the surface, after etching the samples were not subjected to sonication but only rinsed with DI water. In the rest of this work, this state of the surface will be referred to as "as etched".

The "as etched" surfaces were observed by scanning electron microscopy (SEM). Energy dispersive X-ray spectroscopy (EDS) was used for the elemental analysis of the etching products. To determine the elemental composition and the chemical state of the surface, X-ray photoelectron spectroscopy (XPS) was performed with a SPECS system equipped with an Al anode XR50 source operating at 150 W and a Phoibos 150 MCD−9 detector XP. Spectra were recorded with pass energy of 25 eV, 0.1 eV steps and a pressure below 7.5×10^{-9} mbar. Binding energies were referred to the adventitious C 1s signal and background was subtracted. The identification of the local bonding environment of each element was performed by comparing the experimental peak positions with the data from the NIST Standard Reference Database 20, Version 4.1 (http://srdata.nist.gov/xps/).

Additionally, one sample was immersed for two hours in HF 40% and ultrasonically cleaned. A droplet of the DI water used for the sonication was evaporated and the dry residue was observed by SEM, EDS, and Transmission Electron Microscopy (TEM).

2.6. Surface characterization

To assess the effect of etching on the surface properties, a complete chemical and topographical characterization was carried out on samples etched in HF 40%.

The surface morphology was observed by SEM and the elemental composition was determined by EDS. An XPS analysis similar to the one described in 2.5 allowed to quantify the elements constituting the first nanometers of the surface and to determine their chemical state.

Following the same methodology as described in 2.3, AFM and WLI measurements were performed on respectively three and ten samples per experimental point. From these measurements, the 3D roughness parameters described in Table 2 were determined.

Additionally, a scale sensitive fractal analysis of the AFM and WLI data was performed using the software Sfrax (www.surfract.com). Area-scale analysis is based on the principle from fractal geometry that the area of a rough surface is not unique, but depends on the scale of measurement [23,24]. The software uses an iterative tiling algorithm in which the topography of the surface is modeled using triangular tiles to calculate the relative area as a function of the scale of observation. The area of a tile represents the scale, and the relative area is determined from the following formula:

$$A_r = \frac{N \times A_t}{A_p}$$

Table 2
Description of the 3D roughness parameters used in this study [20–22].

Symbol	Category	Parameter	Description
S_a	Amplitude	Average roughness	Average of height values
S_q	Amplitude	RMS roughness	Standard deviation of height values
S_{sk}	Amplitude	Skewness	Degree of symmetry of the surface heights about the mean plane. The sign of S_{sk} indicates the preponderance of peaks ($S_{sk} > 0$) or valley structures ($S_{sk} < 0$)
S_{ku}	Amplitude	Kurtosis	Sharpness or flatness of the height distribution curve $S_{ku} = 3$: Gaussian height distributions $S_{ku} < 3$: "broad" height distributions $S_{ku} > 3$: "narrow" height distributions
S_z	Amplitude	Ten point peak–peak height	Average difference between the five highest peaks and five lowest valleys
S_{al}	Spatial	Fastest decay length	The shortest spatial distance in which the autocorrelation function decreases to 0.2 of its value
S_{tr}	Spatial	Texture aspect ratio	Measure of isotropy or anisotropy of surface topography
S_{ds}	Spatial	Density of summits	Number of summits per unit area
S_{dr}	Hybrid	Developed interfacial area ratio	Percentage of additional surface area contributed by the texture as compared to an ideal plane the size of the measurement region
S_{dq}	Hybrid	RMS gradient	RMS value of the surface slope within the sampling area
S_{sc}	Hybrid	Mean summit curvature	Average of the principal curvature of the summits
S_{bi}	Functional	Bearing index	Measure, relative to S_q, of the surface height at the 5% bearing area ratio
S_{ci}	Functional	Core fluid retention index	Measure, relative to S_q, of the volume (for example, of a fluid filling the core surface) that the surface would support from 5% to 80% of the bearing ratio
S_{vi}	Functional	Valley fluid retention index	Measure relative to S_q of the volume that the surface would support from 80% to 100% of the bearing ratio
S_m	Functional	Surface material volume	Amount of material contained in the surface peaks from 0% to 10% of the bearing area ratio
S_c	Functional	Surface core void volume	Volume that the surface would support from 10% to 80% of the bearing ratio
S_v	Functional	Surface void volume	Volume that the surface would support from 80% to100% of the bearing ratio

where A_r is the relative area, A_t is the area of a tile, A_p is the projected area and N is the number of tiles.

An example of semi-log plot obtained by scale sensitive fractal analysis is shown Fig. 10a. This kind of plot can be split into two parts:

- The left part, in which the curve appears to be steep and linear. The slope of the curve is an indication of the complexity, intricacy or roughness of the surface [23]. The fractal dimension (D) can be estimated by adding two to the absolute value of the slope.
- The right part, in which the relative area approaches one.

The scale (i.e. the area of the tiles) corresponding to the limit between the two parts of the graph is called the smooth–rough crossover (SRC). For scales smaller than the SRC, the surface is considered as "rough", whereas for scales higher than SRC, the surface is considered as "smooth" [24].

3. Results

3.1. Preliminary study: determination of adequate etching conditions

The mass loss of the samples was strongly dependent on the etching time and there seems to be an exponential relationship between the mass loss and the HF concentration (Fig. 1). For the HF 5% solution, the mass loss was almost insignificant during the first hours but increased substantially for the longest etching time (24 h).

The values of the roughness parameters determined from AFM and WLI measurements differed (Fig. 1), which could be expected because of the distinct resolutions and areas of measurement of both techniques, but in general evidenced the same tendencies:

– For HF 5%, S_a, S_{dr} and S_z increased very slowly in a first phase which we will call the "initiation phase", and then more rapidly in a second phase which we will call the "effective etching phase". This evolution correlates with the mass loss measurements.
– For HF 20%, there was a short "initiation phase", followed by an "effective etching phase". For long etching times, the increase rate of S_a and S_{dr} diminished.
– For HF 40%, the "initiation phase" was probably too short to be observed. In a first stage, S_a, S_{dr} and S_z increased rapidly with etching time, then S_a increased more slowly, S_{dr} seemed to decrease and S_z decreased or increased slightly depending on the measurement device. The maximal value of S_{dr} was reached for one hour of etching with AFM and for two hours with WLI. The ratios S_z/S_a and S_z/S_{dr} were low as compared to other concentrations.

3.2. Analysis of the etching solution

The identification of the species present in the solution was performed by comparing the different series of peaks from both positive and negative mass spectra to theoretical simulation. The analysis evidenced the presence of zirconium fluoride, zirconium oxide and zirconium hydroxide complexes (Table 3). The presence of compounds containing Yttrium was not detected. It has to be taken into account that the solution which was subjected to ESI-FTMS was obtained by redissolution of the dry residue of the etching solution, therefore only non-volatile species were present and some structural changes may have occurred during the process. For two series of peaks of the positive-ion spectrum, the search for corresponding chemical compounds resulted in non-matching results however the isotopic profiles were characteristic of the presence in the compound of respectively one or two Zirconium ions.

3.3. Analysis of the etching products

3.3.1. Particles in suspension in the cleaning water

The observation by TEM of the particles present in suspension in the DI water used for ultrasonic cleaning of samples etched two hours in HF 40% showed the presence of octahedral particles (octahedrons) and needle-like particles (needles) (Fig. 2).

The selected area electron diffraction (SAED) pattern of an octahedron showed a crystalline structure, which is consistent with

Table 3
ESI-FTMS peaks identification.

Polarization	Region of the spectrum	Compatible ions	Comments
+	122–132 mDa	$[ZrO(OH)]^+$	Relative intensities slightly diverged from theory
+	140–148 mDa	$[Zr(OH)_3]^+$	
+	182–198 mDa	$[ZrO.2H_2O.HCOOH]^+$; $[ZrF_3.CH_3CN]^+$	HCOOH and CH_3CN come from the redissolution and/or the mobile phase
+	228–236 mDa	$[ZrO.2H_2O.HCOOH.CH_3CN]^+$	HCOOH and CH_3CN come from the redissolution and/or mobile phase
+	359–366 mDa	Not identified	Isotropic profile characteristic of the presence of 1 atom of Zr
+	392–412 mDa	Not identified	Isotropic profile characteristic of the presence of 2 atoms of Zr
–	180–195 mDa	$[ZrF_5]^-$	
–	205–225 mDa	$[ZrF_4.HCOO]^-$	$HCOO^-$ comes from the mobile phase
–	350–365 mDa	$[Zr_2F_9]^-$	

their regular shape. The SAED of a needle revealed a textured polycrystalline structure. In both patterns, low intensity quasi-amorphous rings were observed.

EDS analysis of the octahedrons showed that they are composed of yttrium and fluorine (Fig. 2e). The EDS analysis of the needles substantiated that they are composed of yttrium, zirconium and fluorine (Fig. 2f).

3.3.2. *"As etched" surface*

SEM observations of the "as etched" surface showed the presence of octahedrons (Fig. 3). The average size of the octahedrons increased with the etching time. Besides, an additional "adhered layer" appeared between 40 min and 60 min. Some features similar to the needles described previously could be observed in the layer however it was not possible to acquire images at sufficiently high

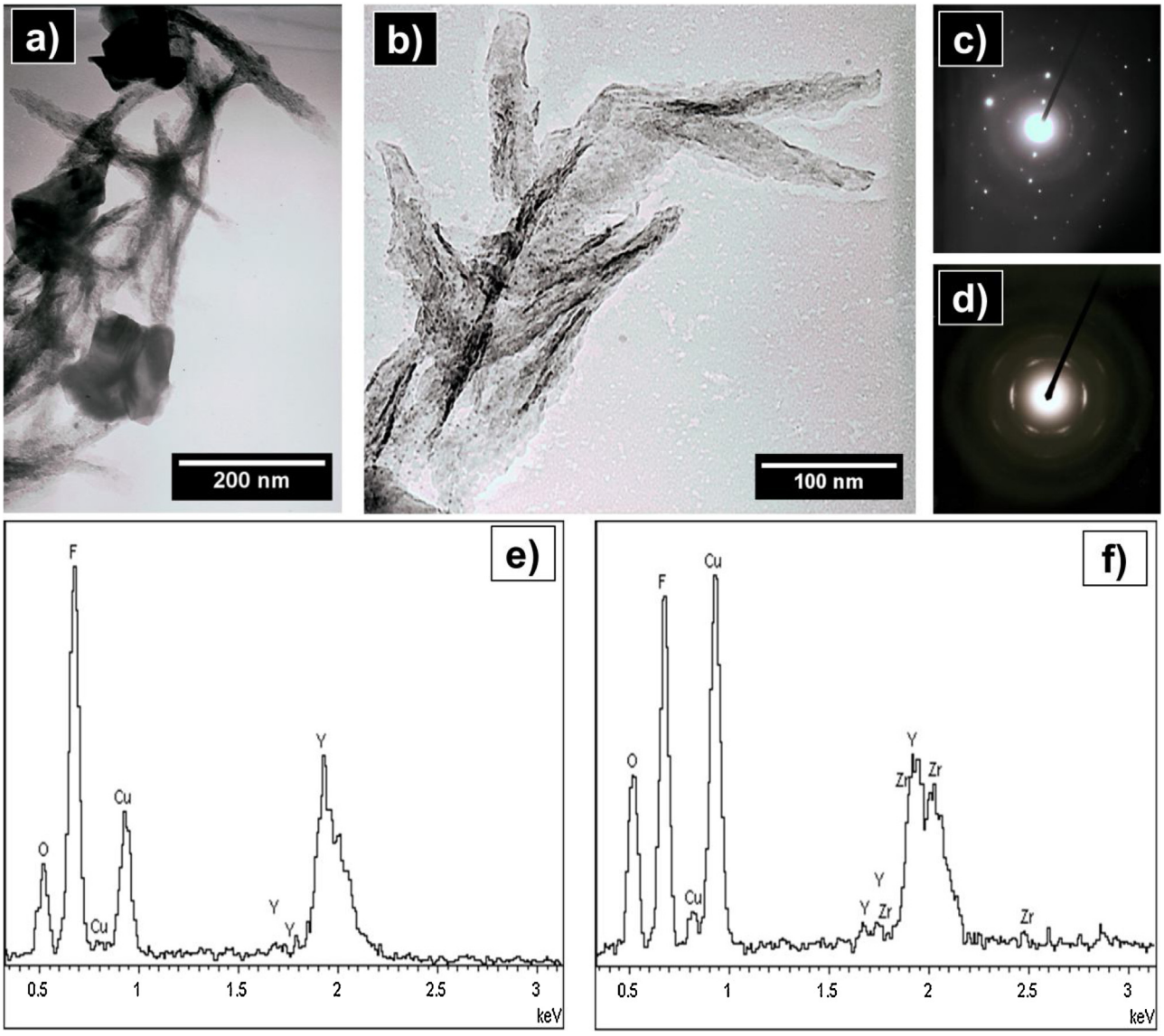

Fig. 2. Observation by TEM (top) and EDS (bottom) of the particles present in the DI water used for ultrasonic cleaning of a sample etched two hours in HF 40% : (a) agglomerate of octahedrons and needles, (b) a needle at high magnification, (c) SAED pattern of an octahedron, evidencing a crystalline structure, (d) SAED pattern of a needle, evidencing a textured polycrystalline structure, (e) EDS spectrum of an octahedron, (f) EDS spectrum of a needle. In (e) and (f), Cu and O signals come from the substrate.

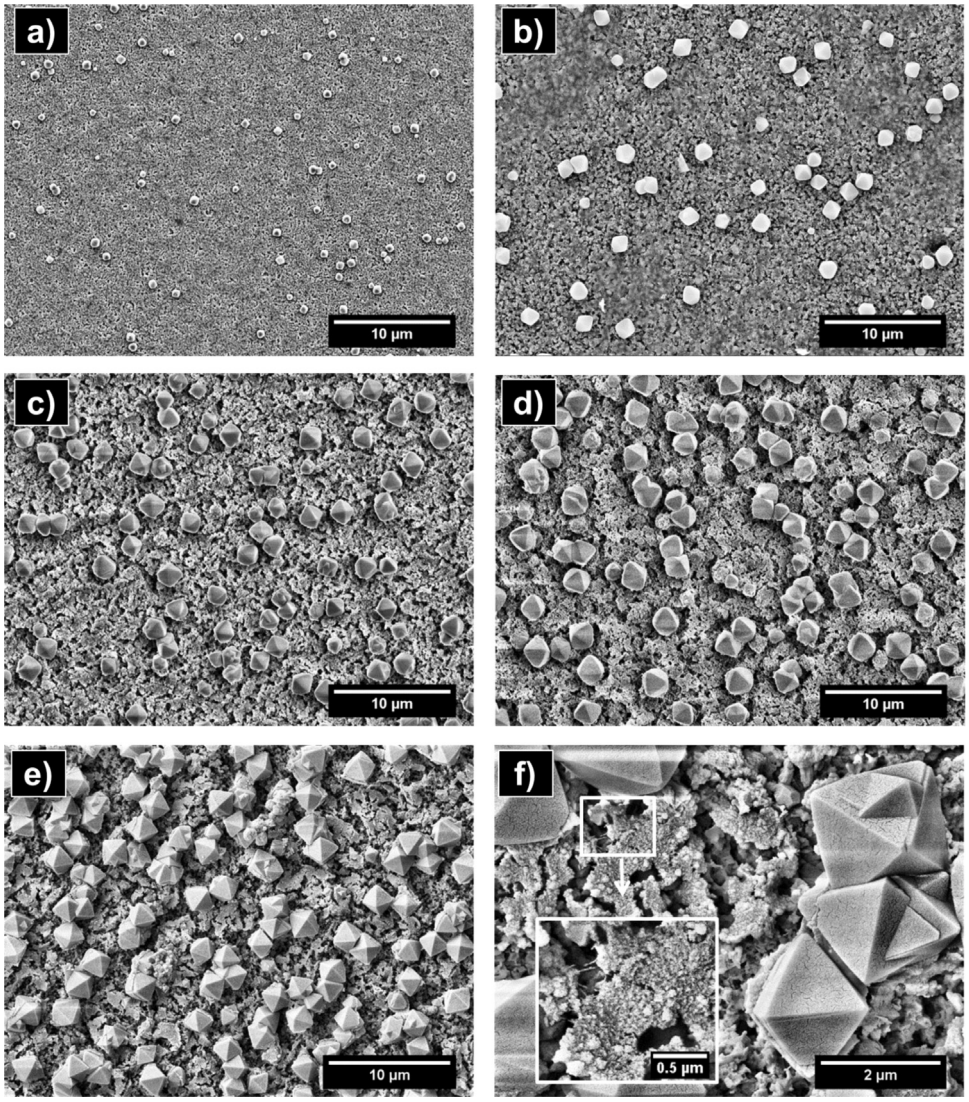

Fig. 3. SEM observations of the surface in the "as etched" state (no ultrasonic cleaning) after etching in HF 40% for: (a) 20 min, (b) 40 min, (c) 60 min, (d) 90 min, (e) 120 min, (f) 120 min (high magnification). The inset in (f) shows a zoom of the "adhered layer" and possibly the same kind of needles as observed in Fig. 2.

magnification to confirm it because of charge effects. EDS analysis of the octahedrons and the "adhered layer" revealed the presence of zirconium, yttrium and fluorine (Fig. 4a and b). However, the proportion of zirconium detected in the octahedrons was low, and given the previous EDS analysis of the particles present in the cleaning water, it is probable that the signal was originated from the material below.

The XPS quantitative analysis evidenced substantial increases in yttrium and fluorine together with substantial decreases in zirconium and oxygen concentrations as compared to the non-etched sample (Fig. 4d). Most of the peaks of the high-resolution spectra could be identified (Table 4). In particular, the presence of ZrF_4 and YF_3 chemical bonds was detected.

3.4. Surface characterization

3.4.1. Surface morphology

After the cleaning procedure, SEM inspection of the samples did not evidence any remaining octahedrons or "adhered layer" on the surface, confirming the ultrasonic cleaning efficiency. Regarding the preferentiality of the etching, SEM observations showed that the attack was both intergranular and intragranular (grain size of the original material measured by the intercept method: 0.3 µm), being slightly faster at the grain boundaries (Fig. 5) and demonstrated a substantial evolution of the morphology at different scales depending on etching time (Fig. 6). Nevertheless, observations at high magnification showed no significant evolution of the granular texture. On the other hand, the presence of randomly dispersed pits was detected on the surface.

3.4.2. Surface chemistry

The results of XPS indicated a slight increase of the fluorine content and a slight decrease of the oxygen content in the first nanometers of the surface of etched samples as compared to the non-etched (control) sample (Fig. 4d). However the results of EDS showed that at the micrometric level the chemical composition of the surface was not substantially affected by etching, in particular the presence of Fluorine was not detected (Fig. 4c). As it will be discussed further, the analysis of the XPS high-resolution spectra allowed identifying the chemical environment corresponding to most of the peaks (Table 5).

AFM and WLI images revealed a substantial evolution of the topography depending on the etching duration (Fig. 7). The appari-

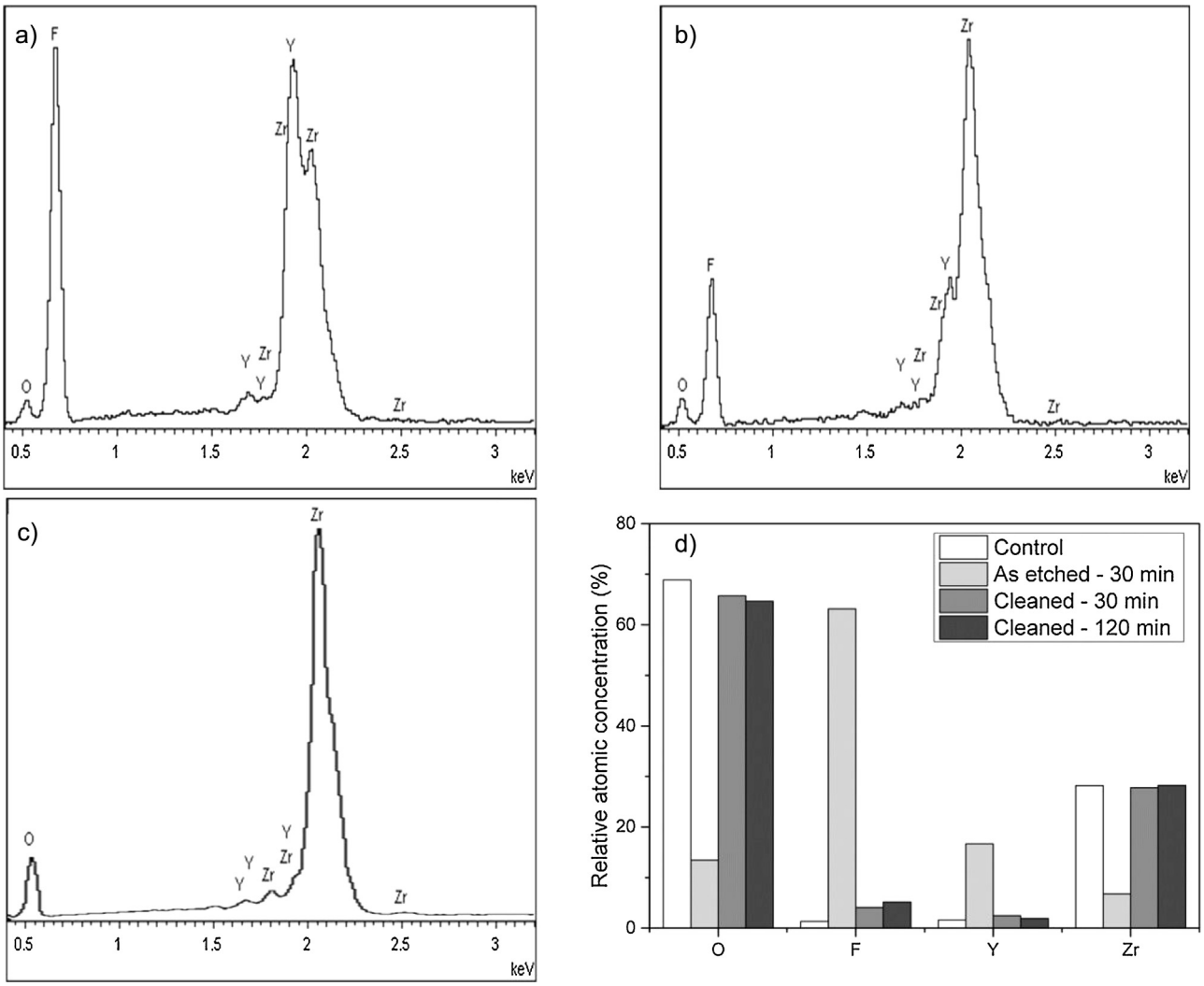

Fig. 4. Quantitative elemental analysis performed on the "as etched" (a, b, d) and on the ultrasonically cleaned (c, d) surface. (a) EDS spectrum of an octahedron, (b) EDS spectrum of the "adhered layer", (c) EDS spectrum of the cleaned surface, (d) XPS quantitative analysis.

Table 4
Identification of the peaks of the XPS high-resolution spectra of an "as etched" surface (spectra available in the supplementary information).

Element	Orbital	Binding energy (eV)	Closest value found in the literature (eV)	Identified chemical environment	Reference
F	1s	683.2	–	–	–
		684.9	685.1	ZrF_4;YF_3	[25,26]
O	1s	526.6	–	–	–
		528.8	528.8	Pure Y_2O_3 (cubic)	[27]
		531.4	531.3	ZrO_2	[28]
Y	3d3/2	161.7	–	YF_3	–
	3d5/2	159.6	159.8	YF_3	[26]
Zr	3d3/2	183.8	184.0	3Y-TZP	[27]
		187.6	–	ZrF_4	–
	3d5/2	181.5	181.6	3Y-TZP	[27]
		185.3	185.3	ZrF_4	[29]

tion of high peaks and deep valleys was more pronounced for long etching times.

3.4.3. *Surface topography*

3.4.3.1. *Roughness analysis.*

– Amplitude parameters (Fig. 8)

For both AFM and WLI measurements, the surface average roughness (S_a) and RMS roughness (S_q) increased substantially from zero to one hour and then slightly between one hour and two hours. The ten point peak–peak height (S_z) increase was substantial even after one hour. The skewness (S_{sk}) was negative after etching, indicating that valleys were predominant on the surface and the kurtosis (S_{ku}) was superior to three, indicating a narrow height distribution and steep side-walls.

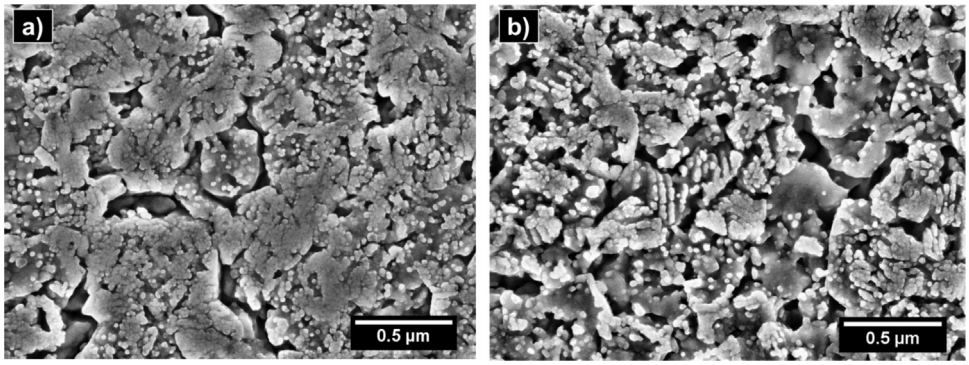

Fig. 5. SEM observations of the surface for 5 min (a) and 10 min (b) of etching in HF 40%, evidencing intergranular and intragranular etching.

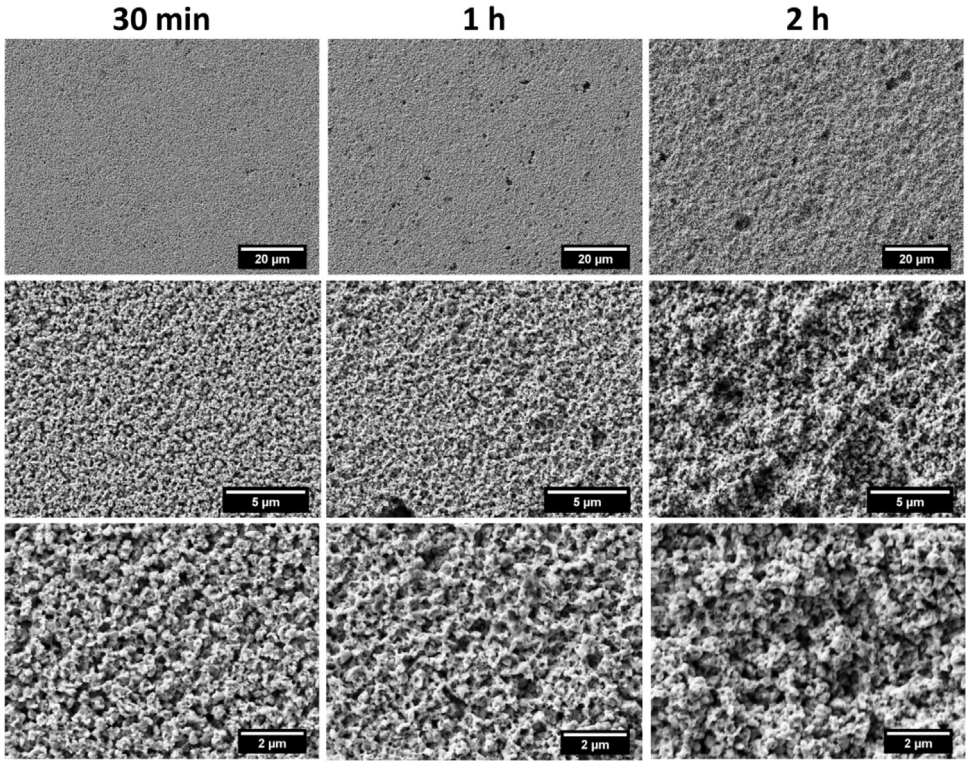

Fig. 6. SEM observations of the surface at different magnifications and for different etching times in HF 40%.

– Spatial parameters (Fig. 8)

For both AFM and WLI measurements, the texture aspect ratio (S_{tr}) approached the value of one when increasing the etching duration, which evidenced that the process leads to an isotropic surface. The fastest decay length (S_{al}) first decreased from zero to thirty minutes but then increased from thirty minutes to two hours. The density of summits (S_{ds}) evidenced a different behavior at small and large scale. At small scale (AFM measurements), the S_{ds} decreased with etching time to reach a minimum at $t = 60$ min, meanwhile it

Table 5
Identification of the peaks of the XPS high-resolution spectra of an etched surface after ultrasonic cleaning (spectra available in the Supplementary information).

Element	Orbital	Binding energy (eV)	Closest value found in the literature (eV)	Identified chemical environment	Reference
F	1s	683.1	–	–	–
O	1s	527.9	–	–	–
		529.3	529.3	3Y-TZP	[27]
		531.3	531.0	YOOH	[27,30]
Y	3d3/2	158.4	158.6	3Y-TZP	[27]
		160.1	–	YOOH	–
	3d5/2	156.3	156.5	3Y-TZP	[27]
		158.1	158.5	YOOH	[30]
Zr	3d3/2	184.1	184.0	3Y-TZP	[27]
	3d5/2	181.7	181.6	3Y-TZP	[27]

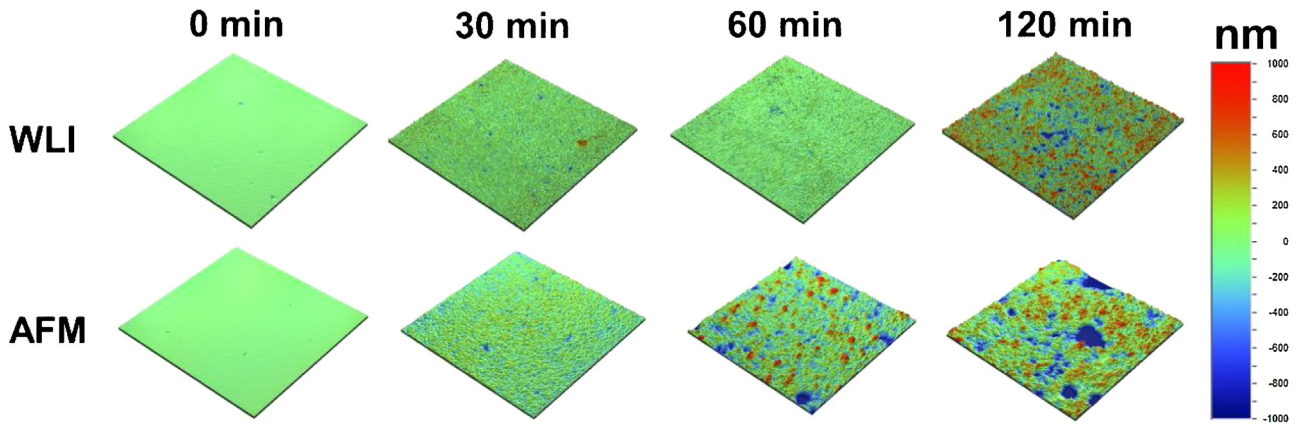

Fig. 7. WLI (150 μm × 150 μm) and AFM (50 μm × 50 μm) topographical images for different etching times in HF 40%.

increased at large scale (WLI measurements) to reach a maximum at the same time point.

– Hybrid parameters (Fig. 9)

For both AFM and WLI measurements, the RMS gradient (S_{dq}), the mean summit curvature (S_{sc}) and the developed interfacial area ratio (S_{dr}) reached a maximum after one hour of etching and then remained almost constant.

– Functional parameters (Fig. 9)

For both AFM and WLI measurements, the bearing index (S_{bi}) first decreased from zero to thirty minutes and then increased slightly from thirty minutes to two hours, whereas the opposite

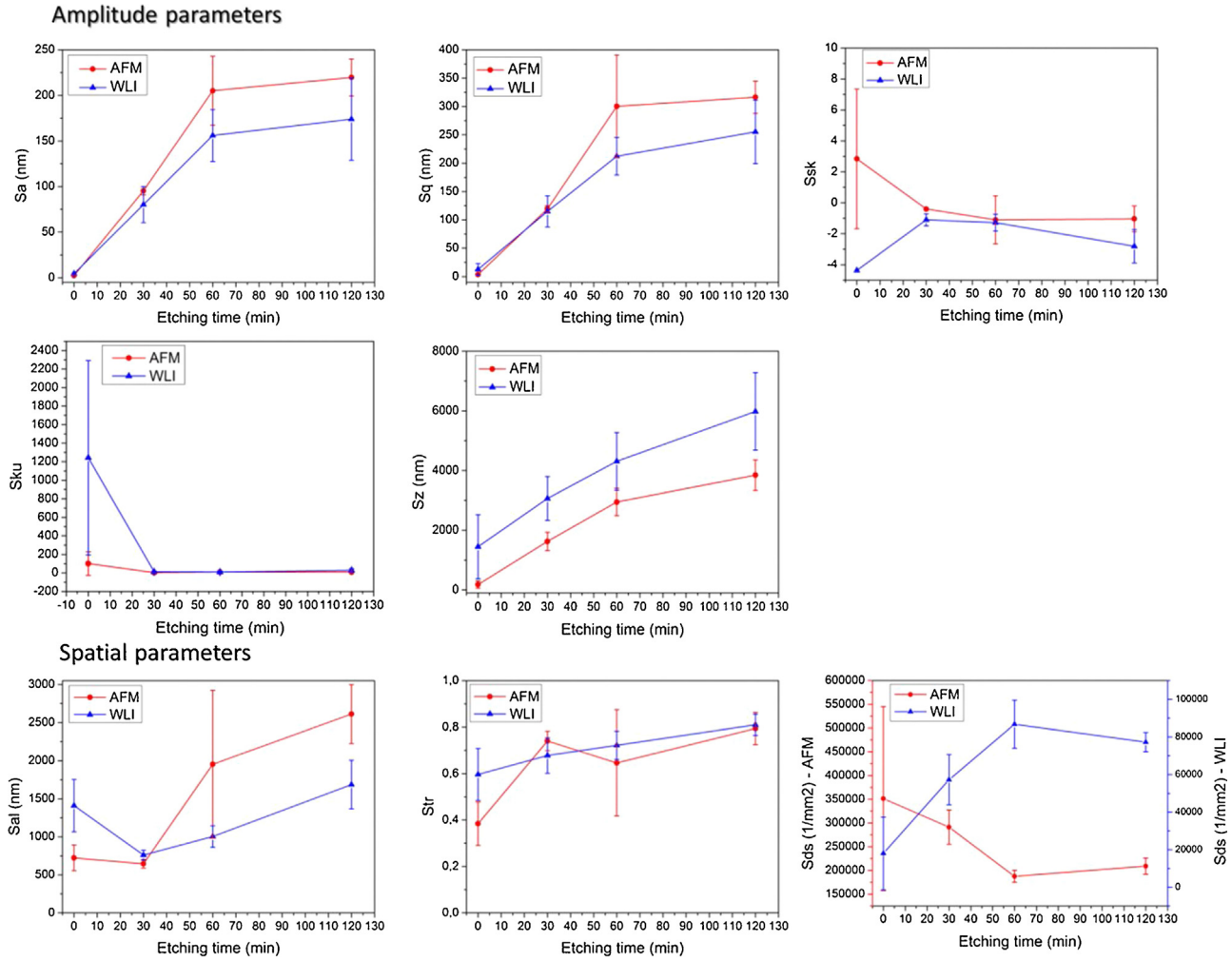

Fig. 8. Evolution of amplitude and spatial roughness parameters over etching time in HF 40% determined from AFM and WLI measurements. Error bars represent the standard deviation.

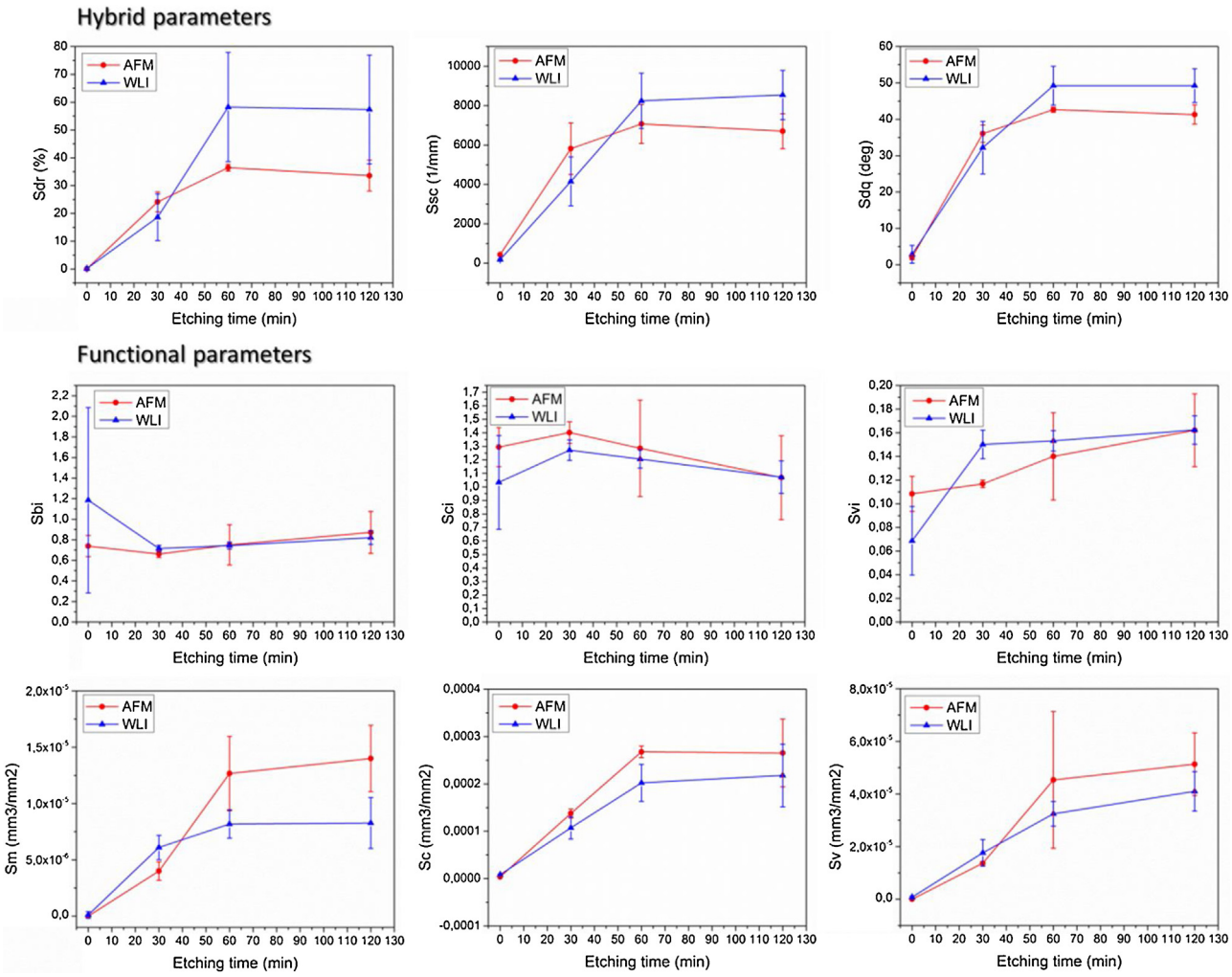

Fig. 9. Evolution of hybrid and functional roughness parameters over etching time in HF 40% determined from AFM and WLI measurements. Error bars represent the standard deviation.

happened with the core fluid retention index (S_{ci}). The valley fluid retention index (S_{vi}) had a slightly different evolution depending on the scale: for WLI measurements it increased until thirty minutes, and then remained constant, whereas for AFM measurements the maximum value was reached only after two hours.

For both AFM and WLI measurements, the surface material volume (S_m) and the surface core void volume (S_c) increased significantly until one hour and then remained almost constant. By contrast, the surface valley void volume (S_v) kept increasing after one hour of etching, especially considering WLI measurements.

3.4.3.2. Fractal analysis. Scale-sensitive fractal analysis of both AFM and WLI data showed that in the first hour of etching the fractal dimension D increased rapidly over time, and then did not evolve substantially (Fig. 10e). Regarding the Smooth–rough crossover, results diverged depending on the technique: the analysis of the AFM data showed that the SRC tended to increase proportionally to the etching time whereas the analysis of the WLI data did not evidence any substantial evolution (Fig. 10d). This discrepancy was probably due to the distinct lateral resolution and area of measurement associated to each technique, which, besides, implies a different range of scales for which the relative area can be computed by the tiling algorithm.

4. Discussion

4.1. Preliminary study: determination of adequate etching conditions

The exponential relationship between the mass loss and the HF concentration may indicate a phenomenon of auto-catalysis as it has been observed for instance during the HF etching of silicon oxide [31,32]. On one hand, the reaction products could increase the etch rate. On the other hand, the S_{dr} increase over time implies an increase of the area available for reacting and thus a faster etching.

Since a high value of S_a is crucial for osseointegration [8], HF 40% seems to be the most suitable etching solution because it leads to the most substantial increase of this parameter in the minimum amount of time. Moreover HF 40% likely leads to a more homogeneous etching of the surface: the value of the relation S_z/S_a is low compared to other concentrations, which indicates probably less exceptional events such as very deep valleys (for instance pits)/high peaks. On the other hand, S_{dr}, which is another important parameter for osseointegration [8] decreased after two hours of etching in HF 40% whereas the mass loss kept increasing, potentially inducing more damage to the material. It appears thus that within the limits of this study a concentration of 40% and an etching time below

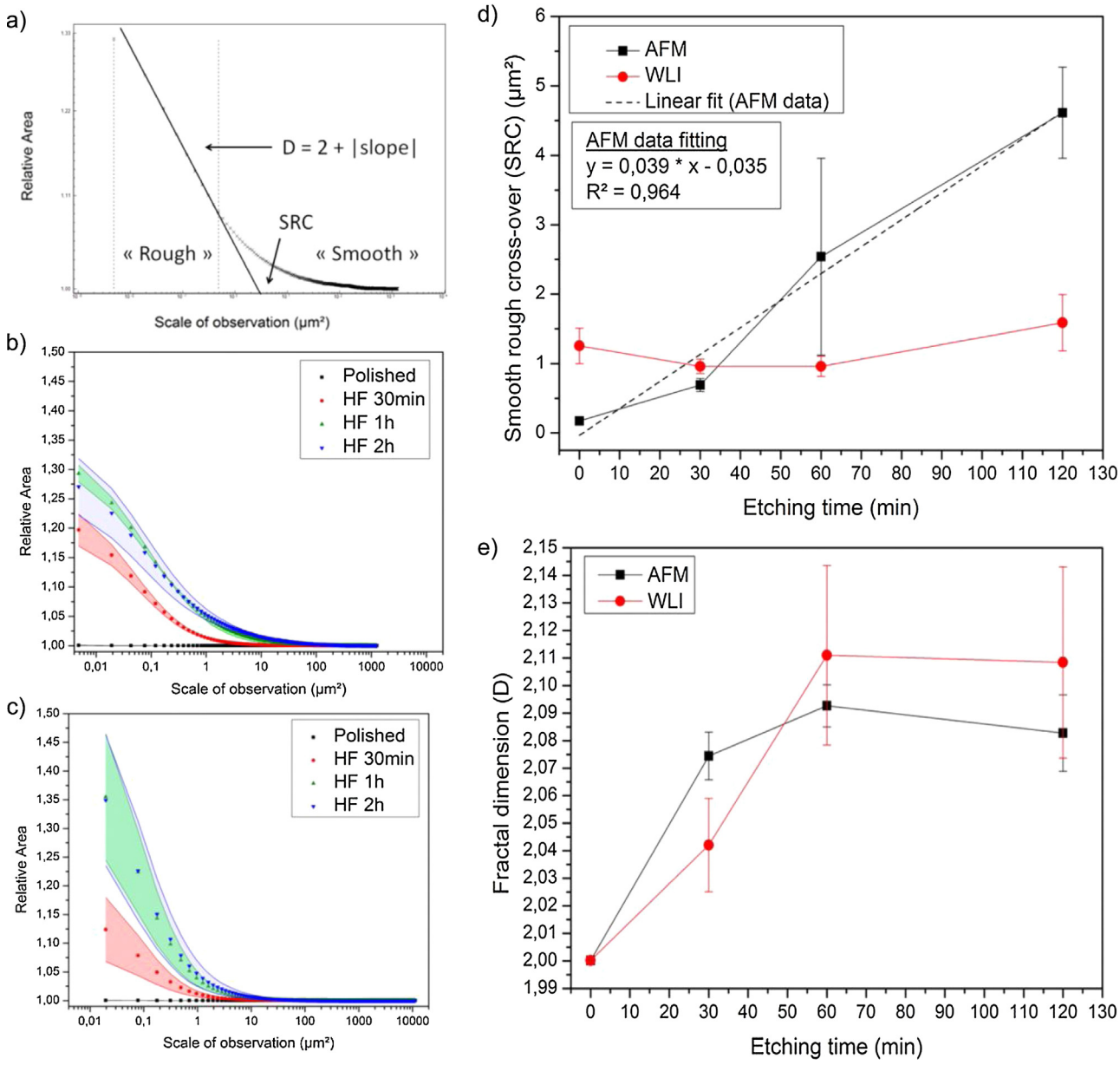

Fig. 10. (a) Example of scale-sensitive fractal analysis, showing how SRC and fractal dimension are obtained, (b) relative area as a function of the scale of observation for different etching times in HF 40% calculated from AFM data, (c) the same with WLI data, (d) smooth–rough crossover as a function of etching time determined from (b) and (c), (e) fractal dimension as a function of etching time determined from (b) and (c). The vertical distance between solid lines in (b) and (c) and the error bars in (d) and (e) represent the standard deviation at each point.

two hours are the most appropriate conditions for the etching of zirconia dental implants.

4.2. Analysis of the etching solution

The results of ESI-FTMS highlighted that the etching of 3Y-TZP with HF leads to the formation of soluble zirconium complexes. Two compounds could not be identified however their isotopic profiles evidenced that they contained zirconium. Consequently the presence of compounds containing yttrium was unlikely although it cannot be discarded. Literature regarding the ESI-FTMS of zirconium complexes is scarce, nevertheless the existence of hydroxides such as $[Zr(OH)_3]+$ and of fluorides such as $[ZrF_5]^-$ and $[Zr_2F_9]^-$ is in good agreement with other studies [33–35]. Doubly charged species $[ZrF_6]^{2-}$ were not observed, but solid salts such as K_2ZrF_6 or $(NH_4)_2ZrF_6$, and hexafluorozirconic acid (H_2ZrF_6) are known to be stable. Therefore, taking into account that structural changes may have occurred during the drying/redissolution process, their presence in the original etching solution should not be excluded.

4.3. Analysis of the etching products

To the best of the knowledge of the authors, this is the first time that the presence of adhered reaction products on the surface of zirconia is reported during HF etching. For short etching times, only octahedrons were present. As evidenced by the SAED and the EDS analysis they are crystalline and composed of Yttrium and Fluorine. Besides, XPS showed the presence of YF_3 bonds at the surface of "as etched" zirconia, which suggest that the octahedrons could be YF_3 crystals. This hypothesis tends to be confirmed by their morphology which is consistent with what can be found in the literature regarding this kind of crystals [36].

After an etching time of about one hour, the "adhered layer" appears. EDS showed that it was composed of zirconium, yttrium and fluorine, which is similar to the needles found in the cleaning water. Besides, some needle-like features were observed by SEM on the "as etched" surface. Therefore the adhered layer could be formed at least partially by an agglomeration of needles. The delayed apparition of the layer could be explained by the saturation of the solution with Zirconium fluorides.

Finally, it should be highlighted that the effect of these reaction products on the bonding between implant and bone and on the patient health is unknown. This underlines the importance of the cleaning step in the fabrication of an HF etched implant. The procedure proposed in this work was very efficient as none of the reaction products described above was observed on the surface after sonication.

4.4. Etching mechanism

Literature regarding the etching mechanism of zirconia is very scarce. It seems that there has been only one attempt to describe the dissolution of ZrO_2 in HF [37], but the study, based on the Pourbaix speciation diagrams, was essentially theoretical. Besides, the case of 3Y-TZP is more complex because of the presence of yttrium oxide.

Based on the experimental results presented above, an attempt to describe the etching mechanism of 3Y-TZP in HF 40%, summarizing previous observations, is presented here:

- F dissolves zirconium oxide and yttrium oxide. Fluoride, oxide, and hydroxide complexes are formed. Etching is slightly preferential at the grain border, but also occurs inside the grains.
- Yttrium complexes have very low solubility. From the beginning of the etching process, yttrium trifluoride (YF_3) octahedral crystals precipitate on the surface.
- Zirconium complexes are partially soluble. After a certain time, an "adhered layer" composed of yttrium, zirconium and fluorine precipitates, probably because the saturation threshold for zirconium fluoride complexes is reached. It may be formed at least partially by agglomerated textured polycrystalline needles.

4.5. Surface characterization

4.5.1. Surface chemistry

The binding energies associated to the Zr 3 d peaks, to the O 1 s peak at 529.3 eV and the Y $3d_{5/2}$ peak at 156.5 eV found during the analysis of the XPS high-resolution spectra were in very good agreement with values found by Majumdar et al. for 3Y-TZP [27]. Besides, fluorine was not detected during the EDS analysis. These two observations tend to indicate that the effect of HF etching on the surface chemistry is limited. Nevertheless, XPS quantitative analysis evidenced a small increase of the fluorine content due to etching which indicates a slight change of composition in the very near surface, which was not related to etching time. Additionally, the presence of an O 1 s peak at 531.3 eV and of the pair of Y 3 d peaks at 158.1 eV and 160.1 eV was compatible with the existence of yttrium hydroxide groups [27,30]. Contrary to what was observed for the "as etched" surface, the presence of YF_3 and ZrF_4 bonds was not detected. This confirms that the ultrasonic cleaning procedure is efficient and that the products precipitated during the reaction are not strongly adhered to the surface.

4.5.2. Evolution of the surface topography over etching time

The roughness parameters analysis showed that a transition takes place around one hour of etching:

- The increase rate of amplitude parameters such as S_a and S_q was high until one hour, and then became much lower. Nevertheless, the ten point peak–peak height S_z kept increasing substantially even after one hour. The same tendency was observed when comparing functional parameters S_m and S_c to S_v. This indicates that although the average roughness, the surface material volume and the surface core void volume do not increase substantially after one hour, localized events such as etching pits likely become bigger. This was confirmed by topographical images (Fig. 7) and is not desirable from the mechanical point of view since those localized events could act as defects originating fracture [18]. On the other hand, it has to be noticed that for the functional indexes S_{bi}, S_{ci} and S_{vi} the transition seems to happen around thirty minutes.
- The density of summits S_{ds} reached a maximum at large scale (WLI measurements) and a minimum at small scale (AFM measurements) for one hour of etching. This means that for longer etching times the number of large peaks tend to increase whereas the small peaks tend to be eroded.
- A maximum was reached around one hour for hybrid parameters S_{dr}, S_{sc} and S_{dq}. This indicates that the specific surface, the summit curvature and the mean surface slope do not increase anymore beyond this time.

The scale sensitive fractal analysis confirmed that a transition takes place around one hour of etching: the fractal dimension first increased rapidly and then reached a plateau (Fig. 10). The interpretation of the evolution of the smooth–rough crossover is not as straightforward given the differences observed depending on the measurement device. As commented previously, these differences are likely to be due to the distinct lateral resolution and area of measurement. However, the analysis of AFM data tended to show that one of the effects of increasing etching time is to increase the scale at which the surface can be considered as "rough", as evidenced by the proportionality between the SRC and the time. This is substantiated by the evolution of the morphology which starts at small scale and continues at large scale for long etching times (Fig. 6).

The main outcome of all these observations is that HF etching makes easy to tailor a surface with the desired smooth–rough transition, fractal dimension and roughness parameters. This constitutes an interesting result given the high sensitivity of osteoblasts to roughness at different scales [7,9,38–41] and the strong influence of fractal dimension on osteoblastic adhesion and differentiation [10]. Regarding the roughness parameters, although the lack of standardization in the measurements makes comparison difficult with other studies, the values of S_a, S_{dr}, S_{ds} and S_{ci} which were obtained here fall within the range of the reported values for commercial dental implants with proved high success rate [8,42–44]. On the other hand, the limited evolution of S_a, S_{dr}, S_{ds} and S_{ci} after one hour of etching tends to indicate that inferior etching times are more appropriate for the treatment of dental implants. Unfortunately most of the studies in the literature omit the other roughness parameters and therefore their influence on the bone response is currently not well documented.

5. Conclusion

The present work shows that HF etching of zirconia is a complex phenomenon involving the dissolution of zirconium and yttrium oxides and the precipitation of fluoride crystals, which is reported for the first time. The formation of these precipitates on the surface highlights the importance of the cleaning step, since their effect on the bonding between implant and bone and on the patient health is unknown. At room temperature and within the limits of this study, a concentration of 40% leads to the fastest and most uniform etching, and appears therefore to be the most appropriate for the treatment of zirconia dental implants. On the other hand, monitoring the etching time allows producing surfaces with con-

trolled roughness, smooth–rough transition and fractal dimension. The roughness analysis was exhaustive and evidenced that a transition was taking place around one hour of etching, after which the evolution of the roughness parameters known to be important for osseointegration was limited. Chemical changes at the surface were moderate and not time related. This work could constitute a sound basis for future biological studies aiming at determining the influence of the topography of zirconia on cell response and osseointegration.

Acknowledgements

The authors would like to acknowledge the European Commission funding under the 7th Framework Programme (Marie Curie Initial Training Networks; grant number: 289958, Bioceramics for bone repair), the support of the Ministry of Economy and Competitiveness (MINECO) of Spain (project ref. MAT2011-23913) and the Government of Catalonia for the grant 2014SGR0137. The authors would also like to thank Dr. Alberto Adeva and Dr. Isidre Casals for their help with ESI-FTMS measurements, Dr. Trifon Trifonov for his help during SEM sessions, Dr. Montserrat Dominguez for her help with XPS analysis, Prof. Christopher Brown and Benjamin Childs from the Worcester Polytechnic Institute (WPI) for providing a free license for the Sfrax software and Bénédicte Londiche, Hugo Pavailler and Gleb Sapunenko for their work related to sample preparation and AFM measurements.

Appendix A. Supplementary data

Supplementary data associated with this article can be found, in the online version, at http://dx.doi.org/10.1016/j.jeurceramsoc.2015.09.021.

References

[1] J. Chevalier, What future for zirconia as a biomaterial? Biomaterials 27 (2006) 535–543, http://dx.doi.org/10.1016/j.biomaterials.2005.07.034.
[2] I. Denry, J.R. Kelly, State of the art of zirconia for dental applications, Dent. Mater. 24 (2008) 299–307, http://dx.doi.org/10.1016/j.dental.2007.05.007.
[3] M. Andreiotelli, H.J. Wenz, R.J. Kohal, Are ceramic implants a viable alternative to titanium implants? A systematic literature review, Clin. Oral. Implants Res. 20 (Suppl. 4) (2009) 32–47, http://dx.doi.org/10.1111/j. 1600-0501.2009.01785. x.
[4] R.-J. Kohal, M. Knauf, B. Larsson, H. Sahlin, F. Butz, One-piece zirconia oral implants: one-year results from a prospective cohort study. 1. Single tooth replacement, J. Clin. Periodontol. 39 (2012) 590–597, http://dx.doi.org/10.1111/j.1600-051X2012.01876.x.
[5] R.B. Osman, M.V. Swain, M. Atieh, S. Ma, W. Duncan, Ceramic implants (Y-TZP): are they a viable alternative to titanium implants for the support of overdentures? A randomized clinical trial, Clin. Oral Implants Res. 25 (2014) 1366–1377, http://dx.doi.org/10.1111/clr.12272.
[6] S. Anil, P.S. Anand, H. Alghamdi, J.A. Jansen, Dental implant surface enhancement and osseointegration, Implant Dent. – Rapidly Evol. Pract. (2005) 83–108, http://dx.doi.org/10.5772/16475.
[7] C. Zink, H. Hall, D.M. Brunette, N.D. Spencer, Orthogonal nanometer–micrometer roughness gradients probe morphological influences on cell behavior, Biomaterials 33 (2012) 8055–8061, http://dx.doi.org/10.1016/j.biomaterials.2012.07.037.
[8] A. Wennerberg, T. Albrektsson, On implant surfaces: a review of current knowledge and opinions, Int. J. Oral Maxillofac. Implants 25 (2009) 63–74.
[9] P.G. Coelho, R. Jimbo, N. Tovar, E.A. Bonfante, Osseointegration: hierarchical designing encompassing the macrometer, micrometer, and nanometer length scales, Dent. Mater. 31 (2015) 37–52, http://dx.doi.org/10.1016/j.dental.2014.10.007.
[10] K. Anselme, M. Bigerelle, B. Noel, E. Dufresne, D. Judas, A. Iost, et al., Qualitative and quantitative study of human osteoblast adhesion on materials with various surface roughnesses, J. Biomed. Mater. Res. 49 (2000) 155–166.
[11] A. Casucci, C. Mazzitelli, F. Monticelli, M. Toledano, R. Osorio, E. Osorio, et al., Morphological analysis of three zirconium oxide ceramics: effect of surface treatments, Dent. Mater. 26 (2010) 751–760, http://dx.doi.org/10.1016/j.dental.2010.03.020.
[12] R. Gruber, E. Hedbom, D. Bosshardt, R. Heuberger, D. Buser, Acid and alkali etching of grit blasted zirconia: impact on adhesion and osteogenic differentiation of MG63 cells in vitro, Dent. Mater. J. 31 (2012) 1097–1102, http://dx.doi.org/10.4012/dmj. 2012-107.
[13] M. Gahlert, S. Röhling, M. Wieland, S. Eichhorn, H. Küchenhoff, H. Kniha, A comparison study of the osseointegration of zirconia and titanium dental implants: a biomechanical evaluation in the maxilla of pigs, Clin. Implant Dent. Relat. Res. 12 (2010) 297–305, http://dx.doi.org/10.1111/j. 1708-8208.2009.00168. x.
[14] H. Ito, H. Sasaki, K. Saito, S. Honma, Y. Yajima, M. Yoshinari, Response of osteoblast-like cells to zirconia with different surface topography, Dent. Mater. J. 32 (2013) 122–129, http://dx.doi.org/10.4012/dmj. 2012-208.
[15] C. Bergemann, K. Duske, J.B. Nebe, A. Schöne, U. Bulnheim, H. Seitz, et al., Microstructured zirconia surfaces modulate osteogenic marker genes in human primary osteoblasts, J. Mater. Sci. Mater. Med. (2015), http://dx.doi.org/10.1007/s10856-014-5350-x.
[16] L.F. Cooper, Y. Zhou, J. Takebe, J. Guo, A. Abron, A. Holmén, et al., Fluoride modification effects on osteoblast behavior and bone formation at TiO_2 grit-blasted c.p. titanium endosseous implants, Biomaterials 27 (2006) 926–936, http://dx.doi.org/10.1016/j.biomaterials.2005.07.009.
[17] J. Oliva, X. Oliva, J.D. Oliva, Five-year success rate of 831 consecutively placed zirconia dental implants in humans: a comparison of three different rough surfaces, Int. J. Oral Maxillofac. Implants 25 (2010) 336–344.
[18] Q. Flamant, M. Anglada, Hydrofluoric acid etching of dental zirconia. Part 2: effect on flexural strength and ageing behavior, J. Eur. Ceram. Soc. 36 (2016) 135–145.
[19] J.A. Muñoz-Tabares, E. Jiménez-Piqué, M.J. Anglada, Subsurface evaluation of hydrothermal degradation of zirconia, Acta Mater. 59 (2011) 473–484, http://dx.doi.org/10.1016/j.actamat.2010.09.047.
[20] W. Dong, P. Sullivan, K. Stout, Comprehensive study of parameters for characterising three- dimensional surface topography III: parameters for characterising amplitude and some functional properties, Wear 178 (1994) 29–43, http://dx.doi.org/10.1016/0043-1648(94) 90127-9.
[21] W.P. Dong, P.J. Sullivan, K.J. Stout, Comprehensive study of parameters for characterising three-dimensional surface topography: IV: parameters for characterising spatial and hybrid properties, Wear 178 (1994) 45–60.
[22] K.J. Stout, L. Blunt, Three Dimensional Surface Topography, Elsevier, 2000, http://dx.doi.org/10.1016/B978-185718026-8/50119-3.
[23] C.A. Brown, P.D. Charles, W.A. Johnsen, S. Chesters, Fractal analysis of topographic data by the patchwork method, Wear 161 (1993) 61–67, http://dx.doi.org/10.1016/0043-1648(93) 90453-S.
[24] Siegmann S. 1997. Scale-Sensitive Fractal Analysis for Understanding the Influence of Substrate Roughness in Thermal Spraying. 1st United Therm. Spray Conf. - Therm. Spray A United Forum Sci. Technol. Adv., p. 665–70.
[25] V.I. Nefedov, N.P. Sergushin, I.M. Band, M.B. Trzhaskovskaya, Relative intensities in X-ray photoelectron spectra, J. Electron. Spectrosc. Relat. Phenom. 2 (1973) 383–403.
[26] C.D. Wagner, Handbook of X-ray photoelectron spectroscopy: a reference book of standard data for use in X-ray photoelectron spectroscopy, in: Physical Electronics Division, Perkin-Elmer Corporation, 1979.
[27] D. Majumdar, D. Chatterjee, X-ray photoelectron spectroscopic studies on yttria, zirconia, and yttria-stabilized zirconia, J. Appl. Phys. 70 (1991) 988, http://dx.doi.org/10.1063/1.349611.
[28] R. Kaufmann, H. Klewe-Nebenius, H. Moers, G. Pfennig, H. Jenett, H.J. Ache, XPS studies of the thermal behaviour of passivated Zircaloy-4 surfaces, Surf. Interface Anal. 11 (1988) 502–509, http://dx.doi.org/10.1002/sia.740111003.
[29] O.A. Baschenko, V.I. Nefedov, Relative intensities in x-ray photoelectron spectra: Part IV: the effect of elastic scattering in a solid on the free path of electrons and their angular distribution, J. Electron. Spectrosc. Relat. Phenom. 17 (1979) 405–420.
[30] T.L. Barr, An ESCA study of the termination of the passivation of elemental metals, J. Phys. Chem. 82 (1978) 1801–1810, http://dx.doi.org/10.1021/j100505a006.
[31] H. Robbins, B. Schwartz, Chemical etching of silicon, J. Electrochem. Soc. 106 (1959) 505, http://dx.doi.org/10.1149/1.2427397.
[32] I.A. Shah, B.M.A. van der Wolf, W.J.P. van Enckevort, E. Vlieg, Wet chemical etching of silicon {1 1 1}: autocatalysis in pit formation, J. Electrochem. Soc. 155 (2008) J79, http://dx.doi.org/10.1149/1.2830841.
[33] T. Sasaki, O. Nakaoka, R. Arakawa, T. Kobayashi, I. Takagi, H. Moriyama, Detection of polynuclear zirconium hydroxide species in aqueous solution by desktop ESI–MS, J. Nucl. Sci. Technol. 47 (2010) 1211–1218, http://dx.doi.org/10.1080/18811248.2010.9720988.
[34] X. Xu, L. Ling, X. Ding, J.O. Burgess, Synthesis and characterization of a novel, fluoride-releasing dimethacrylate monomer and its dental composite, J. Polym. Sci. Part A Polym. Chem. 42 (2004) 985–998, http://dx.doi.org/10.1002/pola.11037.
[35] X. Xu, X. Ding, L. Ling, J.O. Burgess, Synthesis and characterization of novel fluoride-releasing monomers: II. Dimethacrylates containing bis (aminodiacetic acid) and their ternary zirconium fluoride complexes, J. Polym. Sci. Part A Polym. Chem. 43 (2005) 3153–3166, http://dx.doi.org/10.1002/pola.20787.
[36] L. Qian, J. Zai, Z. Chen, J. Zhu, Y. Yuan, X. Qian, Control of the morphology and composition of yttrium fluoridevia a salt-assisted hydrothermal method, CrystEngComm 12 (2010) 199–206, http://dx.doi.org/10.1039/B911401G.
[37] V. Lowalekar, S. Raghavan, Etching of zirconium oxide, hafnium oxide, and hafnium silicates in dilute hydrofluoric acid solutions, J. Mater. Res. 19 (2004) 1149–1156, http://dx.doi.org/10.1557/JMR2004.0149.
[38] O. Zinger, K. Anselme, A. Denzer, P. Habersetzer, M. Wieland, J. Jeanfils, et al., Time-dependent morphology and adhesion of osteoblastic cells on titanium

model surfaces featuring scale-resolved topography, Biomaterials 25 (2004) 2695–2711, http://dx.doi.org/10.1016/j.biomaterials.2003.09.111.
[39] T.P. Kunzler, T. Drobek, M. Schuler, N.D. Spencer, Systematic study of osteoblast and fibroblast response to roughness by means of surface-morphology gradients, Biomaterials 28 (2007) 2175–2182, http://dx.doi.org/10.1016/j.biomaterials.2007.01.019.
[40] J.E. Davies, E. Ajami, R. Moineddin, V.C. Mendes, The roles of different scale ranges of surface implant topography on the stability of the bone/implant interface, Biomaterials 34 (2013) 3535–3546, http://dx.doi.org/10.1016/j.biomaterials.2013.01.024.
[41] R.A. Gittens, R. Olivares-Navarrete, Z. Schwartz, B.D. Boyan, Implant osseointegration and the role of microroughness and nanostructures: lessons for spine implants, Acta Biomater. 10 (2014) 3363–3371, http://dx.doi.org/10.1016/j.actbio.2014.03.037.
[42] L.M. Svanborg, M. Andersson, A. Wennerberg, Surface characterization of commercial oral implants on the nanometer level, J. Biomed. Mater. Res. B Appl. Biomater. 92 (2010) 462–469, http://dx.doi.org/10.1002/jbm.b.31538.
[43] A. Wennerberg, T. Albrektsson, Effects of titanium surface topography on bone integration: a systematic review, Clin. Oral Implants Res. 20 (Suppl. 4) (2009) 172–184, http://dx.doi.org/10.1111/j. 1600-0501.2009.01775.x.
[44] S. Zinelis, K. Thomas a Syres, N. Silikas, G. Eliades, Surface characterization of zirconia dental implants, Dent. Mater. 26 (2010) 295–305, http://dx.doi.org/10.1016/j.dental.2009.11.079.

Supplementary information

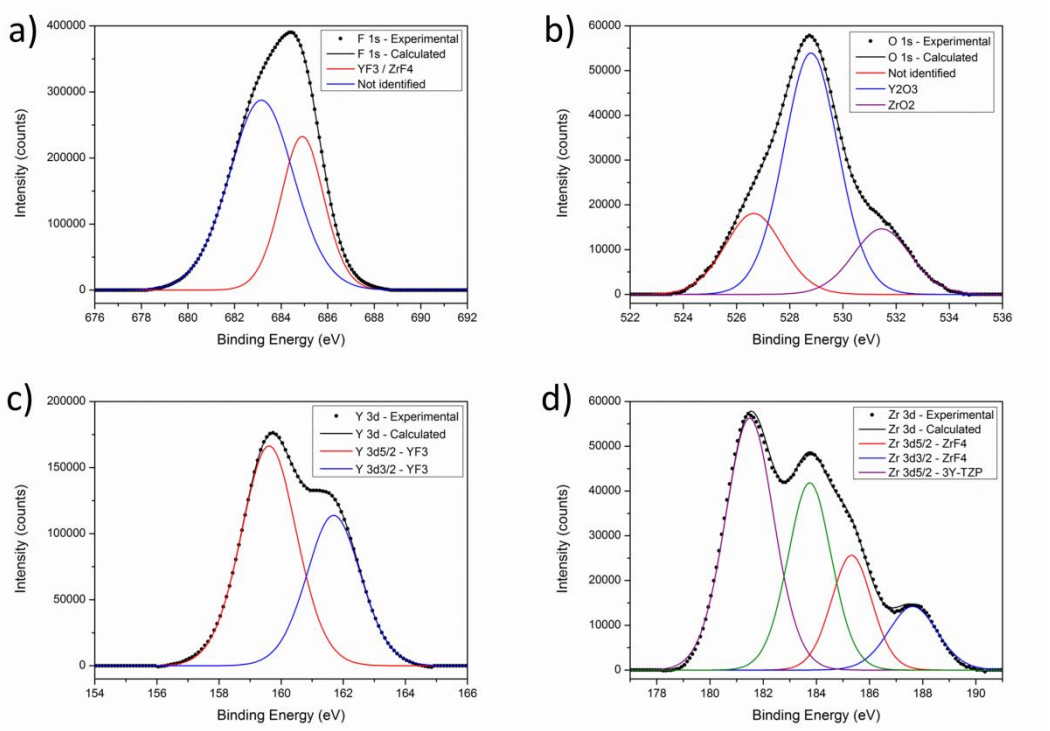

XPS high-resolution spectra and deconvoluted peaks of an "as etched" surface for different ranges of binding energy corresponding to the following elements: a) Fluorine, b) Oxygen, c) Yttrium, d) Zirconium.

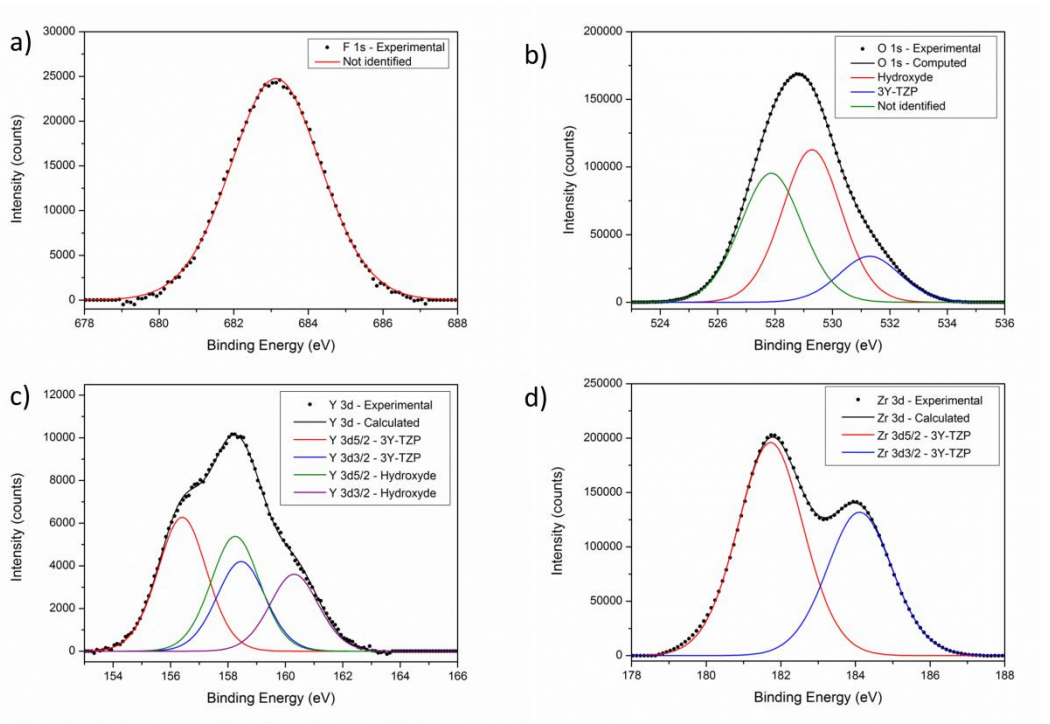

XPS high-resolution spectra and deconvoluted peaks of etched zirconia after ultrasonic cleaning for different ranges of binding energy corresponding to the following elements: a) Fluorine, b) Oxygen, c) Yttrium, d) Zirconium.

Article II.

Hydrofluoric acid etching of dental zirconia. Part 2: effect on flexural strength and ageing behavior.

Journal of the European Ceramic Society 36 (2016) 135–145

Contents lists available at www.sciencedirect.com

Journal of the European Ceramic Society

journal homepage: www.elsevier.com/locate/jeurceramsoc

Hydrofluoric acid etching of dental zirconia. Part 2: effect on flexural strength and ageing behavior

Quentin Flamant[a,b,*], Marc Anglada[a,b,*]

[a] Department of Materials Science and Metallurgical Engineering, Universitat Politècnica de Catalunya, Av. Diagonal 647, 08028 Barcelona, Spain
[b] Center for Research in Nano-Engineering, CRNE, Universitat Politecnica de Catalunya, C. Pascual i Vila, 15, 08028 Barcelona, Spain

ARTICLE INFO

Article history:
Received 9 July 2015
Received in revised form
14 September 2015
Accepted 15 September 2015
Available online 2 October 2015

Keywords:
Zirconia
Etching
Dental
Ageing
Strength

ABSTRACT

Among the diverse treatments proposed to promote the osseointegration of zirconia dental implants, hydrofluoric acid (HF) etching appears to be a good candidate. However little is known on the effect of this process on the mechanical properties and long-term reliability. In this work, the surface integrity, the flexural strength and the ageing sensitivity of yttria-stabilized zirconia were assessed after etching in HF 40%. Results show that etching induces an increase of monoclinic phase content and a decrease in flexural strength. The strength decrease is limited to 15% for etching times below 60 min, whereas it reaches 29% after 120 min because of the formation of large etching pits. No substantial change in the ageing sensitivity was evidenced. Within the limits of this study, HF 40% etched zirconia appears to be reliable for long-term implantation provided that the etching duration does not exceed 60 min.

1. Introduction

Yttria-stabilized tetragonal zirconia polycrystals (Y-TZP, short: zirconia) are biocompatible and exhibit the best combination of strength and toughness of single-phase oxide ceramics. They were introduced as biomaterials in the end of the 1980s to overcome the limitations of alumina in the field of orthopedics [1]. Their excellent mechanical properties are due to phase transformation toughening: under stress the metastable tetragonal grains at the crack tip transform into monoclinic phase with a volume expansion, and this induces compressive stresses on the crack [2]. Unfortunately, the phase transformation is also the cause of their main weakness: in the presence of water the tetragonal phase can transform spontaneously, inducing micro-cracks and a loss of integrity of the material (see for instance the review from Lawson [3]). The impact of this phenomenon, known as Low Temperature Degradation (LTD) or ageing, was thought to be limited in vivo until 2001, when 400 Prozyr® femoral heads failed in a very short period because of accelerated LTD [1]. This unfortunate event highlighted that minor changes in the fabrication process of zirconia ceramics may induce a dramatic increase of ageing sensitivity and that any modification should thus be followed by a careful assessment of its impact on long-term reliability.

While monolithic zirconia has been almost abandoned for orthopedic applications, in the last decade its use in restorative dentistry has been growing fast [4]. In particular, its good esthetics, high resistance to corrosion and the absence of allergic reaction make zirconia a good candidate to replace titanium for the fabrication of dental implants [5]. However, some authors reported a higher failure rate and a higher marginal bone loss when comparing zirconia to titanium. According to them, the use of zirconia implants does not appear recommendable at the moment except for specific cases (e.g. allergy to titanium), and there is a need for further research before generalizing their clinical use [6,7].

To solve the problem of bone loss mentioned above, the key is to achieve a good osseointegration, which was shown to be promoted by rough surfaces [8]. Among the different surface chemical treatments already proposed in the literature for this purpose, hydrofluoric acid (HF) etching appears to be a good candidate [9–12]. Besides zirconia dental implants with acid etched surface are already commercialized (CeraRoot implants with ICE™ surface) and apparently have shown a similar success rate as compared to titanium implants after five years of follow-up study [13].

Despite the Prozyr® failure event, the dental industry may not have been sufficiently concerned with the problems related to age-

Abbreviations: DI water, deionized water; FIB, focused ion beam; HF, hydrofluoric acid; LTD, low temperature degradation; SEM, scanning electron microscopy; Y-TZP, yttria-stabilized tetragonal zirconia polycrystals; 3Y-TZP, 3 mol% Y-TZP.

* Corresponding authors. Fax: +34 934016706.
E-mail addresses: quentin.flamant@upc.edu (Q. Flamant), marc.j.anglada@upc.edu (M. Anglada).

http://dx.doi.org/10.1016/j.jeurceramsoc.2015.09.022
0955-2219/

Table 1
Names of the different groups of samples and description of the associated treatments.

Group	Description of the treatment
Control	No treatment (polished surface)
HF40-30	Immersed 30 min in HF 40%
HF40-60	Immersed 60 min in HF 40%
HF40-120	Immersed 120 min in HF 40%
Control-Aged	Polished and aged
HF40-30-Aged	Immersed 30 min in HF 40% and aged
HF40-60-Aged	Immersed 60 min in HF 40% and aged
HF40-120-Aged	Immersed 120 min in HF 40% and aged

ing [1,14]. As a result, as far as the authors know, there is currently no study of the effect of acid etching on the long-term reliability of dental zirconia. The objective of this work is therefore to address this lack of knowledge by assessing the impact of HF etching on the surface integrity, the flexural strength and the ageing sensitivity. The surface characterization and the questions related to the etching mechanism are treated in a separated article [12].

2. Materials and methods

2.1. Zirconia disks preparation

Commercial 3Y-TZP powder (TZ-3YSB-E Tosoh Co., Japan) was cold isostatically compacted under pressure of 200 MPa in a cylindrical mold for producing a green body, and then sintered in an alumina tube furnace at 1450 °C for two hours (3 °C/min heating and cooling rates). The sintered ceramic cylinders were cut into specimens in the form of disks (2 mm thick, 9 mm diameter), which were ground and polished down to a 3 μm diamond suspension. The samples were then successively cleaned for five minutes with acetone, ethanol and deionized water (DI water) in an ultrasonic bath in order to remove contaminants. The polishing step, which is not likely to be part of the processing for a commercial implant, was introduced in order to facilitate the study of the impact of etching on surface integrity, phase transformation and strength. It was assumed that the effects of etching on a machined and annealed surface or on a sintered surface would be comparable. Samples were divided into different groups according to the treatment they received as reported in Table 1 (ten samples per group).

2.2. Chemical etching

Etching was carried out in HF 40% (Hydrofluoric Acid 40% QP Panreac, Spain) and followed by ultrasonic cleaning in DI water. The volume of acid was 1 mL by sample. Etching times between zero and two hours and a concentration of 40% were used rather than longer times and more diluted solutions because these conditions were shown to be the most appropriate for a fast and uniform roughening [12].

2.3. Surface integrity

An estimation of the average thickness of the layer of material removed during etching was calculated using the following formula:

$$t = \frac{\rho}{S}\Delta m \tag{1}$$

where t is the estimated removed thickness, Δm is the mass loss due to etching, ρ is the theoretical density of 3Y-TZP ($\rho = 6.1\ \mathrm{g\,cm^{-3}}$) and S is the total sample external area.

The surface of etched samples was examined by Scanning Electron Microscopy (SEM) and the near-surface was observed on transversal sections milled with a Focused Ion Beam (FIB, Neon40, Carl Zeiss AG, Germany) in order to detect phase transformation and damage. Sample surfaces were protected with a thin platinum coating to flatten the surface and minimize ion-beam damage and curtain effect during milling. The final polishing of the cross-sections was performed at 500 pA.

2.4. Ageing

Hydrothermal degradation tests (which will also be referred to as "ageing") were performed in an autoclave, at 134 °C, 100% steam atmosphere at 0.2 MPa pressure during thirty hours. These conditions have been suggested to be equivalent to roughly sixty years in vivo for polished 3Y-TZP [15].

2.5. Monoclinic phase content

Three specimens of each group (Table 1) were analyzed by X-ray diffraction (XRD) with a Bruker AXS D8 diffractometer using Cu-Kα radiation to detect and quantify the tetragonal–monoclinic transformation. The monoclinic fraction was determined by using the relation proposed by Toraya et al. [16]:

$$V_m = 1.311\frac{I_m\left(\bar{1}11\right) + I_m(111)}{1.311\left[I_m\left(\bar{1}11\right) + I_m(111) + I_t(101)\right]} \tag{2}$$

where V_m is the monoclinic volume fraction, $I_m\left(\bar{1}11\right)$ and $I_m(111)$ are the intensities of the monoclinic peaks and $I_t(101)$ is the intensity of the tetragonal peak.

2.6. Biaxial flexural strength

The biaxial flexural strength of the samples from the different groups (Table 1) was assessed by ball on three balls testing. The specimens were tested in an Instron 8511 servohydraulic fatigue testing machine with cobalt-cemented tungsten carbide balls of 5.9 mm diameter and a loading rate of 200 N/s. The fracture strength was calculated by using a numerical approximation of the maximum tensile stress as proposed by Börger et al. [17]:

$$\sigma_{max} = f.\frac{F}{t^2} \tag{3}$$

where F is the applied load, t the sample thickness and f a dimensionless factor. Provided that $0.55 < \frac{R_a}{R} < 0.9$ and $0.05 < \frac{t}{R} < 0.6$, an approximation of f for a determined Poisson's ratio can be calculated with the following formula:

$$f = c_0 + \frac{\left(c_1 + c_2\frac{t}{R} + c_3\left(\frac{t}{R}\right)^2 + c_4\left(\frac{t}{R}\right)^3\right)}{1 + c_5\frac{t}{R}}\left(1 + c_6\frac{R_a}{R}\right) \tag{4}$$

where R is the radius of the disk, R_a the support radius ($R_a = 3.4$ mm) and c_i (i = 0,...6) tabulated constants which depend on the Poisson's ratio ν [17]. For 3Y-TZP, $\nu \approx 0.3$ [18], which leads to the following values: $c_0 = -17.346$, $c_1 = 20.774$, $c_2 = 622.62$, $c_3 = -76.879$, $c_4 = 50.383$, $c_5 = 33.736$, $c_6 = 0.0613$.

2.7. Fractography

The fractographic examination was a complicated task because samples were broken into tiny pieces. However for some of the specimens it was possible to identify the fracture origin by SEM.

2.8. Statistical analysis

Statistical analysis of the strength testing results was performed using SPSS® software (version 20, SPSS Inc., Chicago, IL, USA). A two-way ANOVA with a 5% significance level was used to evaluate the

effects of etching time and ageing and to assess possible interaction. The homogeneity of variance between groups was verified with a Levene test. A simple main effects analysis with Sidak-adjusted α was applied to investigate specific comparisons.

The variability of the strength was analyzed using the Weibull distribution function:

$$P_F(\sigma) = 1 - e^{-\left(\frac{\sigma}{\sigma_0}\right)^m} \quad (5)$$

where P_F is the probability of failure, σ is the fracture strength, σ_0 is the Weibull characteristic strength, and m is the Weibull modulus.

For the graphical evaluation of m and σ_0 the measured strength data were ranked in increasing order and numbered from 1 to N. Then the single strength values σ_i were related to the failure probability P_{Fi} according to the following relation:

$$P_{Fi} = \frac{i - 0.5}{N} \quad (6)$$

where i is the ranking number and N is the total number of measurements (for a more detailed description of the methodology, see for instance Munz and Fett [19]). Finally, the 90% confidence bounds for m and σ_0 were determined according to ASTM C1239-00.

3. Results

3.1. Surface integrity after etching

The thickness of the layer of material removed during etching was estimated to be (mean value ± SD): 6.0 ± 1.9 μm, 12 ± 1.0 μm and 18 ± 4.5 μm for respectively 30, 60 and 120 min of etching.

The observation of the FIB cross-sections evidenced that a small porosity was produced under the surface (Fig. 2). The etch-damaged layer had an average thickness of about 1 μm, which reached locally 3 μm but did not seem to increase substantially over time.

On the other hand, etching produced numerous randomly dispersed pits on the surface, whose typical size increased with etching duration (Fig. 3b–d). The presence of pits of exceptionally big size was detected in few cases (Fig. 1). As it will be discussed further, although this kind of defects was uncommon, they may have a critical impact on strength.

3.2. Phase transformation

Etching induced an increase of monoclinic phase content at the surface in the range 10–23% nevertheless the results do not show a simple relation between this increase and etching time (Fig. 4). On the other hand, the amount of monoclinic phase in samples of the different etched-aged groups (HF40-30-Aged, HF40-60-Aged, HF40-120-Aged) was very similar (in the range 71–73%), indicating that the monoclinic content after ageing did not depend on the initial etching time. In the case of the Control-Aged group, the amount of monoclinic phase was lower (about 56%). However, the increase in monoclinic content (+55%) was roughly the same as in the etched-aged sample groups (between +48% and +61%). In other words, the difference in the final monoclinic content after ageing between the control-aged and the etched-aged samples was mainly associated to the difference in the initial amount of monoclinic phase.

Finally, the thickness of the micro-cracked layer induced by the phase transformation measured on a FIB cross-section of a sample from the HF40-120-Aged group was estimated to be d ≈5 μm (Fig. 5). The same measurement performed on a sample from the Control–Aged group gave a similar result (≈6 μm). This tends to confirm that etched samples do not age more rapidly than the control ones.

3.3. Fractography

Fractographic observations could only be performed on a limited number of samples but evidenced that:

- Etching pits could initiate failure (Fig. 1b, Fig. 6b).
- Similarly, porous zones, which may result from a locally deeper penetration of the acid in the material, could initiate failure (Fig. 6a). These zones will be referred to as “deep porous zones”.
- The monoclinic micro-cracked layer induced by ageing was thicker in some zones, which could also nucleate failure: for instance in the case presented Fig. 6c it reached 13 μm, which is approximately 2.5 times more than the average thickness.

One sample from each of the HF40-30 and HF40-60 groups had substantially lower strength than the rest because of very uncommon defects. In the first case the failure was associated to a “tunnel-like” defect (Fig. 6e). The acid seems to have removed preferentially the material under the surface, which could be due to some large pre-existing sub-superficial defect, like a pre-existing pore or a less densified zone. In the second case, the failure seems to have been initiated by a huge sub-superficial defect (Fig. 6f), but there was no evidence that it could be related to etching. Because these defects were very unusual and distinct from the others, the data points associated to those samples were discarded for the calculation of the mean strength and the standard deviation of the group they belonged to, as well as for the statistical analysis.

3.4. Strength analysis

The mean biaxial flexural strength results are shown Fig. 7. The two-way ANOVA evidenced a main effect of etching time ($F(3,69) = 10.272$, $p < 0.001$), no main effect of ageing ($F(1,69) = 0.488$, $p = 0.487$) and an interaction between etching time and ageing, ($F(3,69) = 8.869$, $p < 0.001$). The assumption of homogeneity of the variance was verified ($p = 0.356$).

The results of the simple main effects analysis which indicate statistically significant differences between groups are represented by letters in Fig. 7. In particular, they show that:

- All etched groups exhibited a significantly lower strength than the Control group and there was no significant difference between the HF40-30 and HF40-60 groups.
- There was no significant difference between any of the aged groups.
- The Control-Aged group exhibited a significantly lower strength than the Control group, there was no significant difference between respectively the HF40-30, HF40-60 and the HF40-30-Aged, HF40-60-Aged groups whereas the HF40-120-Aged group exhibited a significantly higher strength than the HF40-120 group.

Weibull analysis (Fig. 8, Table 2) confirmed the decrease of strength associated to etching observed in the two-way ANOVA. The strength distributions of HF40-30 and HF40-60 groups were very similar. The decrease in strength was more pronounced for the HF40-120 group.

Regarding the effect of ageing, Weibull analysis confirmed that:

- The strength distributions of the all the aged groups were very similar.
- Ageing induced a decrease in strength for the control samples.
- Ageing induced an increase in strength for the samples etched two hours.

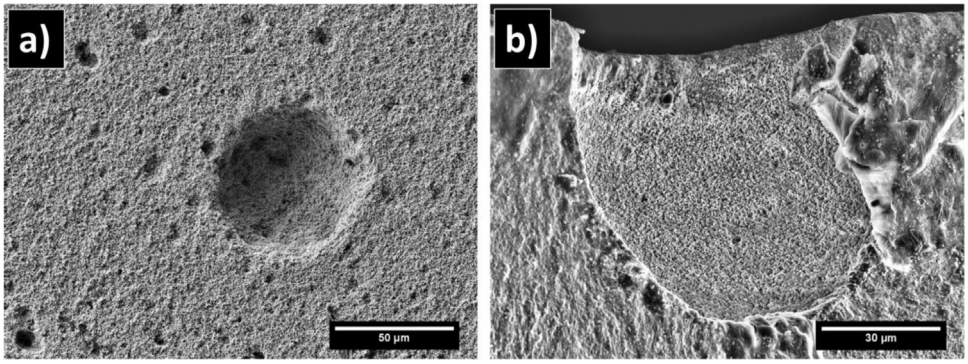

Fig. 1. Pits of exceptionally big size observed: (a) on the surface of a sample from the HF40-120 group, (b) on the fracture surface of a sample from the HF40-120-aged group, in which it nucleated failure (σ_{max} = 816 MPa).

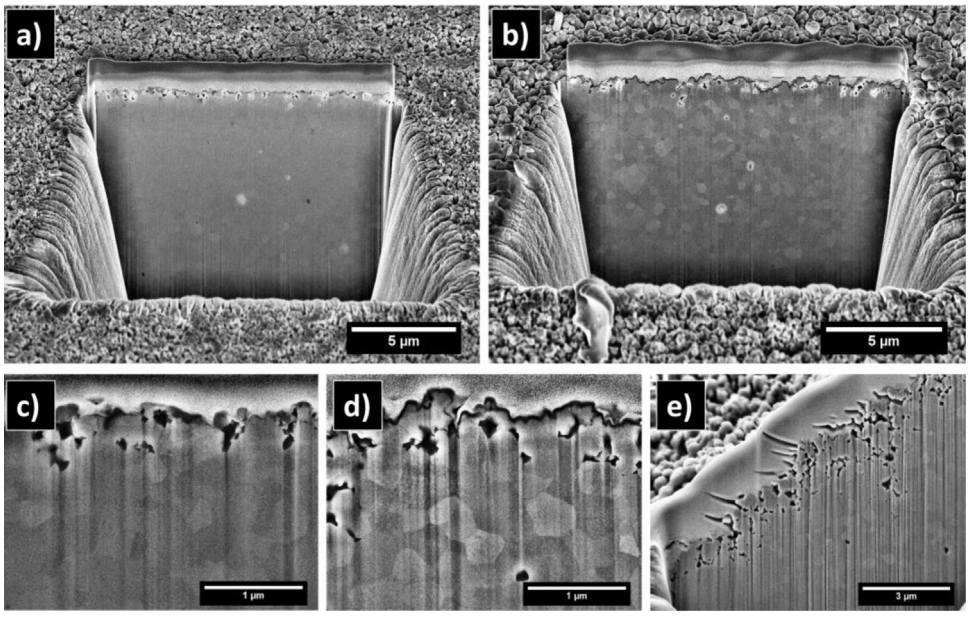

Fig. 2. FIB cross-sections at the surface of 3Y-TZP after etching for one hour (a, c) and two hours (b, d, e).

Table 2
Weibull modulus (biased), characteristic strengths and associated linear regression coefficients for different etching conditions, before and after ageing.

Sample group	m (90% confidence interval)	σ_0 [MPa] (90% confidence interval)	R^2
Control	11 (6–14)	1278 (1202–1362)	0.9504
HF40-30	10 (5–14)	1064 (994–1141)	0.9483
HF40-60	8 (4–11)	1071 (981–1173)	0.9852
HF40-120	10 (6–13)	912 (855–975)	0.9167
Control-Aged	10 (6–14)	1105 (1039–1178)	0.9591
HF40-30-Aged	20 (11–27)	1068 (1033–1103)	0.9804
HF40-60-Aged	13 (7–17)	1142 (1085–1204)	0.8779
HF40-120-Aged	12 (6–16)	1081 (1022–1145)	0.9215

Because of the limited number of samples, interpretations regarding the Weibull modulus are subjected to caution. It seems however that neither etching, nor ageing induced substantial changes in the Weibull modulus.

4. Discussion

4.1. Effects of HF etching

4.1.1. Qualitative interpretation

HF etching induced an increase of monoclinic phase content at the surface. This could be explained by differences in the dissolution kinetics of yttrium oxide and zirconium oxide by HF, which could create an yttrium depleted layer of zirconia, in which the tetragonal phase is less stable.

Besides etching induced different kind of defects in the material:

- The formation of a thin etch-damaged layer on the whole surface, whose depth did not appear to evolve substantially over time, but could be locally thicker (Fig. 2). Because the porosity was formed by dissolution, it is necessarily interconnected. The etch-damaged layer could thus be considered as microcracked. Besides, as commented before, etching induced some

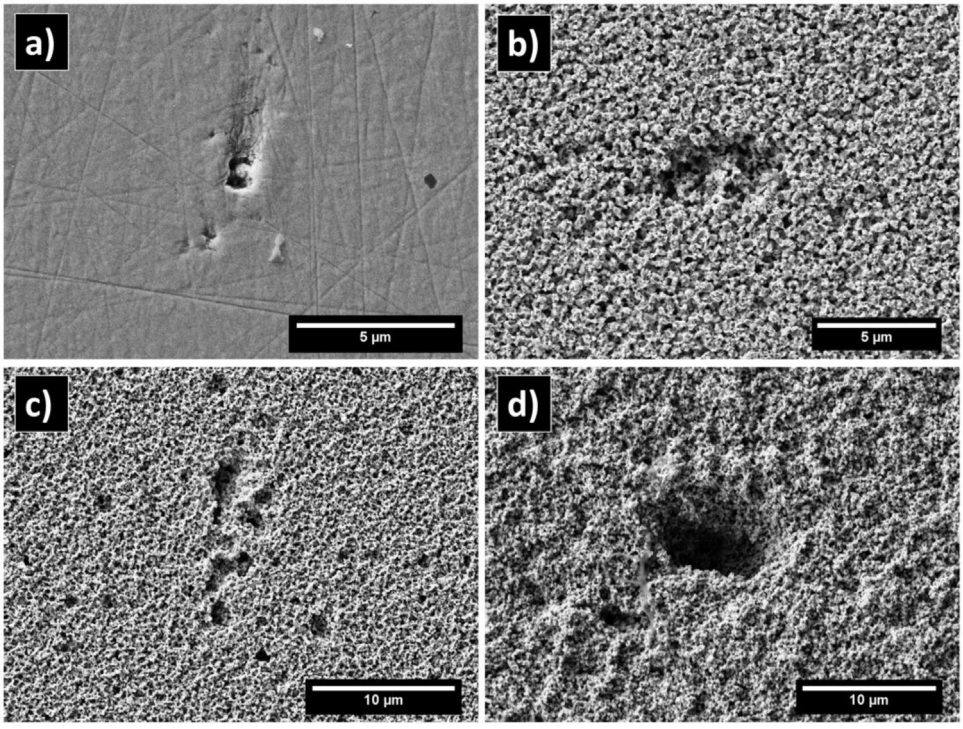

Fig. 3. SEM observations of a pore on the polished surface (a), and typical pits after etching for: 30 min (b), 1 h (c), 2 h (d).

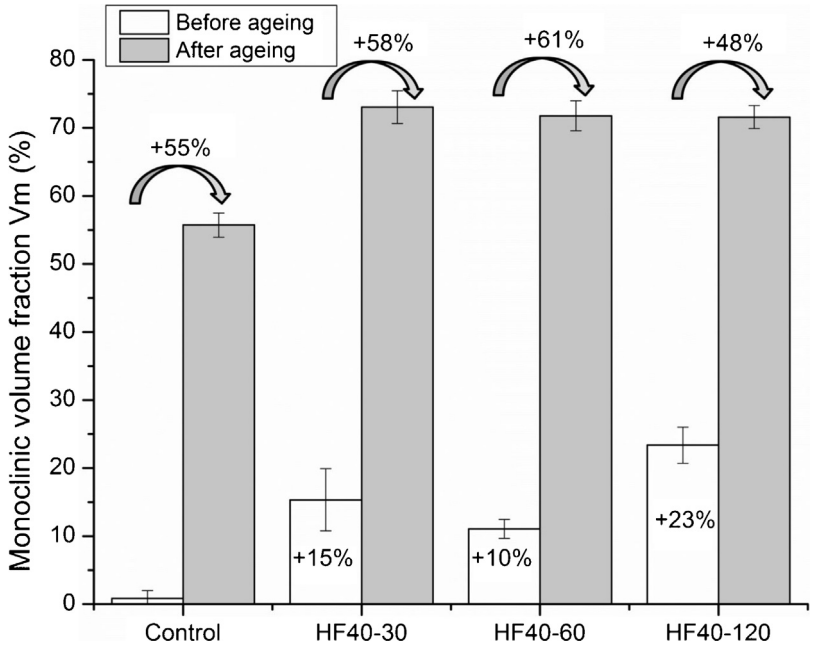

Fig. 4. Monoclinic volume fraction determined from XRD measurements for different etching times, before and after ageing. Values inside the columns indicate the absolute variation with respect to the Control group. Values above the columns indicate the absolute variation after ageing. Error bars represent the standard deviations.

phase transformation. As a result, the fracture toughness of the surface is lower since it is that of monoclinic zirconia.

- Localized damage such as pits (Figs. 1, 3, 6b) or deep porous zones (Fig. 6a). This kind of flaws could result from the interaction of HF with pre-existing defects, such as pre-existing pores on the polished surface (Fig. 3a) or low densified regions. However the formation of pits could also be favored by a phenomenon of autocatalysis, in which the reaction products would increase the etch rate locally, as it has been observed for instance in silicon [20]. This would be consistent with the exponential relationship between mass loss and HF concentration which was previously reported [12].
- Additionally, etching could bring to the surface flaws which were just below by dissolving the material that separated them from the outside. For instance, even though the case was isolated, it is worthwhile recalling that the fracture of a sample from the HF40-30 group was associated to a "tunnel-like" defect (Fig. 6e). This defect probably existed previously but was shown up by etching.

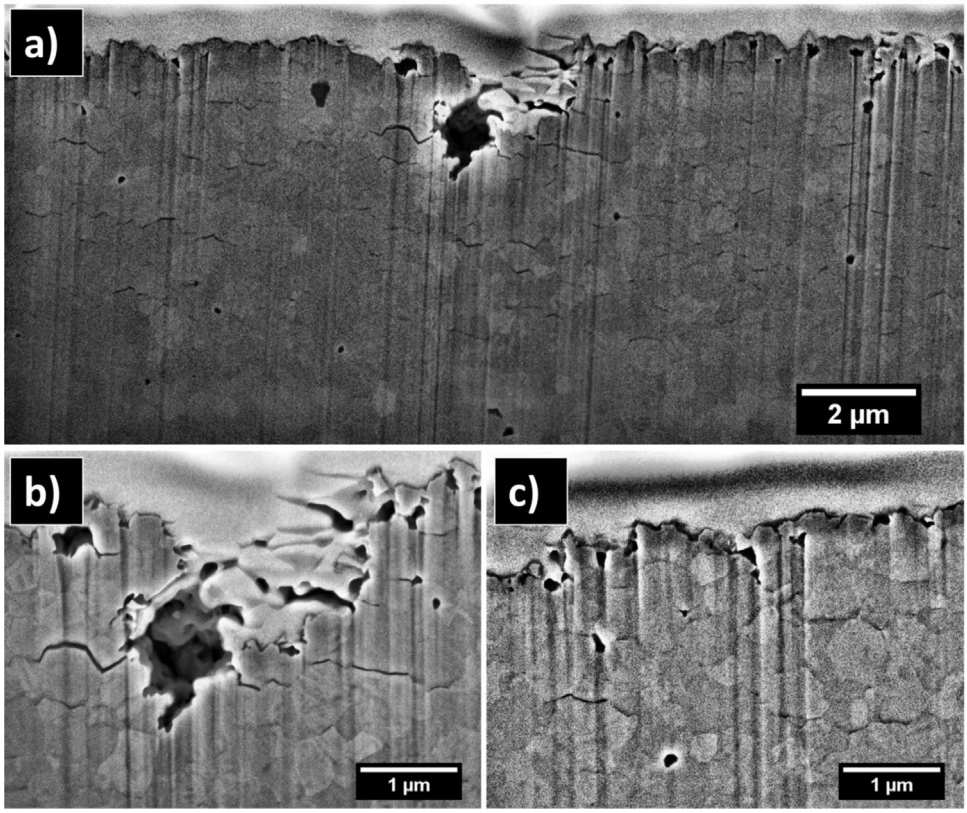

Fig. 5. FIB cross-section at the surface of 3Y-TZP after etching for two hours and subsequent ageing: (a) full cross-section, (b) etching pit at high magnification, (c) micro-cracked zone at high magnification.

As a consequence, etching induced a decrease in the average strength, without apparently affecting the strength variability. This decrease appeared to be much more important for the HF40-120 group (−29%) than for the HF40-30 and the HF40-60 groups, for which the decrease (−15% in both cases) and the Weibull strength distributions were similar. It seems thus recommendable not to use etching times superior to one hour, which moreover don't bring clear benefits in terms of roughness [12].

4.1.2. Modeling

To understand how the decrease of strength discussed above is related to the effect of etching on the population of superficial defects, some simple models are proposed below.

First of all, to estimate the size of the critical defect in each sample group, let us consider a hypothetical semi-circular surface crack of radius a. The stress intensity factor K_I for an applied stress σ_A is:

$$K_I = 1.26 \times \sigma_A \sqrt{a} \tag{7}$$

To determine *a*, the knowledge of the fracture toughness of the material is needed. Unfortunately, because of the small grain size and of the phase transformation phenomenon, its measurement is challenging for 3Y-TZP and the values reported in the literature differ substantially depending on the method used. Nevertheless measurement techniques involving a notch with a small tip radius appear more reliable, and the value retained here is $K_{IC} = 4.1\ MPa.m^{1/2}$ [21]. Considering $\sigma_{A1} = 1220$ MPa, $\sigma_{A2} = 1040$ MPa, $\sigma_{A3} = 1040$ MPa, $\sigma_{A4} = 870$ MPa which are respectively the mean strength of the Control, HF40-30, HF40-60 and HF-40-120 groups, the critical crack radii are $a_1 \approx 7\ \mu m$, $a_2 \approx 10\ \mu m$, $a_3 \approx 10\ \mu m$, $a_4 \approx 14\ \mu m$.

The etch-damaged layer, which could extend an existing surface flaw, can reach locally 3 μm (Fig. 2). Therefore, according to this model, it could explain the increase of the critical defect size and thus the drop in strength observed for the HF40-30 and HF40-60 groups, but not for the HF40-120 group.

On the other hand, big pits were observed on the surface of samples from the HF40-120 groups and fractographic analysis evidenced that they can play a role in failure (Fig. 1, Fig. 6b). As a simple model for these pits, let us consider a surface spherical pore of radius R under a constant biaxial tension σ_A. For a Poisson ratio $\nu = 0.3$, the maximum tensile stress σ at a radial distance r from the pore is given by [22]:

$$\sigma = \sigma_A \left[1 + 1.091 \left(1 + \frac{r}{R} \right)^{-5} + 9.091 \times 10^{-2} \left(1 + \frac{r}{R} \right)^{-3} \right] \tag{8}$$

Let us then consider then that this pore is associated to a circumferential crack (Fig. 9a and b). The stress intensity factor can be determined by the methodology proposed by Zimmermann and Rodel [22] which is briefly summarized here.The calculation of the stress intensity factor *K* is based on:

$$K = \int_0^c h(r, c)\, \sigma(r)\, dr \tag{9}$$

where c is the crack extension, σ(r) can be determined from Eq. (8) and the weight function *h* is given by:

$$h = \beta h_{edgecrack} + \left(1 - \beta\right) h_{circularcrack} \tag{10}$$

where $h_{edgecrack}$ and $h_{circularcrack}$ are the weight functions of an edge crack and a circular crack and β is an interpolation function.

β, $h_{edgecrack}$ and $h_{circularcrack}$ can be determined from the following formulas:

$$\beta = \frac{1}{\left(1 + 2\frac{c}{R}\right)^2} \tag{11}$$

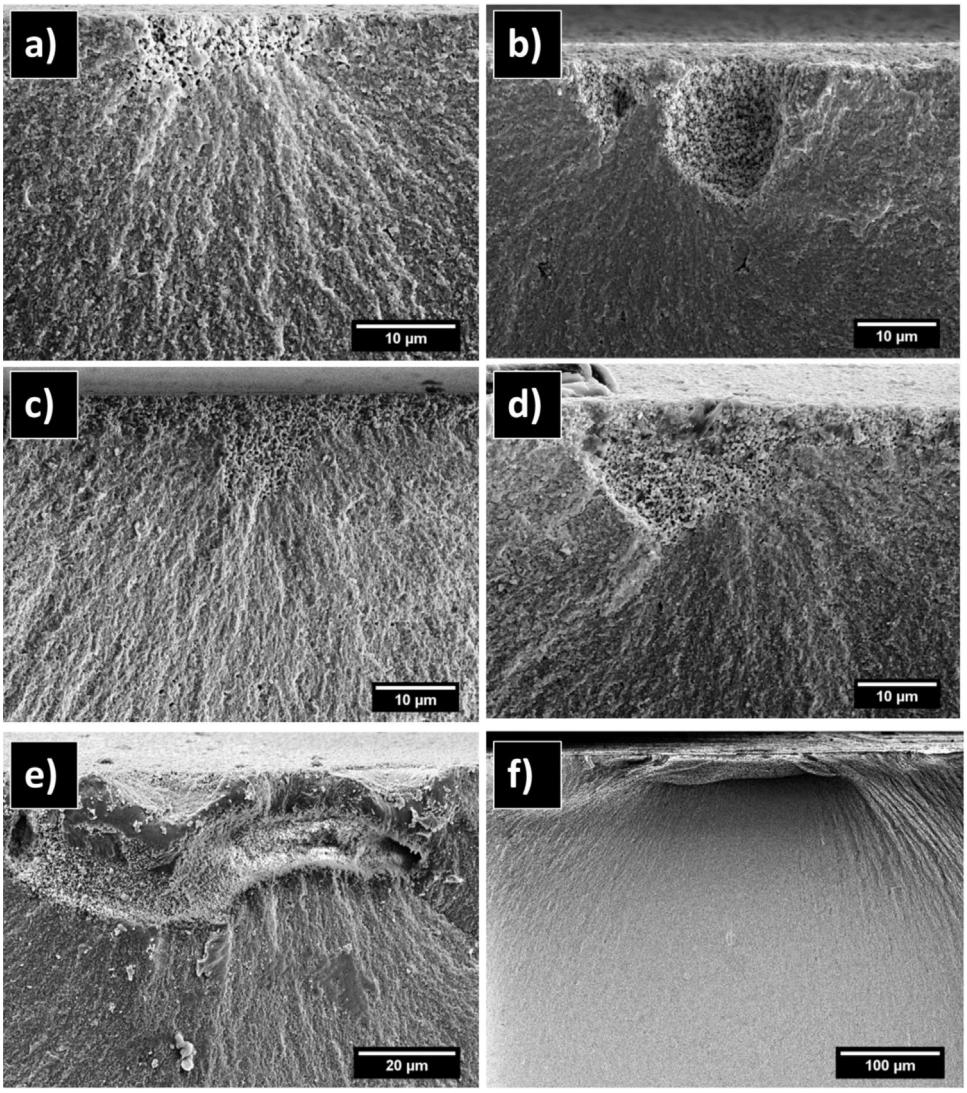

Fig. 6. Observation by SEM of the failure origin of samples from: (a) HF40-120 group (σ_{max} = 1042 MPa), (b) HF40-120 group (σ_{max} = 732 MPa), (c) Control-Aged group (σ_{max} = 970 MPa), (d) HF40-120-aged group (σ_{max} = 1146 MPa), (e) HF40-30 group (σ_{max} = 588 MPa), (f) HF40-60 group (σ_{max} = 359 MPa).

$$h_{edgecrack} = \frac{2}{(\pi c)^{1/2}} \frac{\left[1.3 - 0.71\left(\frac{r}{c}\right)^2 + 0.41\left(\frac{r}{c}\right)^3\right]}{\left[1 - \left(\frac{r}{c}\right)^2\right]^{1/2}} \quad (12)$$

$$h_{circularcrack} = \frac{2}{[\pi (c+R)]^{\frac{1}{2}}} \frac{(r+R)}{\left[(c+R)^2 - (r+R)^2\right]^{1/2}} \quad (13)$$

The software Maple (version 17, Maple Inc., Waterloo, Ontario, Canada) was used to calculate numerically the integral of Eq. (9) for different pore radii and a given applied tension as a function of crack extension. The curves obtained for σ_A = 1040 MPa and σ_A = 870 MPa, which are respectively the mean flexural strength from both the HF40-30 and HF40-60 group and from the HF40-120 group are shown in Fig. 9. From these curves it can be seen that:

For an applied tension σ_A = 1040 MPa, pits of radius $R \leq 5$ μm are unlikely to provoke failure because they should be associated to a crack of at least 7 μm, whereas pits of radius $R \geq 7.5$ μm could become critical for small crack extensions: $c \geq 2.6$ μm for R = 7.5 μm, $c \geq 1.2$ μm for R = 15 μm, $c \geq 1$ μm for R = 30 μm.

For an applied tension σ_A = 870 MPa, pits of radius $R \leq 10$ μm are unlikely to provoke failure because they should be associated to a crack of at least 4.5 μm, whereas pits of radius $R \geq 15$ μm could become critical for small crack extensions: $c \geq 2.2$ μm for R = 15 μm, $c \geq 1.6$ μm for R = 30 μm.

Considering these results, the presence of big pits (Fig. 1) associated to the cracks of the etch-damaged layer may explain the important decrease in strength of the HF40-120 group. The pits observed in the HF40-30 and in the HF40-60 specimens were smaller, which makes less probable their potential role in failure.

Finally, fractographic analysis also evidenced that deep porous zones could initiate fracture (Fig. 6). The complicated geometry of this kind of defects makes modeling difficult. However, on the same manner as pits, they could be considered as stress concentrators associated to a crack.

To summarize, the models presented above tend to show that:

- For the HF40-30 and HF40-60 groups in which the pits are smaller than in the HF40-120 group, the model of an existing crack whose dimension is increased by the etch-damaged layer gives a satisfying explanation of the drop in strength induced by etching. The fact that the thickness of the etch-damaged layer was not related to etching time supports this hypothesis, because it explains the similarity between the HF40-30 and HF40-60 strength distributions.

- For the HF40-120 group, the presence of big pits associated to the etch-damaged layer and of deep porous zones explains the more important drop in strength.

4.2. Effects of ageing

4.2.1. Qualitative interpretation

There was no substantial difference in the amount of monoclinic phase between the different groups of etched-aged specimens. Another observation worthwhile recalling is that the increase of monoclinic content associated to ageing in the etched samples was close to the increase observed in the Control-Aged group. Furthermore it was observed on FIB cross-sections that the thickness of the micro-cracked layer induced by phase transformation during ageing was not more important in a sample etched for two hours than in the control one. Accordingly the influence of previous etching on ageing appears to be limited.

Moreover, there was surprisingly no significant difference in the strength distributions among all the specimen groups after ageing (see Figs. 7 and 8). The average strength of all etched groups remained constant or increased after ageing, whereas that of the samples from the Control-Aged group decreased. This opposite behavior must be related to a distinct effect of ageing on control and on etched specimens, or to two competing mechanisms, one of them tending to neutralize etching defects.

The drop in strength induced by ageing of polished zirconia has already been reported in numerous studies [23–27]. It has been suggested to be caused by the apparition of micro-cracks due to the phase transformation and by the depletion of transformable tetragonal phase on the surface. The fractographic observations presented in this work bring an additional element: they show that failure can be initiated in regions in which the micro-cracked layer induced by ageing is locally thicker (Fig. 6c).

On the other hand, the increase in strength subsequent to ageing etched specimens has never been reported. At first, two hypotheses appear to be reasonable to explain this phenomenon. One is that ageing of etched specimens could induce a change in the critical defects responsible for fracture, and the other is that ageing may induce a change in the stress distribution at the surface of etched specimens. However, this second hypothesis appears to be unlikely, since there is no apparent reason for which the presence of a residual compressive stress on the surface would induce an increase in strength for etched specimens but not for control ones.

On the contrary, the effect of ageing on the critical defects could explain the differences observed, as it will be demonstrated in the next section. Indeed, a critical flaw induced by etching is necessarily connected to the surface and is therefore necessarily under direct exposure of water vapor. The tip of the crack could thus be transformed, reducing its sharpness. A similar phenomenon of crack tip blunting was suggested to exist by Marro et al. [28], who found a large increase of strength after ageing pre-indented zirconia bars.

4.2.2. Modeling

4.2.2.1. Strength decrease. To explain the drop in strength induced by ageing in the Control-Aged group, let us consider first the case of the sample shown in Fig. 6c, for which the depth of the micro-cracked layer induced by ageing reached locally $d \approx 13\ \mu m$ and broke at $\sigma_A = 970$ MPa. The radius of an equivalent semi-circular crack which would provoke a failure at this stress is $a \approx 11\ \mu m$, therefore the dimensions of this flaw are close to that of the theoretical critical defect.

On the other hand, let us consider the case that the degraded layer thickness is homogenous ($d \approx 5\ \mu m$). It has been suggested that the minimum value of d necessary for a crack to continue propagating through the tetragonal bulk can be estimated from [27]:

$$d_{min} \approx 0.49 \times a_c \quad (14)$$

where a_c is the critical defect size in the material before ageing. As shown previously, in the case of the Control group $a_c \approx 7\ \mu m$, therefore $d \gg d_{min}$ ($d_{min} \approx 3.5\ \mu m$).

These two observations tend to demonstrate that the strength of the Control-Aged samples is governed by the aged damaged layer, which is responsible for the drop in strength, and not by the pre-existing flaws. The mechanism of crack tip blunting discussed below has thus no effect in this case.

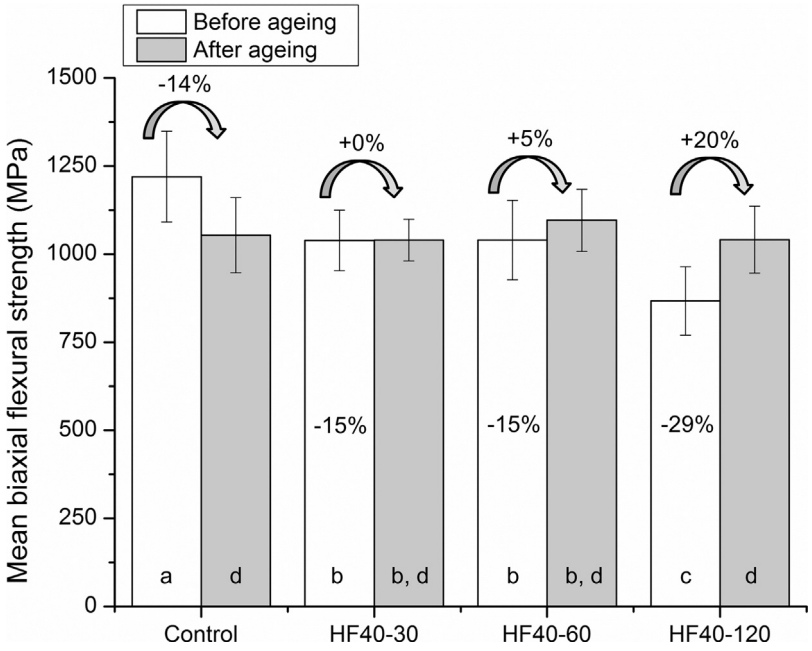

Fig. 7. Mean biaxial flexural strength for different etching times, before and after ageing. Values inside the columns indicate the relative variation with respect to the Control group. Values above the columns indicate the relative variation after ageing. Letters indicate the groups which are statistically similars. Error bars represent the standard deviations.

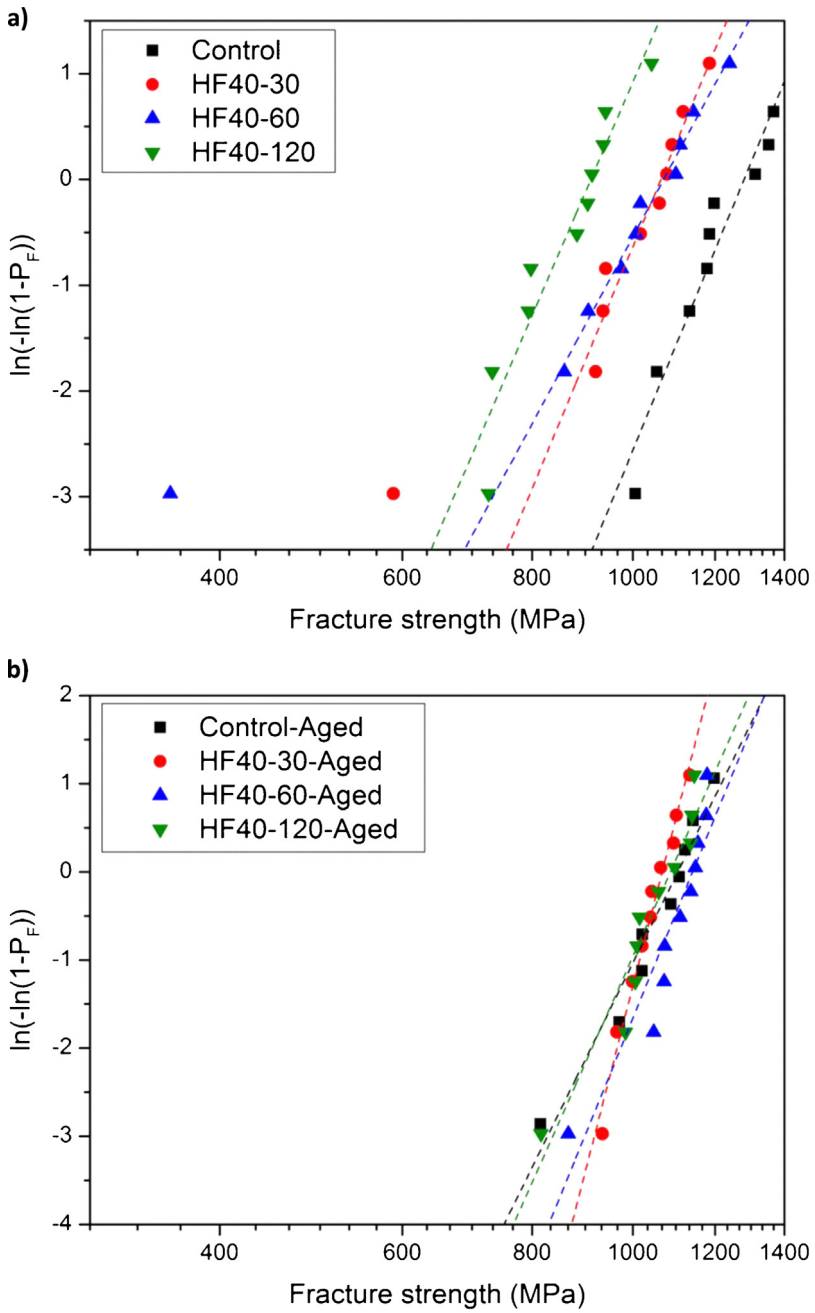

Fig. 8. Weibull analysis of the fracture strength of 3Y-TZP before (a) and after ageing (b) for different etching times.

4.2.2.2. Strength increase. To explain how pre-existing etching defects could be neutralized and how it could lead to strength increase for the HF40-120 samples, let us consider the hypothesis that ageing could induce some crack tip blunting. Modeling the case of a cracked pit is not straightforward. Therefore, to get an order of magnitude of the blunting necessary to explain the strength increase observed, let us consider the relationship between the stress intensity factors at fracture of a blunt and a sharp crack [29]:

$$\frac{K_{IC,blunt}}{K_{IC}} = \left(1 + \frac{\rho_0}{2r_0}\right)^{1/2} \quad (15)$$

where $K_{IC,blunt}$ is the stress intensity factor of the blunt crack at fracture, K_{IC} is the fracture toughness, ρ_0 is the root radius of the blunt crack and $r_0 = w \sim 2\,w$ with w an effective grain width at the crack tip. Assuming that $w \approx 0.3\,\mu m$ (grain size of the 3Y-TZP used in this work measured by the intercept method) and that the relationship between the strength of the HF40-120-aged (blunt crack) and HF40-120 (sharp crack) specimens corresponds to the relationship of Eq. (15), we obtain $\rho_0 = 0.3 \sim 0.6\,\mu m$, which shows that a blunting of the crack tip to a radius of the order of magnitude of the grain size could explain the strength increase.

4.2.2.3. Summary. Ageing seems to lead to two competing mechanisms:

- On the one hand, etching defects, which are directly accessible to water vapor, are neutralized: a moderate blunting of the crack tip is sufficient to explain the strength increase observed for the HF40-120 samples.
- On the other hand, the apparition of the degraded layer explains the drop in strength for the control samples. Considering that etching defects are fully inactivated, the strength will be also gov-

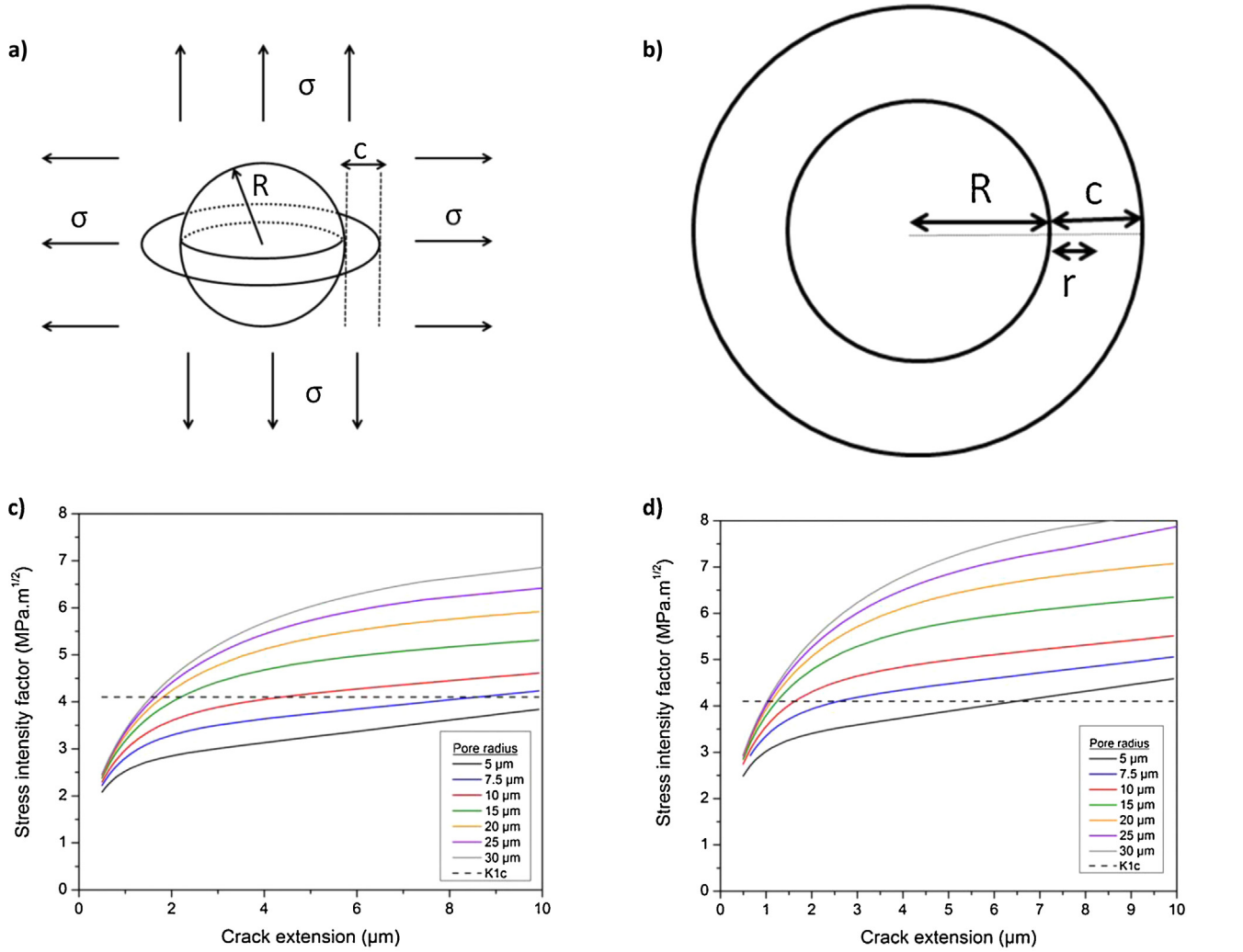

Fig. 9. Top: (a) Schematic three-dimensional representation of a spherical pore with a circumferential crack under biaxial tension, (b) Schematic two-dimensional representation of an intersection through the crack plane. Bottom: theoretical stress intensity factor as function of crack extension for different pore radii and an applied biaxial stress of 870 MPa (c) and 1040 MPa (d).

erned by the degraded layer in the etched-aged groups, which explains the similarity between all the strength distributions after ageing.

5. Conclusion

Etching of 3Y-TZP with HF 40% for times up to two hours has been studied in terms of surface integrity, flexural strength and resistance to hydrothermal degradation. It is concluded that etching induces an increase in monoclinic phase content and a decrease in the biaxial flexural strength of polished specimens. In both cases, these changes do not exceed 15% for etching times below one hour. Besides, HF etched zirconia apparently does not exhibit an increased sensitivity to LTD and the biaxial strength of etched specimens can even increase with ageing, which can be explained in terms of crack tip blunting by phase transformation. Accordingly, within the limits of this study, dental zirconia etched with HF 40% should be reliable for long-term implantations provided that the etching duration does not exceed one hour.

Acknowledgements

The authors would like to acknowledge the European Commission funding under the 7th Framework Programme (Marie Curie Initial Training Networks; grant number: 289958, Bioceramics for bone repair), the support of the Ministry of Economy and Competitiveness (MINECO) of Spain (project ref. MAT2011-23913) and the Government of Catalonia for the grant 2014SGR0137. The authors would also like to thank Dr. Trifon Trifonov for his help during FIB/SEM sessions.

References

[1] J. Chevalier, What future for zirconia as a biomaterial? Biomaterials 27 (2006) 535–543, http://dx.doi.org/10.1016/j.biomaterials.2005.07.034.
[2] R. Garvie, R. Hannink, R. Pascoe, Ceramic steel? Nature 258 (1975) 703–704.
[3] S. Lawson, Environmental degradation of zirconia ceramics, J. Eur. Ceram. Soc. 15 (1995) 485–502, http://dx.doi.org/10.1016/0955-2219(95)35-S.
[4] I. Denry, J.R. Kelly, State of the art of zirconia for dental applications, Dent. Mater. 24 (2008) 299–307, http://dx.doi.org/10.1016/j.dental.2007.05.007.
[5] M. Andreiotelli, R.-J. Kohal, Fracture strength of zirconia implants after artificial aging, Clin. Implant Dent. Relat. Res. 11 (2009) 158–166, http://dx.doi.org/10.1111/j.1708-8208.2008.00105.x.
[6] R.B. Osman, M.V. Swain, M. Atieh, S. Ma, W. Duncan, Ceramic implants (Y-TZP): are they a viable alternative to titanium implants for the support of overdentures? A randomized clinical trial, Clin. Oral Implants Res. 25 (2014) 1366–1377, http://dx.doi.org/10.1111/clr.12272.
[7] R.-J. Kohal, M. Knauf, B. Larsson, H. Sahlin, F. Butz, One-piece zirconia oral implants: one-year results from a prospective cohort study. 1. Single tooth replacement, J. Clin. Periodontol. 39 (2012) 590–597, http://dx.doi.org/10.1111/j.1600-051X.2012.01876.x.

[8] A. Wennerberg, T. Albrektsson, On implant surfaces: a review of current knowledge and opinions, Int. J. Oral Maxillofac Implants 25 (2009) 63–74.
[9] M. Gahlert, S. Röhling, M. Wieland, S. Eichhorn, H. Küchenhoff, H. Kniha, A comparison study of the osseointegration of zirconia and titanium dental implants. A biomechanical evaluation in the maxilla of pigs, Clin. Implant Dent. Relat. Res. 12 (2010) 297–305, http://dx.doi.org/10.1111/j.1708-8208.2009.00168.x.
[10] H. Ito, H. Sasaki, K. Saito, S. Honma, Y. Yajima, M. Yoshinari, Response of osteoblast-like cells to zirconia with different surface topography, Dent. Mater. J 32 (2013) 122–129, http://dx.doi.org/10.4012/dmj.2012-208.
[11] C. Bergemann, K. Duske, J.B. Nebe, A. Schöne, U. Bulnheim, H. Seitz, et al., Microstructured zirconia surfaces modulate osteogenic marker genes in human primary osteoblasts, J. Mater. Sci. Mater. Med. (2015), http://dx.doi.org/10.1007/s10856-014-5350-x.
[12] Q. Flamant, F. García Marro, J.J. Roa Rovira, M. Anglada, Hydrofluoric acid etching of dental zirconia. Part 1: etching mechanism and surface characterization, J. Eur. Ceram. Soc. 36 (2016) 121–134.
[13] J. Oliva, X. Oliva, J.D. Oliva, Five-year success rate of 831 consecutively placed Zirconia dental implants in humans: a comparison of three different rough surfaces, Int. J. Oral Maxillofac Implants 25 (2010) 336–344.
[14] C. Sanon, J. Chevalier, T. Douillard, M. Cattani-Lorente, S.S. Scherrer, L. Gremillard, A new testing protocol for zirconia dental implants, Dent. Mater. 31 (2015) 15–25, http://dx.doi.org/10.1016/j.dental.2014.09.002.
[15] J. Chevalier, B. Cales, J.M. Drouin, Low-temperature aging of Y-TZP ceramics, J. Am. Ceram. Soc. 82 (1999) 2150–2154.
[16] H. Toraya, M. Yoshimura, S. Somiya, Calibration curve for quantitative analysis of the monoclinic–tetragonal ZrO_2 system by X-ray diffraction, J. Am. Ceram. Soc. 67 (1984) C-119–C-121.
[17] A. Börger, P. Supancic, R. Danzer, The ball on three balls test for strength testing of brittle discs: stress distribution in the disc, J. Eur. Ceram. Soc. 22 (2002) 1425–1436, http://dx.doi.org/10.1016/s0955-2219(01)458-7.
[18] K. Shah, J. Holloway, D. a, I.L. enry, Effect of coloring with various metal oxides on the microstructure, color, and flexural strength of 3Y-TZP, J. Biomed. Mate.r Res. B Appl. Biomater. 87 (2008) 329–337, http://dx.doi.org/10.1002/jbm.b.31107.
[19] D. Munz, T. Fett, Ceramics Mechanical Properties, Failure Behaviour, Materials Selection, 36, Springer Science & Business Media, 1999.
[20] I.A. Shah, van, W. der, B.M.A. olf, E. van, W.J.P. nckevort, E. Vlieg, Wet Chemical Etching of Silicon {111}: autocatalysis in pit formation, J. Electrochem. Soc. 155 (2008) J79, http://dx.doi.org/10.1149/1.2830841.
[21] M. Turon-vinas, M. Anglada, Fracture toughness of zirconia from a shallow notch produced by ultra-short pulsed laser ablation, J. Eur. Ceram. Soc. 34 (2014) 3865–3870, http://dx.doi.org/10.1016/j.jeurceramsoc.2014.05.009.
[22] A. Zimmermann, J. Rodel, Generalized orowan-petch plot for brittle fracture, J. Am. Ceram. Soc. 81 (1998) 2527–2532, http://dx.doi.org/10.1111/j.1151-2916.1998.tb02657.x.
[23] J.L. Drummond, In vitro aging of yttria-stabilized zirconia, J Am Ceram Soc 72 (1989) 675–676, http://dx.doi.org/10.1111/j.1151-2916.1989.tb06194.x.
[24] B.I. Ardlin, Transformation-toughened zirconia for dental inlays, crowns and bridges: chemical stability and effect of low-temperature aging on flexural strength and surface structure, Dent. Mater. 18 (2002) 590–595, http://dx.doi.org/10.1016/s0109-5641(01)95-1.
[25] H.-T. Kim, J. Han, J. Yang, J. Lee, S. Kim, The effect of low temperature aging on the mechanical property & phase stability of Y-TZP ceramics, J. Adv. Prosthodont. 1 (2009) 113–117, http://dx.doi.org/10.4047/jap.2009.1.3.113.
[26] P. Kohorst, L. Borchers, J. Strempel, M. Stiesch, T. Hassel, F.-W. Bach, et al, Low-temperature degradation of different zirconia ceramics for dental applications, Acta Biomater. 8 (2012) 1213–1220, http://dx.doi.org/10.1016/j.actbio.2011.11.016.
[27] F.G. Marro, Mestra a, M. Anglada, Weibull strength statistics of hydrothermally aged 3 mol% yttria-stabilised tetragonal zirconia, Ceram. Int. 40 (2014) 12777–12782, http://dx.doi.org/10.1016/j.ceramint.2014.04.131.
[28] F.G. Marro, M. Anglada, Strengthening of Vickers indented 3Y-TZP by hydrothermal ageing, J. Eur. Ceram. Soc. 32 (2012) 317–324, http://dx.doi.org/10.1016/j.jeurceramsoc.2011.08.019.
[29] Z.-Y. Deng, J. She, Y. Inagaki, J.-F. Yang, T. Ohji, Y. Tanaka, Reinforcement by crack-tip blunting in porous ceramics, J. Eur. Ceram. Soc. 24 (2004) 2055–2059, http://dx.doi.org/10.1016/s0955-2219(03)365-0.

Journal of the European Ceramic Society xxx (2016) xxx–xxx

Contents lists available at www.sciencedirect.com

Journal of the European Ceramic Society

journal homepage: www.elsevier.com/locate/jeurceramsoc

Corrigendum

Corrigendum to "Hydrofluoric acid etching of dental zirconia. Part 2: Effect on flexural strength and ageing behavior" [J. Eur. Ceram. Soc. 36 (1) (January 2016) 135–145]

Quentin Flamant[a,b,*], Marc Anglada[a,b,*]

[a] Department of Materials Science and Metallurgical Engineering, Universitat Politècnica de Catalunya, Av. Diagonal 647, 08028 Barcelona, Spain
[b] Center for Research in Nano-Engineering, CRNE, Universitat Politècnica de Catalunya, C. Pascual i Vila, 15, 08028 Barcelona, Spain

The authors regret that formula (2) on page 136 was written incorrectly:

$$V_m = 1.311\frac{I_m(\bar{1}11)+I_m(111)}{1.311[I_m(\bar{1}11)+I_m(111)+I_t(101)]}$$

Formula (2) should read as follows:

$$V_m = 1.311\frac{I_m(\bar{1}11)+I_m(111)}{I_t(101)+1.311[I_m(\bar{1}11)+I_m(111)]}$$

The authors would like to apologise for any inconvenience caused.

DOI of original article: http://dx.doi.org/10.1016/j.jeurceramsoc.2015.09.022.
* Corresponding authors.
E-mail addresses: quentin.flamant@upc.edu (Q. Flamant), marc.j.anglada@upc.edu (M. Anglada).

http://dx.doi.org/10.1016/j.jeurceramsoc.2016.05.040

Please cite this article in press as: Q. Flamant, M. Anglada, Corrigendum to "Hydrofluoric acid etching of dental zirconia. Part 2: Effect on flexural strength and ageing behavior" [J. Eur. Ceram. Soc. 36 (1) (January 2016) 135–145], *J Eur Ceram Soc* (2016), http://dx.doi.org/10.1016/j.jeurceramsoc.2016.05.040

Article III.

Roughness gradients on zirconia for rapid screening of cell-surface interactions: fabrication, characterization and application.

Society For Biomaterials

Roughness gradients on zirconia for rapid screening of cell-surface interactions: Fabrication, characterization and application

Quentin Flamant,[1,2] Ana-Maria Stanciuc,[3] Hugo Pavailler,[1] Christoph Martin Sprecher,[3] Mauro Alini,[3] Marianna Peroglio,[3] Marc Anglada[1,2]

[1]Department of Materials Science and Metallurgical Engineering, Universitat Politècnica De Catalunya, Av. Diagonal 647, Barcelona 08028, Spain

[2]Center for Research in Nano-Engineering, CRNE, Universitat Politècnica De Catalunya, C. Pascual I Vila, 15, Barcelona 08028, Spain

[3]AO Research Institute Davos, Clavadelerstrasse 8, 7270, Davos Platz, Switzerland

Received 23 March 2016; revised 21 May 2016; accepted 24 May 2016
Published online 00 Month 2016 in Wiley Online Library (wileyonlinelibrary.com). DOI: 10.1002/jbm.a.35791

Abstract: Roughness is one of the key parameters for successful osseointegration of dental implants. The understanding of how roughness affects cell response is thus crucial to improve implant performance. Surface gradients, which allow rapid and systematic investigations of cell-surface interactions, have the potential to facilitate this task. In this study, a novel method aiming to produce roughness gradients at the surface of zirconia using hydrofluoric acid etching was implemented. The topography was exhaustively characterized at the microscale and nanoscale by white light interferometry and atomic force microscopy, including the analysis of amplitude, spatial, hybrid, functional, and fractal parameters. A rapid screening of the influence of roughness on human mesenchymal stem cell morphology was conducted and potential correlations between roughness parameters and cell morphology were investigated. The roughness gradient induced significant changes in cell area ($p < 0.001$), aspect ratio ($p = 0.01$), and solidity ($p = 0.026$). Nanoroughness parameters were linearly correlated to cell solidity ($p < 0.005$), while microroughness parameters appeared nonlinearly correlated to cell area, highlighting the importance of multiscale optimization of implant topography to induce the desired cell response. The gradient method proposed here drastically reduces the efforts and resources necessary to study cell-surface interactions and provides results directly transferable to industry. © 2016 Wiley Periodicals, Inc. J Biomed Mater Res Part A: 00A:000–000, 2016.

Key Words: Y-TZP ceramics, surface modification, hydrofluoric acid etching, topography, human mesenchymal stem cells

How to cite this article: Flamant Q, Stanciuc A-M, Pavailler H, Martin Sprecher C, Alini M, Peroglio M, Anglada M. 2016. Roughness gradients on zirconia for rapid screening of cell-surface interactions: Fabrication, characterization and application. J Biomed Mater Res Part A 2016:00A:000–000.

INTRODUCTION

Yttria-stabilized tetragonal zirconia polycrystals (Y-TZP, short: zirconia) are biocompatible and exhibit the best combination of strength and toughness of single-phase oxide ceramics. They were introduced as biomaterials at the end of the 1980s to overcome the limitations of alumina in the field of orthopedics.[1] While monolithic zirconia has been almost abandoned for orthopedic applications, in the last decade its use in restorative dentistry has been growing fast.[2] In particular, its good esthetics, high resistance to corrosion, and the absence of allergic reaction make zirconia a good candidate to replace titanium for the fabrication of dental implants.[3] However, some issues still need to be solved before generalizing the clinical use of zirconia implants. Indeed, several authors reported a higher marginal bone loss and fracture rate as compared to titanium, which shows the need for further development.[3–5] On the one hand, zirconia can suffer from the so-called low temperature degradation phenomenon (also known as ageing),[6] and, as other ceramics, it is sensitive to surface defects and subcritical crack growth. The impact of these phenomena, which account for the higher fracture rate, could be minimized by optimizing the implant design and the fabrication process.[7] On the other hand, the higher bone loss observed in some cases could be related to the higher elastic modulus mismatch between zirconia and bone, which induces higher

Additional Supporting Information may be found in the online version of this article.
Correspondence to: Q. Flamant; e-mail: quentin.flamant@upc.edu or M. Anglada; e-mail: marc.j.anglada@upc.edu
Contract grant sponsor: European Commission (7th Framework Programme [Marie Curie Initial Training Networks, Bioceramics for bone repair]); contract grant number: 289958
Contract grant sponsor: Ministry of Economy and Competitiveness (MINECO) of Spain; contract grant number: MAT2014-60720-R
Contract grant sponsor: Government of Catalonia; contract grant number: 2014SGR0137

stress concentration, and to a lack of optimization of the implant surface, which leads to a poor osseointegration.[5]

Indeed, a successful osseointegration depends on numerous surface properties such as topography and chemistry.[8] In particular, it has been shown that moderately rough surfaces exhibit a stronger bone response than smoother and rougher ones, suggesting the existence of an optimal roughness range. Nevertheless, what is the optimal surface topography for a dental implant remains unclear.[9,10]

One of the reasons for this lack of knowledge is that, with a classical approach, the investigation of the influence of surface roughness on cell response requires experiments on large series of homogenous and individual specimens for each condition tested. Testing a high number of surface types is thus lengthy and costly. To overcome this problem, surface gradients appear as a very appealing tool: they allow the high-throughput and systematic investigation of cell response to the variation of surface properties, one single sample containing the whole range of values for the studied parameters.[11] Besides, homogenous experimental conditions are ensured, which reduces drastically the number of specimens needed from a statistical point of view.

In addition, while there is an agreement that implant surface topography is best described using a multiple-scale, three-dimensional (3D) analysis,[12–14] the correlation between both microtopographical and nanotopographical characteristics of surfaces and stem cell morphology has not been fully explored yet. Since stem cell size and shape is indicative of the cell function,[15] such analyses hold the potential to clarify the role of specific roughness parameters on cell fate.

The gradient approach has been successfully implemented by some authors to investigate the influence of roughness on osteoblast response, osteoclast resorption, and stem cell differentiation on several materials (polycaprolactone, epoxy resin, titanium, silicon, and hydroxyapatite among others).[16–25] However, to the best of the knowledge of the authors, it has never been applied to zirconia. Besides, the aforementioned studies often limit the roughness analysis to the average roughness parameter (R_a), which is not sufficient to fully characterize surface topography.[14]

Among the numerous existing methods to fabricate morphology gradients (for a review see Ref. 26), few are easily transposable to zirconia. One possible approach would be to use the route proposed by Kunzler et al. which is material independent[27]: an aluminum sheet is sandblasted and progressively eroded by chemical polishing, the surface is then replicated in epoxy and sputter-coated with the desired material. Nevertheless, this process presents some inconveniency: it is not directly transposable to the fabrication of a real component such as an implant and the coating process might affect the surface properties and consequently the cell response. Another possibility would be to use a dip coating process to bind particles to the surface, as proposed for instance by Huwiler et al.[28] However, this approach is limited to the fabrication of nanomorphology gradients.

A biomechanical study[29] and a histological study[30] in pigs suggested that hydrofluoric acid (HF) etching of zirconia implants could enhance bone apposition and that such implants presented performances comparable to those of commercial titanium implants. Based on a previous work which showed that HF etching allows controlling zirconia roughness,[31] the present article proposes therefore a novel method to fabricate zirconia samples with a surface roughness gradient, associated to an advanced characterization of the topography involving a multiscale roughness analysis and a fractal analysis. To get an insight of the influence of topography on the early response of human bone marrow derived mesenchymal stem cells (hMSCs) and to validate the method, hMSCs were cultured on the gradient samples, and potential correlations between topographical parameters and cell morphology were systematically investigated.

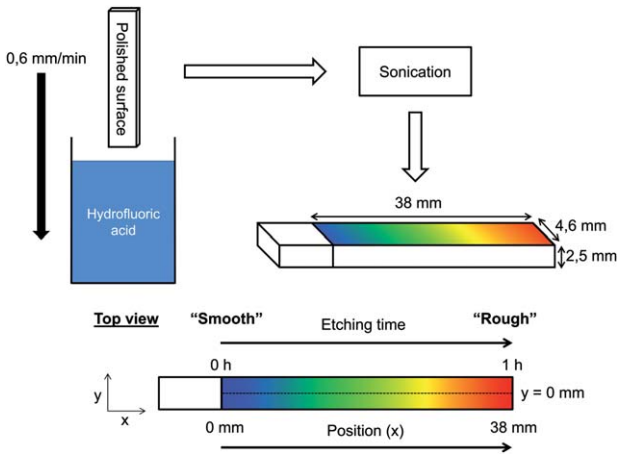

FIGURE 1. Experimental procedure for producing a roughness gradient at the surface of zirconia specimens.

MATERIALS AND METHODS

Sample fabrication

Fabrication of zirconia bars. Commercial 3Y-TZP (3 mol% Y-TZP) powder (TZ-3YSB-E Tosoh Co., Japan) was cold uniaxially pressed at 100 MPa and then sintered in an alumina tube furnace at 1450°C for 2 h (3°C/min heating and cooling rates), obtaining prismatic bars of 2.5 mm × 4.6 mm × 45 mm which were ground and polished down to a 3 μm diamond suspension. The specimens were then successively cleaned for 5 min with acetone, ethanol, and deionized water in an ultrasonic bath to remove contaminants.

Surface modification for obtaining roughness gradients. A previous work showed that HF etching allows producing roughness on zirconia and that it is possible to control the topography by monitoring etching time.[31] Based on these results, in the present study roughness gradients were obtained by subjecting specimens to etching into concentrated HF (40% QP Panreac, Spain) with a continuous variation of etching time along the axis of the bar. As shown in Figure 1, the samples were immersed into a volume of 40 mL of HF contained in a polyethylene flask at a speed of 0.6 mm/min by using an automated device (ND-R Rotary Dip Coater, Nadetech Innovations, Spain). The total duration of the process was set to 1 h, which leads to a substantial

TABLE I. Description of the 3D Roughness Parameters Used in this Study[31–33]

Symbol	Category	Parameter	Description
S_a	Amplitude	Average roughness	Average of height values.
S_q	Amplitude	RMS roughness	Standard deviation of height values.
S_{sk}	Amplitude	Skewness	Degree of symmetry of the surface heights about the mean plane. The sign of S_{sk} indicates the preponderance of peaks ($S_{sk}>0$) or valley structures ($S_{sk}<0$).
S_{ku}	Amplitude	Kurtosis	Sharpness or flatness of the height distribution curve. $S_{ku}=3$: Gaussian height distributions $S_{ku}<3$: "broad" height distributions $S_{ku}>3$: "narrow" height distributions
S_{al}	Spatial	Fastest decay length	The shortest spatial distance in which the autocorrelation function decreases to 0.2 of its value.
S_{ds}	Spatial	Density of summits	Number of summits per unit area.
S_{dr}	Hybrid	Developed interfacial area ratio	Percentage of additional surface area contributed by the texture as compared to an ideal plane the size of the measurement region.
S_{dq}	Hybrid	RMS gradient	RMS value of the surface slope within the sampling area.
S_{sc}	Hybrid	Mean summit curvature	Average of the principal curvature of the summits.
S_m	Functional	Surface material volume	Amount of material contained in the surface peaks from 0% to 10% of the bearing area ratio.
S_c	Functional	Surface core void volume	Volume that the surface would support from 10% to 80% of the bearing ratio.
S_v	Functional	Surface void volume	Volume that the surface would support from 80% to 100% of the bearing ratio.

roughness for the part of the sample immersed for the longest time without damaging too severely the material.[31,32] After etching, the specimens were rinsed with deionized water in order to stop the reaction. Finally, they were cleaned in an ultrasonic bath (2 × 10 min with fresh deionized water) to remove the precipitates formed during the process.

Surface characterization

Measurements. All surface measurements were performed on the *x*-*y* surface (see Fig. 1). The evolution of the surface morphology along the axis of the bar was assessed at evenly spaced positions in the *x* direction ($y=0$ mm) by scanning electron microscopy (SEM, Neon 40, Carl Zeiss AG, Germany). Atomic force microscopy (AFM Veeco Dimension 3100) in tapping mode, and white light interferometry (WLI, Veeco Wyko 9300NT) were used in order to characterize the topography at different scales. AFM measurements were performed at five *x*-positions with $y=0$ mm on three specimens (one measurement per position, area: 50 μm × 50 μm, resolution: 512 × 512 pixels). WLI measurements were performed at 13 evenly spaced *x*-positions on three specimens (measurements at $y=-1$ mm, $y=0$ mm, and $y=1$ mm for each *x* position, area: 150 μm × 150 μm obtained by stitching of four images acquired at magnification 50×, resolution: 758 × 758 pixels). Additionally, for the $t=0$ min data point, three AFM measurements and 10 WLI measurements were performed on polished samples (with no gradient). Finally, to get a better understanding of the etching process and to identify possible correlations between the formation of precipitates on the surface and the evolution of the topography, SEM observations were performed on a sample which was not subjected to sonication after etching.

Roughness analysis. The roughness analysis of the data from AFM and WLI was carried out using Veeco's Vision® software. Tilt was corrected and a robust short wavelength pass Gaussian filter was applied to the data in order to separate waviness from roughness. The cut-off wavelength of the filter was set to 10 μm for WLI and 1 μm for AFM. The roughness parameters described in Table I were then determined. Considering the cut-off wavelengths and the lateral resolutions (micrometric for WLI, nanometric for AFM) associated to each device, the roughness measurements obtained from AFM data analysis will be referred to as "nanoroughness" whereas the measurements obtained from the WLI data will be referred to as "microroughness."

Fractal analysis. A scale sensitive fractal analysis of the AFM and WLI data was performed using the software Sfrax (www.surfract.com). Area-scale analysis is based on the principle from fractal geometry that the area of a rough surface is not unique, but depends on the scale of measurement.[33,34] The software uses an iterative tiling algorithm in which the topography of the surface is modeled using triangular tiles to calculate the relative area as a function of the scale of observation. The area of a tile represents the scale, and the relative area is determined from the following formula:

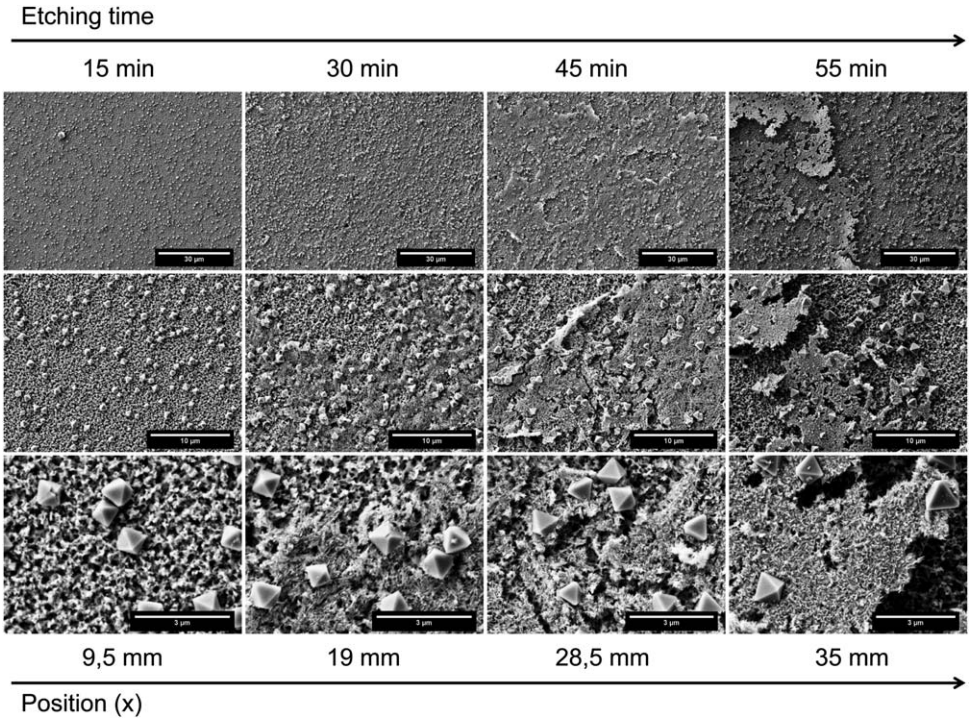

FIGURE 2. Scanning electron microscopy (SEM) observations at different positions and magnifications of a gradient sample which was not sonicated after etching, evidencing the presence of adhered reaction precipitates. Dimensions of the scale bars: 30 μm (top), 10 μm (middle), 3 μm (bottom).

$$A_r = \frac{N * A_t}{A_p}$$

where A_r is the relative area, A_t is the area of a tile, A_p is the projected area, and N is the number of tiles.

An example of semi-log plot obtained by scale sensitive fractal analysis is shown Figure 7(a). This kind of plot can be split into two parts:

- The left part, in which the curve appears to be steep and linear. The slope of the curve is an indication of the complexity, intricacy, or roughness of the surface.[33] The fractal dimension (D) can be estimated by adding two to the absolute value of the slope.
- The right part, in which the relative area approaches one.

The scale (i.e., the area of the tiles) corresponding to the limit between the two parts of the graph is called the smooth-rough crossover (SRC). For scales smaller than the SRC, the surface is considered as "rough," whereas for scales higher than SRC, the surface is considered as "smooth."[34]

Cell cultures

Isolation and expansion of hMSCs. hMSCs were isolated by Ficoll gradient centrifugation and adherence to tissue culture plastic from a human bone marrow aspirate (44-year old, male) obtained from the University Hospital of Bern after approval by the local ethical commission (KEK 188/10) and written consent of the patient. Cell expansion was performed in α-minimum essential medium (α-MEM) supplemented with penicillin (100 U/mL) and streptomycin sulfate (100 μg/mL) (all products from Gibco, Basel, Switzerland), 10% fetal bovine serum (Sera Plus, Pan-Biotech, Aindenbach, Germany), and 5 ng/mL basic fibroblast growth factor (R&D Systems, Minneapolis, MN) with a medium change twice a week.

Cell seeding, culture, and staining on zirconia bars. Prior to cell seeding, specimens were cleaned in an ultrasonic bath using an enzymatic detergent (Terg-A-Zyme®, Sigma-Aldrich, Buchs, Switzerland), followed by extensive rinses with deionized water, 70% ethanol and deionized water again. Samples were then transferred to a single-well chamber (Lab-Tek®, Milian, Vernier, Switzerland) and sterilized using ethylene oxide. hMSCs (passage 3) were seeded on the sample surface at a density of 5000 cells/cm^2 using a diluted cell suspension (10,000 cells/mL, 5 mL) in α-MEM supplemented with 10% fetal calf serum, penicillin (100 U/mL) and streptomycin sulfate (100 μg/mL). Cell-seeded samples were cultured for 48 h in an incubator set at 37°C, 5% CO_2, and 90% humidity. They were then rinsed once with 5 mL of phosphate buffered saline solution, fixed with 70% ethanol and stained with 0.5% toluidine blue solution for 5 min, followed by three rinses with deionized water. Cells were imaged under transmitted light using an optical microscope (Leica MacroFluo™, Wetzlar, Germany). The acquisition time was kept constant for all samples.

Morphometric analysis and cell measurements. Analysis of single cell area and shape (solidity, aspect ratio and

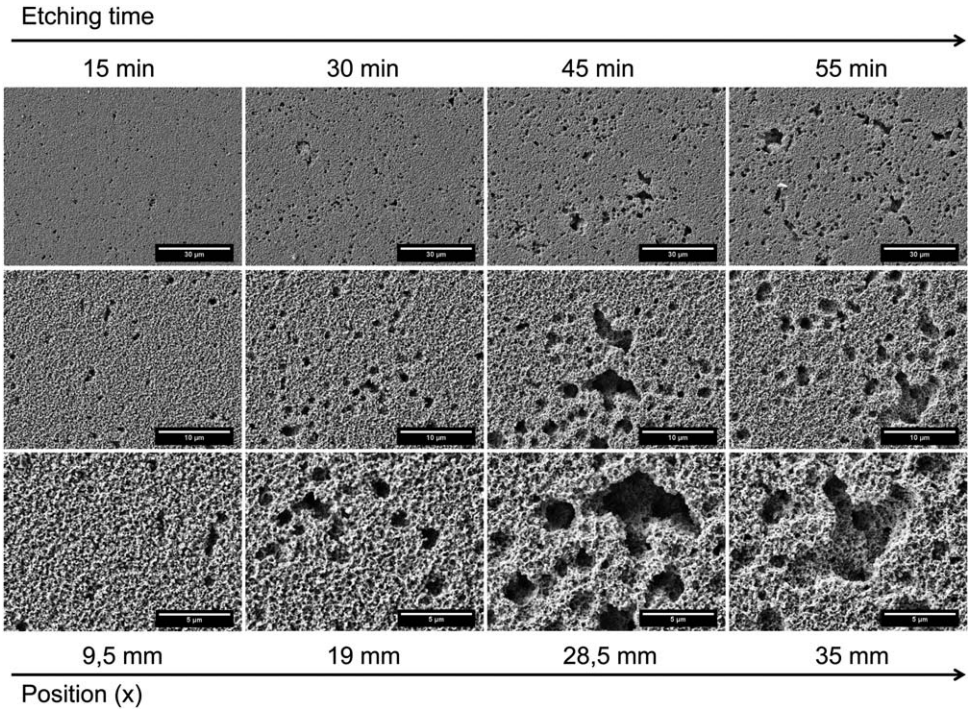

FIGURE 3. SEM observations of the surface of the gradient at different positions and magnifications. Dimensions of the scale bars: 30 μm (top), 10 μm (middle), 5 μm (bottom).

circularity) was performed using ImageJ (NIH, version 1.47). Three gradient samples and three polished (control) samples were characterized, and 20 cells for each region and sample were analyzed. Solidity was calculated as $\frac{\text{Area}}{\text{Convex Area}^2}$, where the convex area is the imaginary convex hull around the object. Aspect ratio was defined as $\frac{\text{Major Axis}}{\text{Minor Axis}}$ of the object's fitted ellipse. Circularity was calculated as $\frac{4\pi\times \text{Area}}{\text{Perimeter}^2}$. Circularity ranges from 1.0 (perfect circle) to values approaching 0 (which indicate an increasingly elongated shape).

Statistical analysis. Statistical analysis of the cell measurements was performed using SPSS® software (version 20, SPSS, Chicago, IL). Normality of the data was assessed by a Shapiro–Wilk test and the homogeneity of variance between groups was verified with a Levene test. Area, aspect ratio, and circularity were log-transformed prior to analysis to normalize the distributions. A one-way ANOVA with Tukey's multiple comparison tests was carried out with a significance level set at $p < 0.05$.

The existence of correlations between topographical parameters and cell morphology was assessed by computing Pearson product-moment and Kendall's tau correlation coefficients, with a two-tailed test of significance. For the calculation, the mean values of each topographical and morphological parameter were computed. In the case of the nanoroughness measurements, the data was linearly interpolated to match the position of the cell measurements when necessary. Besides, a visual inspection of cell morphological parameter vs. topographical parameter graphs was carried out to identify potential nonlinear relationships that cannot be detected with the previous method.

RESULTS

Surface characterization

Surface before sonication. The observation of the surface of a specimen which was not subjected to sonication evidenced the presence of adhered precipitates formed during etching (Fig. 2). For distances comprised between 0 mm and 19 mm (corresponding to and etching time between 0 and 30 min), they consisted exclusively in particles with an octahedral shape (octahedrons) whose size increases with distance/time. Beyond 19 mm, an adhered layer composed of needle-like particles (needles) appears. The layer seems to detach progressively when increasing etching time until it totally disappears at a distance of 35 mm (etching time: 55 min). A previous study showed that the octahedrons are YF_3 crystals and that the needles are composed of yttrium, zirconium, and fluorine.[31]

Surface after sonication. The observation of the surface morphology and topography of the gradient evidenced a clear evolution from smooth to rough (Figs. 3 and 4). The appearance of a granular texture and etch pits, whose number, diameter and depth increased with time, provided both a nanoroughness and microroughness gradient as it will be discussed later.

Roughness analysis. The induced roughness gradients were found to be homogenous in the y direction (transversally) on a width of 2 mm (see Supporting Information).

- Amplitude parameters

  At the microscale, the average roughness (S_a) and RMS roughness (S_q) increase approximately proportionally to the distance (Fig. 5). The kurtosis (S_{ku}) decreases strongly in

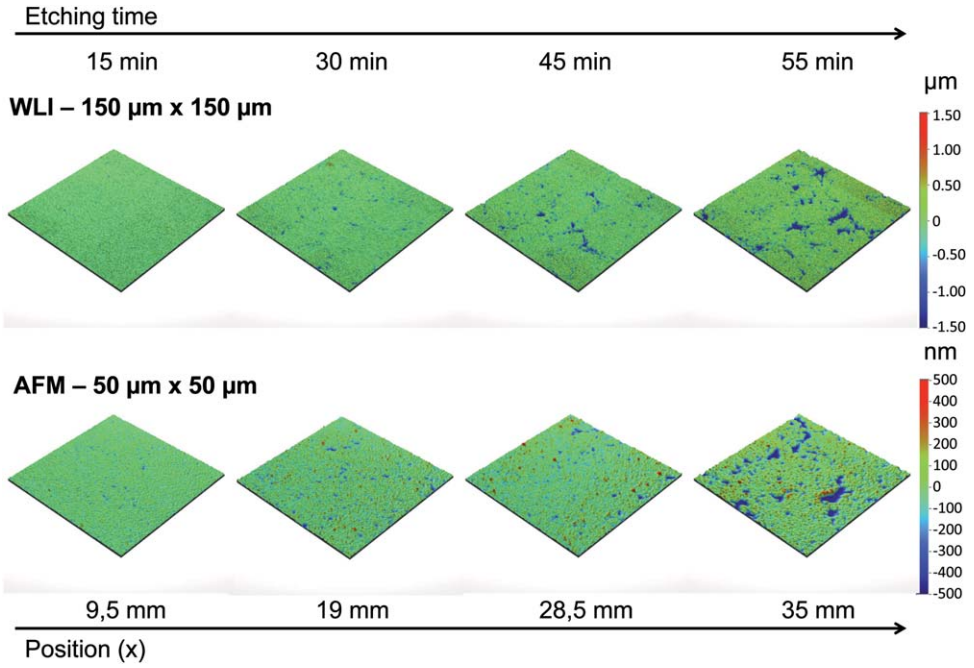

FIGURE 4. White light interferometry (WLI) and atomic force microscopy (AFM) topographical images of the surface at different positions on the gradient.

the first 7 mm and then has moderate variations without showing a clear tendency. Its value remains superior to three indicating a narrow height distribution and steep sidewalls. The skewness (S_{sk}) is first close to 0 and then decreases substantially. The decreasing negative values indicate that valleys are becoming more and more predominant on the surface along the gradient direction, which is consistent with the apparition of etch pits reported above.

At the nanoscale, the average roughness (S_a) and RMS roughness (S_q) increase up to the half of the gradient and then decrease slightly. The kurtosis (S_{ku}) presents a similar behavior than at the micrometric scale. The skewness (S_{sk}) is first largely positive and then decreases substantially. The positive values indicate that the peaks are always predominant, and the decreasing tendency shows that this predominance becomes less and less important along the distance. The discrepancy between the nanoskewness and the microskewness results can be explained by the fact that the Gaussian filter eliminates features that are larger than the cut-off wavelength, which implies that etch pits larger than 1 µm have little or no influence on nanoroughness.

- Spatial parameters

  At both the microscale and the nanoscale, the fastest decay length (S_{al}) tends to decrease at the beginning of the gradient and then increases along the distance. (Fig. 5) At the microscale, the density of summits (S_{ds}) increases along the distance up to a maximum at approximately 25 mm and then decreases slightly, whereas at the nanoscale it increases up to a maximum at about 10 mm and then decreases. This probably indicates that in a first step numerous small peaks are formed and in a second step a part of them gets eroded to form broader peaks.

- Hybrid parameters

  At the microscale, the RMS gradient (S_{dq}), the mean summit curvature (S_{sc}), and the developed interfacial area ratio (S_{dr}) increase proportionally to the distance up to a plateau which is reached at about 28 mm. (Fig. 6)

  At the nanoscale, the RMS gradient (S_{dq}), the mean summit curvature (S_{sc}), and the developed interfacial area ratio (S_{dr}) increase up to a maximum which is reached at about half of the gradient (19 mm) and then undergo a moderate decrease.

  The increase in the hybrid parameters indicates an increase of the intricacy of the surface and of the ratio surface area/projected area.

- Functional parameters

  At the microscale, the surface material volume (S_m) increases up to 28 mm and then reaches a plateau. (Fig. 6) The surface core void volume (S_c) increases all over the gradient but the increase rate tends to decrease along the distance. The surface valley void volume (S_v) increases proportionally to the distance all over the gradient.

  At the nanoscale, the surface material volume (S_m) increases up to half of the gradient and then decreases slightly. The surface core void volume (S_c) increases up to a maximum at half of the gradient and then decreases, whereas the surface valley void volume (S_v) always increases along the gradient.

Fractal analysis. The scale sensitive fractal analysis of the AFM and the WLI data showed that (Fig. 7):

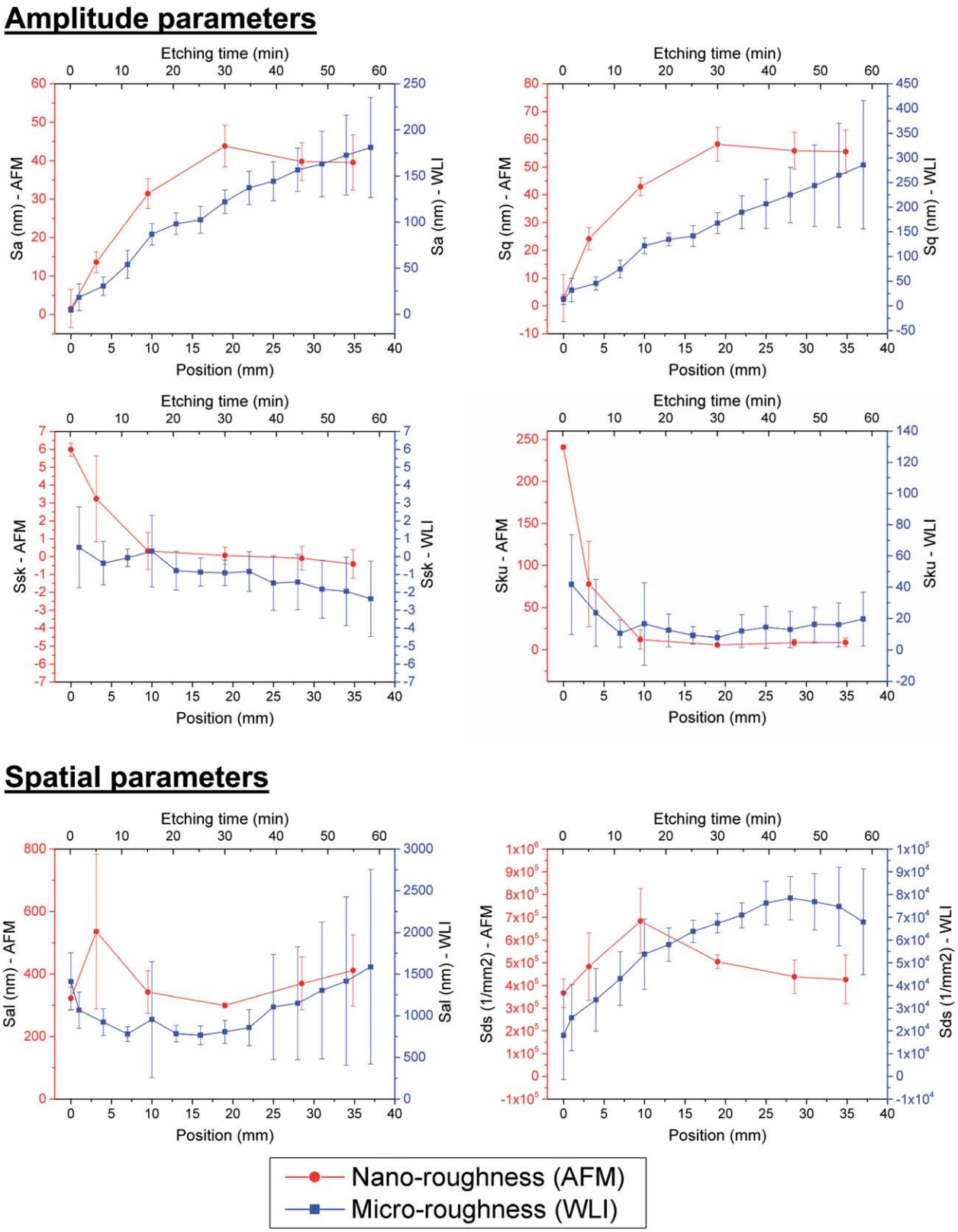

FIGURE 5. Evolution of amplitude and spatial roughness parameters along the gradient. AFM measurements correspond to the nanoroughness and WLI measurement correspond to the microroughness. Error bars represent the standard deviations.

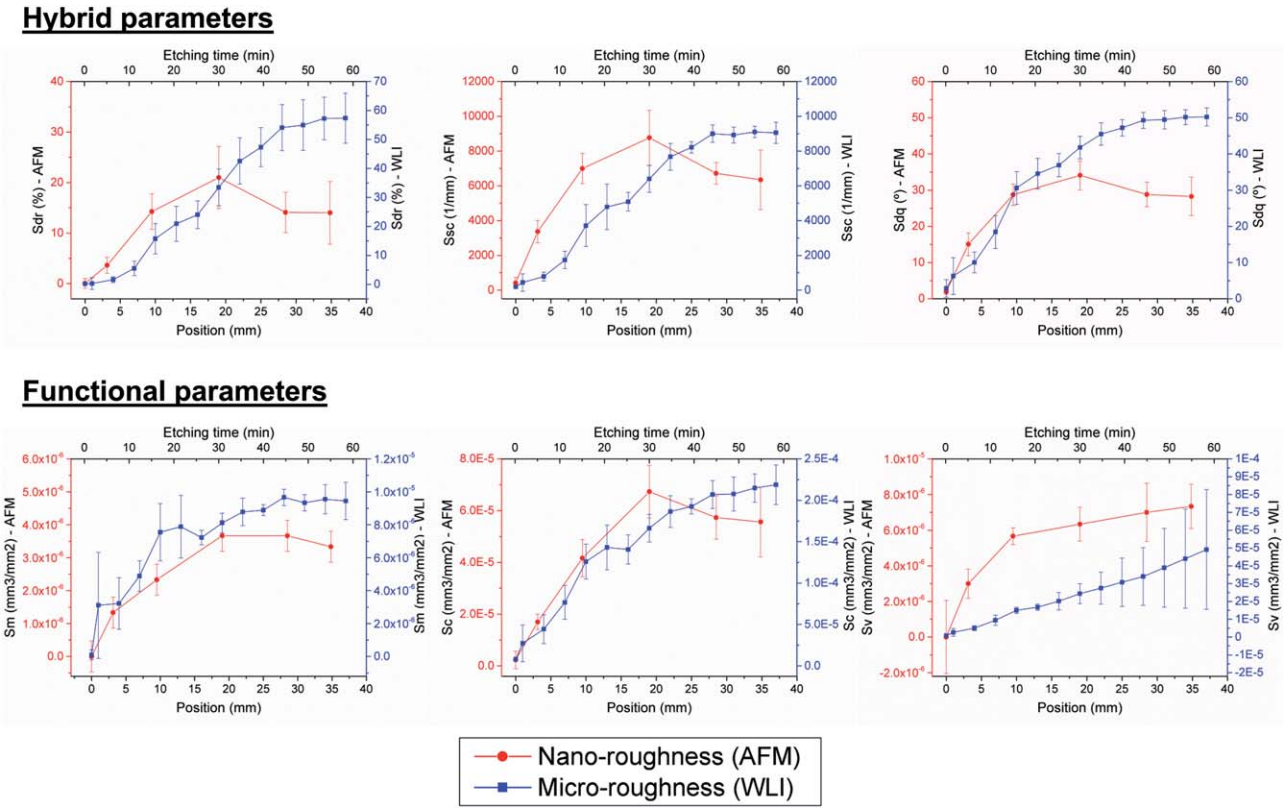

FIGURE 6. Evolution of hybrid and functional roughness parameters along the gradient. AFM measurements correspond to the nanoroughness and WLI measurements correspond to the microroughness. Error bars represent the standard deviations.

TABLE II. Pearson Product-Moment and Kendall's Tau Correlation Coefficients for all the Combinations of Topographical and Morphological Parameters

			Microroughness (WLI)				Nanoroughness (AFM)			
Type	Param.	Coeff.	Area	Aspect Ratio	Circularity	Solidity	Area	Aspect Ratio	Circularity	Solidity
Amplitude	S_a	r	−0,18	−0,17	−0,31	−0,71	0,22	−0,20	−0,65	**−0,92**
		τ	−0,05	−0,05	−0,05	−0,43	0,33	0,14	−0,43	**−0,81**
	S_q	r	−0,26	−0,16	−0,23	−0,64	0,16	−0,19	−0,62	**−0,91**
		τ	−0,05	−0,05	−0,05	−0,43	0,33	0,14	−0,43	**−0,81**
	S_{sk}	r	0,25	0,22	0,20	0,63	−0,13	0,27	0,51	**0,84**
		τ	0,05	0,05	0,05	0,43	0,05	0,05	0,05	0,43
	S_{ku}	r	−0,44	0,09	0,70	**0,76**	−0,24	0,28	0,59	**0,87**
		τ	−0,62	−0,24	**0,71**	0,33	−0,33	−0,14	0,43	**−0,81**
Spatial	S_{al}	r	−0,70	−0,01	0,37	0,02	−0,51	0,26	**−0,76**	**0,90**
		τ	−0,33	−0,14	0,24	−0,14	−0,62	0,14	0,52	**−0,71**
	S_{ds}	r	−0,03	−0,21	−0,50	**−0,83**	0,66	−0,33	−0,29	−0,22
		τ	−0,05	−0,05	−0,05	−0,43	0,52	−0,05	−0,43	−0,24
Hybrid	S_{dq}	r	−0,05	−0,22	−0,44	**−0,80**	0,39	−0,23	−0,72	**−0,93**
		τ	−0,05	−0,05	−0,05	−0,43	0,52	−0,05	−0,62	**−0,81**
	S_{dr}	r	−0,29	−0,14	−0,25	−0,64	0,46	−0,19	**−0,78**	**−0,95**
		τ	−0,05	−0,05	−0,05	−0,43	0,62	−0,14	−0,52	**−0,71**
	S_{sc}	r	−0,18	−0,19	−0,34	−0,72	0,50	−0,21	**−0,78**	**−0,93**
		τ	−0,05	−0,05	−0,05	−0,43	0,62	−0,14	−0,52	**−0,71**
Functional	S_m	r	−0,01	−0,29	−0,41	**−0,79**	0,15	−0,16	−0,65	**−0,91**
		τ	−0,05	−0,05	−0,05	−0,43	0,29	0,10	−0,39	**−0,78**
	S_c	r	−0,10	−0,22	−0,38	**−0,76**	0,26	−0,16	−0,71	**−0,94**
		τ	−0,05	−0,05	−0,05	−0,43	0,33	0,14	−0,43	**−0,81**
	S_v	r	−0,33	−0,10	−0,17	−0,57	0,00	−0,23	−0,45	**−0,81**
		τ	−0,05	−0,05	−0,05	−0,43	−0,05	−0,05	−0,05	−0,43
Fractal	SRC	r	−0,32	0,02	0,34	0,12	−0,51	−0,04	0,05	−0,35
		τ	−0,59	−0,20	0,49	0,29	−0,14	−0,14	0,05	−0,33
	D	r	−0,34	−0,13	−0,15	−0,56	0,28	−0,16	−0,71	**−0,94**
		τ	−0,05	−0,05	−0,05	−0,43	0,33	0,14	−0,43	**−0,81**

Significance of the correlation: $\boldsymbol{p < 0.05}$; $\underline{p \leq 0.005}$.

- The SRC values obtained from both techniques differ substantially. The analysis of the AFM data leads to a SRC which is roughly proportional to the distance, whereas the analysis of the WLI data leads to a SRC which remains approximately constant from 0 mm to 31 mm and increases strongly from 31 mm to 38 mm. Besides, the values obtained from WLI are much more elevated.
- Regarding the fractal dimension (D), the results correlate well for both techniques up to half of the gradient, showing an increase proportional to the distance. Then for WLI the fractal dimension keeps increasing whereas for AFM it slightly decreases.

It is important to note that the discrepancies between the results obtained from the fractal analysis of the AFM and the WLI data are not related to errors in the measurements: the results of the calculation performed by the tiling algorithm strongly depend on the resolution and the area of observation, which define the range of scales (i.e., the area of the tiles) over which the relative area can be computed and are different for both techniques. Both values obtained should thus be considered as valid.

Cell cultures

The gradient in roughness influenced significantly the area ($p < 0.001$), aspect ratio ($p = 0.01$) and solidity ($p = 0.026$) of stem cells [Fig. 8(a,b,d)], while the circularity was not significantly affected ($p = 0.073$) [Fig. 8(c)]. A significant increase in cell area (20 min vs. 50 min HF treatment: $p = 0.014$) and aspect ratio (20 min vs. 30 min HF treatment: $p = 0.009$) were observed in the central part of the bar. The aspect ratio was sensitive to the gradient (10 min vs. 20 min treatment: $p = 0.096$, 20 min vs. 30 min: $p = 0.009$ and 30 min vs. 40 min: $p = 0.069$). The solidity reached a minimum in the region of the bar exposed for 30 min to HF (0 min vs. 30 min HF treatment: $p = 0.075$ and 10 min vs. 30 min HF treatment: $p = 0.083$). Cells in this region also had the highest aspect ratio. Stem cells had a spindle-like morphology over the whole sample range, but a significantly more elongated cell shape was observed in the region of the sample exposed for 30 min to HF as compared to both shorter and longer treatment times [Fig. 8(e,g)]. As compared to the polished control, the mean cell area was significantly reduced in all regions of the gradient bar except the one corresponding to 20 min of HF exposure ($p < 0.01$ for each pairwise comparison), while the aspect ratio, circularity and solidity were not significantly different.

Significant correlations were found between cell solidity and several topographical parameters. The correlation was particularly important ($p < 0.005$) for nanoroughness parameters (S_a, S_q, S_{al}, S_{dq}, S_{dr}, S_{sc}, S_m, and S_c) and the AFM fractal dimension (D) (Table II, Fig. 9). Additionally, possible curvilinear correlations between several microroughness parameters (S_a, S_q, S_{sk}, S_{dr}, S_{dq}, S_m, S_c, and S_v), the WLI fractal dimension and cell area were identified (Fig. 9). In particular, a good fitting could be obtained with a second-order polynomial regression for the developed interfacial area ratio (S_{dr}, $R^2 = 0.73$) and the mean summit curvature (S_{sc}, $R^2 = 0.70$) and a third-order polynomial regression for the fractal dimension (D, $R^2 = 0.65$).

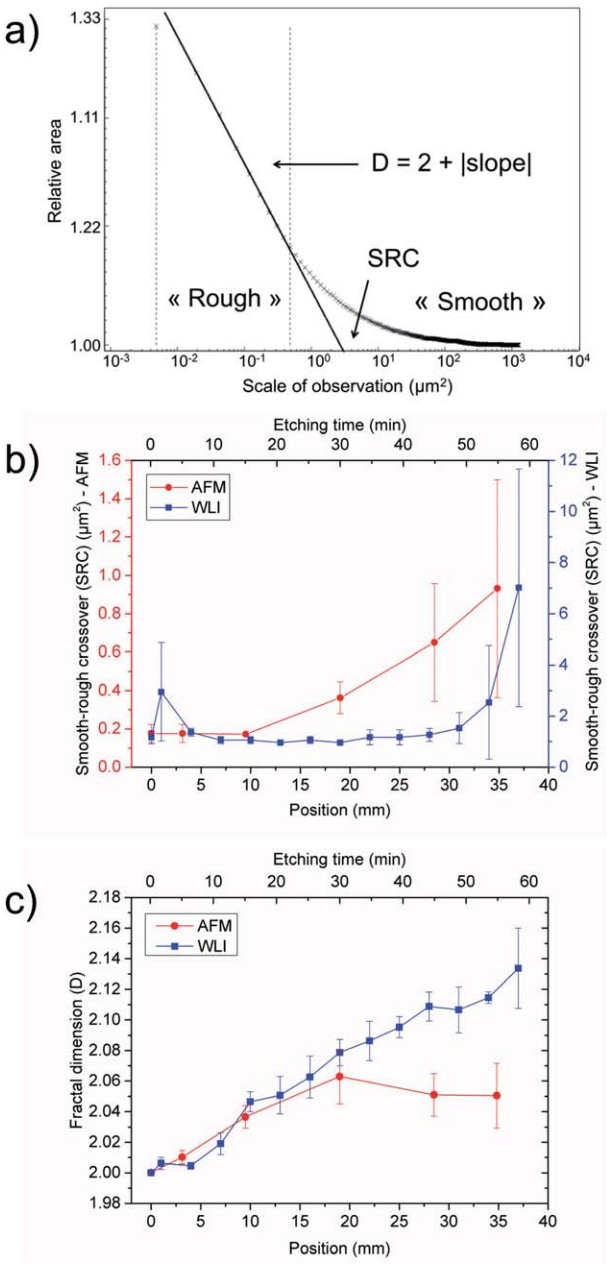

FIGURE 7. (a) Example of scale-sensitive fractal analysis, showing how smooth-rough crossover (SRC) and fractal dimension are obtained, (b) SRC as a function of position on the gradient and etching time, (c) fractal dimension as a function of position on the gradient and etching time.

DISCUSSION

The method proposed in this study was successful to produce surface gradients on zirconia both at the microscale and at the nanoscale. In particular, a large range of variation was obtained for roughness parameters belonging to different categories such as S_a, S_q (amplitude), S_{ds} (spatial), S_{dr},

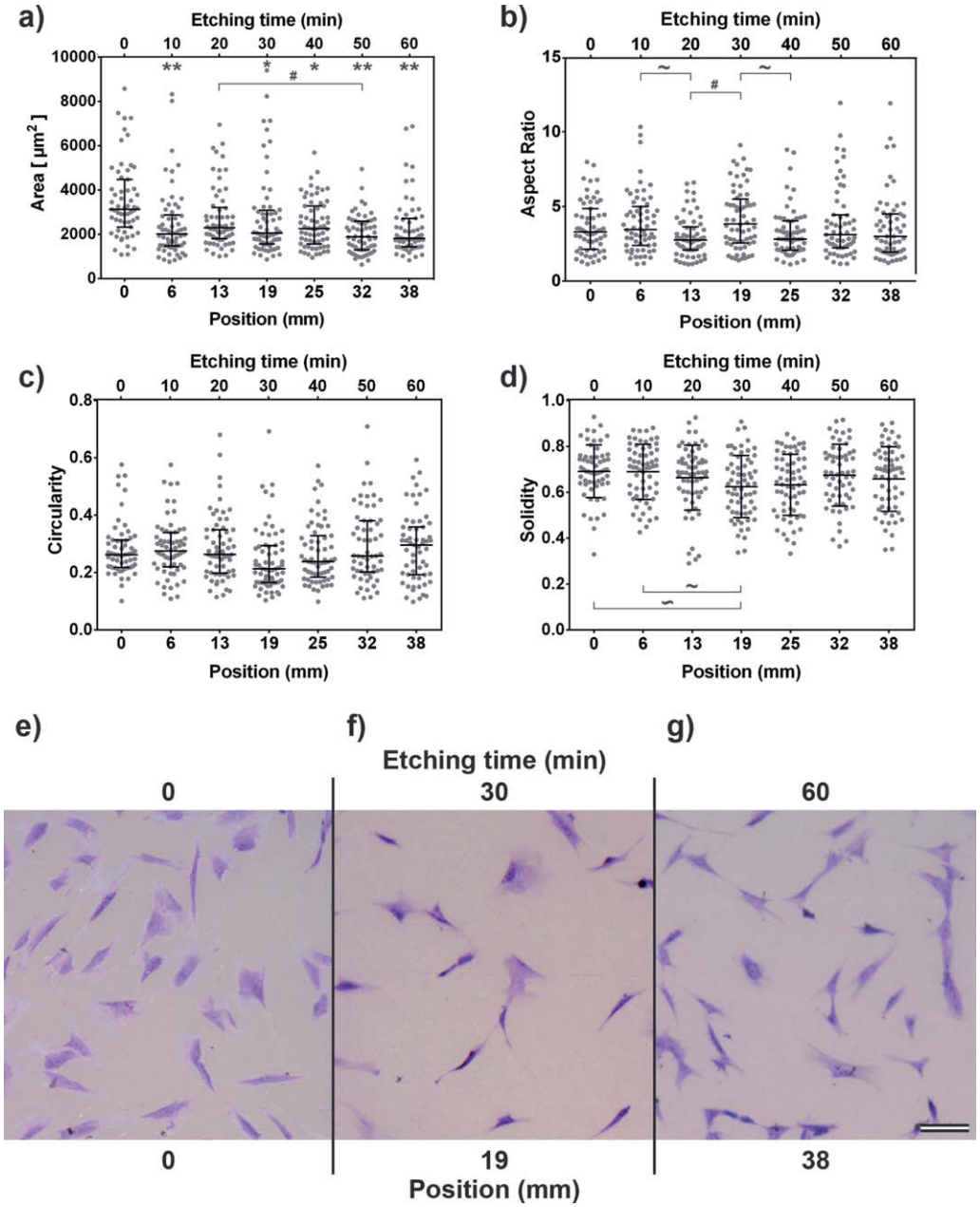

FIGURE 8. Top: evolution of human mesenchymal stem cell morphology along the gradient: (a) area, (b) aspect ratio, (c) circularity, and (d) solidity. Statistical differences: ** is $p < 0.001$ and * is $p < 0.01$ relative to 0; # is $p < 0.05$ and $\sim$ is $p < 0.1$ between the highlighted groups. Bottom: representative images of the toluidine blue stained human mesenchymal stem cells on gradient zirconia bars after 48 h of culture: (e) polished control, (f) 30 min, and (g) 60 min of hydrofluoric acid treatment. Scale bar = 100 µm.

S_{sc}, S_{dq} (hybrid), S_m, S_c, and S_v (functional), as well as for fractal parameters (D, SRC) (Figs. 5–7). In addition to these topographical changes, previous works showed that HF etching induces an increase in the fluorine content of the surface[31] and the formation of a superficial submicrometric porosity.[32] Nevertheless, these surface alterations were shown to be nearly independent from etching time. Surface structural and chemical changes along the gradients can thus be considered as negligible.

The HF etching mechanism, which accounts for the zirconia topography remodeling, has been extensively studied previously.[31] In particular, it was demonstrated that etching is faster at the grain border, but also occurs inside the grains, which leads to a granular texture (observable on Fig. 3 of this article) and participates to the increase in nanoroughness. Besides, it was showed that HF induces the formation of etch pits (observable on Figs. 3 and 4 of this article), which grow over time, contributing to the increase in microroughness. The present work brings an additional observation: the apparition of the adhered layer of needle-like precipitates (Fig. 2) corresponds to an inflection point for some curves such as S_a, S_q, S_{da}, S_{sc}, S_{dq} vs. distance/

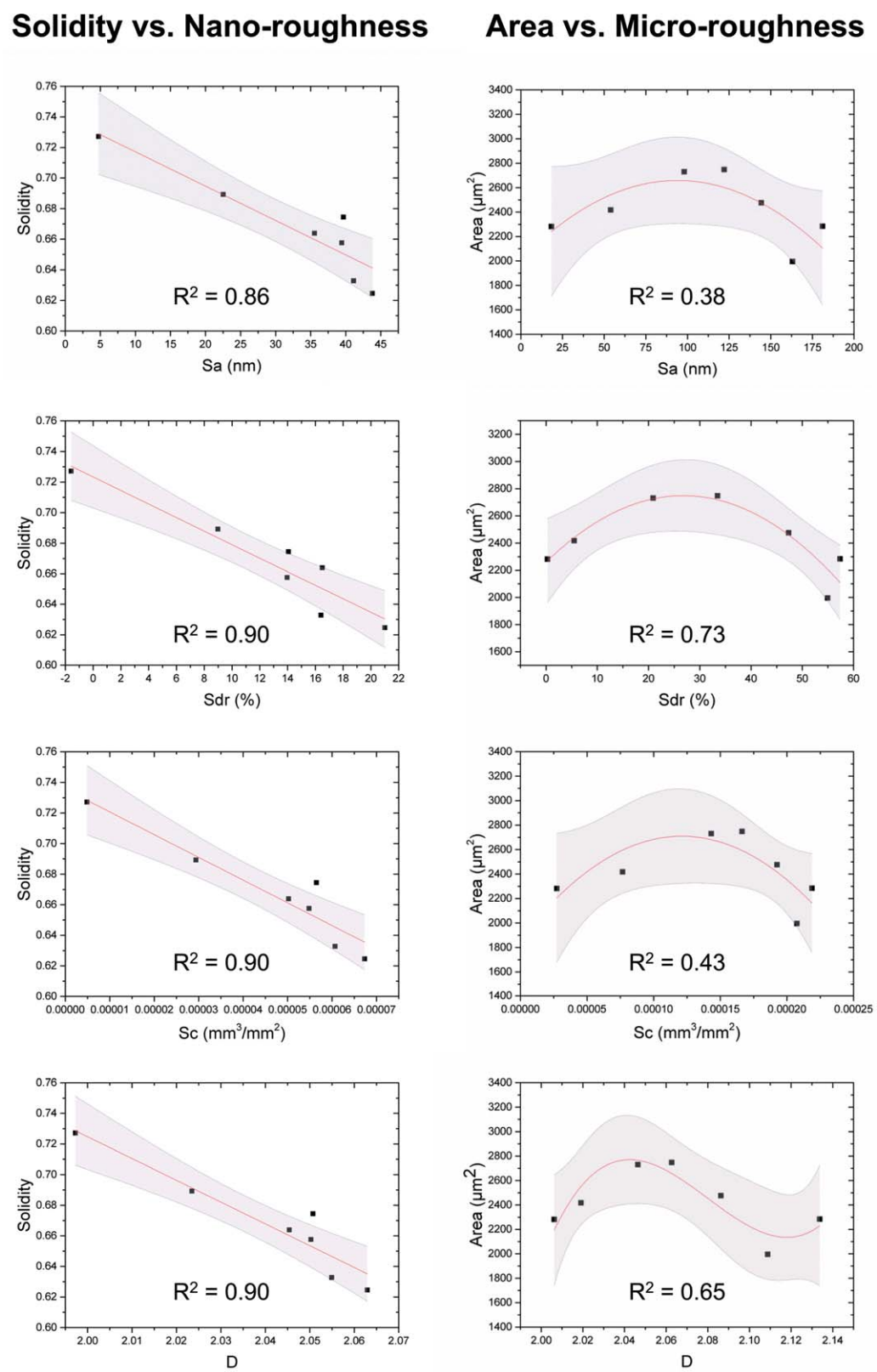

FIGURE 9. Left: hMSC solidity as a function of three representative nanoroughness parameters and the AFM fractal dimension (mean values). Data are represented with linear regression lines and associated 95% confidence bands. Right: hMSC area as a function three representative microroughness parameters and the WLI fractal dimension (mean values). Data are represented with second-order (for S_a, S_{dr}, and S_c) or third-order (for D) polynomial regression lines and associated 95% confidence bands.

etching time (Fig. 5, AFM data). The layer might thus influence the etching process by shielding the material below from the etching solution.

The gradients were homogenous transversally on a 2 mm wide band, which provides a large area for cell culture analyses and makes the specimens obtained valuable for the high-throughput screening of cell-surface interactions. The gradient fabrication process proposed in this work is flexible: polished bars were used here but the method has the potential to be applied to any type of surface (for instance: ground, sandblasted, etc.). Finally, zirconia etching is a process which is already used in the industry (for instance: CeraRoot implants with ICE^{TM} surface). The results obtained with this type of gradients present thus the advantage to be directly applicable to the fabrication of commercial dental components.

Regarding cell cultures, the gradient did induce changes in hMSC response. A minimum in the solidity was associated to a maximum in the aspect ratio for an etching time of 30 min ($x = 19$ mm) (Fig. 8). This may indicate a stronger commitment toward the small spindle-shaped rapid self-renewing cell type described by Colter et al.,[35] which is associated to more rapid proliferation and mineralization as compared to other cells present in the hMSC heterogeneous population. Cell solidity was found to be linearly correlated with some nanoroughness parameters and the AFM fractal dimension, whereas cell area seemed to present a curvilinear correlation with some microroughness parameters and the WLI fractal dimension (Fig. 9 and Table II). hMSC solidity appears thus to be sensitive to the nanotopography whereas hMSC area seems more influenced by the microtopography, which could be explained by the different sizes of the cell structures involved (tens of microns for whole cell in the case of cell area, submicron to micron range for cell pseudopodia in the case of cell solidity). This suggests that tuning of both microtopography and nanotopography is required to achieve optimal control over stem cell morphology and phenotype, and can possibly explain why in many studies, including work on roughened zirconia, the combination of microtopography and nanotopography had a synergistic effect on cell responses like matrix mineralization.[36] Furthermore, it highlights the interest of performing a multiscale analysis of biomaterial surfaces, combining both WLI and AFM measurements. Several authors suggested the existence of correlations between roughness parameters and cell response. For instance, Anselme et al. showed that fractal dimension obtained from confocal microscopy measurements correlated statistically with the proliferation and the adhesion index of human osteoblasts[37] and Gentile et al. have reported that silicon surfaces with R_a in the range of 10–45 nm measured by AFM and fractal dimension $D \sim 2.5$ promoted the attachment and proliferation of four different cell types.[38] However, there is a lack of studies that combine multiscale and multiparameter surface roughness analysis. Indeed, the present work shows the benefit of coupling multiscale surface topography evaluation with systematic correlation analysis of roughness and cell parameters as a way to unveil which roughness parameter and which topographical scale have the strongest impact on early cell behavior.

The effects observed in this study might appear as moderate. This is, however, counterbalanced by the fact that, given the absence of sample-to-sample variations, the gradient approach provides a much higher statistical power than a classical approach. The method is thus promising for further high-throughput studies of cell interaction with roughened surfaces, which could focus on diverse topics such as for instance the influence of roughness on stem cell differentiation, osteoblast mineralization or osteoclast resorption. It is anticipated that the use of gradient materials and correlation analyses of roughness and cell parameters will provide a better understanding of cell-material interactions and help rationalizing the design of implant topography. The main shortcoming of this approach, however, lies in the intrinsic limitations of *in vitro* studies: while *in vitro* models allow a precise control of the culture conditions, they lack to reproduce the complex environment encountered by the implant inside the human body. Gradients should thus be used for screening purpose before moving to further *in vivo* evaluation of the most promising surfaces.

CONCLUSION

HF-induced roughness gradients have been successfully produced at the surface of zirconia by controlling the speed of immersion of specimens into the etching solution. The gradients achieved present a large range of variation of fractal and roughness parameters at both the microscale and nanoscale. The variation of topography influenced hMSC morphology, with significant changes in cell area, aspect ratio and solidity. Nanoroughness parameters and the AFM fractal dimension were linearly correlated to cell solidity, while microroughness parameters and WLI fractal dimension appeared to be nonlinearly correlated to cell area, which highlights the importance of multiscale optimization of implant topography. The method proposed in this work has the potential to be transposed to other type of surfaces and cell-surface interaction studies, drastically reducing the amount of samples and resources required and providing results directly transferable to industry.

ACKNOWLEDGMENTS

The authors would also like to acknowledge Dr. Erica Roitero and Dr. Roberta Fraioli for their valuable advice and Prof. Christopher Brown and Benjamin Childs from the Worcester Polytechnic Institute for providing a free license for the Sfrax software. Conflict of Interest: No benefit of any kind will be received either directly or indirectly by the authors.

REFERENCES

1. Chevalier J. What future for zirconia as a biomaterial? Biomaterials 2006;27:535–543.
2. Denry I, Kelly JR. State of the art of zirconia for dental applications. Dent Mater 2008;24:299–307.
3. Andreiotelli M, Wenz HJ, Kohal RJ. Are ceramic implants a viable alternative to titanium implants? A systematic literature review. Clin Oral Implants Res 2009;20:32–47.
4. Kohal R-J, Knauf M, Larsson B, Sahlin H, Butz F. One-piece zirconia oral implants: One-year results from a prospective cohort

study. 1. Single tooth replacement. J Clin Periodontol 2012;39: 590–597.
5. Osman RB, Swain MV, Atieh M, Ma S, Duncan W. Ceramic implants (Y-TZP): Are they a viable alternative to titanium implants for the support of overdentures? A randomized clinical trial. Clin Oral Implants Res 2014;25:1366–1377.
6. Lawson S. Environmental degradation of zirconia ceramics. J Eur Ceram Soc 1995;15:485–502.
7. Sanon C, Chevalier J, Douillard T, Cattani-Lorente M, Scherrer SS, Gremillard L. A new testing protocol for zirconia dental implants. Dent Mater 2015;31:15–25.
8. Anil S, Anand PS, Alghamdi H, Jansen JA. Dental implant surface enhancement and osseointegration. Implant Dent – A Rapidly Evol Pract 2011. 83-108 p.
9. Wennerberg A, Albrektsson T. On implant surfaces: A review of current knowledge and opinions. Int J Oral Maxillofac Implants 2009;25:63–74.
10. Coelho PG, Jimbo R, Tovar N, Bonfante E. a. Osseointegration: Hierarchical designing encompassing the macrometer, micrometer, and nanometer length scales. Dent Mater 2015;31:37–52.
11. Simon CG, Lin-Gibson S. Combinatorial and high-throughput screening of biomaterials. Adv Mater 2011;23:369–387.
12. Wennerberg A, Albrektsson T, Wennerberg AAT. Suggested guidelines for the topographic evaluation of implant surfaces. Int J Oral Maxillofac Implants 2000;15:331–344.
13. Dohan Ehrenfest DM, Coelho PG, Kang B-S, Sul Y-T, Albrektsson T. Classification of osseointegrated implant surfaces: Materials, chemistry and topography. Trends Biotechnol 2010;28:198–206.
14. Wennerberg A, Albrektsson T. Effects of titanium surface topography on bone integration: A systematic review. Clin Oral Implants Res 2009;20 Suppl 4:172–184.
15. Yu H, Lim KP, Xiong S, Tan LP, Shim W. Functional morphometric analysis in cellular behaviors: Shape and size matter. Adv Healthc Mater 2013;2:1188–1197.
16. Zink C, Hall H, Brunette DM, Spencer ND. Orthogonal nanometer-micrometer roughness gradients probe morphological influences on cell behavior. Biomaterials 2012;33:8055–8061.
17. Kunzler TP, Drobek T, Schuler M, Spencer ND. Systematic study of osteoblast and fibroblast response to roughness by means of surface-morphology gradients. Biomaterials 2007;28:2175–2182.
18. Faia-Torres AB, Guimond-Lischer S, Rottmar M, Charnley M, Goren T, Maniura-Weber K, Spencer ND, Reis RL, Textor M, Neves NM. Differential regulation of osteogenic differentiation of stem cells on surface roughness gradients. Biomaterials 2014;35: 9023–9032.
19. Lin NJ, Lin-Gibson S. Osteoblast response to dimethacrylate composites varying in composition, conversion and roughness using a combinatorial approach. Biomaterials 2009;30:4480–4487.
20. Cremmel CVM, Zink C, Maniura-Weber K, Isa L, Spencer ND. Orthogonal morphological feature size and density gradients for exploring synergistic effects in biology. Langmuir 2015;31:8446–8452.
21. Dinca V, Alloncle P, Delaporte P, Ion V, Rusen L, Filipescu M, Mustaciosu C, Luculescu C, Dinescu M. Excimer laser texturing of natural composite polymer surfaces for studying cell-to-substrate specific response. Appl Surf Sci 2015;352:82–90.
22. Geblinger D, Zink C, Spencer ND, Addadi L, Geiger B. Effects of surface microtopography on the assembly of the osteoclast resorption apparatus. J R Soc Interface 2012;9:1599–1608.
23. Ranella a, Barberoglou M, Bakogianni S, Fotakis C, Stratakis E. Tuning cell adhesion by controlling the roughness and wettability of 3D micro/nano silicon structures. Acta Biomater 2010;6:2711–2720.
24. Wang PY, Clements LR, Thissen H, Jane A, Tsai WB, Voelcker NH. Screening mesenchymal stem cell attachment and differentiation on porous silicon gradients. Adv Funct Mater 2012;22:3414–3423.
25. Yang W, Han W, He W, Li J, Wang J, Feng H, Qian Y. Surface topography of hydroxyapatite promotes osteogenic differentiation of human bone marrow mesenchymal stem cells. Mater Sci Eng C 2016;60:45–53.
26. Morgenthaler S, Zink C, Spencer ND. Surface-chemical and -morphological gradients. Soft Matter 2008;4:419
27. Kunzler TP, Drobek T, Sprecher CM, Schuler M, Spencer ND. Fabrication of material-independent morphology gradients for high-throughput applications. Appl Surf Sci 2006;253:2148–2153.
28. Huwiler C, Kunzler TP, Textor M, Vörös J, Spencer ND. Functionalizable nanomorphology gradients via colloidal self-assembly. Langmuir 2007;23:5929–5935.
29. Gahlert M, Röhling S, Wieland M, Eichhorn S, Küchenhoff H, Kniha H. A comparison study of the osseointegration of zirconia and titanium dental implants. A biomechanical evaluation in the maxilla of pigs. Clin Implant Dent Relat Res 2010;12:297–305.
30. Gahlert M, Röhling S, Wieland M, Sprecher CM, Kniha H, Milz S. Osseointegration of zirconia and titanium dental implants: A histological and histomorphometrical study in the maxilla of pigs. Clin Oral Implants Res 2009;20:1247–1253.
31. Flamant Q, García Marro F, Roa Rovira JJ, Anglada M. Hydrofluoric acid etching of dental zirconia. Part 1: Etching mechanism and surface characterization. J Eur Ceram Soc 2016;36:121–134.
32. Flamant Q, Anglada M. Hydrofluoric acid etching of dental zirconia. Part 2: Effect on flexural strength and ageing behavior. J Eur Ceram Soc 2016;36:135–145.
33. Brown CA, Charles PD, Johnsen WA, Chesters S. Fractal analysis of topographic data by the patchwork method. Wear 1993;161:61–67.
34. Siegmann S. Scale-sensitive fractal analysis for understanding the influence of substrate roughness in thermal spraying. In: 1st United Therm Spray Conference—Thermal Spray: A United Forum for Scientific and Technological Advances, Indianapolis, Indiana, 1997.
35. Colter DC, Sekiya I, Prockop DJ. Identification of a subpopulation of rapidly self-renewing and multipotential adult stem cells in colonies of human marrow stromal cells. Proc Natl Acad Sci USA 2001;98:7841–7845.
36. Ito H, Sasaki H, Saito K, Honma S, Yajima Y, Yoshinari M. Response of osteoblast-like cells to zirconia with different surface topography. Dent Mater J 2013;32:122–129.
37. Anselme K, Bigerelle M, Noel B, Dufresne E, Judas D, Iost A, Hardouin P. Qualitative and quantitative study of human osteoblast adhesion on materials with various surface roughnesses. J Biomed Mater Res 2000;49:155–166.
38. Gentile F, Tirinato L, Battista E, Causa F, Liberale C, di Fabrizio EM, Decuzzi P. Cells preferentially grow on rough substrates. Biomaterials 2010;31:7205–7212.

Supplementary information

Homogeneity of the roughness gradient in the transverse direction (y-direction)

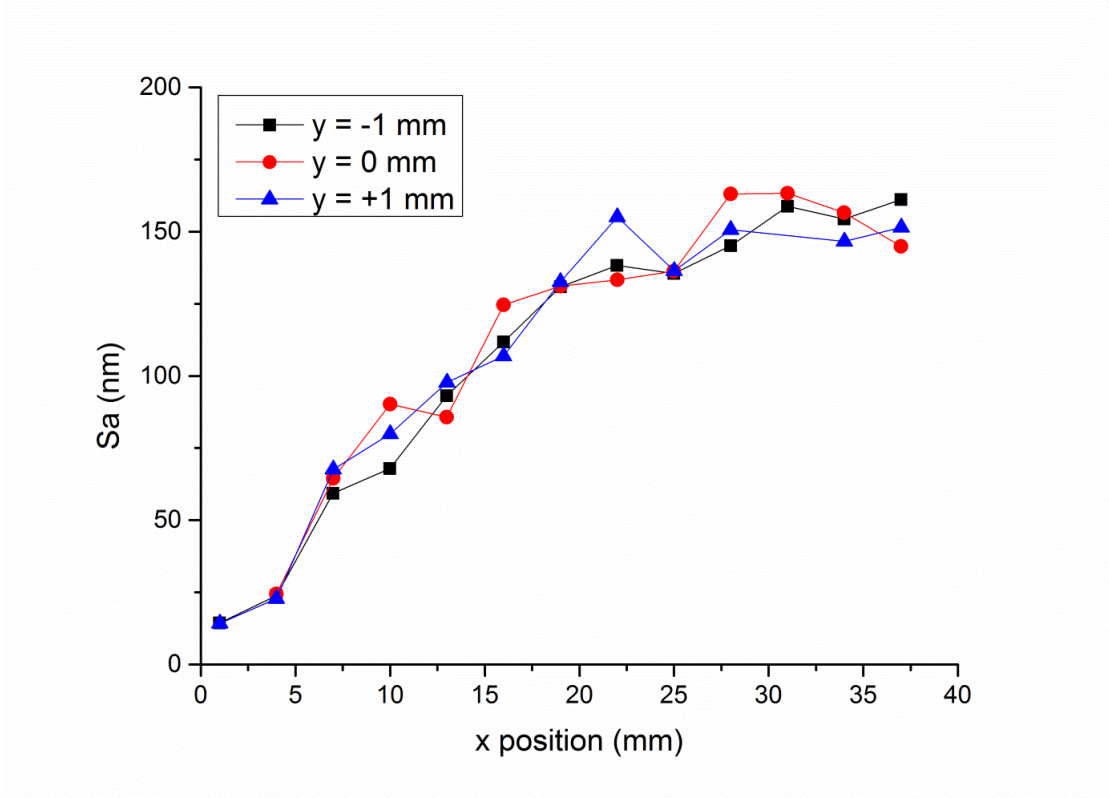

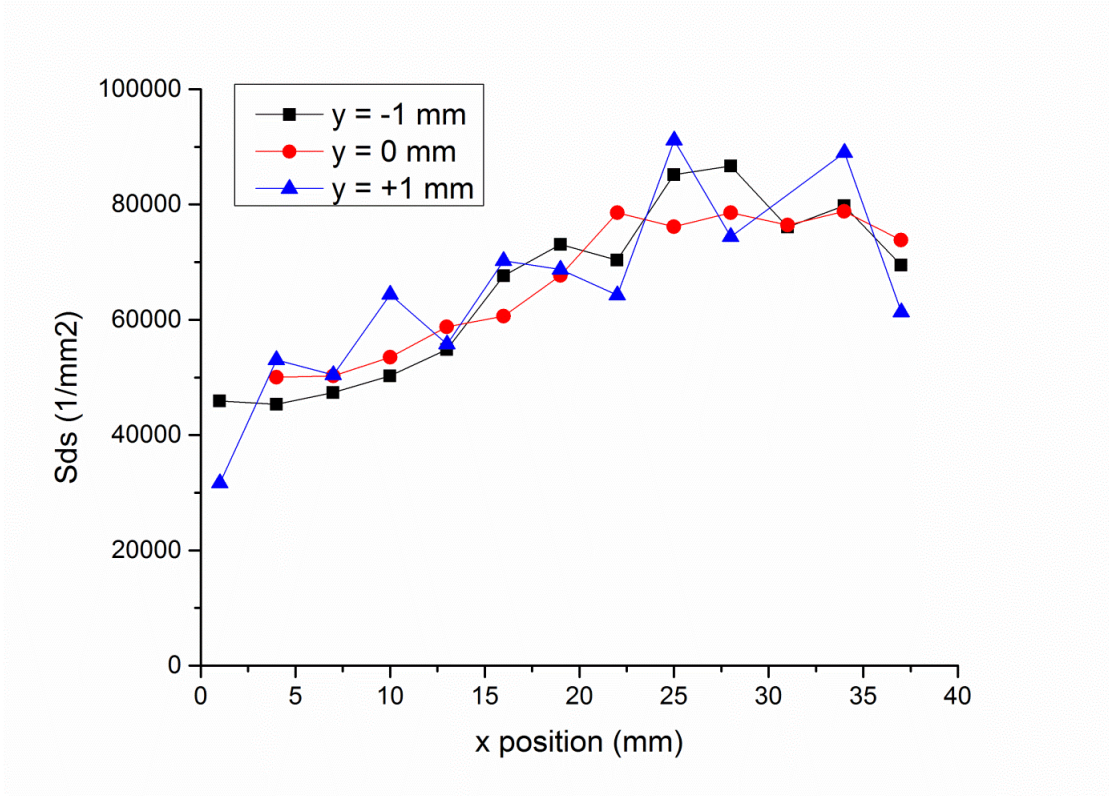

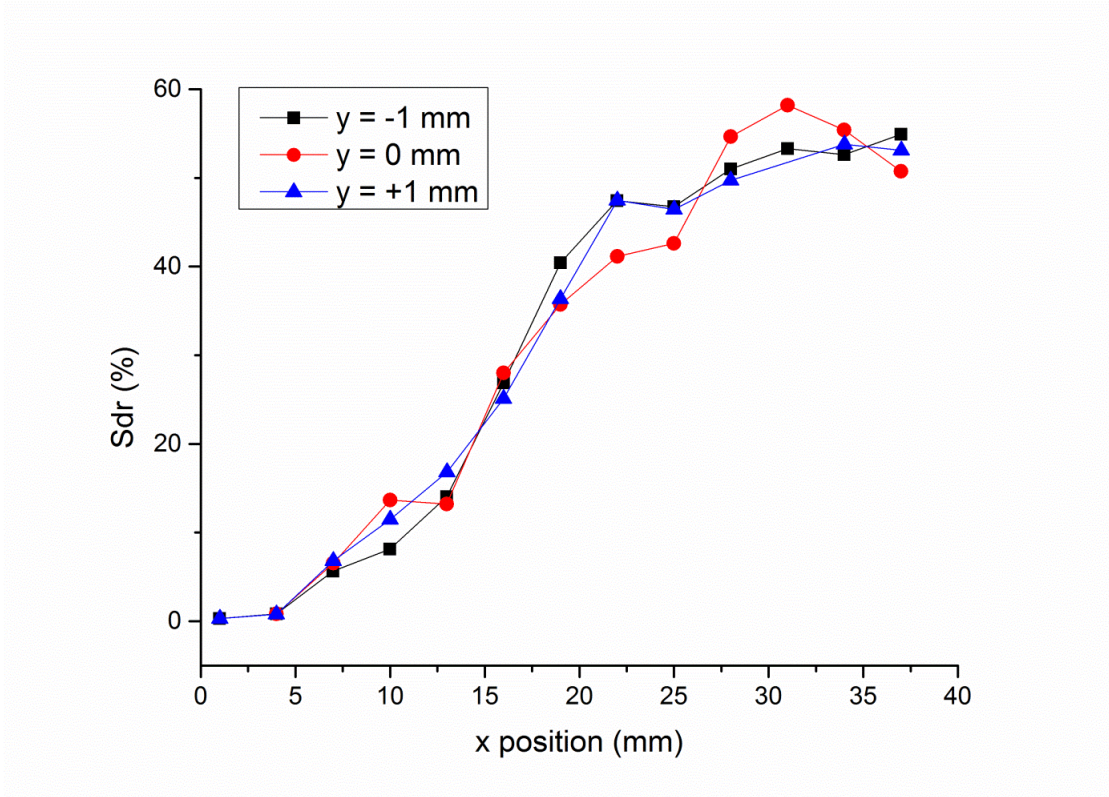
y = -1 mm
y = 0 mm
y = +1 mm
Sdr (%)
x position (mm)
0
20
40
60
0
5
10
15
20
25
30
35
40

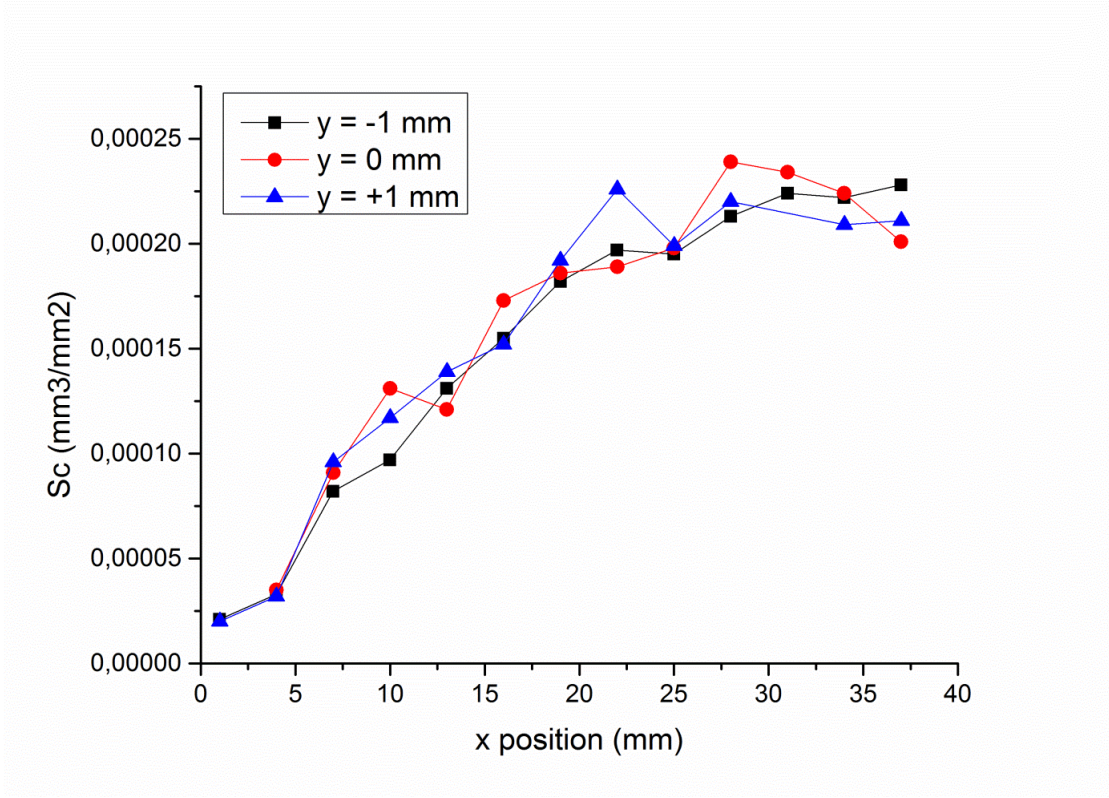
y = -1 mm
y = 0 mm
y = +1 mm
Sc (mm3/mm2)
x position (mm)
0,00000
0,00005
0,00010
0,00015
0,00020
0,00025
0
5
10
15
20
25
30
35
40

Solidity / Area / Aspect ratio vs. nano-roughness parameters (AFM)

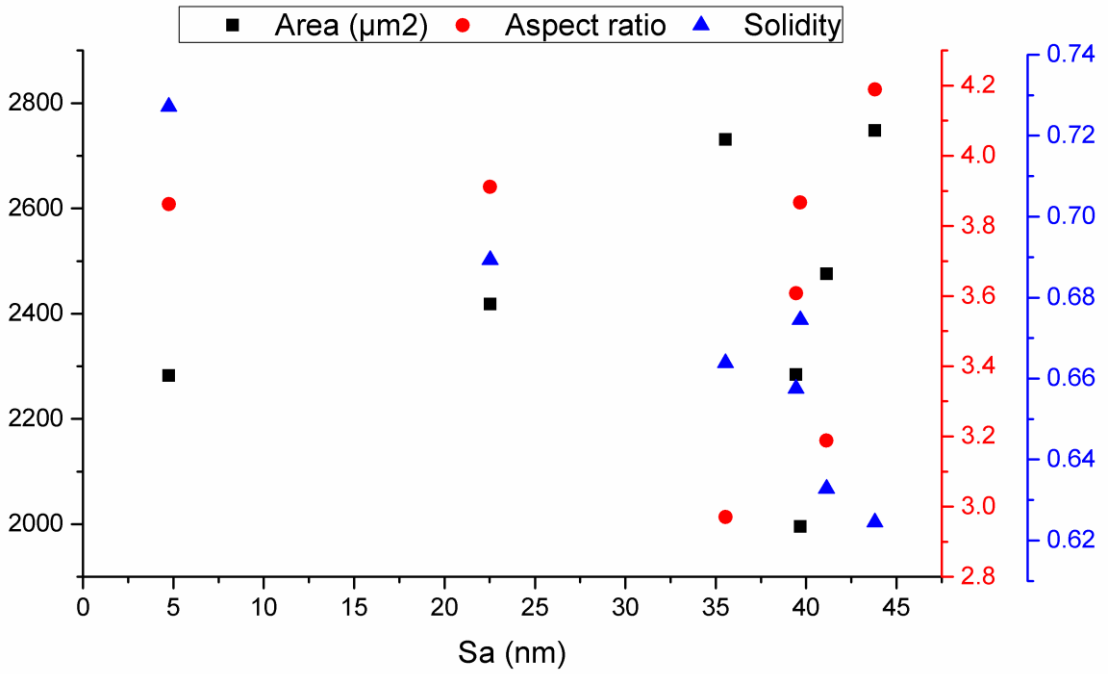

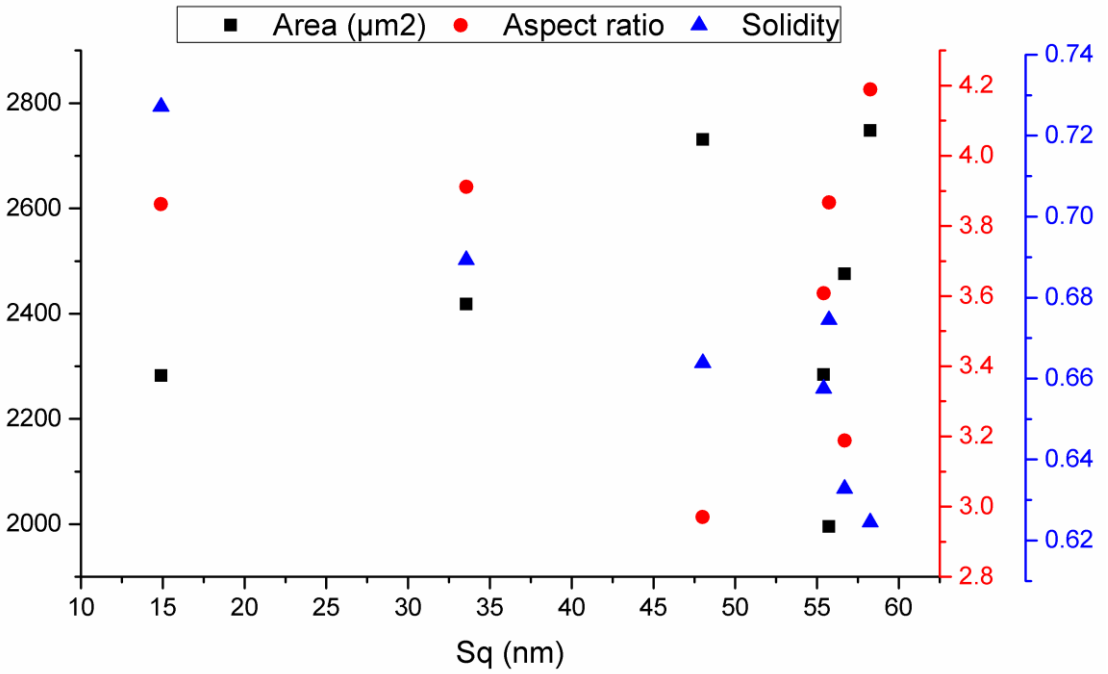

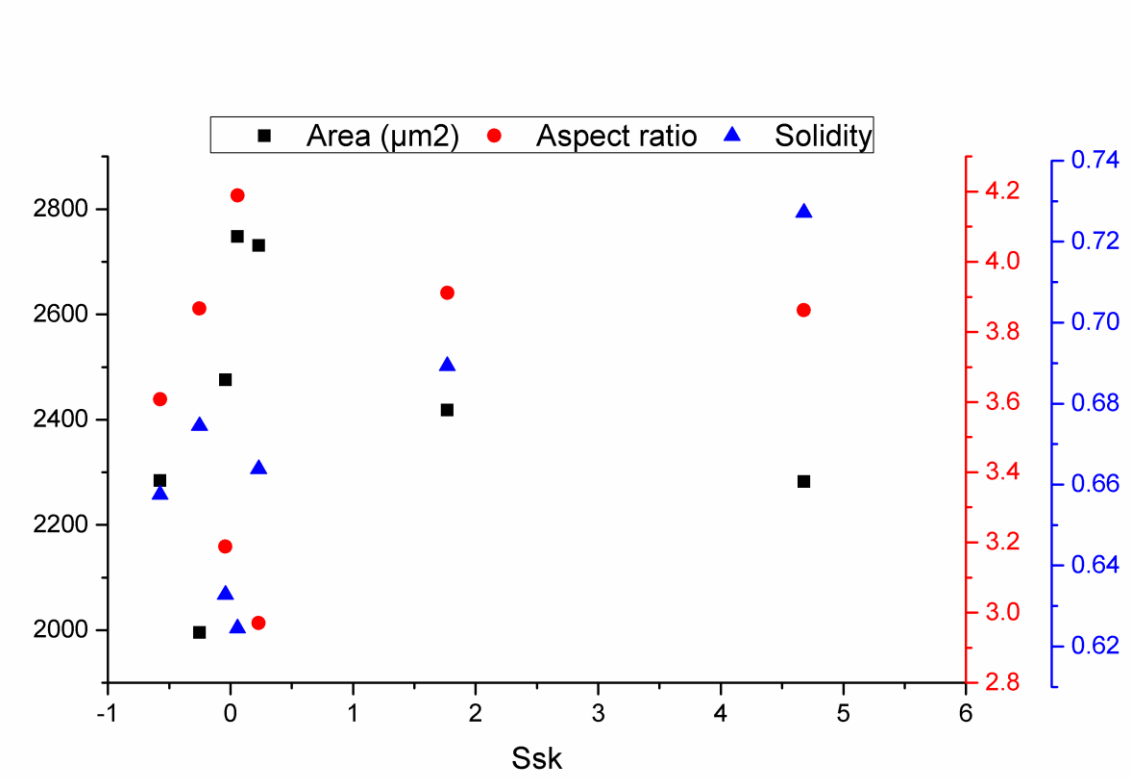
Area (μm2)
Aspect ratio
Solidity
2800
2600
2400
2200
2000
4.2
4.0
3.8
3.6
3.4
3.2
3.0
2.8
0.74
0.72
0.70
0.68
0.66
0.64
0.62
-1
0
1
2
3
4
5
6
Ssk

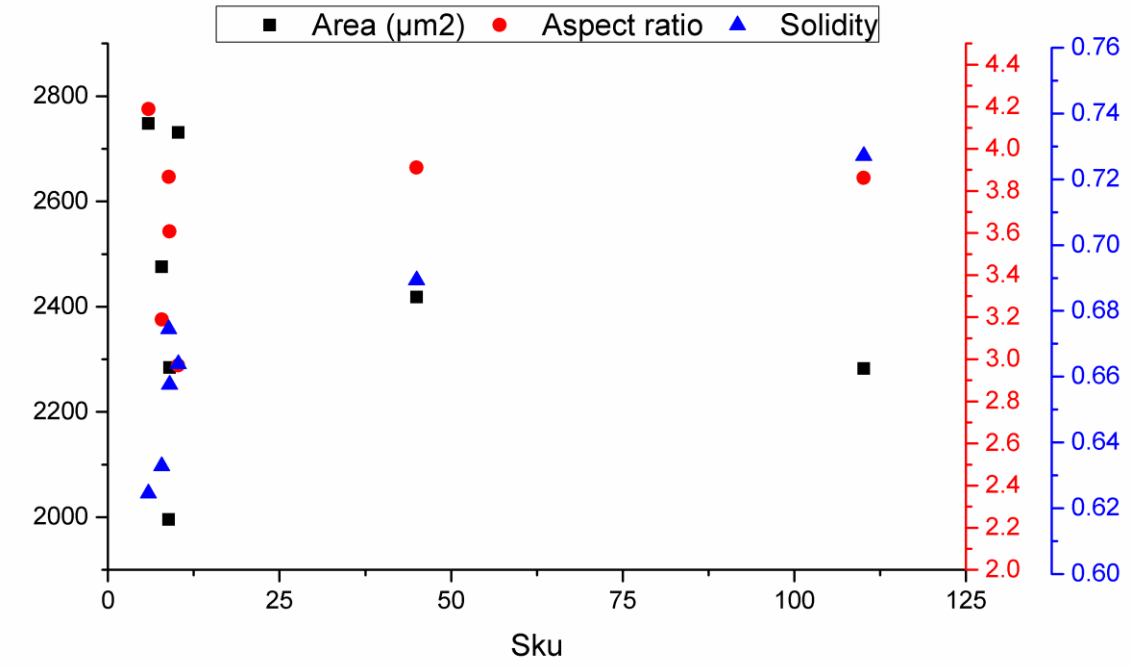
Area (μm2)
Aspect ratio
Solidity
2800
2600
2400
2200
2000
4.4
4.2
4.0
3.8
3.6
3.4
3.2
3.0
2.8
2.6
2.4
2.2
2.0
0.76
0.74
0.72
0.70
0.68
0.66
0.64
0.62
0.60
0
25
50
75
100
125
Sku

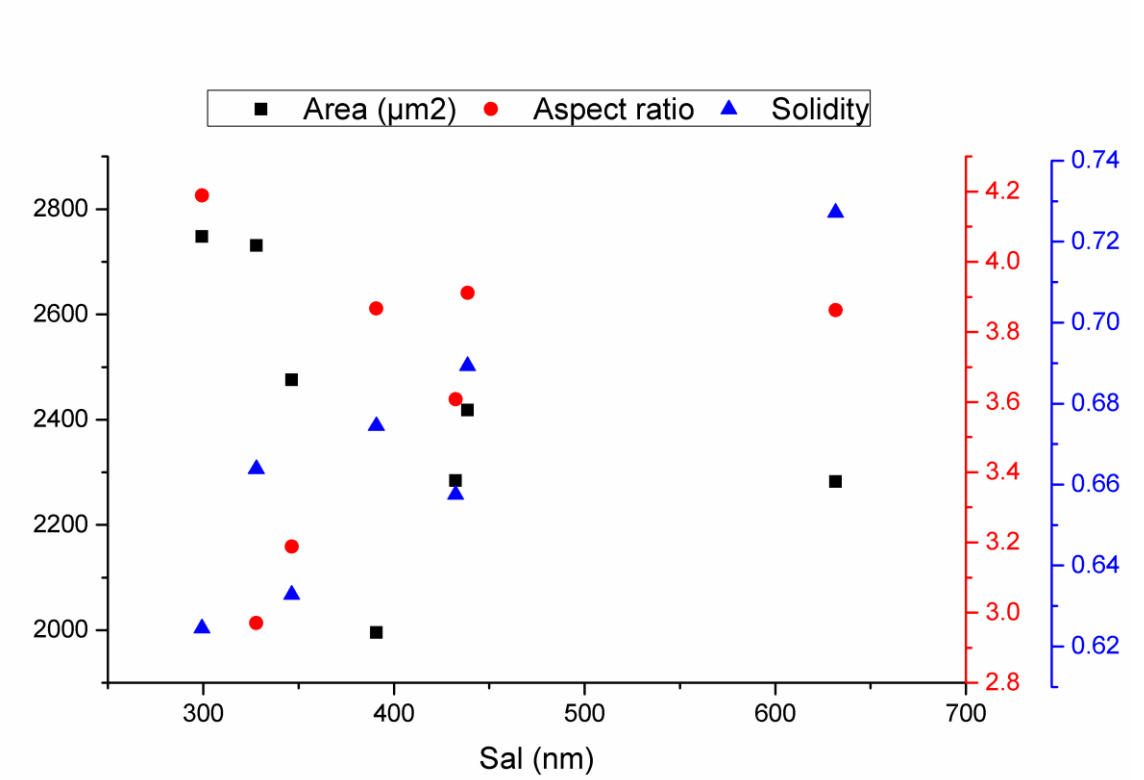
Area (µm2)
Aspect ratio
Solidity
2800
2600
2400
2200
2000
4.2
4.0
3.8
3.6
3.4
3.2
3.0
2.8
0.74
0.72
0.70
0.68
0.66
0.64
0.62
300
400
500
600
700
Sal (nm)

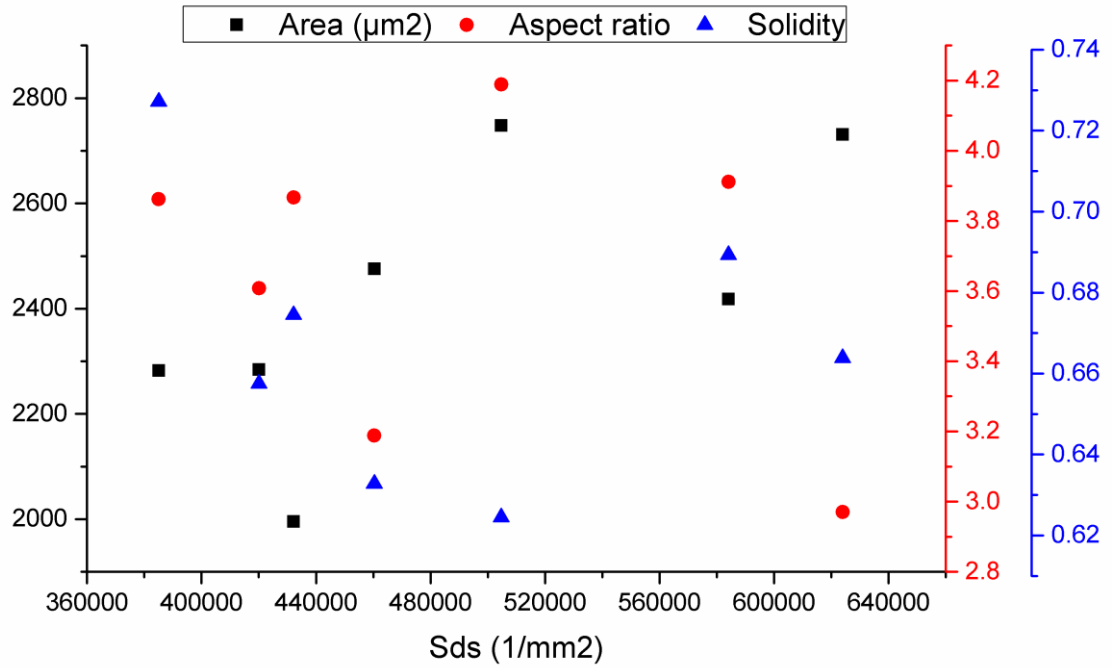
Area (µm2)
Aspect ratio
Solidity
2800
2600
2400
2200
2000
4.2
4.0
3.8
3.6
3.4
3.2
3.0
2.8
0.74
0.72
0.70
0.68
0.66
0.64
0.62
360000
400000
440000
480000
520000
560000
600000
640000
Sds (1/mm2)

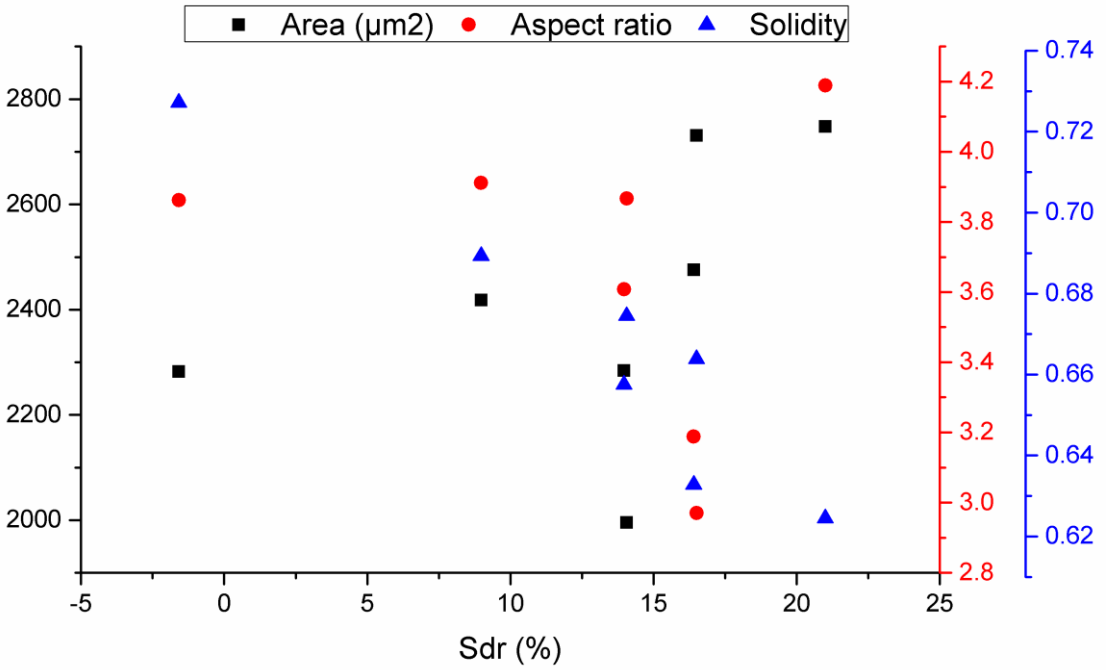
Area (µm2)
Aspect ratio
Solidity
2800
2600
2400
2200
2000
4.2
4.0
3.8
3.6
3.4
3.2
3.0
2.8
0.74
0.72
0.70
0.68
0.66
0.64
0.62
-5
0
5
10
15
20
25
Sdr (%)

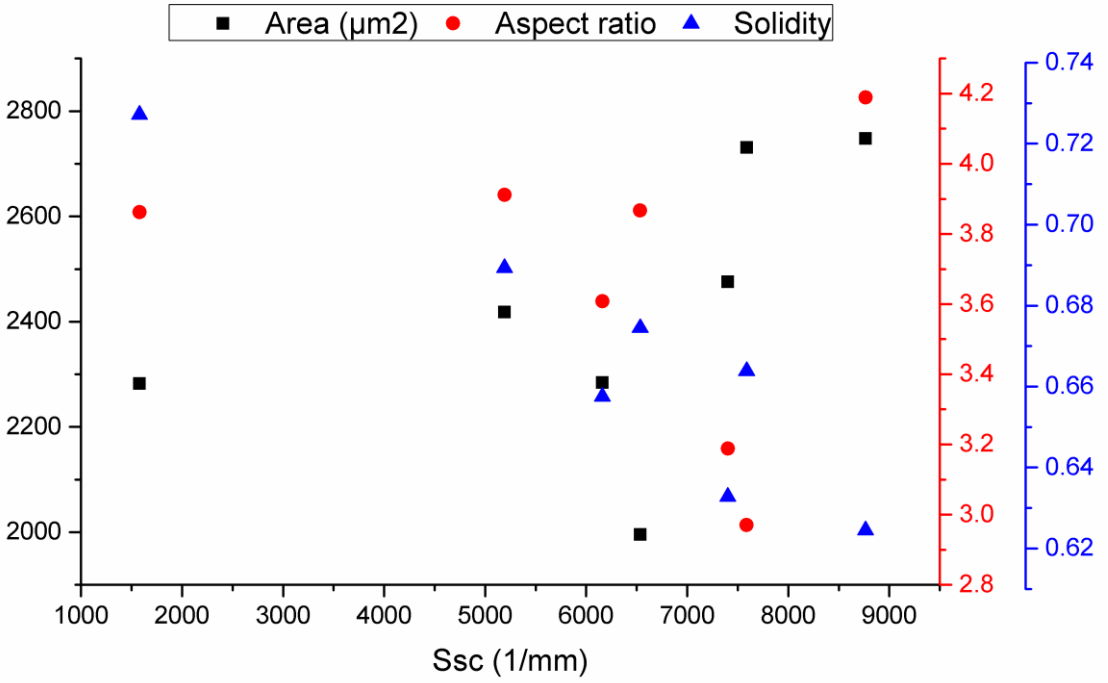
Area (µm2)
Aspect ratio
Solidity
2800
2600
2400
2200
2000
4.2
4.0
3.8
3.6
3.4
3.2
3.0
2.8
0.74
0.72
0.70
0.68
0.66
0.64
0.62
1000
2000
3000
4000
5000
6000
7000
8000
9000
Ssc (1/mm)

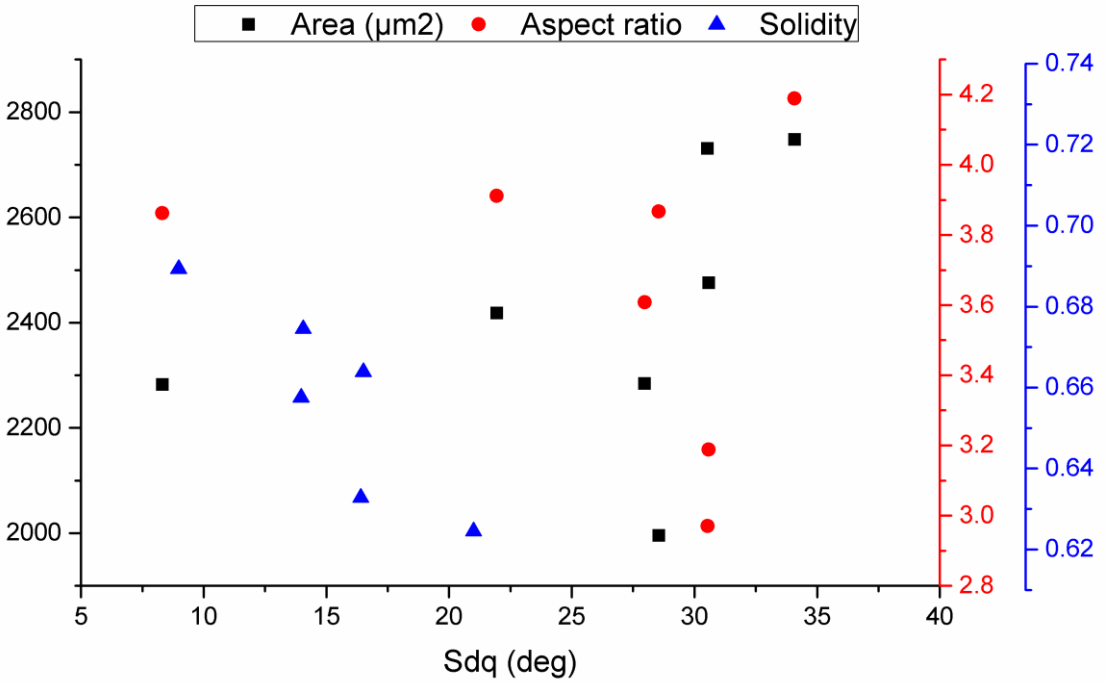
Area (μm2)
Aspect ratio
Solidity
2800
2600
2400
2200
2000
4.2
4.0
3.8
3.6
3.4
3.2
3.0
2.8
0.74
0.72
0.70
0.68
0.66
0.64
0.62
5
10
15
20
25
30
35
40
Sdq (deg)

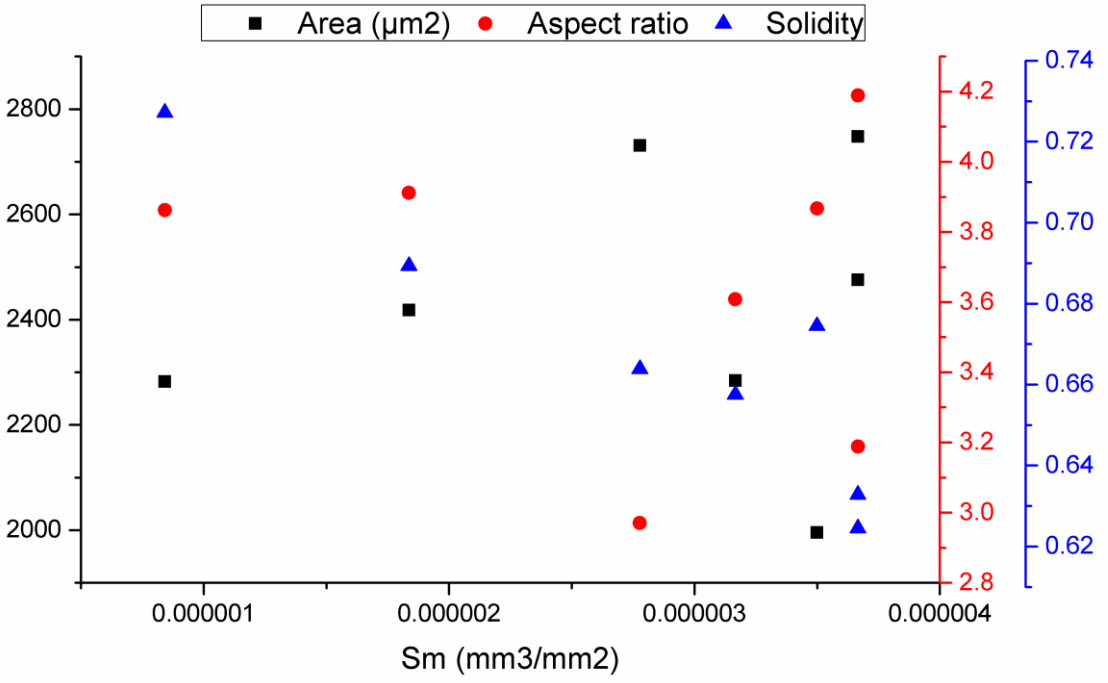
Area (μm2)
Aspect ratio
Solidity
2800
2600
2400
2200
2000
4.2
4.0
3.8
3.6
3.4
3.2
3.0
2.8
0.74
0.72
0.70
0.68
0.66
0.64
0.62
0.000001
0.000002
0.000003
0.000004
Sm (mm3/mm2)

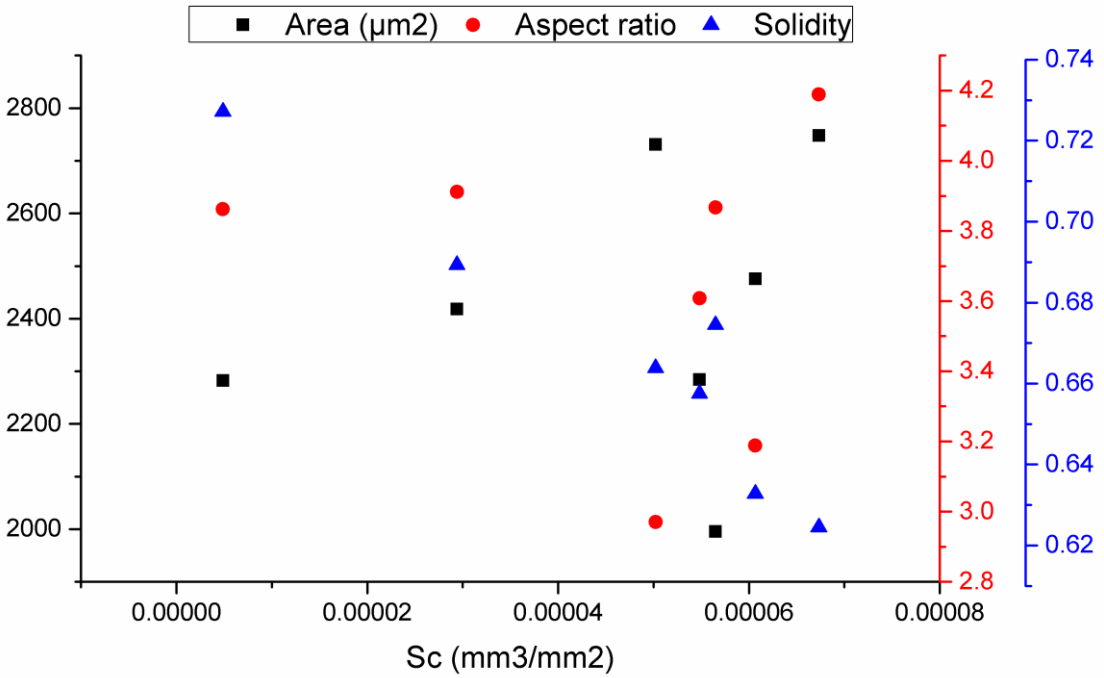
Area (μm2)
Aspect ratio
Solidity
2800
2600
2400
2200
2000
4.2
4.0
3.8
3.6
3.4
3.2
3.0
2.8
0.74
0.72
0.70
0.68
0.66
0.64
0.62
0.00000
0.00002
0.00004
0.00006
0.00008
Sc (mm3/mm2)

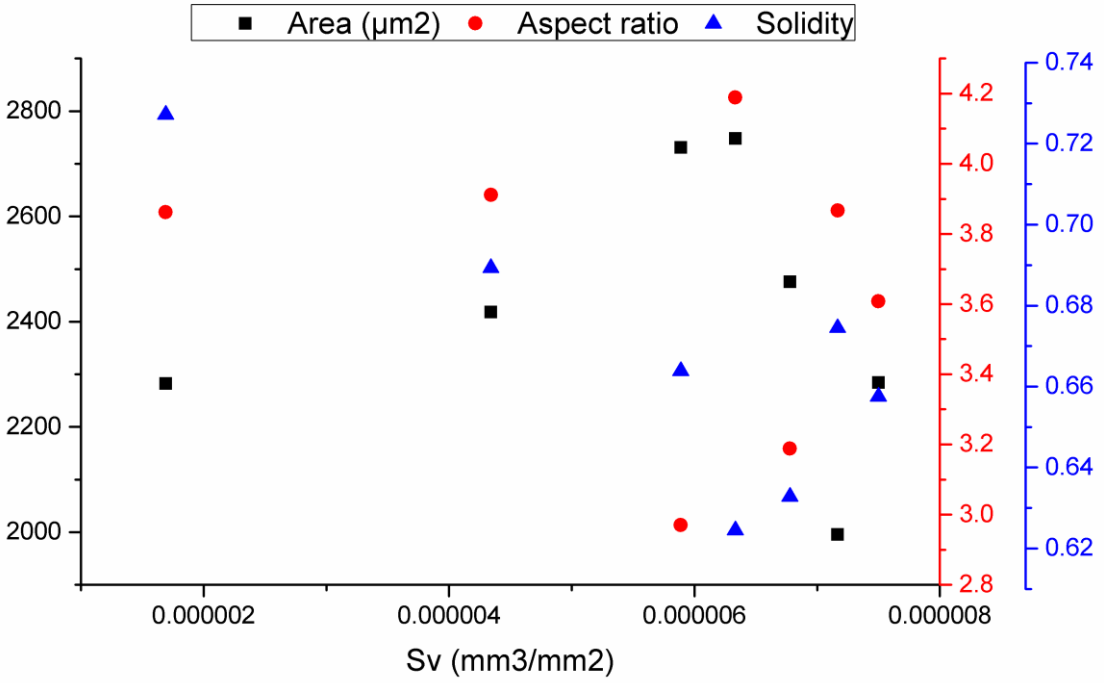
Area (μm2)
Aspect ratio
Solidity
2800
2600
2400
2200
2000
4.2
4.0
3.8
3.6
3.4
3.2
3.0
2.8
0.74
0.72
0.70
0.68
0.66
0.64
0.62
0.000002
0.000004
0.000006
0.000008
Sv (mm3/mm2)

Solidity / Area / Aspect ratio vs. micro-roughness parameters (WLI)

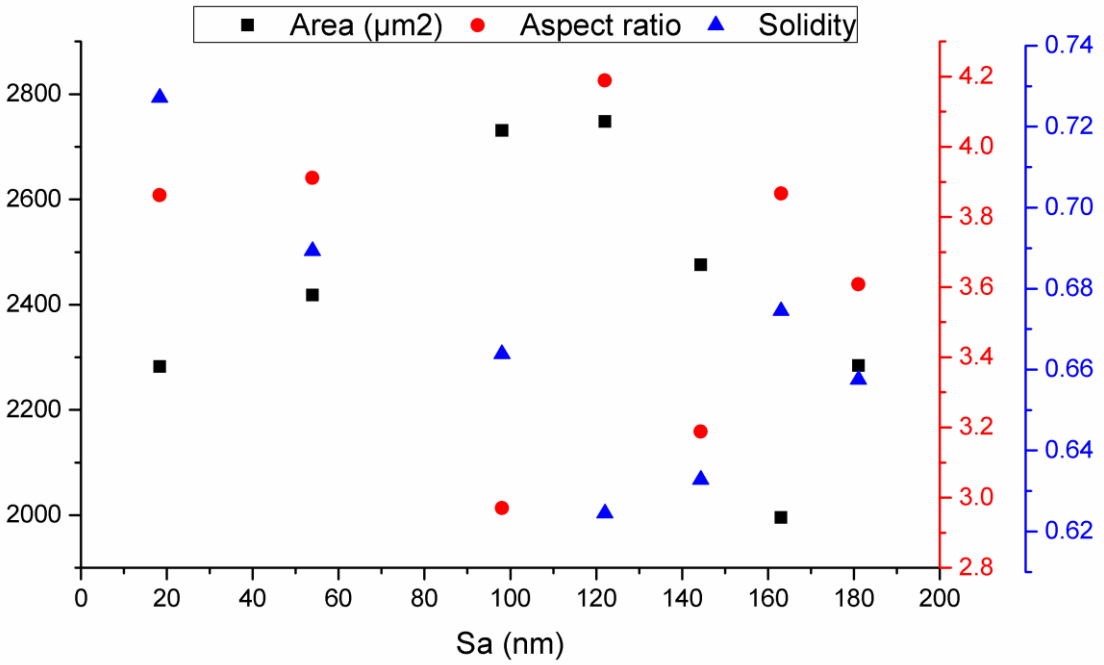

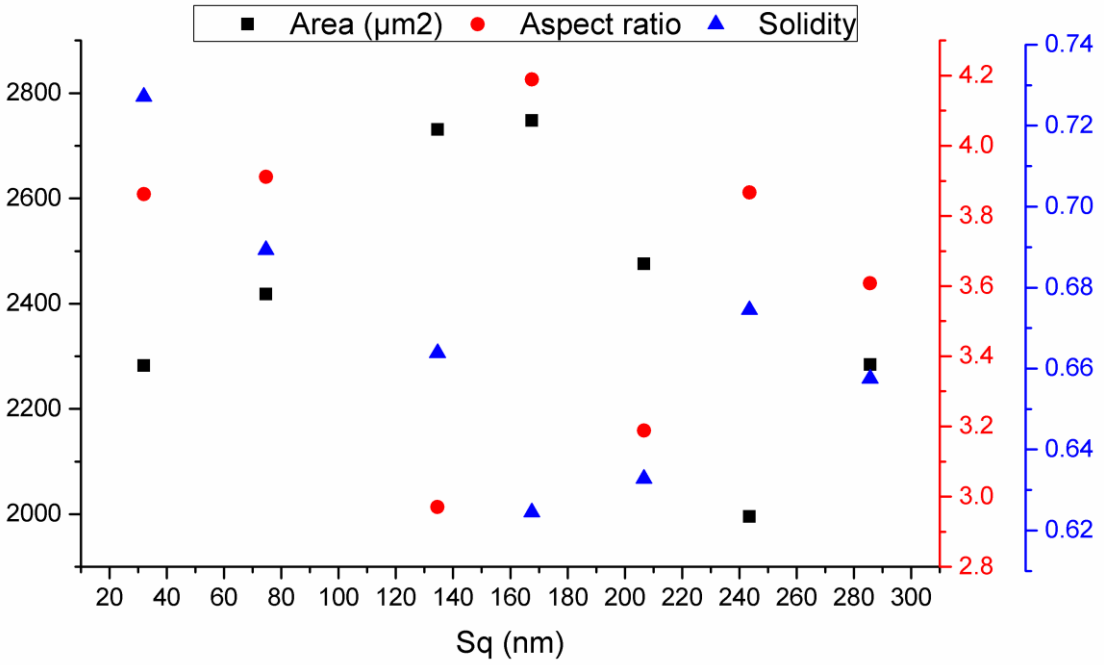

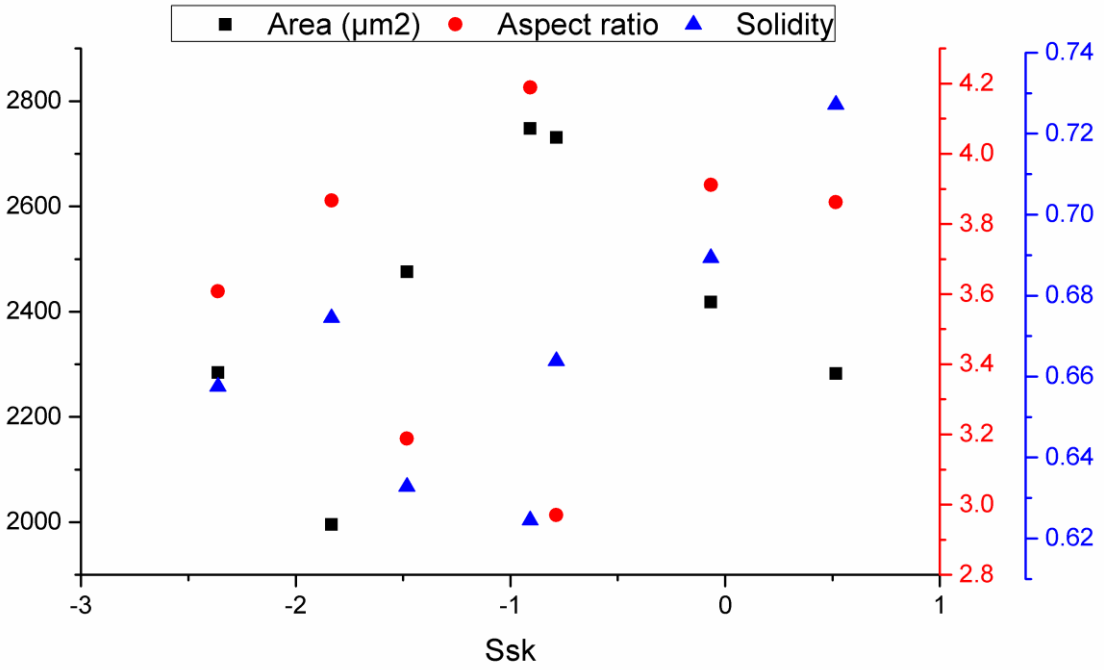
Area (μm2)
Aspect ratio
Solidity
2800
2600
2400
2200
2000
4.2
4.0
3.8
3.6
3.4
3.2
3.0
2.8
0.74
0.72
0.70
0.68
0.66
0.64
0.62
-3
-2
-1
0
1
Ssk

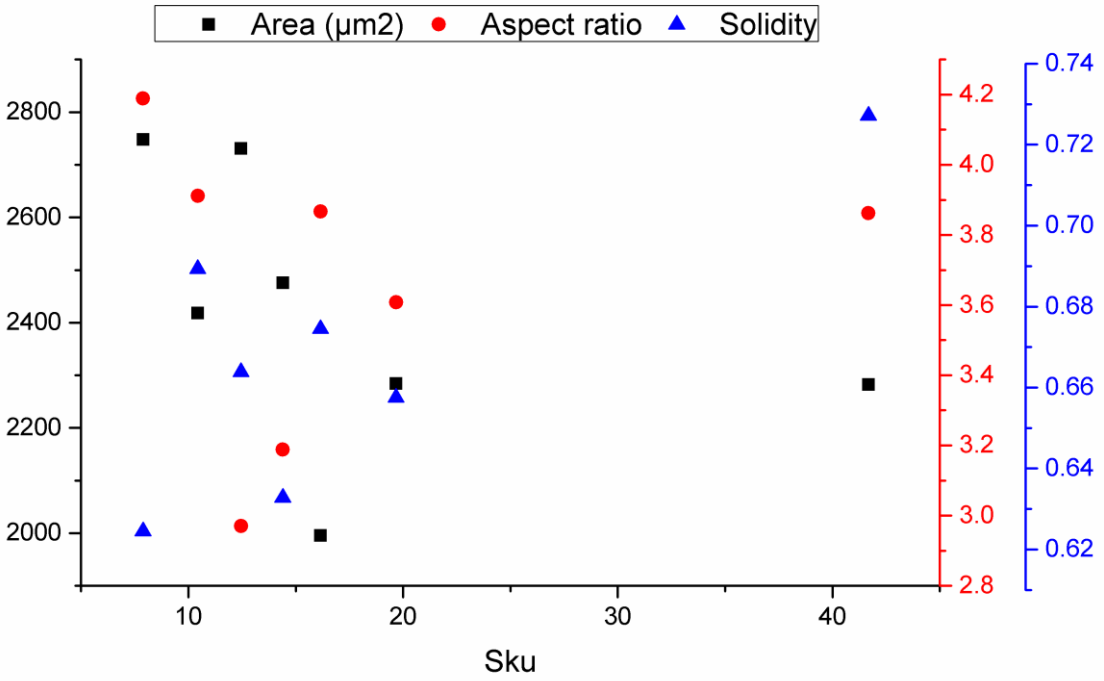
Area (μm2)
Aspect ratio
Solidity
2800
2600
2400
2200
2000
4.2
4.0
3.8
3.6
3.4
3.2
3.0
2.8
0.74
0.72
0.70
0.68
0.66
0.64
0.62
10
20
30
40
Sku

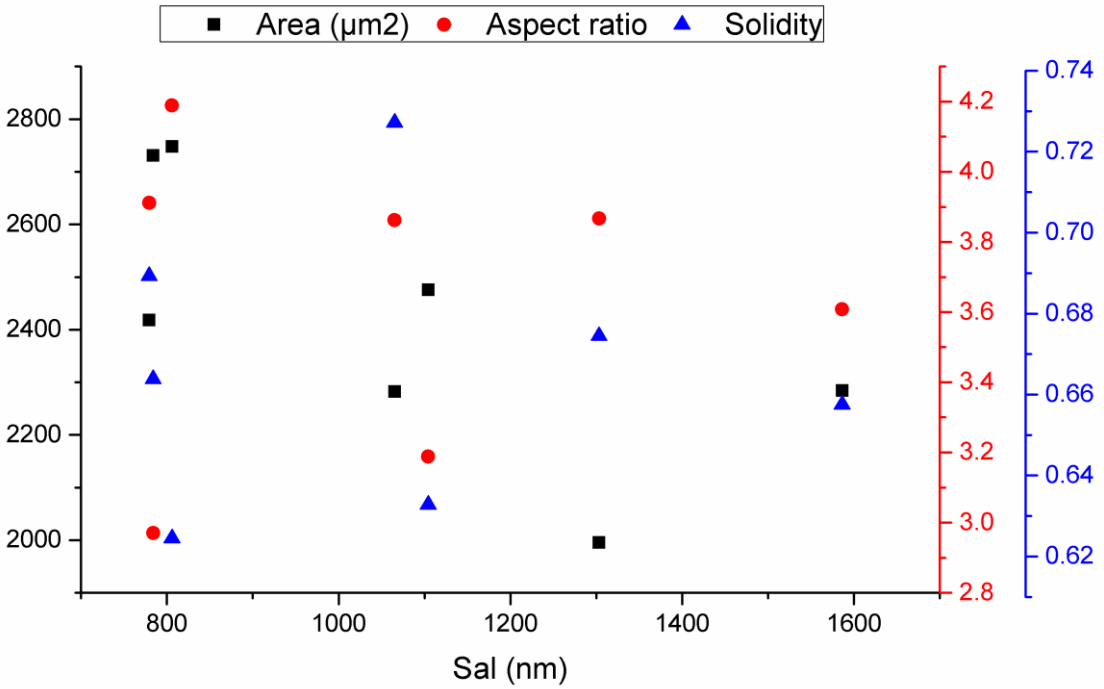
Area (μm2)
Aspect ratio
Solidity
2800
2600
2400
2200
2000
4.2
4.0
3.8
3.6
3.4
3.2
3.0
2.8
0.74
0.72
0.70
0.68
0.66
0.64
0.62
800
1000
1200
1400
1600
Sal (nm)

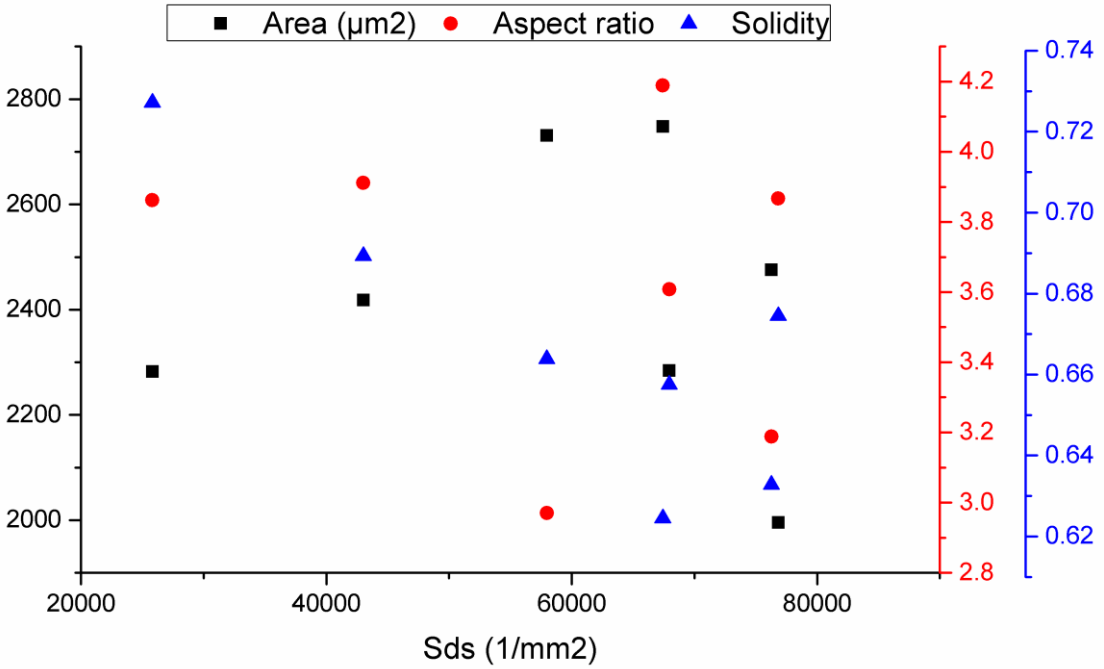
Area (μm2)
Aspect ratio
Solidity
2800
2600
2400
2200
2000
4.2
4.0
3.8
3.6
3.4
3.2
3.0
2.8
0.74
0.72
0.70
0.68
0.66
0.64
0.62
20000
40000
60000
80000
Sds (1/mm2)

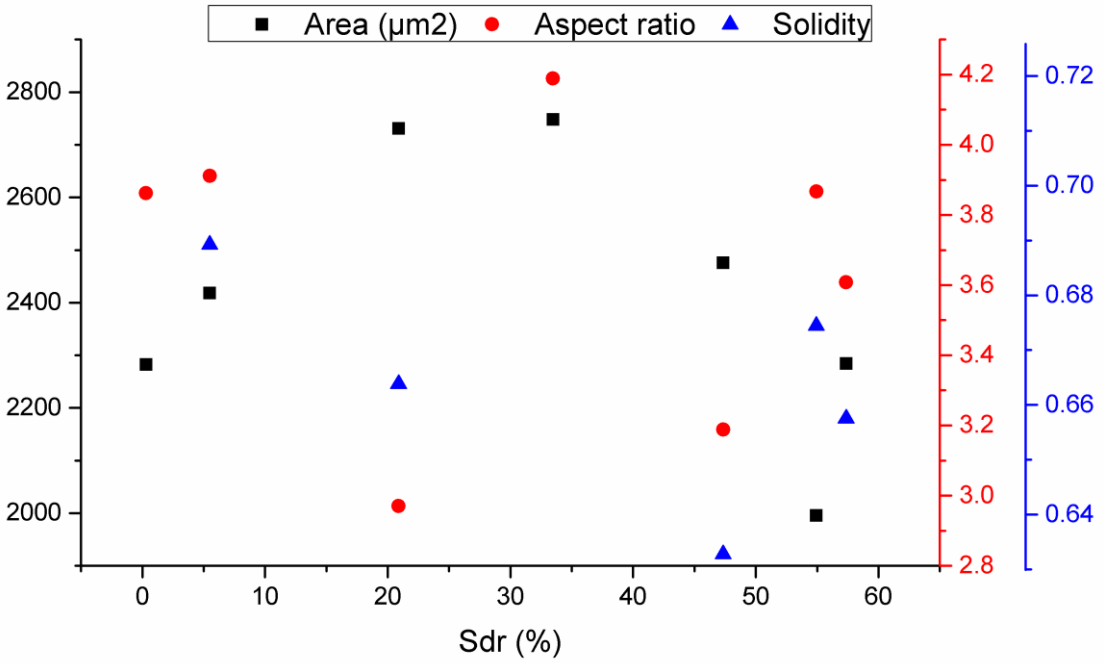
Area (μm2)
Aspect ratio
Solidity
2800
2600
2400
2200
2000
4.2
4.0
3.8
3.6
3.4
3.2
3.0
2.8
0.72
0.70
0.68
0.66
0.64
0
10
20
30
40
50
60
Sdr (%)

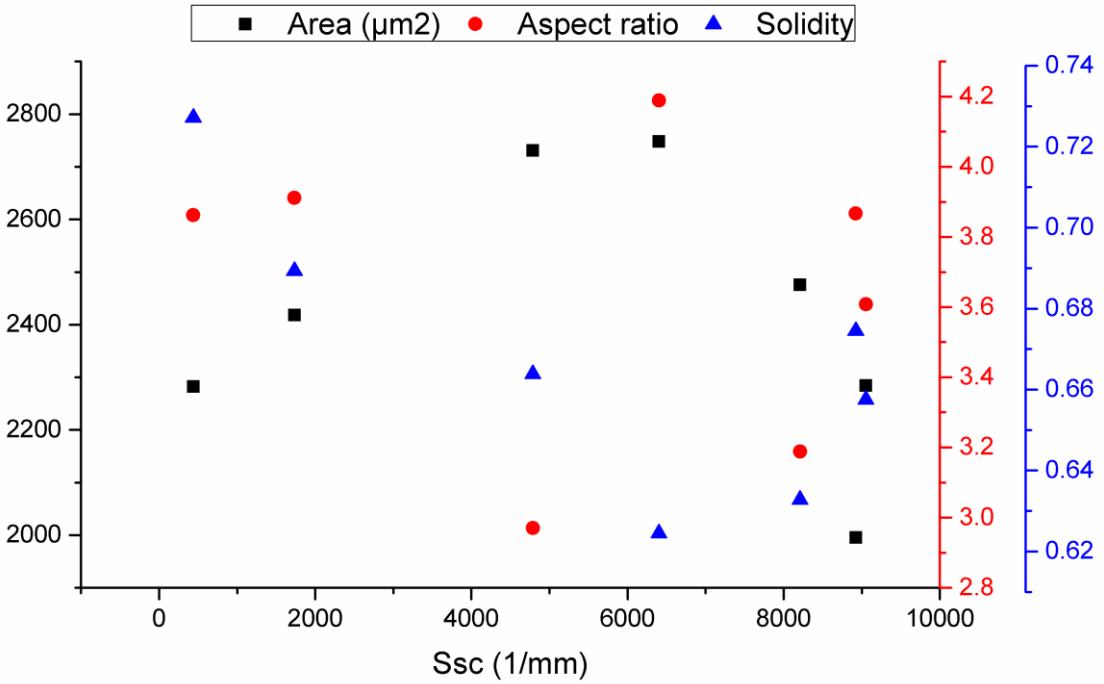
Area (μm2)
Aspect ratio
Solidity
2800
2600
2400
2200
2000
4.2
4.0
3.8
3.6
3.4
3.2
3.0
2.8
0.74
0.72
0.70
0.68
0.66
0.64
0.62
0
2000
4000
6000
8000
10000
Ssc (1/mm)

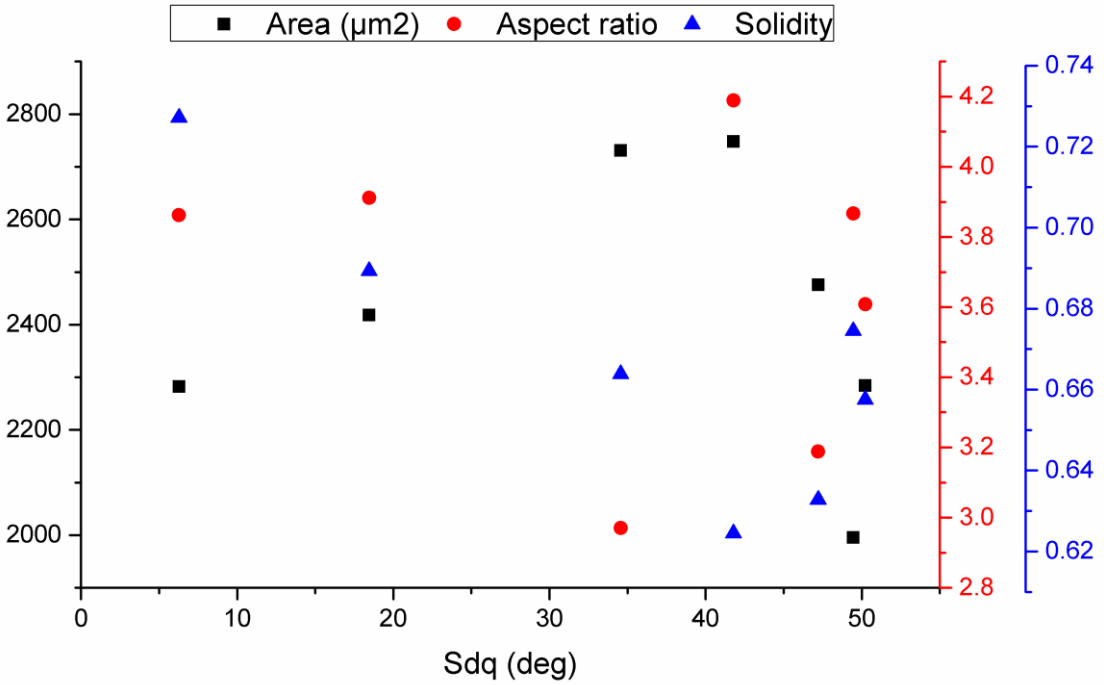
Area (μm2)
Aspect ratio
Solidity
2800
2600
2400
2200
2000
4.2
4.0
3.8
3.6
3.4
3.2
3.0
2.8
0.74
0.72
0.70
0.68
0.66
0.64
0.62
0
10
20
30
40
50
Sdq (deg)

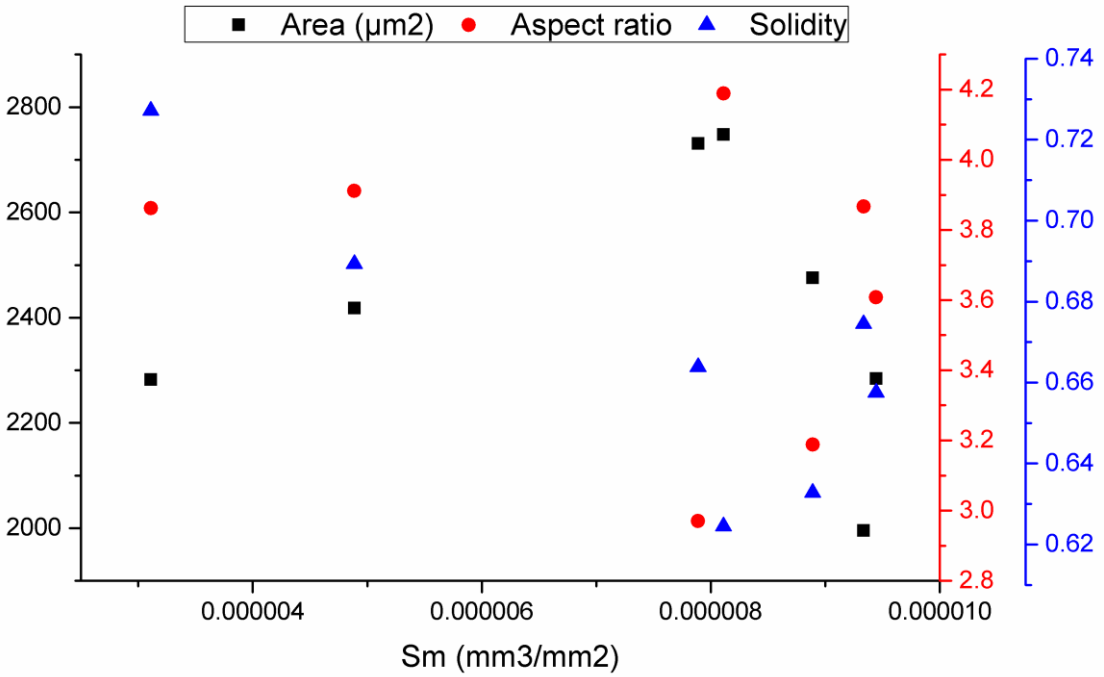
Area (μm2)
Aspect ratio
Solidity
2800
2600
2400
2200
2000
4.2
4.0
3.8
3.6
3.4
3.2
3.0
2.8
0.74
0.72
0.70
0.68
0.66
0.64
0.62
0.000004
0.000006
0.000008
0.000010
Sm (mm3/mm2)

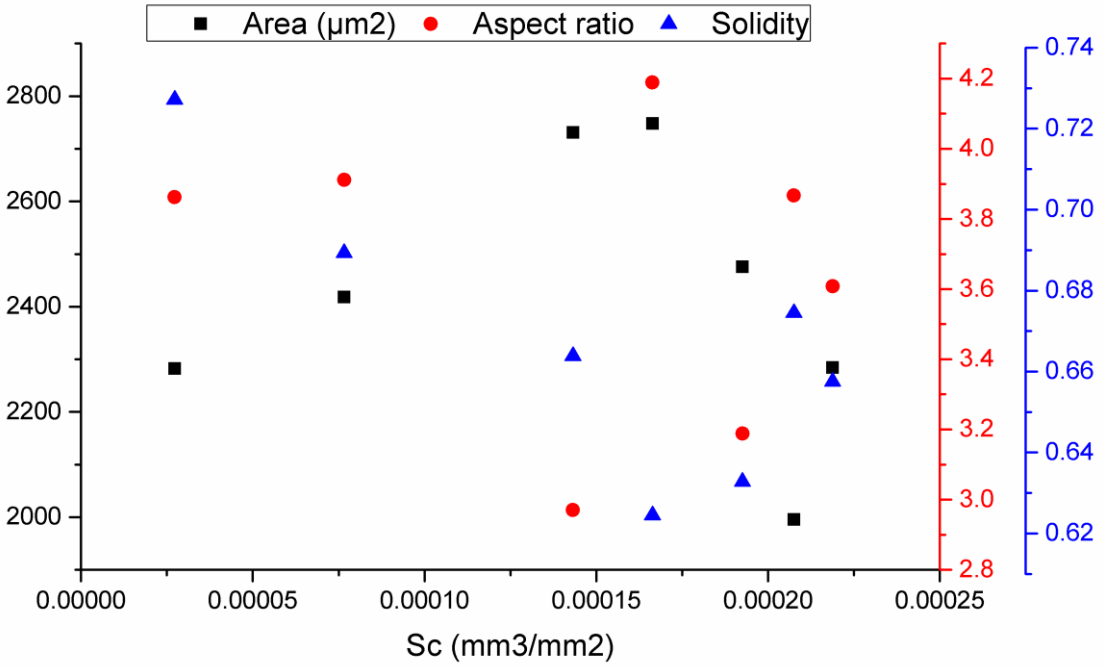
Area (μm2)
Aspect ratio
Solidity
2800
2600
2400
2200
2000
4.2
4.0
3.8
3.6
3.4
3.2
3.0
2.8
0.74
0.72
0.70
0.68
0.66
0.64
0.62
0.00000
0.00005
0.00010
0.00015
0.00020
0.00025
Sc (mm3/mm2)

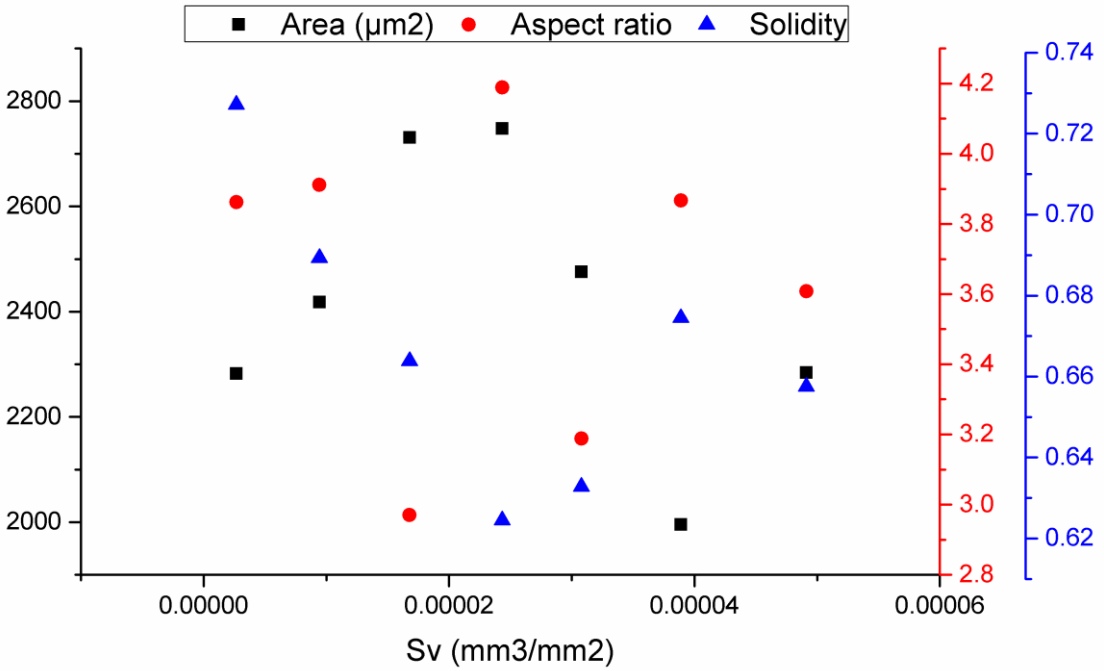
Area (μm2)
Aspect ratio
Solidity
2800
2600
2400
2200
2000
4.2
4.0
3.8
3.6
3.4
3.2
3.0
2.8
0.74
0.72
0.70
0.68
0.66
0.64
0.62
0.00000
0.00002
0.00004
0.00006
Sv (mm3/mm2)

Annex A.

Selective etching of injection molded zirconia-toughened alumina: towards osseointegrated and antibacterial ceramic implants.

1. Introduction

Zirconia-toughened alumina (ZTA) ceramics combine the advantageous properties of monolithic alumina and zirconia: they exhibit high strength, high toughness, outstanding wear resistance and excellent biocompatibility [1–4]. Thanks to these remarkable properties, in the last decade they have become the new gold standard in orthopedics for the fabrication of ceramic bearing components. In particular, in the case of hip replacements, their superior mechanical properties when compared to alumina improve the reliability and enable the manufacture of larger femoral heads and thinner liners, providing a larger range of motion in the joint [5,6].

Nevertheless ZTA is a bioinert material that does not bind directly to bone [7]. In the absence of adequate surface modification, this can lead to poor osseointegration and subsequent aseptic loosening [8]. For this reason, in current hip replacement systems, a metal shell with an osseointegrative surface needs to be placed between the acetabular bone and the ceramic liner, which restricts the maximal head diameter because of the limited anatomical space [9]. It would thus be beneficial to develop surface modification processes that enable the implantation of ZTA monoblock components in direct contact with bone.

Despite the high success rate of joint replacement surgeries, approximately 10 % of implants still fail within the first 10-20 years [10]. Infections are responsible for approximately 20 % of these failures and have become the leading cause for arthroplasty revision [11–13]. Indeed, it is well known that biomedical implants provide a substrate for the adhesion of bacteria, which can proliferate and form biofilms, dramatically increasing the resistance to therapeutic agents [14]. The so-called “race for the surface” between bacteria and host cells makes it therefore critical to eliminate or contain pathogens as early as possible [15,16] and there is a strong interest in developing surfaces that can prevent infection.

Osseointegration and infection prophylaxis are often treated as separated issues. However, as has been recently highlighted by Raphel *et al.*, they are intimately related and should be addressed simultaneously [13]. The key to achieve both objectives is an adequate surface design. On the one hand, controlling topography is crucial to obtain successful osseointegration. In particular it has been shown that rough surfaces exhibit a better bone response than smooth ones and that the combination of micro- and nano-scale roughness can have synergistic effects [17–19]. On the other hand, numerous surface engineering strategies have been explored to prevent infection. Most of them involve coatings, either to prevent bacterial adhesion or to release antibacterial agents [13].

There is little literature regarding surface modifications of ZTA ceramics, and, as discussed above, it would be highly valuable to develop processes that allow the design of implants with controlled micro- and nano-topography and antibacterial properties. Among the diverse surface micro-structuring techniques existing for ceramics, injection molding appears very promising [20]. In contrast to grinding or sandblasting for instance, it does not induce additional surface defects. Besides, it provides a high flexibility since it is theoretically possible to obtain any kind of micro-topography. Finally, it enables the mass production of complex components, which is an advantage from an industrial point of view. In the last decade, injection molding of ZTA has been successfully implemented by several authors [21–24]. However it has not yet been applied to surface micro-structuring which shows the need for further development. On the other hand, among the numerous types of coating proposed for implants, alumina with pores in the 10 nm – 200 nm range (nanoporous alumina) appears an appealing solution for the combination of osseointegrative and antibacterial properties: it can be used as a carrier for drug delivery [25–28] and *in vitro* studies have suggested that thanks to its nano-structure it could improve osteoblast adhesion and proliferation, increase matrix production and induce osteogenic differentiation [29–31]. Nevertheless, coatings present several disadvantages; in particular they induce residual stresses and risks of delamination, which may lead to implant failure.

Long-term reliability is a major concern for orthopedic implants, and ceramics can be sensitive to surface alterations. In particular surface defects have a strong influence on their strength [32]. Furthermore, even a moderate porosity can have a substantial impact on their elastic modulus, strength and resistance to contact damage [33–35]. Finally, zirconia-containing ceramics require special attention: the tetragonal to monoclinic phase transformation, which accounts for their exceptional toughness, can occur spontaneously at low temperature in the presence of water, potentially deteriorating the material properties [36,37]. The kinetics of this phenomenon, known as low temperature degradation (LTD) or ageing, are highly sensitive to processing changes, as attested by the failure of Prozyr® zirconia femoral heads in 2002 [38]. Even if ZTA is much more resistant to LTD than monolithic zirconia, it has been shown that it can still present a certain degree of surface tetragonal to monoclinic phase transformation in the presence of water [39–41]. All these elements lead to the following conclusion: to ensure long-term reliability and patient safety, any change in the processing of zirconia-containing ceramics should be accompanied with a careful assessment of its impact on mechanical properties and ageing sensitivity, especially in the presence of porosity.

To address the issues mentioned above, here we develop new methods for the fabrication of ZTA ceramics with surface properties tailored for promoting osseointegration and preventing infections. Samples with a controlled micro-topography were obtained by injection molding and a novel process, based on the selective dissolution of the zirconia phase (selective etching), allowed the induction of nano-roughness and the formation of an interconnected porous alumina layer. A careful assessment of the impact of selective etching on mechanical properties and ageing sensitivity was conducted and a proof of concept that the porous layer can be used as a carrier for drug delivery was demonstrated.

2. Materials and methods

2.1. Fabrication of samples with a controlled micro-topography by injection molding

The ZTA composites produced in this study consisted of an alumina matrix (80 vol. %) containing a small amount of chromia (about 0.3 wt. %) reinforced with a secondary phase composed of yttria-stabilized zirconia (Y-TZP, 17 vol. %) and $SrAl_{12}O_{19}$ platelets (3 vol. %). A powder mixture containing alumina, zirconia, strontia, chromia and yttria was prepared by wet milling and spray drying (similar to commercial processing). The plastic feedstock, which contained an organic binder system content (proprietary, confidential composition) of approximately 45 vol. %, was homogenized using a shear roller plant. Green bodies in the shape of disks were obtained by injection molding and subsequently subjected to a three-step heat treatment: sintering, hot isostatic pressing and whitening (final disk diameter: 20 mm, final disk thickness: 2 mm). To achieve different micro-topographies, the surfaces of three molds were sandblasted with increasing impact energy. The resulting surfaces, ordered from smoothest to roughest, will be referred to as “low”, “medium” and “high” in the rest of the manuscript. Additionally, a batch of samples injected in a flat mold and a batch of polished samples were produced. The back surface of all disks was ground in order to remove the “gate”, which is inherent to the injection molding process.

2.2. Generation of nano-roughness and interconnected porosity by selective etching

Specimens obtained by injection molding were successively cleaned by sonication in acetone, ethanol and deionized water in order to remove contaminants. Based on the fact that zirconium dioxide can be dissolved in hydrofluoric acid (HF) [42] while α-alumina is highly resistant to HF [43], a selective removal of the zirconia phase was achieved by immersing the samples in concentrated HF (Hydrofluoric Acid 40% QP, Panreac, Spain) at room temperature

for times comprised between 6 h and 12 days. Each sample was placed in an individual high-density polyethylene flask with 4 mL of solution. After etching, the samples were rinsed and sonicated in deionized water. The formation of fluoride precipitates, which remained trapped into the pores, was detected when observing the surface by scanning electron microscopy (SEM). To dissolve them, the specimens were immersed in 8 mL of concentrated HCl (Hydrochloric acid 37%, Panreac, Spain) for 1 h. As will be discussed later, monitoring etching time made possible to obtain either a superficial removal of zirconia, inducing nano-roughness, or an in-depth removal which resulted in the formation of both nano-roughness and interconnected porosity in a surface layer.

2.3. Surface characterization

2.3.1. Surface morphology

The surface morphology of polished and micro-rough specimens was observed by SEM after the main steps of the fabrication process (sintering, etching in HF, dissolution of the reaction precipitates in HCl).

2.3.2. Surface topography

White light interferometry (WLI, Veeco Wyko 9300NT) and atomic force microscopy (AFM Veeco Dimension 3100) in tapping mode were used to characterize micro- and nano-topography, respectively. WLI measurements were performed on ten polished specimens and ten micro-rough specimens for each type of injection mold surface (area of observation: 150 µm x 150 µm obtained by stitching of four images acquired at magnification 50x, resolution: 758 x 758 pixels). AFM measurements were performed on five polished samples before and after selective etching (area of observation: 50 µm x 50 µm, resolution: 512 x 512 pixels). The roughness analysis of the data from WLI and AFM was carried out using Veeco's Vision® software. Tilt was corrected and a robust short wavelength pass Gaussian filter was applied to the data in order to separate waviness from roughness. The cut-off wavelength of the filter was set to 10 µm for WLI and 1 µm for AFM. In order to fully characterize the topography, one 3D roughness parameter of each of the usual categories was determined as recommended by Wennerberg *et al.* [44,45] (Table 1). Considering the cut-off wavelengths and the lateral resolutions (micrometric for WLI, nanometric for AFM) associated to each device, the roughness measurements obtained from AFM data analysis will be referred to as “nano-roughness” whereas the measurements obtained from WLI data will be referred to as “micro-roughness”.

Table 1. Description of the 3D roughness parameters used in this study [46–48]

Symbol	Category	Name of the parameter	Description
S_a	Amplitude	Average roughness	Average of height values
S_{ds}	Spatial	Density of summits	Number of summits per unit area
S_{dr}	Hybrid	Developed interfacial area ratio	Percentage of additional surface area contributed by the texture as compared to an ideal plane the size of the measurement region
S_{ci}	Functional	Core fluid retention index	Measure, relative to S_q (RMS roughness), of the volume (for example, of a fluid filling the core surface) that the surface would support from 5% - 80% of the bearing ratio

2.3.3. Surface chemistry

To determine the influence of selective etching on the elemental composition and the chemical state of the surface, three samples were subjected to X-ray photoelectron spectroscopy (XPS) after respectively: sintering, etching in HF (4 days) and immersion in HCl. The analysis was conducted using a SPECS system equipped with an Al anode XR50 source operating at 150 W and a Phoibos 150 MCD-9 detector XP. Spectra were recorded with pass energy of 25 eV, 0.1 eV steps and a pressure below 7.5×10^{-9} mbar. Binding energies were referred to the adventitious C1s signal and background was subtracted. The identification of the local bonding environment of each element was performed by comparing the experimental peak positions with the data from the NIST Standard Reference Database 20, Version 4.1 (http://srdata.nist.gov/xps/).

2.3.4. Porous layer thickness

To monitor the evolution of the interconnected porous layer produced by selective etching over time, polished samples were cross-sectioned (two samples per time point). For short times (6 h, 1 day and 2 days), which resulted in thin layers, 10 µm wide transversal sections were milled with a Focused Ion Beam (FIB, Neon40, Carl Zeiss AG, Germany). Sample surfaces were protected with a thin platinum coating to flatten the surface and minimize ion-beam damage and

curtain effect during milling. The final polishing of the cross-sections was performed at 500 pA. For long times (4 days, 8 days, 12 days), which resulted in thick layers, full cross-sections were obtained by cutting the entire specimens with a diamond wheel. The transversal sections were ground and polished down to a 3 µm diamond suspension and subsequently observed by SEM. The mean value and standard deviation of the thickness of the layer for each individual sample were computed using the ImageJ software.

2.3.5. 3D microstructure

To characterize the interconnected porosity induced by selective etching, a stack of 50 transversal section images (width: 15 µm, height: 10 µm, spacing: 20 nm) was obtained by automatizing the FIB milling procedure described in 2.3.4. Alignment, segmentation and 3D reconstruction of the stack were performed using the Avizo® software (FEI Software, Hillsboro, Oregon) with a voxel size of 16 nm x 16 nm x 20 nm. The porous structure was skeletonized using Avizo® XSkeleton Pack to determine the distribution of the local radius, which is a measurement of the distance to the nearest boundary at every point of the skeleton. The results were used to estimate the pore size.

2.4. Porous layer as a carrier for drug delivery

To demonstrate that the porous layer produced by selective etching could be used as a carrier for drug delivery, micro-rough samples (with the "medium" topography) were subjected to selective etching for times comprised between 4 and 12 days to achieve different porous layer thicknesses. The antibiotic gentamicin, commonly used in orthopedic surgery for systemic application or local delivery, was loaded either in solution or encapsulated in liposomes.

2.4.1. Preparation of the gentamicin solutions and the gentamicin-loaded liposomes

Solutions of the gentamicin sulfate at 10 mg/mL (stock solution), 100, 50, 25, 10, 5, 2.5 and 1 µg/mL were prepared by dissolution and successive dilutions in phosphate buffered saline (PBS). Unilamellar gentamicin-loaded liposomes were prepared by evaporation of the chloroform from a lipid solution at 50 mg/mL of DPPC (1,2-dipalmitoyl-sn-glycero-3-phosphocholine, phase transition temperature: 41 °C) under nitrogen for 1 h, followed by hydration with 10 mg/mL gentamicin solution. The solutions obtained were extruded through 100 nm filters (9 times) and 50 nm filters (11 times) to obtain liposomes with a monodisperse diameter close to the pore size, and subsequently passed through Sephadex® G-25 columns to remove excess non-loaded antibiotic. About 20 % of the initial gentamicin quantity was encapsulated. Solutions were reconcentrated using Amicon® Ultra Centrifugal Filter Units

(MWCO 100 kDa), and the volume was adjusted with PBS to obtain liposomes with a lipid concentration of 1 mg/mL.

2.4.2. Loading procedure

The loading of the gentamicin into the ZTA samples was performed in 12-well culture plates. The samples were placed in wells with 1.5 mL of either a gentamicin solution at 100 µg/mL or a gentamicin-encapsulated liposome solution at 1 mg/mL DPPC, and left overnight on a shaking plate (50 cycles/min). The samples were rinsed three times in PBS after loading.

2.4.3. In vitro drug release experiments

In vitro drug release experiments were carried out in duplicate in 12-well culture plates at 37 ºC. Each sample loaded with gentamicin or gentamicin-encapsulated liposomes was placed into an individual well with 3 mL of PBS. For each time point an aliquot of 500 µL was taken from the solution and replaced by 500 µL of fresh PBS. Gentamicin was quantified by adapting an existing method [49–51]. An *o*-phtaldialdehyde reagent (OPA reagent) was formulated by adding 0.8 g *o*-phtaldialdehyde, 20 mL methanol and 0.96 mL 2-mercaptoethanol to 180 mL of 40 mM sodium borate in distilled water. Aliquots of the solution to analyze were mixed in equal proportions with isopropanol and OPA reagent. Fluorescence readings were carried out in duplicate in 96-well plates with a SpectraMax M5 microplate reader (Molecular Devices, USA; excitation wavelength: 340 nm; emission wavelength: 455 nm). For each plate a calibration curve was obtained from gentamicin solutions at 100, 50, 25, 10, 5, 2.5 and 1 µg/mL. A kinetic study of the reaction indicated that 5 min was a suitable time for the reading and that the presence of DPPC did not interfere with the measurement. To determine the cumulative release profiles, correction factors were applied in order to take into account the evaporation of the solution in the well and the replacement of aliquots by fresh PBS, and the total quantity released was divided by the average total sample surface area (7.9 cm^2).

2.4.4. Assessment of antibacterial properties against E. coli

Table 2. Nomenclature of the sample groups used for the assessment of antibacterial properties

Name	Surface treatment
Control	None
Etched	Selective etching (4 days)
Etched+Loaded	Selective etching (4 days) + loading with gentamicin-encapsulated liposomes

Based on the *in vitro* release experiments, loading with gentamicin-encapsulated liposomes was selected as the best method to test antibacterial properties against *E.coli*, which is the most frequently isolated microorganism from gram-negative periprosthetic joint infections [52–54]. Three types of samples were prepared as described in Table 2. A small amount of a glycerol stock of *E. coli* (strain: Rosetta(DE3)pLysS, Novagen) was incubated in LB medium at 37 ºC under constant shaking overnight. The suspension was subsequently diluted to $2x10^7$ cells/mL in fresh medium. Samples were incubated in 3 mL of this bacterial suspension for 4 h at 37 ºC in 12-well culture plates. To evaluate bacteria concentration, 1 mL aliquots were taken from the supernatants for flow cytometry (Fortessa, BD Biosciences) and fixed with 2 % paraformaldehyde (PFA) in PBS. To assess bacterial adhesion and viability on the different surfaces, staining solutions were prepared in individual wells by adding 3 µL of SYTO® 9 and 3 µL of ethidium bromide to 2 mL of a NaCl aqueous solution at 0.85 wt%. The samples were rinsed with the NaCl solution three times and then immersed in the staining solutions for 15 min at 37 °C. Fluorescence imaging of the stained samples was carried out on a confocal microscope (Leica SP5, Leica Microsystems, Germany) with a 20x dry objective. Measurements of surface area covered by living *E. coli* cells were carried out using the ImageJ software (three images per specimen).

2.5. Contact behavior and mechanical properties of the porous layer

2.5.1. Experiments

For the study of the mechanical properties and local contact behavior of the porous layer produced by selective etching, two polished samples were fabricated and one of them was selectively etched for 12 days (thickness of the porous layer: 27 µm). Instrumented nanoindentation tests were carried out with a MTS Nanoindenter XP equipped with a continuous stiffness measurement (CSM) module and a diamond spherical tip (nominal radius: 50 µm). Due to the difficulty to machine diamond at such a small scale, the real shape of the tip can differ substantially from a perfect sphere. For this reason, the real tip shape was measured by AFM. A Python script was developed and used to extract the curve $a = f(h_c)$ with a the contact radius and h_c the contact depth, which was fitted with a power law of the type $a = A + B \times {h_c}^C$. The best fitting parameters were adjusted by performing calibration tests against reference materials with well-known elastic moduli (pyrocarbon, fused silica and tungsten, see supplementary information).

Indentations of the porous layer were performed up to a maximum load of 7.5 N (maximum indentation depth: ~ 3.5 µm) and under a constant deformation rate of 0.05 s^{-1} with

an inter-indentation spacing of 100 µm (3x3 arrays). At maximum penetration, the circular contact area was very large in comparison to the pore size (contact radius: ~ 17 µm). The contact point was corrected implementing the method proposed by Moseson *et al.* [55] and the polished sample was used as a reference for stiffness correction. The models chosen to interpret analytically the indentation data were those of Hertz, Oliver and Pharr and Tabor, following the approach of He and Swain [56].

Finally, profiles of residual indents were measured with a laser scanning confocal microscope (Olympus LEXT) and a FIB cross-section of an indentation was realized in order to identify the deformation mechanism of the porous layer under compression and to detect potential damage and densification.

2.5.2. Numerical analysis

Based on previous works on porous ceramics [57,58], an inverse finite element (FE) analysis was used to identify the properties of the porous layer. Lowest, average and highest experimental load-displacement curves were used for the identification, and the plateau separating loading and unloading sections was removed. The FE simulation was carried out using the ABAQUS/Standard software (Dassault Systèmes, Simulia, Vélizy-Villacoublay, France). The model consisted of a 2D axisymmetric mesh (available in supplementary information) which contained approximately 6000 elements (CAX8 and CAX8-R) and was refined towards the contact zone with an element size of about 0.5 µm. Loading was achieved by imposing a quasi-static vertical displacement ("hard contact", sliding formulation: finite sliding, discretization method: surface to surface). The indenter and the bulk of the sample were modeled as elastic materials, whereas the porous layer was modeled using a modified Drucker-Prager/cap-plasticity criterion which accounts for hydrostatic pressure sensitivity of material failure through two surfaces: the Drucker-Prager surface for shear failure and the cap surface for high hydrostatic pressure failure [59] (see Appendix D for the definition of the model and of the related parameters). The increase in elastic modulus associated to densification of the porous material was taken into account using ABAQUS user subroutine USDFLD (time increment was kept small enough to maintain the accuracy of the solution).

The inverse identification was carried out using the MIC2M software (http://mic2m.univ-fcomte.fr/). The Poisson ratio v of the porous layer was set to 0.22 (taken from literature for porous alumina [35]), the cap eccentricity R was set to 0.25 to obtain a cap yield surface neither too circular nor too steep, α (a small number used to define the transition yield surface) was set to 0.01 and W (the porous volume fraction) was set to 0.17. A preliminary calculation showed that

variation of the friction coefficient *f* between the indenter and the sample surface had negligible effect on the results and *f* was set to 0.1. The parameters to identify were the elastic modulus of the porous layer (*E*), the yield stress in simple compression (σ_c), the angle of friction (β), the initial hydrostatic compression yield stress (p_{b0}) and the maximum plastic volumetric strain rate (*D*).

2.6. Impact of selective etching on strength and ageing kinetics

Table 3. Nomenclature of the sample groups used for strength and ageing kinetics testing

Name of the group	Surface treatment
As sintered (AS)	None
Polished+Annealed (P+A)	Polishing + Annealing (1200 ºC, 10 min)
As sintered+Etched (AS+E)	Selective etching (4 days)
Polished+Annealed+Etched (P+A+E)	Polishing + Annealing (1200 ºC, 10 min) + Selective etching (4 days)

To assess the impact of selective etching on strength and ageing sensitivity, 48 flat samples were fabricated. Half of them were polished down to a 1 μm diamond suspension and annealed at 1200 °C for 10 min in air using heating and cooling rates of 5 °C/min, and they were divided into four groups as described in Table 3. The polishing was introduced to remove surface defects and the annealing to remove residual stresses. The annealing temperature was chosen based on a preliminary study involving an indentation technique [60] in which 1200 °C was found to be the minimum annealing temperature capable of removing the majority of residual stresses without affecting significantly the grain size. The etching time was chosen to be the same as for the testing of antibacterial properties (2.4.4), and the thickness of the porous layer was measured by performing cross-sections on three samples from each etched group (same procedure as described in 2.3.4).

2.6.1. Biaxial flexural strength testing

The biaxial flexural strength of ten samples from each group was assessed by 3-balls-on-3-balls testing with a "sphere-in-line" configuration. The specimens were tested in a universal testing machine (Model 8502, Instron Corp., Canton, USA) in air up to fracture of the specimen,

using a constant test speed of 0.5 mm/min. The radius of the inner sphere location circle was $R_1 = 4.08$ *mm* and the ratio of outer to inner sphere circles was $R_1/R_2 = 2$. The fracture strength was calculated using a numerical approximation of the maximum tensile stress:

$$\sigma_{max} = f \times \frac{F}{t^2} \qquad (1)$$

where *F* is the applied load on failure, *t* the sample thickness and *f* a dimensionless factor. For $R/R_1 = 2.25$ (*R* being the diameter of the test samples), *f* can be calculated with the following formula [61]:

$$f = 0.656\left(\frac{t}{R_1}\right)^{-0.196} + 0.274\left(\frac{t}{R_1}\right)^{-0.448} \times \nu \qquad (2)$$

where *t* is the thickness of the sample and *v* is the Poisson ratio. In the present study, $R/R_1 = 2.45$, nevertheless it is still possible to use equation (2) with an error inferior to 5 % [62].

Statistical analysis of the strength testing results was performed using SPSS® software (version 20, SPSS Inc., Chicago, IL, USA). A two-way ANOVA with a 5% significance level was used to evaluate the effects of polishing and selective etching. The data was log-transformed prior to analysis. The normality and the homogeneity of variances were verified with respectively a Shapiro-Wilk test and a Levene test.

The variability of the strength was analyzed using the Weibull distribution function:

$$P_F(\sigma) = 1 - \exp\left(-\left(\frac{\sigma}{\sigma_0}\right)^m\right) \qquad (3)$$

where P_F is the cumulative probability of failure, σ is the fracture strength, σ_0 is the Weibull characteristic strength, and *m* is the Weibull modulus. For the evaluation of *m* and σ_0 the measured strength data were ranked in increasing order and numbered from 1 to *N*. Then the single strength values σ_i were related to the failure probability P_{Fi} according to the following relation:

$$P_{Fi} = \frac{i-0.5}{N} \qquad (4)$$

where *i* is the ranking number and *N* is the total number of measurements (for a more detailed description of the methodology, see for instance Munz *et al.* [63]). Finally, the 90% confidence bounds for *m* and σ_0 were determined according to ASTM C1239-00.

2.6.2. Ageing kinetics

Two samples from each group were subjected to hydrothermal degradation tests. The tests were performed in an autoclave, at 134 ºC, 100% steam atmosphere at 0.2 MPa pressure for times up to 600 h. This time is far beyond the requirement of 10 h recommended by the ISO 6474-2 standard and according to [41] it is equivalent to about 1500 years at 37 ºC. It is thus extremely conservative but monitoring the long-term evolution of the monoclinic phase content allows amplifying potential differences between groups. The specimens were analyzed by X-ray diffraction (XRD) (Model D8, Bruker AXS, Madison, USA) using Cu-K_α radiation to detect and quantify the tetragonal–monoclinic transformation. The monoclinic fraction was determined using the relation proposed by Toraya *et al.* [64]:

$$V_m = 1.311 \frac{I_m(\bar{1}11)+I_m(111)}{I_t(101)+1.311[I_m(\bar{1}11)+I_m(111)]} \qquad (5)$$

where V_m is the monoclinic volume fraction, $I_m(\bar{1}11)$ and $I_m(111)$ are the intensities of the monoclinic peaks and $I_t(101)$ is the intensity of the tetragonal peak.

3. Results

3.1. Surface characterization of injection molded and selectively etched samples

3D topographical images obtained by WLI showed that injection molded ZTA samples presented very diverse micro-topographies (Figure 1). Furthermore, the micro-roughness analysis showed that a large range of values could be obtained for the average roughness (S_a comprised between 175 nm and 415 nm) and the developed interfacial area ratio (S_{dr} comprised between 45 % and 100 %).

Regarding selective etching, the zirconia phase was successfully removed by immersion in HF whereas neither the alumina matrix nor the $SrAl_{12}O_{19}$ platelets were affected, which allowed the integrity of the micro-topography obtained by injection molding to be preserved (Figure 2). The formation of fluoride precipitates, which remained trapped in the pores of the surface, was detected. Energy dispersive spectroscopy evidenced that they were mainly composed of yttrium and fluorine. Some of them had an octahedral shape suggesting the presence of YF_3 crystals, similar to those observed when etching Y-TZP [65]. XPS analysis confirmed the presence of YF_3 chemical bonds and additionally suggested the existence of zirconium oxyfluorides (Table 4). Inspection of the specimens by SEM evidenced that all precipitates were successfully removed by immersion in HCl (Figure 2).

The selective etching process induced a substantial increase in nano-roughness (Figure 3). Indeed, the average roughness (S_a) was multiplied by 10 with respect to the polished surface

and the developed interfacial area ratio (S_{dr}) was multiplied by 100. In terms of surface chemistry, the most notable changes were an increase in the fluorine content and a decrease in the zirconium content (Figure 4).

The thickness of the layer affected by selective etching depended on etching time (Figure 5-a,c). During a short time period (t = 6 h), only the superficial zirconia grains were dissolved, leaving the bulk unaffected. For longer etching times (t ≥ 24 h), an interconnected porous layer was produced. The FIB/SEM tomography provided evidence that with the exception of some isolated grains the zirconia phase was percolated (Figure 5-b). The local radius distribution appeared to be centered at approximately 50 nm with a maximum at 160 nm, which can be considered as the maximal pore size (Figure 5-d). It was not possible to determine the minimum of the distribution with certainty because of the limit of resolution fixed by the voxel size.

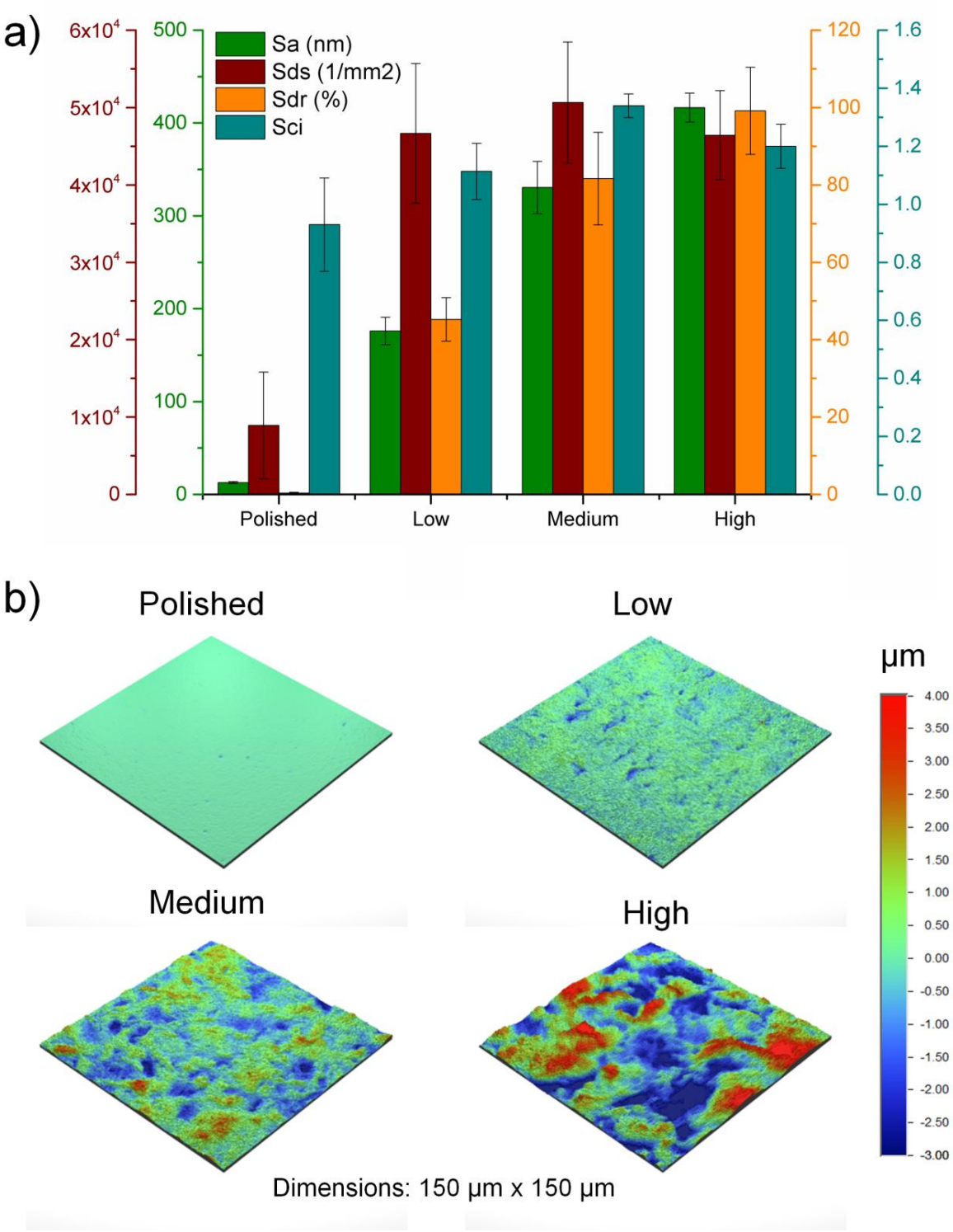

Figure 1. White light interferometry measurements at the surface of injection molded zirconia toughened alumina samples with different induced micro-topographies: a) roughness analysis; b) 3D topographical images. "Low", "Medium" and "High" designate micro-topographies obtained from increasingly rough molds.

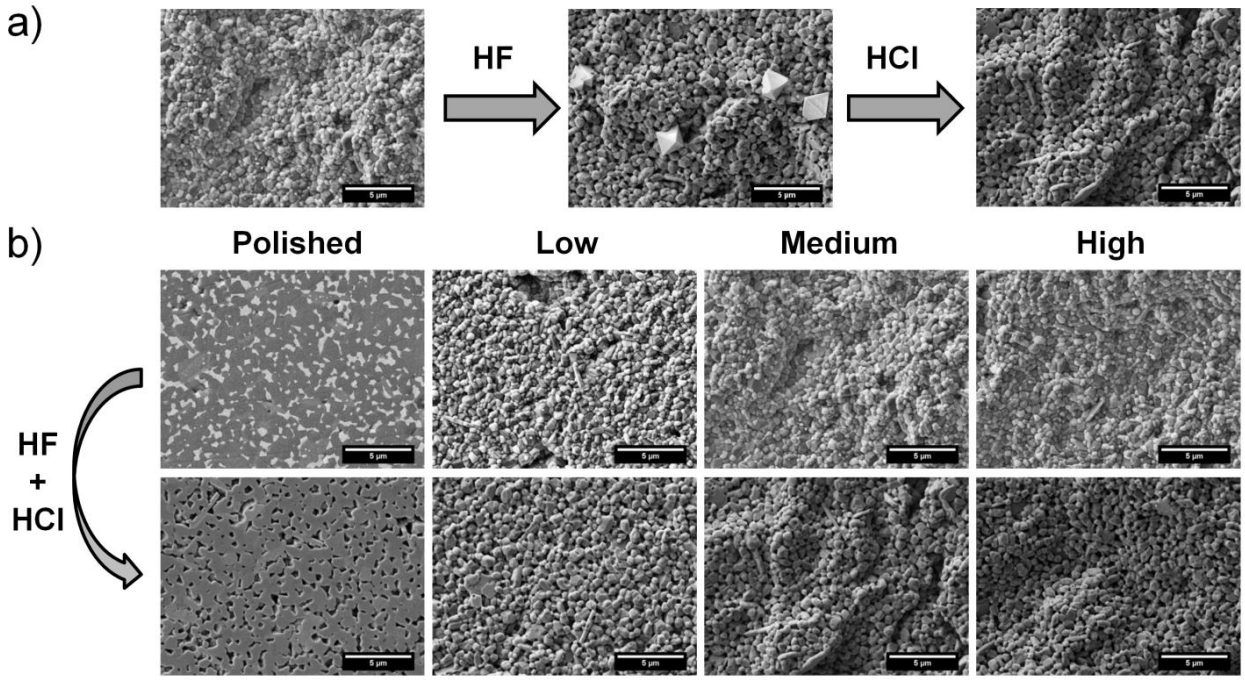

Figure 2. a) Scanning electron microscopy observations of the surface of zirconia toughened alumina at the different steps of the selective etching process, evidencing the formation of fluoride precipitates during HF etching and their subsequent removal in HCl; b) scanning electron microscopy observations of the surface of injection molded samples with different micro-topographies before and after selective etching. "Low", "Medium" and "High" designate micro-topographies obtained from increasingly rough molds. Scale bars: 5 µm.

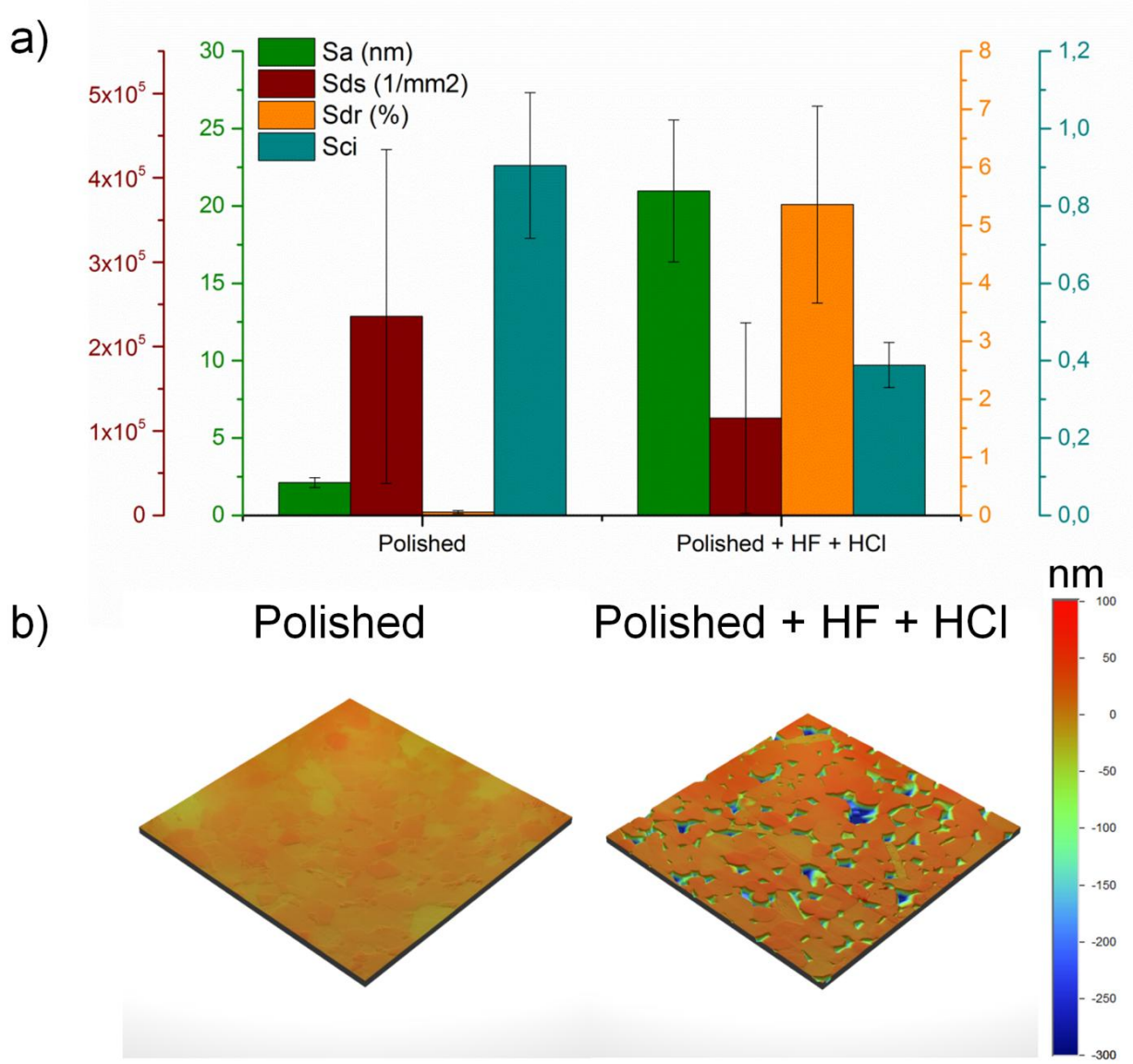

Figure 3. Atomic force microscopy measurements at the surface of polished zirconia toughened alumina samples before and after HF and HCl treatment: a) roughness analysis; b) 3D topographical images.

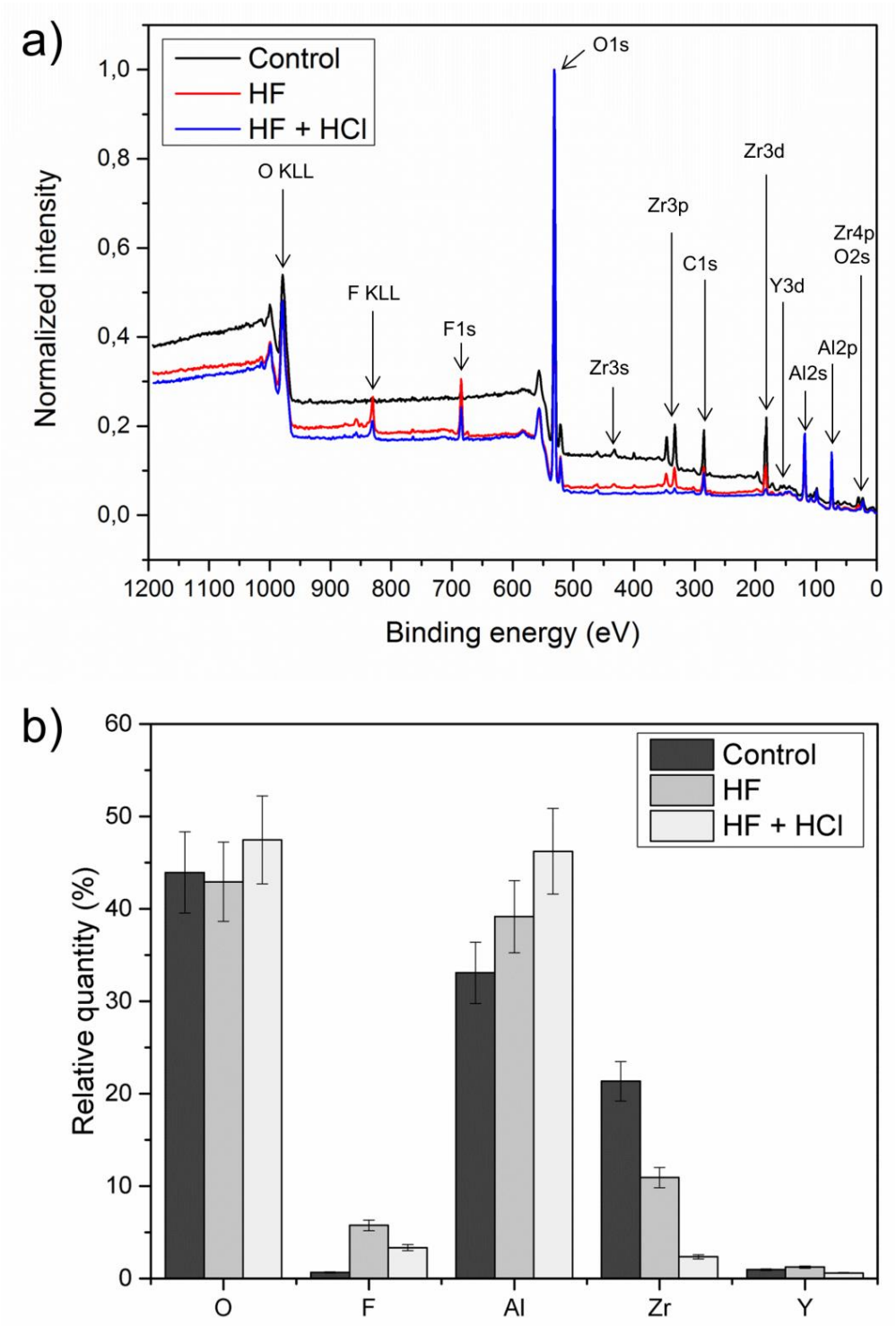

Figure 4. XPS analysis of the surfaces of an "as sintered" zirconia toughened alumina sample, an HF treated sample and an HF+HCl treated sample: a) full spectra normalized to the O1s peak intensity; b) quantitative elemental analysis. Error bars represent the typical uncertainty (10 %) associated to XPS quantitative measurements.

Table 4. Identification of the peaks of the XPS high-resolution spectra of Figure 4

	Sample	Al2p	O1s	F1s	$Zr3d_{5/2}$	$Zr3d_{3/2}$	$Y3d_{5/2}$	$Y3d_{3/2}$
Binding energies (eV)	Control	74.3	529.5 531.2 532.7	685.2	181.5 181.9	183.9 184.3	157.7	159.8
	HF	74.3	529.2 531.2 532.8	684.9	182.5	184.9	158.7	160.7
	HF + HCl	74.2	529.0 531.0 532.4	685.1	182.2	184.6	158.7	160.7
Identified chemical environment (references available in supplementary information)	Control	Al_20_3	YSZ Al_20_3 / ZrO_2 H_2O or hydroxide	ZrF_4 or YF_3	YSZ ZrO_2	YSZ ZrO_2	YSZ	YSZ
	HF	Al_20_3	Y_2O_3 Al_20_3 / ZrO_2 H_2O or hydroxide	$Zr_xO_yF_z$	$Zr_xO_yF_z$	$Zr_xO_yF_z$	YF_3	YF_3
	HF + HCl	Al_20_3	Y_2O_3 [66] Al_20_3 / ZrO_2 H_2O or hydroxide	ZrF_4 or YF_3	ZrO_2	ZrO_2	YF_3	YF_3

YSZ: Yttria stabilized zirconia

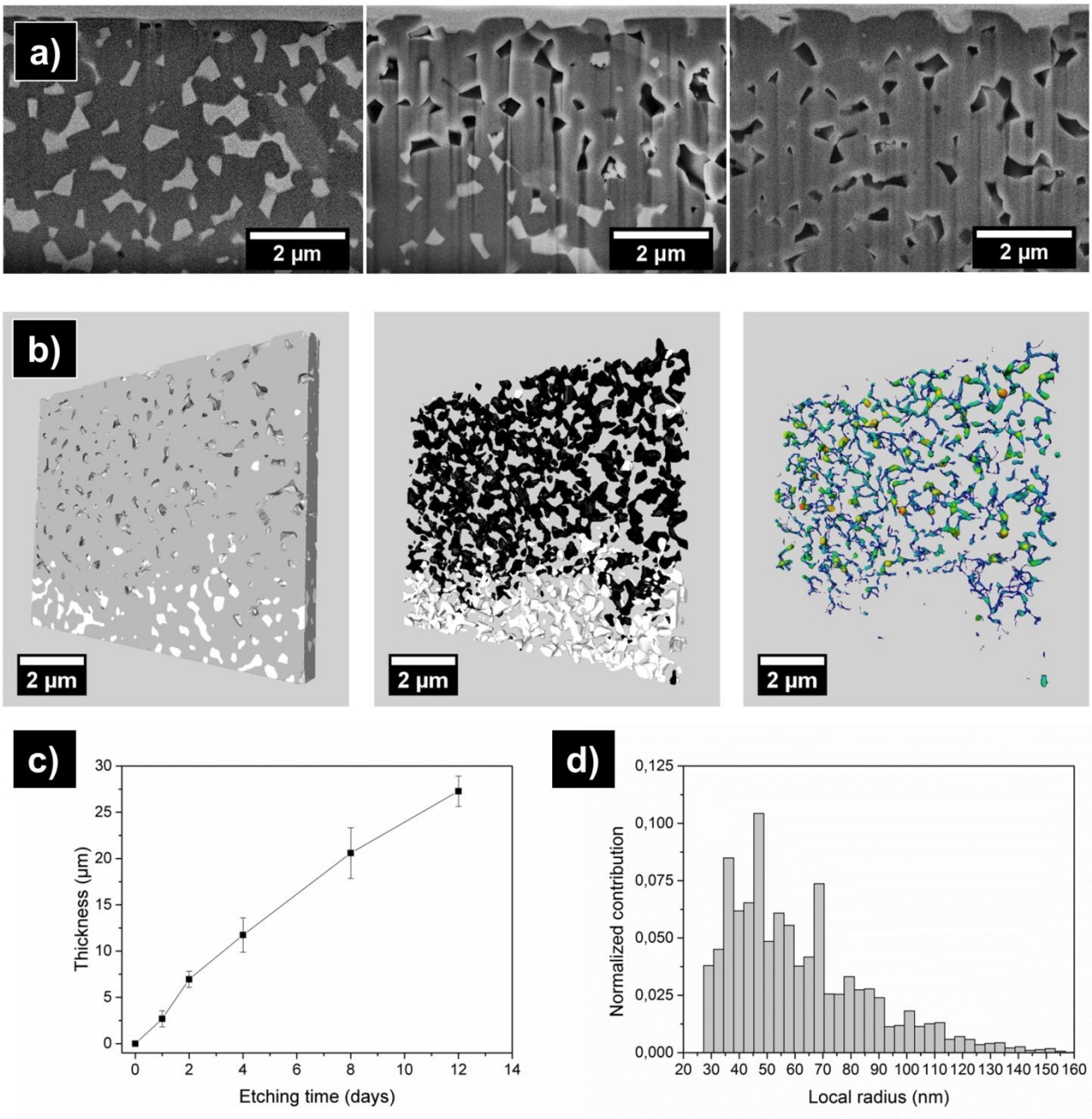

Figure 5. a) FIB cross-sections of polished zirconia toughened alumina samples after 6 h (left), 24 h (middle) and 48 h (right) of immersion in HF, evidencing the progressive removal of zirconia over time; b) FIB/SEM tomography of the surface after selective etching (4 days): external view (left), internal structure with pores in black and zirconia in white (middle), skeleton of the porous structure (right); c) evolution of the porous layer thickness over time for a polished surface. Error bars represent the combined standard deviations of single samples; d) local radius distribution of the porous structure.

3.2. Proof of concept: use of the porous layer as a carrier for drug delivery

It was found that the thickness of the porous layer strongly depended on the surface state. In particular the layer was much thicker on the back surface of the disks, which was ground after sintering (see supplementary information), possibly because of combined effects of residual stresses and machining defects. Because this surface has to be taken into account for the release, each sample used for drug delivery was cross-sectioned and observed following the procedure described in 2.3.4 and the thickness value was reported as an average over the whole specimen (Figure 6).

Impregnation of the samples with gentamicin solution led to small quantities of drug loaded and released (about 16 µg/sample which corresponds to 2 µg/cm^2), and there was no substantial influence of the porous layer thickness (Figure 6-a). This is probably due to the fact that alumina surface and gentamicin are both positively charged, which leads to poor adsorption. Liposome encapsulation enabled an increased amount of gentamicin loaded (up to about 80 µg which corresponds to 10 µg/cm^2), and the quantity loaded and released was roughly proportional to the porous layer thickness (Figure 6-b). This likely results from the higher affinity of the lipid to the alumina surface, as attested by quartz crystal microbalance measurements (see supplementary information), and from the greater size of the liposomes compared to the free gentamicin, which may thus remain trapped in the pores.

Bacteria cultures evidenced two effects (Figure 6-c,d). On the one hand the selectively etched surface reduced the bacterial adhesion as compared to the "as sintered" surface, even in the absence of loaded antibiotic (surface area covered by living *E. coli* after 4 h: 5 % vs. 12 %). On the other hand, samples loaded with gentamicin-encapsulated liposomes limited the growth of bacteria in the medium and consequently reduced the surface area covered by living *E. coli* as compared to non-loaded specimens (bacterial concentration after 4 h: 2.8x10^7 cells/mL vs. 1.8x10^8 cells/mL; surface area covered by living *E. coli* after 4 h: 0.4 % vs. 5 %).

3.3. Impact of selective etching on reliability

3.3.1. Contact behavior and mechanical properties of the porous layer

Indentation hardness vs. strain analytical curves showed a plateau at 8 GPa for the selectively etched sample and 20 GPa for the polished sample (see supplementary information). The observation of the surface and cross-section of an indentation demonstrated that the deformation of the porous layer was quasi-plastic with a limited elastic recovery (Figure 7-a,b,c). No cracks were detected on the surface around the indent and densification could be observed below the residual imprint, which justifies the introduction of a cap in the Drucker-Prager

plasticity model. The inverse FE identification carried out with the different experimental curves led to stable values for the elastic modulus (E) and the yield stress in simple compression (σ_c) whereas a moderate fluctuation was observed for the initial hydrostatic compression yield stress (p_{b0}), and important variations occurred for the friction angle and the maximum plastic volumetric strain rate (D) (Table 5). The elastic modulus values were in good agreement with that obtained by theoretical calculation for porous alumina using Roberts and Garboczi model [35] ($E_{theoretical} = 277\ GPa$, considering overlapping spherical pores), but slightly superior to that computed from the analytical analysis of the indentation data ($E_{analytical} = 215\ GPa$, see supplementary information). Simulations with the identified parameters led to realistic results, with good consistency between experimental and numerical load-displacement curves, residual imprints and densification behavior (Figure 7-d,e,f).

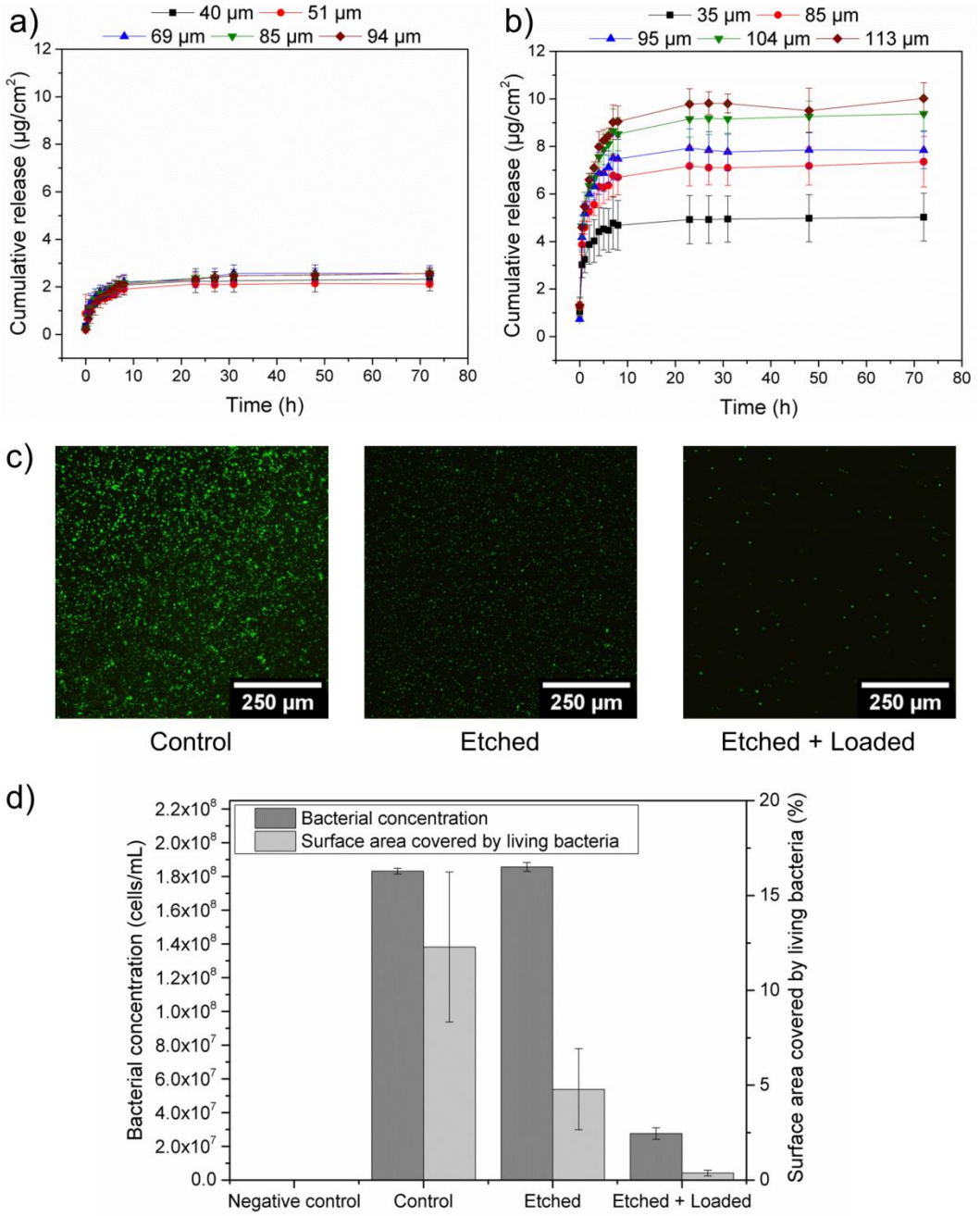

Figure 6. Cumulative drug release profiles from selectively etched zirconia toughened alumina samples loaded with a) gentamicin solution and b) gentamicin-encapsulated liposomes. Legend indicates the average thickness of the porous layer. Results from *E. coli* cultures (t = 4 h) on the surface of "as sintered" (control), selectively etched, and selectively etched liposome-loaded zirconia toughened alumina samples (average porous layer thickness: 35 µm): c) fluorescence microscopy images of living bacteria on the surface; d) bacterial concentration in the medium monitored by flow cytometry and surface area covered by living bacteria. Error bars represent the standard deviations.

3.3.2. Biaxial flexural strength and ageing kinetics

The thickness of the layer produced by selective etching was about 11 µm for both the "as sintered+etched" and the "polished+annealed+etched" samples. Two-way ANOVA analysis of the strength testing results evidenced a significant main effect of polishing ($p=0.007$) and a significant main effect of selective etching ($p=0.015$), but no interaction ($p=0.307$). Etching induced a moderate decrease in the average strength, which was more important for the "polished+annealed" samples (-25 %) than for the "as sintered" samples (-11 %). This can be explained by the presence of pre-existing surface defects in the "as sintered" specimens: the impact of the new defects produced by etching is thus relatively less important in this case (Figure 8-a,b). Furthermore, for both the "as sintered" and "polished+annealed" surfaces, selective etching induced an increase in the Weibull modulus (Table 6) and no decrease in the minimum strength (Figure 8-b). Therefore, the flaws created by selective etching were not the most critical. Indeed, the "polished+annealed" group had the highest mean strength and σ_0 but the lowest Weibull modulus (Figure 8-a,b, Table 6), which suggests the presence of intrinsic defects in the bulk related to injection molding. The process would thus require further optimization to obtain samples with the same reliability as those obtained by conventional pressing.

Regarding phase transformation, it can be observed that selective etching induced a small increase in the initial monoclinic phase content in the "as sintered" samples but not in the "polished+annealed" samples, which contained a comparable amount of monoclinic phase. In terms of kinetics, the trend was similar for all the groups tested and thus the ageing sensitivity does not appear to be significantly affected by selective etching.

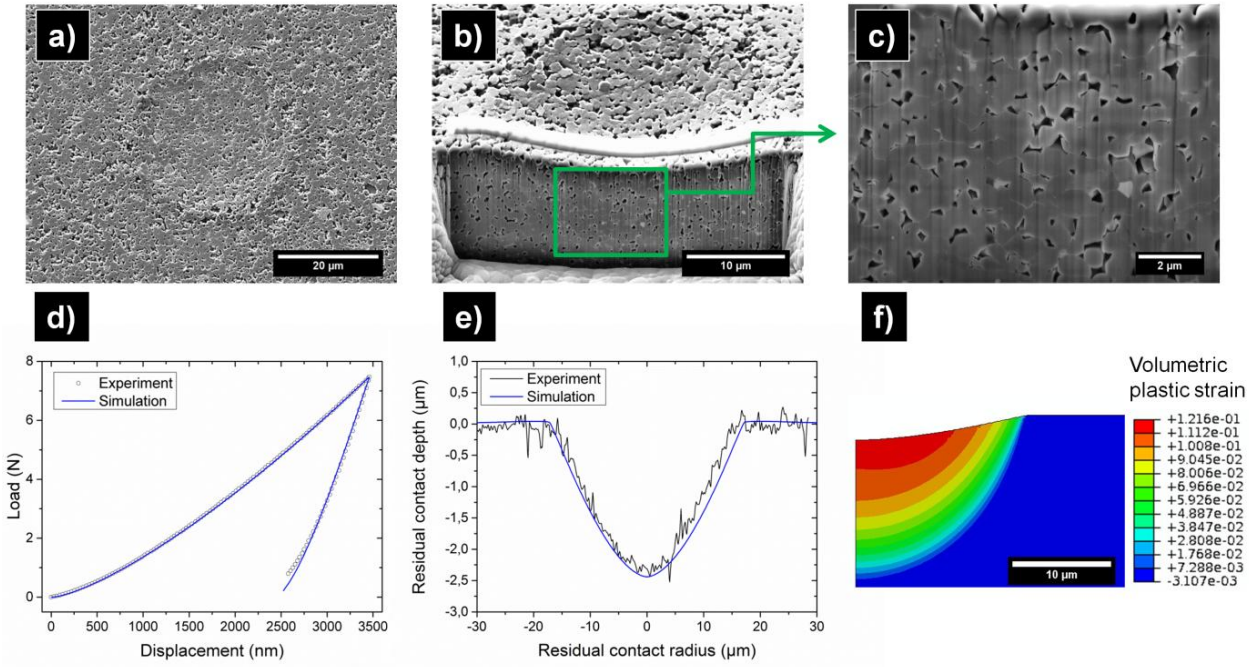

Figure 7. Results from spherical nanoindentation testing of a 27 µm thick porous layer obtained by selective etching of polished zirconia toughened alumina: a) surface of an indentation observed by SEM; b), c) FIB cross-section of an indentation displaying densification of the porous layer which presents a quasi-plastic behavior; d) experimental (average) and simulated load-displacement curves; e) experimental (average) and simulated residual imprint; f) finite element calculation of the volumetric plastic strain (which corresponds to densification).

Table 5. Parameters identified by inverse finite element analysis describing the mechanical behavior of the porous layer obtained by selective etching

Experimental curve	Lowest	Average	Highest
E (GPa)	272	278	279
β (°)	0.3	15.4	0.6
σ_c (MPa)	3300	3210	3460
p_{b0} (MPa)	4930	4680	5730
D (MPa^{-1})	$2.6x10^{-4}$	$5.3x10^{-4}$	$1.2x10^{-3}$

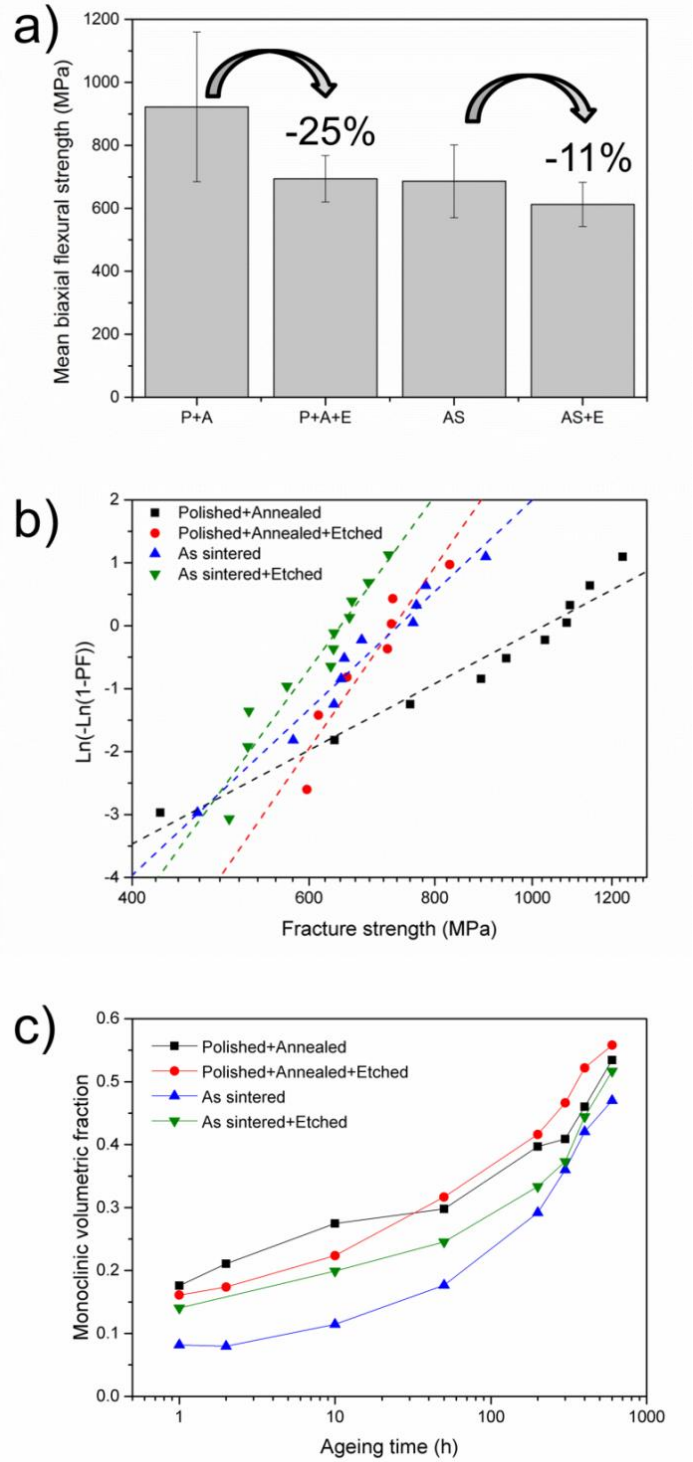

Figure 8. Assessment of the effect of selective etching on strength and ageing sensitivity of zirconia toughened alumina samples: a) mean strength (error bars represent the standard deviations), b) Weibull analysis of the strength, c) evolution of the monoclinic phase content during accelerated ageing tests.

Table 6. Weibull modulus (biased), characteristic strengths and associated confidence intervals resulting from 3-balls-on-3-balls testing of zirconia toughened alumina specimens

Sample group	m (90% confidence interval)	σ_0 [MPa] (90% confidence interval)
Polished + Annealed	3.7 (2 – 5)	1029 (865 – 1232)
Polished + Annealed + Etched	10 (4.6 – 14.1)	729 (671 – 796)
As sintered	6.5 (3.6 – 8.8)	736 (667 - 815)
As sintered + Etched	9.5 (5.5 – 12.8)	669 (628 – 714)

4. Discussion

The combination of surface modifications proposed in this work is promising for the design of ZTA components implantable in direct contact with bone, with tailored surface properties for promoting osseointegration and preventing infections.

Injection molding was shown to be a versatile process for surface micro-structuring, with a large possible range of values for roughness parameters (Figure 1). Additionally, as discussed in the introduction, it presents several advantages over other roughening treatments and has a high potential for industrialization.

On the other hand, selective etching is a totally novel process for ZTA, which can be used for two purposes:

- With a short etching time, it allows superposing of a substantial nano-roughness to the micro-topography produced by injection molding (Figure 2, Figure 3), without affecting the bulk of the material (Figure 5-a). According to the literature, this combination of micro- and nano-roughness should be favorable in terms of osseointegration [17–19]. Besides, the increase in the fluorine content of the surface (Figure 4) could enhance osteoblastic differentiation and interfacial bone formation as it does for titanium [67]. Finally, the selectively etched surface might reduce bacterial adhesion (Figure 6-c,d). This could be explained either by the nano-roughness (Figure 3) or the changes observed in the surface chemistry, in particular the increase in the fluorine content (Figure 4, Table 4), or a combination of both [68,69].

- With a longer etching time, it allows the production of an interconnected nanoporous alumina layer with controlled thickness (Figure 5). As described previously, it has been suggested that nanoporous alumina can improve osteoblast adhesion and proliferation, increase matrix production and induce osteogenic differentiation [29–31]. Furthermore, the porous layer has the potential to be used as a carrier for drug delivery, providing antibacterial properties to the surface (Figure 6). The liposome encapsulation technique proposed in this work improves the loading of gentamicin. Besides, since liposomes can be loaded with both hydrophobic and hydrophilic molecules the method is potentially applicable to many other therapeutic agents [70] (for an example with vancomycin, see supplementary information). Nevertheless, the quantities loaded which represent about 0.5%-1% of the total porous volume available still appear small and there is thus room for optimization: in particular it should be possible to increase the quantity of drug loaded and the sustainability of the release by tuning liposome size.

The main benefit of selective etching when compared to other existing processes to produce nanoporous alumina on implants, such as for instance anodization [28,71], is that the layer obtained is not a coating. There is no interface with the bulk, which is highly beneficial in terms of reliability since it avoids any problem related to lack of adhesion or delamination. Furthermore, the contact behavior of the porous layer obtained is quasi-plastic (no cracks were observed under indentations), and the elastic modulus ($E \approx 275\ GPa$), the yield stress ($\sigma_y \approx 3300\ MPa$) and the indentation hardness (plateau at 8 GPa) are maintained at high values (Figure 7, Table 5). Besides, it was shown that the presence of the porous layer does not impair flexural strength: the decrease in average strength, which was moderate, was compensated by an increase in Weibull modulus and the minimum strength was not affected (Figure 8, Table 6). Therefore, in a component larger than the tested specimens (e.g., an acetabular cup), the failure would likely be governed by intrinsic flaws, whose maximum size statistically increases with material volume. Since the pore size is too small for the cells to enter, the layer thickness tested (11 µm) can be considered as a conservative estimate of the thickness necessary to promote osseointegration. Nevertheless, depending on the quantity of antibiotic which needs to be released and on the loading efficiency, a thicker layer might be required for drug loading. In this case, further study of the influence of the layer thickness on strength would be required. Finally, regarding phase transformation, the influence of selective etching is limited to a small increase in the initial volume of monoclinic phase content, without any impact on LTD kinetics. The excellent resistance to ageing of ZTA is thus not compromised by the treatment.

5. Conclusion

The combination of injection molding and selective etching allows the manufacture of ZTA samples with a substantial nano-roughness superposed to a controlled micro-topography. Selective etching also enables the formation of an interconnected porous alumina layer, which can be used as a carrier for drug delivery. The impact of selective etching on mechanical properties and hydrothermal stability is limited. Future studies will aim to optimize drug loading and to assess the impact of these surface modifications on cell and bone response.

6. References

[1] S.M. Kurtz, S. Kocagöz, C. Arnholt, R. Huet, M. Ueno, W.L. Walter, Advances in zirconia toughened alumina biomaterials for total joint replacement, J. Mech. Behav. Biomed. Mater. 31 (2014) 107–116. doi:10.1016/j.jmbbm.2013.03.022.

[2] O. Roualdes, M.E. Duclos, D. Gutknecht, L. Frappart, J. Chevalier, D.J. Hartmann, In vitro and in vivo evaluation of an alumina-zirconia composite for arthroplasty applications, Biomaterials. 31 (2010) 2043–2054. doi:10.1016/j.biomaterials.2009.11.107.

[3] G. Pezzotti, K. Yamada, A.A. Porporati, M. Kuntz, K. Yamamoto, Fracture toughness analysis of advanced ceramic composite for hip prosthesis, J. Am. Ceram. Soc. 92 (2009) 1817–1822. doi:10.1111/j.1551-2916.2009.03114.x.

[4] A.H. De Aza, J. Chevalier, G. Fantozzi, M. Schehl, R. Torrecillas, Crack growth resistance of alumina, zirconia and zirconia toughened alumina ceramics for joint prostheses, Biomaterials. 23 (2002) 937–945. doi:10.1016/S0142-9612(01)00206-X.

[5] C. Piconi, G. Maccauro, F. Muratori, Alumina Matrix Composites in Arthroplasty, Key Eng. Mater. 284-286 (2005) 979–982. doi:10.4028/www.scientific.net/KEM.284-286.979.

[6] K. Lee, S.B. Goodman, Current state and future of joint replacements in the hip and knee., Expert Rev. Med. Devices. 5 (2008) 383–93. doi:10.1586/17434440.5.3.383.

[7] L.L. Hench, Bioceramics: From Concept to Clinic, J. Am. Ceram. Soc. 74 (1991) 1487–1510. doi:10.1111/j.1151-2916.1991.tb07132.x.

[8] M. Sundfeldt, L. V Carlsson, C.B. Johansson, P. Thomsen, C. Gretzer, Aseptic loosening, not only a question of wear: a review of different theories., Acta Orthop. 77 (2006) 177–97. doi:10.1080/17453670610045902.

[9] R. Burgkart, E. Steinhauser, M. Grassel, M. Kuntz, Direct to bone - possible ceramic solutions for monolithic hip implants, Biol. Symp. 11 (2006) 259–262.

[10] S. Kurtz, Prevalence of Primary and Revision Total Hip and Knee Arthroplasty in the United States From 1990 Through 2002, J. Bone Jt. Surg. 87 (2005) 1487. doi:10.2106/JBJS.D.02441.

[11] K.J. Bozic, S.M. Kurtz, E. Lau, K. Ong, T.P. Vail, D.J. Berry, The Epidemiology of Revision Total Hip Arthroplasty in the United States, J. Bone Jt. Surg. 91 (2009) 128–133. doi:10.2106/JBJS.H.00155.

[12] K.J. Bozic, S.M. Kurtz, E. Lau, K. Ong, V. Chiu, T.P. Vail, et al., The epidemiology of revision total knee arthroplasty in the united states, in: Clin. Orthop. Relat. Res., 2010: pp. 45–51. doi:10.1007/s11999-009-0945-0.

[13] J. Raphel, M. Holodniy, S.B. Goodman, S.C. Heilshorn, Multifunctional Coatings to Simultaneously Promote Osseointegration and Prevent Infection of Orthopaedic Implants, Elsevier Ltd, 2016. doi:10.1016/j.biomaterials.2016.01.016.

[14] J.W. Costerton, Bacterial bofilms: a common cause of persistent infections, Science (80-.). 284 (1999) 1318–1322. doi:10.1126/science.284.5418.1318.

[15] A.G. Gristina, P. Naylor, Q. Myrvik, Infections from biomaterials and implants: a race for the surface., Med. Prog. Technol. 14 (1987) 205–224.

[16] H.J. Busscher, H.C. van der Mei, G. Subbiahdoss, P.C. Jutte, J.J. a. M. van den Dungen, S. a. J. Zaat, et al., Biomaterial-Associated Infection: Locating the Finish Line in the Race for the Surface, Sci. Transl. Med. 4 (2012) 153rv10–153rv10. doi:10.1126/scitranslmed.3004528.

[17] C. Zink, H. Hall, D.M. Brunette, N.D. Spencer, Orthogonal nanometer-micrometer roughness gradients probe morphological influences on cell behavior., Biomaterials. 33 (2012) 8055–61. doi:10.1016/j.biomaterials.2012.07.037.

[18] A. Wennerberg, T. Albrektsson, On implant surfaces: a review of current knowledge and opinions., Int. J. Oral Maxillofac. Implants. 25 (2009) 63–74. doi:10.1111/j.1600-051X.2008.01321.x.

[19] P.G. Coelho, R. Jimbo, N. Tovar, E. a Bonfante, Osseointegration: hierarchical designing encompassing the macrometer, micrometer, and nanometer length scales., Dent. Mater. 31 (2015) 37–52. doi:10.1016/j.dental.2014.10.007.

[20] Y.S. Park, S.H. Chung, W.J. Shon, Peri-implant bone formation and surface characteristics of rough surface zirconia implants manufactured by powder injection molding technique in rabbit tibiae, Clin. Oral Implants Res. 24 (2013) 586–591. doi:10.1111/j.1600-0501.2012.02468.x.

[21] R. Gadow, F. Kern, Pressureless Sintering of Injection Molded Zirconia Toughened Alumina Nanocomposites, J. Ceram. Soc. Japan. 114 (2006) 958–962. doi:10.2109/jcersj.114.958.

[22] M.A. Elezz, F. Kern, R. Gadow, Manufacturing of ZTA composites for biomedical applications, in: Int. Conf. Eng. Technol. ICET 2012 - Conf. Bookl., 2012: pp. 10–14. doi:10.1109/ICEngTechnol.2012.6396123.

[23] F. Sommer, H. Walcher, F. Kern, M. Maetzig, R. Gadow, Influence of feedstock preparation on ceramic injection molding and microstructural features of zirconia toughened alumina, J. Eur. Ceram. Soc. 34 (2014) 745–751. doi:10.1016/j.jeurceramsoc.2013.09.020.

[24] S. Md Ani, A. Muchtar, N. Muhamad, J. a. Ghani, Fabrication of zirconia-toughened alumina parts by powder injection molding process: Optimized processing parameters, Ceram. Int. 40 (2014) 273–280. doi:10.1016/j.ceramint.2013.05.134.

[25] S. Kapoor, R. Hegde, A.J. Bhattacharyya, Influence of surface chemistry of mesoporous alumina with wide pore distribution on controlled drug release, J. Control. Release. 140 (2009) 34–39. doi:10.1016/j.jconrel.2009.07.015.

[26] E. Gultepe, D. Nagesha, S. Sridhar, M. Amiji, Nanoporous inorganic membranes or coatings for sustained drug delivery in implantable devices, Adv. Drug Deliv. Rev. 62 (2010) 305–315. doi:10.1016/j.addr.2009.11.003.

[27] A. Krajewski, A. Ravaglioli, E. Roncari, P. Pinasco, L. Montanari, Porous ceramic bodies for drug delivery, J. Mater. Sci. Mater. Med. 11 (2000) 763–771. doi:10.1023/A:1008988127294.

[28] A.R. Walpole, Z. Xia, C.W. Wilson, J.T. Triffitt, P.R. Wilshaw, A novel nano-porous alumina biomaterial with potential for loading with bioactive materials, J. Biomed. Mater. Res. - Part A. 90 (2009) 46–54. doi:10.1002/jbm.a.32067.

[29] S. Pujari-Palmer, T. Lind, W. Xia, L. Tang, M.K. Ott, Controlling Osteogenic Differentiation through Nanoporous Alumina, J. Biomater. Nanobiotechnol. 5 (2014) 98–104. doi:10.4236/jbnb.2014.52012.

[30] K.C. Popat, E.E. Leary, V. Mukhatyar, K. Chatvanichkul, G.K. Mor, C.A. Grimes, et al., Influence of nanoporous alumina membranes on long-term osteoblast response, 26 (2005) 4516–4522. doi:10.1016/j.biomaterials.2004.11.026.

[31] K. Popat, Osteogenic differentiation of marrow stromal cells cultured on nanoporous alumina, J. Biomed. Mater. Res. A. 81 (2007) 771–780. doi:10.1002/jbm.a.

[32] S. Usami, H. Kimoto, I. Takahashi, S. Shida, Strength of ceramic materials containing small flaws, Eng. Fract. Mech. 23 (1986) 745–761. doi:10.1016/0013-7944(86)90120-7.

[33] E. Ryshkewitch, Compression Strength of Porous Sintered Alumina and Zirconia, J. Am. Ceram. Soc. 36 (1953) 65–68. doi:10.1111/j.1151-2916.1953.tb12837.x.

[34] B.A. Latella, B.H. OConnor, N.P. Padture, B.R. Lawn, Hertzian Contact Damage in Porous Alumina Ceramics, J. Am. Ceram. Soc. 80 (2005) 1027–1031. doi:10.1111/j.1151-2916.1997.tb02940.x.

[35] A.P. Roberts, E.J. Garboczi, Elastic Properties of Model Porous Ceramics, J. Am. Ceram. Soc. 83 (2000) 3041–3048. doi:10.1111/j.1151-2916.2000.tb01680.x.

[36] R.H.J. Hannink, P.M. Kelly, B.C. Muddle, Transformation Toughening in Zirconia-Containing Ceramics, J Am Ceram Soc. 83 (2000) 461–87. doi:10.1111/j.1151-2916.1987.tb04865.x.

[37] S. Lawson, Environmental degradation of zirconia ceramics, J. Eur. Ceram. Soc. 15 (1995) 485–502. doi:10.1016/0955-2219(95)00035-S.

[38] J. Chevalier, What future for zirconia as a biomaterial?, Biomaterials. 27 (2006) 535–543. doi:10.1016/j.biomaterials.2005.07.034.

[39] P. Fabbri, C. Piconi, E. Burresi, G. Magnani, F. Mazzanti, C. Mingazzini, Lifetime estimation of a zirconia-alumina composite for biomedical applications, Dent. Mater. 30 (2014) 138–142. doi:10.1016/j.dental.2013.10.006.

[40] S. Deville, J. Chevalier, G. Fantozzi, J.F. Bartolomé, J. Requena, J.S. Moya, et al., Low-temperature ageing of zirconia-toughened alumina ceramics and its implication in biomedical implants, J. Eur. Ceram. Soc. 23 (2003) 2975–2982. doi:10.1016/S0955-2219(03)00313-3.

[41] J. Chevalier, S. Grandjean, M. Kuntz, G. Pezzotti, On the kinetics and impact of tetragonal to monoclinic transformation in an alumina/zirconia composite for arthroplasty applications, Biomaterials. 30 (2009) 5279–5282. doi:10.1016/j.biomaterials.2009.06.022.

[42] V. Lowalekar, S. Raghavan, Etching of Zirconium Oxide, Hafnium Oxide, and Hafnium Silicates in Dilute Hydrofluoric Acid Solutions, J. Mater. Res. 19 (2004) 1149–1156. doi:10.1557/JMR.2004.0149.

[43] K.R. Williams, K. Gupta, M. Wasilik, Etch rates for micromachining processing - Part II, J. Microelectromechanical Syst. 12 (2003) 761–778. doi:10.1109/JMEMS.2003.820936.

[44] A. Wennerberg, T. Albrektsson, A.T. Wennerberg A, Suggested guidelines for the topographic evaluation of implant surfaces., Int. J. Oral Maxillofac. Implants. 15 (2000) 331–344.

[45] L.M. Svanborg, M. Andersson, A. Wennerberg, Surface characterization of commercial oral implants on the nanometer level, J. Biomed. Mater. Res. - Part B Appl. Biomater. 92 (2010) 462–469. doi:10.1002/jbm.b.31538.

[46] W.P. Dong, P.J. Sullivan, K.J. Stout, Comprehensive study of parameters for characterising three- dimensional surface topography. III: Parameters for characterising amplitude and some functional properties, Wear. 178 (1994) 29–43. doi:10.1016/0043-1648(94)90127-9.

[47] W.P. Dong, P.J. Sullivan, K.J. Stout, Comprehensive study of parameters for characterising three-dimensional surface topography. IV: Parameters for characterising spatial and hybrid properties, Wear. 178 (1994) 45–60. doi:10.1016/0043-1648(94)90128-7.

[48] K.J. Stout, L. Blunt, Three Dimensional Surface Topography, Elsevier, 2000. doi:10.1016/B978-185718026-8/50119-3.

[49] S.S. Sampath, D.H. Robinson, Comparison of new and existing spectrophotometric methods for the analysis of tobramycin and other aminoglycosides, J. Pharm. Sci. 79 (1990) 428–431. doi:10.1002/jps.2600790514.

[50] P. Frutos Cabanillas, E. Díez Peña, J.M. Barrales-Rienda, G. Frutos, Validation and in vitro characterization of antibiotic-loaded bone cement release, Int. J. Pharm. 209 (2000) 15–26. doi:10.1016/S0378-5173(00)00520-2.

[51] J. Gubernator, Z. Drulis-Kawa, A. Kozubek, A simply and sensitive fluorometric method for determination of gentamicin in liposomal suspensions, Int. J. Pharm. 327 (2006) 104–109. doi:10.1016/j.ijpharm.2006.07.039.

[52] B. Zmistowski, C.J. Fedorka, E. Sheehan, G. Deirmengian, M.S. Austin, J. Parvizi, Prosthetic joint infection caused by gram-negative organisms., J. Arthroplasty. 26 (2011) 104–108. doi:10.1016/j.arth.2011.03.044.

[53] T.N. Peel, A.C. Cheng, K.L. Buising, P.F.M. Choong, Microbiological aetiology, epidemiology, and clinical profile of prosthetic joint infections: Are current antibiotic prophylaxis guidelines effective?, Antimicrob. Agents Chemother. 56 (2012) 2386–2391. doi:10.1128/AAC.06246-11.

[54] D. Rodríguez-Pardo, C. Pigrau, J. Lora-Tamayo, A. Soriano, M.D. del Toro, J. Cobo, et al., Gram-negative prosthetic joint infection: Outcome of a debridement, antibiotics and implant retention approach. A large multicentre study, Clin. Microbiol. Infect. 20 (2014) O911–O919. doi:10.1111/1469-0691.12649.

[55] A.J. Moseson, S. Basu, M.W. Barsoum, Determination of the effective zero point of contact for spherical nanoindentation, J. Mater. Res. 23 (2008) 204–209. doi:10.1557/JMR.2008.0012.

[56] L.H. He, N. Fujisawa, M. V Swain, Elastic modulus and stress-strain response of human enamel by nano-indentation, Biomaterials. 27 (2006) 4388–4398. doi:10.1016/j.biomaterials.2006.03.045.

[57] P. Clément, S. Meille, J. Chevalier, C. Olagnon, Mechanical characterization of highly porous inorganic solids materials by instrumented micro-indentation, Acta Mater. 61 (2013) 6649–6660. doi:10.1016/j.actamat.2013.07.005.

[58] D. Staub, S. Meille, V. Le Corre, L. Rouleau, J. Chevalier, Identification of a damage criterion of a highly porous alumina ceramic, Acta Mater. 107 (2016) 261–272. doi:10.1016/j.actamat.2016.01.071.

[59] F.L. DiMaggio, I.S. Sandler, Material model for granular soils, J. Eng. Mech. Div. 97 (1971) 935–950.

[60] J. Chevalier, C. Olagnon, G. Fantozzi, Study of the residual stress field around Vickers indentations in a 3Y-TZP, J. Mater. Sci. 31 (1996) 2711–2717. doi:10.1007/bf00687305.

[61] T. Fett, G. Rizzi, E. Ernst, R. M??ller, R. Oberacker, A 3-balls-on-3-balls strength test for ceramic disks, J. Eur. Ceram. Soc. 27 (2007) 1–12. doi:10.1016/j.jeurceramsoc.2006.02.033.

[62] T. Fett, G. Rizzi, 3-balls-on-3-balls test for ceramic disks: A finite element study, 2004. http://d-nb.info/973573007/34 (accessed April 15, 2016).

[63] D. Munz, T. Fett, Ceramics: mechanical properties, failure behaviour, materials selection, Springer Science & Business Media, 1999.

[64] H. Toraya, M. Yoshimura, S. Somiya, Calibration Curve for Quantitative Analysis of the Monoclinic-Tetragonal ZrO2 System by X-Ray Diffraction, Commun. Am. Ceram. Soc. 67 (1984) 119–121. doi:10.1111/j.1151-2916.1984.tb19715.x.

[65] Q. Flamant, F. García Marro, J.J. Roa Rovira, M. Anglada, Hydrofluoric acid etching of dental zirconia. Part 1: Etching mechanism and surface characterization, J. Eur. Ceram. Soc. 36 (2016) 121–134. doi:10.1016/j.jeurceramsoc.2015.09.021.

[66] D. Majumdar, D. Chatterjee, X-ray photoelectron spectroscopic studies on yttria, zirconia, and yttria-stabilized zirconia, J. Appl. Phys. 70 (1991) 988–992. doi:10.1063/1.349611.

[67] L.F. Cooper, Y. Zhou, J. Takebe, J. Guo, A. Abron, A. Holm??n, et al., Fluoride modification effects on osteoblast behavior and bone formation at TiO2 grit-blasted c.p. titanium endosseous implants, Biomaterials. 27 (2006) 926–936. doi:10.1016/j.biomaterials.2005.07.009.

[68] K. Bazaka, R.J. Crawford, E.P. Ivanova, Do bacteria differentiate between degrees of nanoscale surface roughness?, Biotechnol. J. 6 (2011) 1103–1114. doi:10.1002/biot.201100027.

[69] M. Yoshinari, Y. Oda, T. Kato, K. Okuda, Influence of surface modifications to titanium on antibacterial activity in vitro, Biomaterials. 22 (2001) 2043–2048. doi:10.1016/S0142-9612(00)00392-6.

[70] H. Pinto-Alphandary, A. Andremont, P. Couvreur, Targeted delivery of antibiotics using liposomes and nanoparticles: Research and applications, Int. J. Antimicrob. Agents. 13 (2000) 155–168. doi:10.1016/S0924-8579(99)00121-1.

[71] A.R. Walpole, E.P. Briggs, M. Karlsson, E. Pålsgård, P.R. Wilshaw, Nano-porous Alumina Coatings for Improved Bone Implant Interfaces, in: Materwiss. Werksttech., 2003: pp. 1064–1068. doi:10.1002/mawe.200300707.

[72] S. Dolarevic, A. Ibrahimbegovic, A modified three-surface elasto-plastic cap model and its numerical implementation, Comput. Struct. 85 (2007) 419–430. doi:10.1016/j.compstruc.2006.10.001.

Appendix A. Porous layer thickness measurement

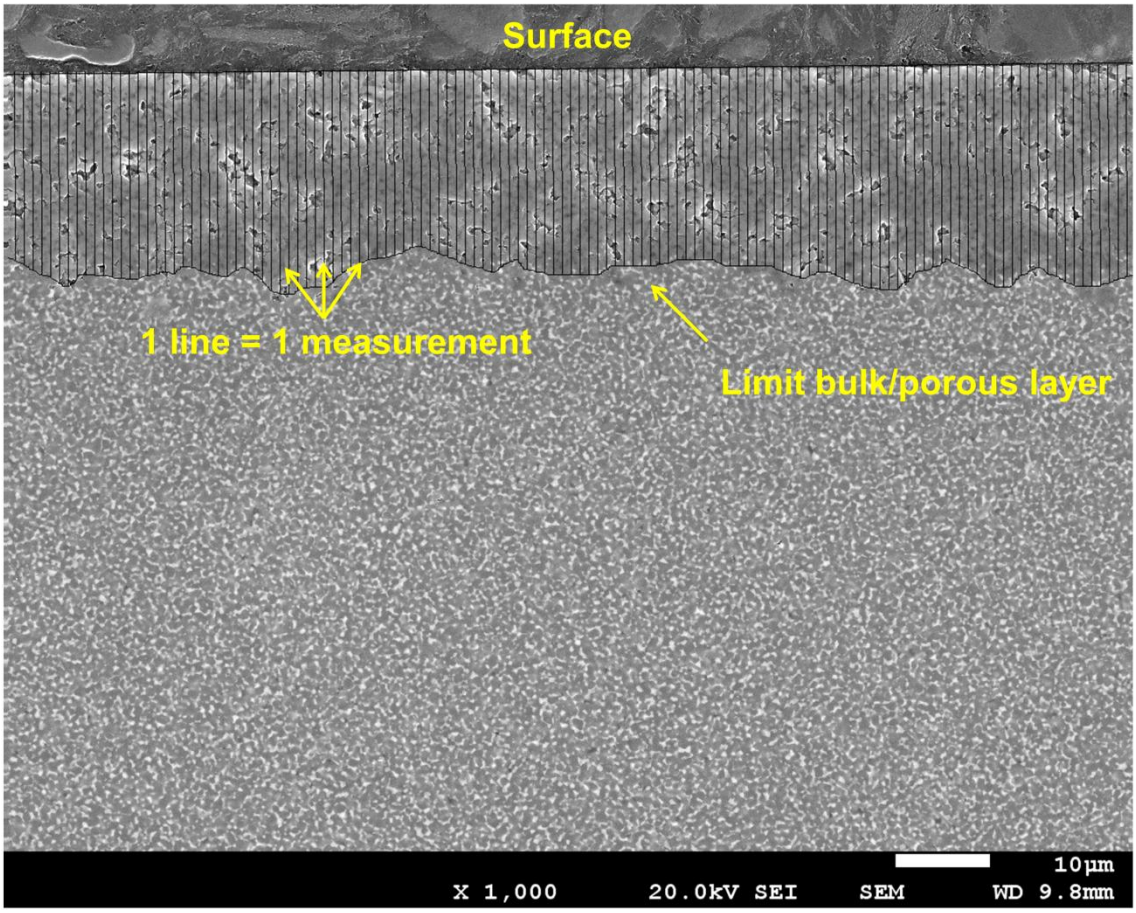

Example of porous layer thickness measurement performed on a cross-section image using ImageJ

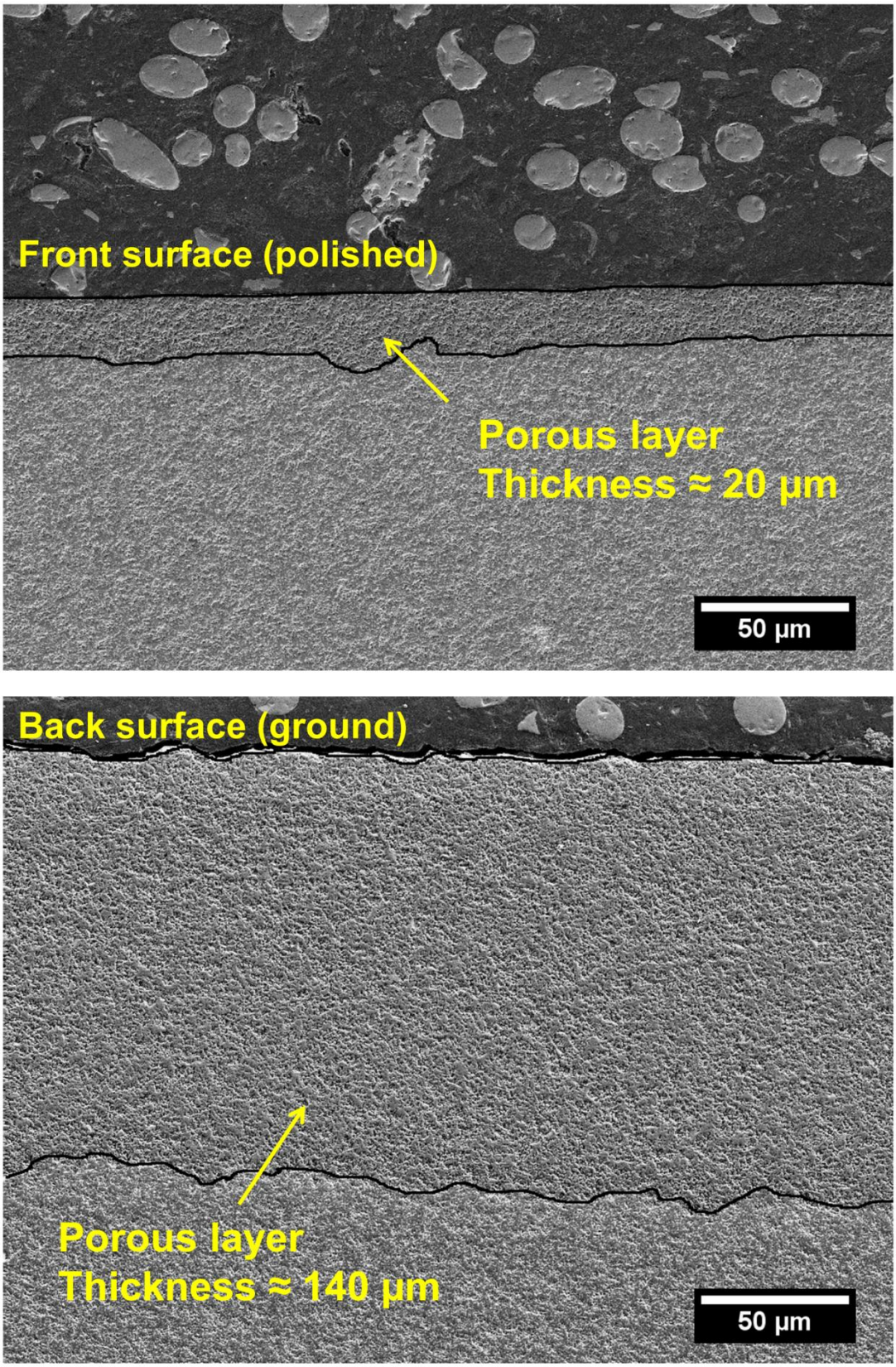

Example showing the difference in the porous layer thickness achieved by selective etching depending on the initial surface state.

Appendix B. Quartz crystal microbalance measurements

A quartz crystal microbalance (QCM, Q-Sense Instruments) equipped with an Al_2O_3 sensor was used to evaluate the affinity of gentamicin and liposomes to the alumina surface. Concentration of the solutions tested: 1 mg/mL in PBS.

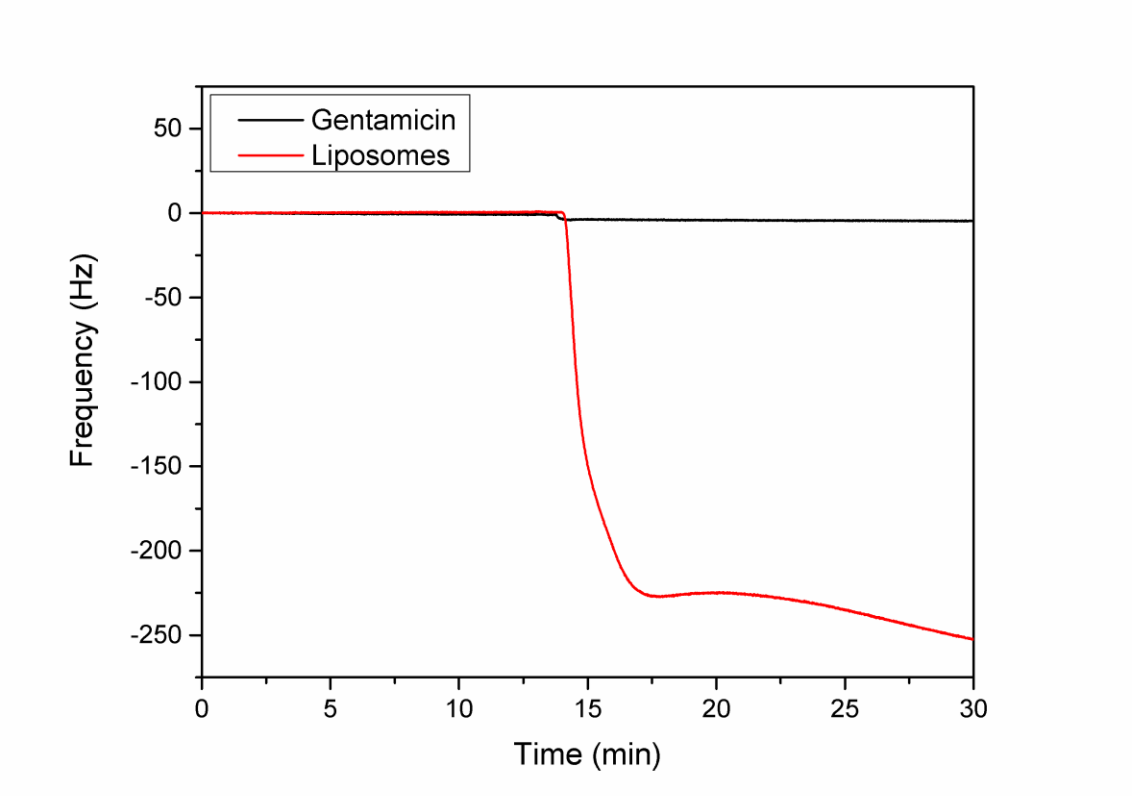

As can be seen above, the affinity of liposomes to the alumina surface (frequency change ≈ 250 Hz) is much higher than that of gentamicin, which is very low (frequency change ≈ 3 Hz).

Appendix C. *In vitro* drug release experiments with vancomycin

The exact same procedure as described for gentamicin in sections 2.4.1, 2.4.2 and 2.4.3 was used with vancomycin hydrochloride.

The results obtained showed that:

- Liposomal encapsulation improved loading and release (same as for gentamicin)
- Quantities loaded and released were more important, which can be explained by the higher molecular weight of vancomycin.
- Vancomycin release appeared more sustained than gentamicin release for large porous layer thicknesses (> 100 µm).
- The liposomal encapsulation technique is thus flexible and can be applied to other therapeutic molecules.

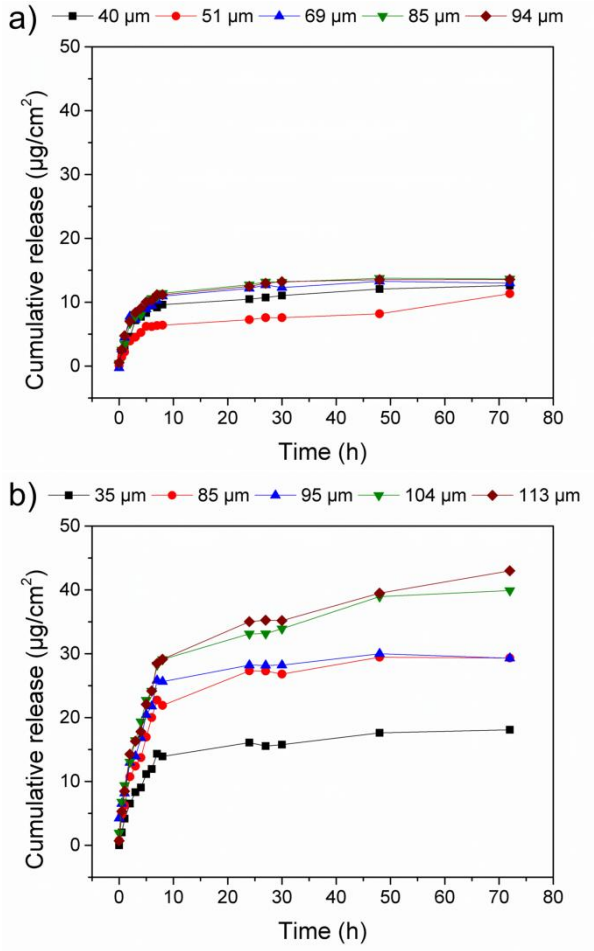

Cumulative drug release profiles from selectively etched zirconia toughened alumina samples loaded with a) vancomycin solution and b) vancomycin-encapsulated liposomes. Legend indicates the average thickness of the porous layer.

Appendix D. Modified Drucker-Prager/cap model [58]

The Drucker-Prager failure surface is defined in the meridional (p-t) plane by:

$$F_s = t - p\tan\beta - d = 0 \qquad \text{(A.1)}$$

where p is the equivalent pressure stress, t is the deviatoric stress, β is the angle of friction of the material and d is its cohesion which can be expressed as a function of the yield stress in simple compression σ_c as:

$$d = (1 - \tfrac{1}{3}\tan\beta)\sigma_c \qquad \text{(A.2)}$$

The cap yield failure surface, which binds the yield surface in hydrostatic compression, is defined in the p-t plane by:

$$F_c = \sqrt{(p - p_a)^2 + \left(\frac{Rt}{1+\alpha-\frac{\alpha}{\cos\beta}}\right)^2} - R(d + p_a\tan\beta) = 0 \qquad \text{(A.3)}$$

where R is the cap eccentricity (which controls the shape of the cap), α is a small number (typically comprised between 0.01 and 0.05) used to define the transition yield surface and p_a is an evolution parameter that represents the volumetric inelastic strain driven hardening given as:

$$p_a = \frac{p_b - Rd}{(1+R\tan\beta)} \qquad \text{(A.4)}$$

where p_b is the hydrostatic compression yield stress. In this work, the evolution of p_b was modeled with the following law:

$$p_b(\varepsilon_V) = \frac{1}{D}\ln\left(1 + \frac{\varepsilon_V}{W}\right) + P_{b0} \qquad \text{(A.5)}$$

where ε_V is the hydrostatic plastic strain, p_{b0} the initial hydrostatic compression yield stress, W is the maximum plastic volumetric strain (which theoretically corresponds to the porosity) and D is the maximum plastic volumetric strain rate [72].

To provide a smooth intersection between the cap and the Drucker-Prager failure surfaces, a transition yield surface is defined as:

$$F_t = \sqrt{(p - p_a)^2 + \left[t - (1 - \frac{\alpha}{\cos\beta})(d + p_a\tan\beta)\right]^2} - \alpha(d + p_a\tan\beta) = 0 \qquad \text{(A.6)}$$

The plastic flow is defined by a flow potential that is associated in the cap region in the meridional plane and non-associated in the Drucker-Prager failure surface and transition regions. It consists in an elliptical portion in the cap region that is identical to the cap yield surface:

$$G_c = \sqrt{(p - p_a)^2 + \left(\frac{Rt}{1+\alpha-\frac{\alpha}{\cos\beta}}\right)^2} \qquad \text{(A.7)}$$

and another elliptical portion in the failure and transition regions:

$$G_s = \sqrt{[(p_a - p)\tan\beta]^2 + \left(\frac{t}{1+\alpha-\frac{\alpha}{\cos\beta}}\right)^2} \qquad \text{(A.8)}$$

Appendix E. Finite element model

2D axisymmetric mesh used for the finite element simulation

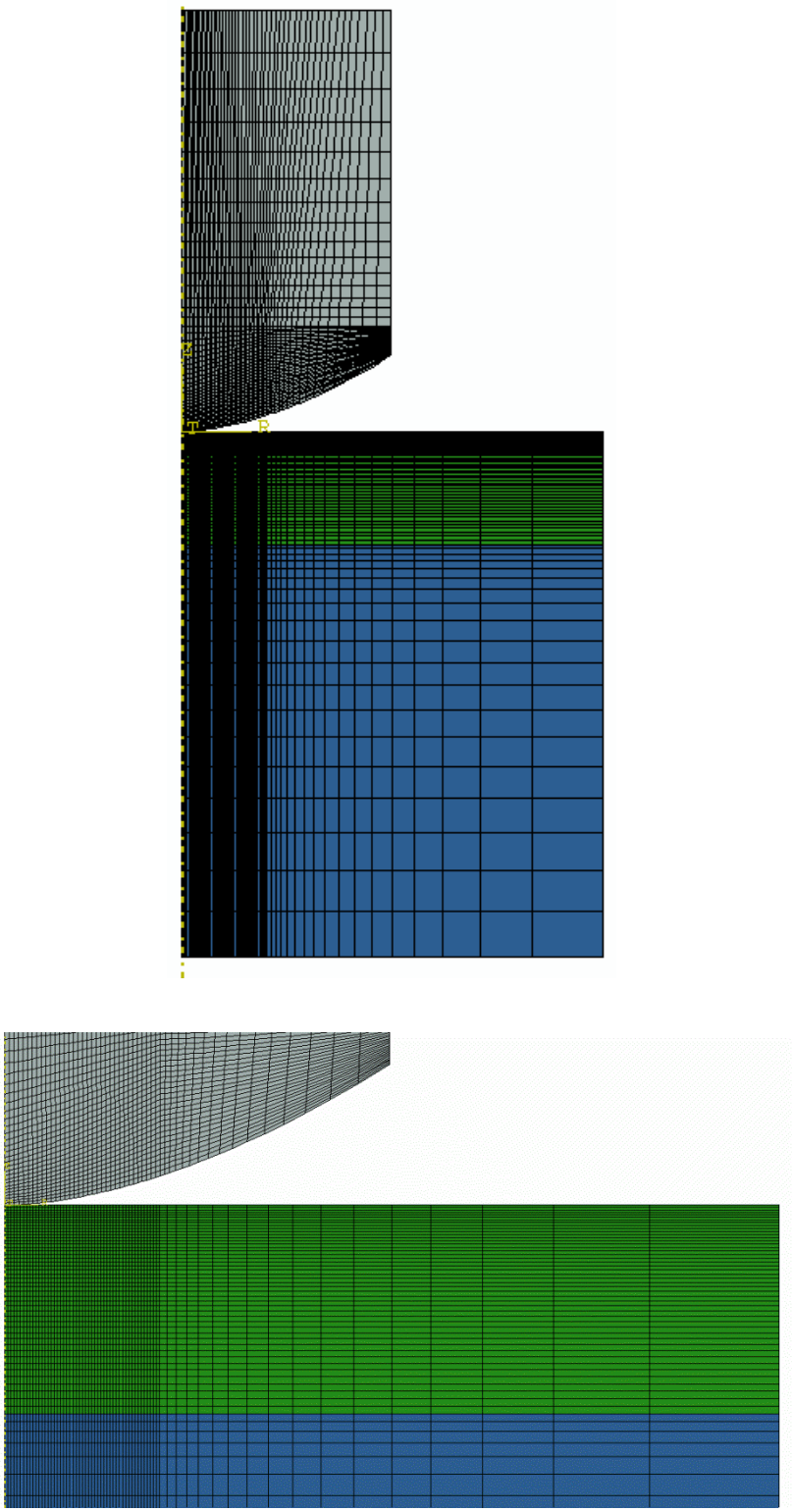

Legend: Grey: diamond indenter; Green: porous layer; Blue: zirconia-toughened alumina (bulk)

Boundary conditions

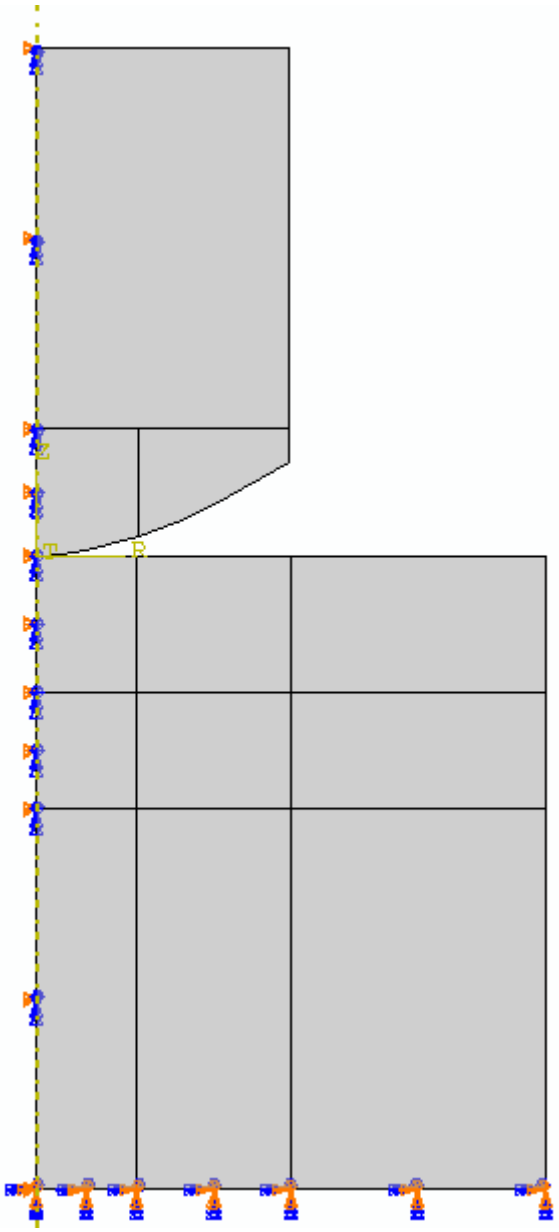

Appendix F. Indenter tip calibration method and experiments

Calibration method

1) **Measurement of the spherical tip by atomic force microscopy**

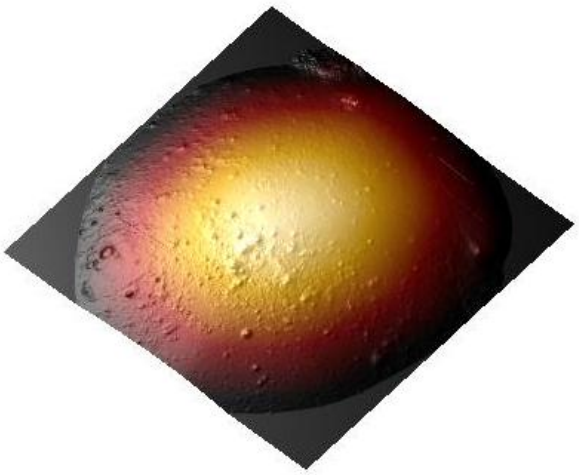

2) **Determination of the tip shape function**

Thanks to a Python script:

- The tip was cut into virtual horizontal slices (distance between slices: 1.5 nm) starting from the top.
- For each slice, the data points extracted were fitted with an ellipse (equation: $\frac{x^2}{{R_1}^2} + \frac{y^2}{{R_2}^2} = 1$ where x and y are the Cartesian coordinates and R_1 and R_2 are the ellipse radii).
- The radius of the equivalent circle (same area as the ellipse), given by $R = \sqrt{(R_1 R_2)}$ was taken as the contact radius a and the distance from the slice to the top was taken as the contact depth h_c.

3) **Determination of the effective indenter tip apex position**

To adjust the effective position of the indenter tip apex, i.e. to determine the value of a for which $h_c = 0$, the tip shape function $a = f(h_c)$ was plotted considering different offsets on h_c (0 nm, -10 nm, -20 nm, …., -100 nm) and fitted with a power law. Calibration experiments were carried out against materials with different well-known elastic moduli (Pyrocarbon, Fused silica, Tungsten). The offset value retained was the one leading to the load/hardness/modulus vs.

displacement and indentation stress vs. strain curves which were more realistic and closer to the theory.

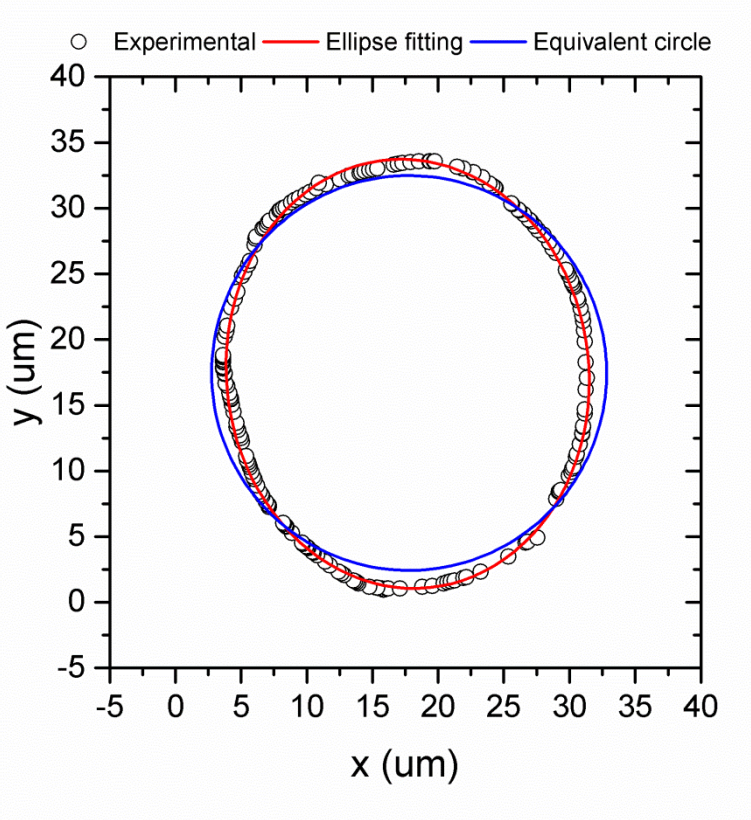

Example: fitting of a "horizontal “slice” of the indenter tip

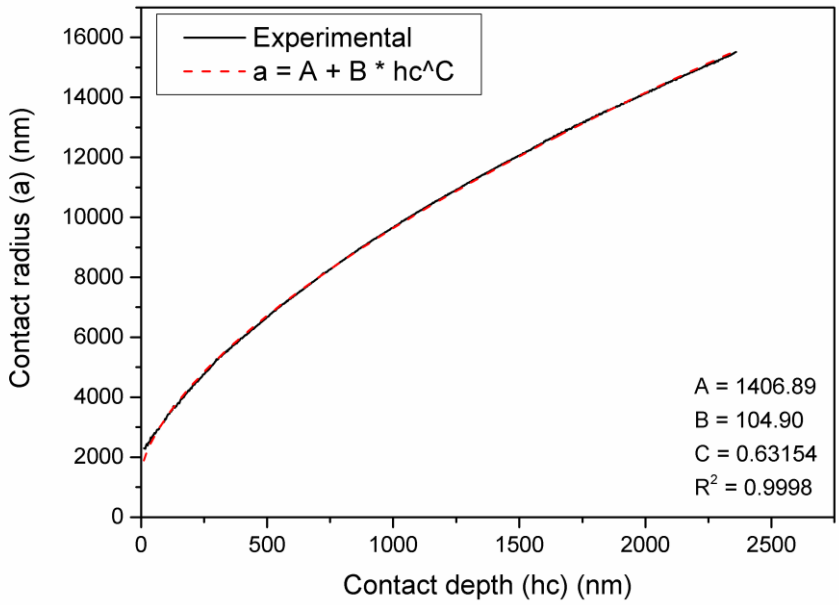

Tip shape function obtained after adjusting the tip apex position

Calibration experiments

1) Fused silica (E = 74.56 GPa)

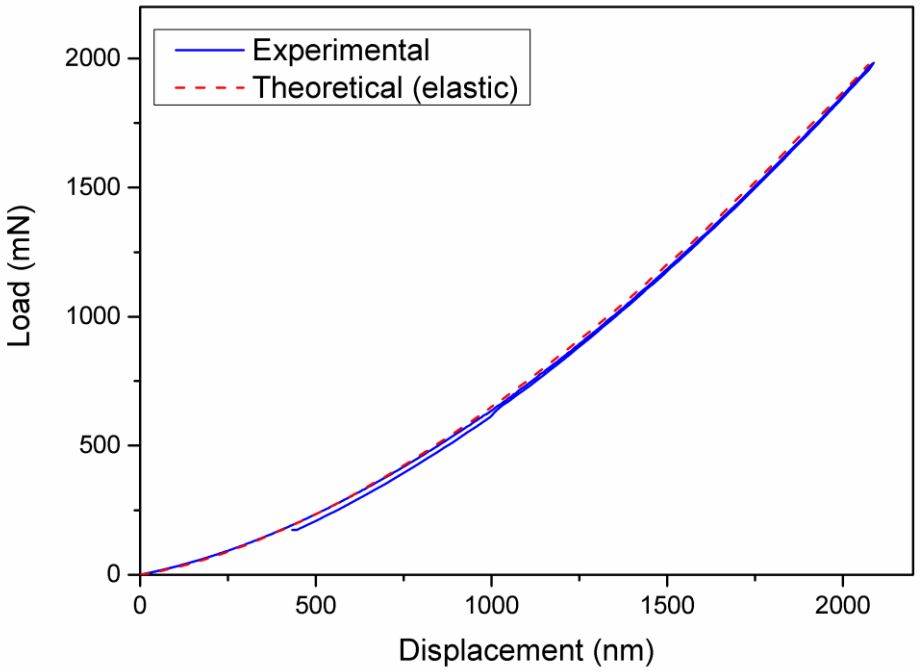

The theoretical curve was determined from Hertz theory.

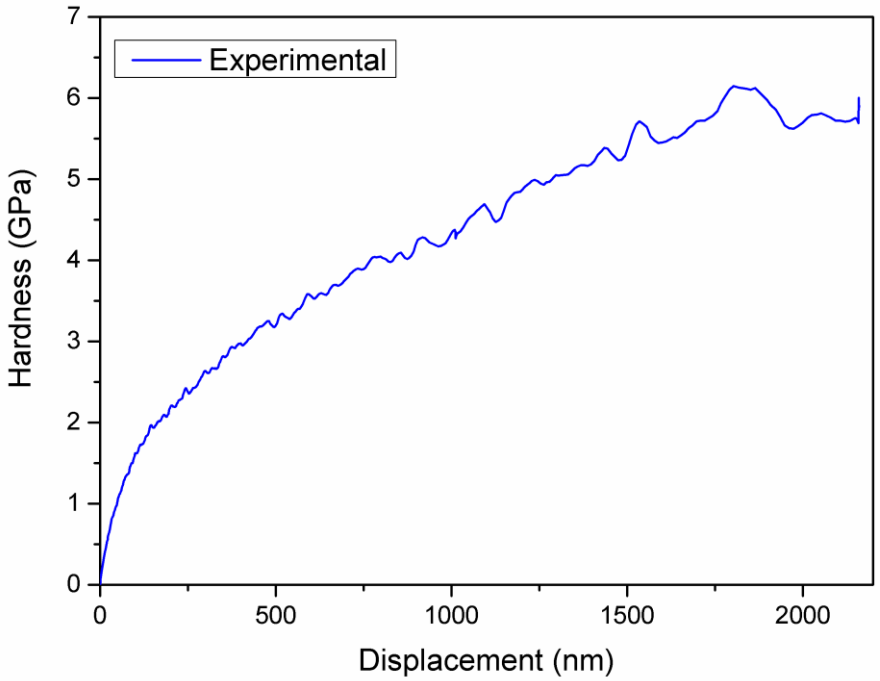

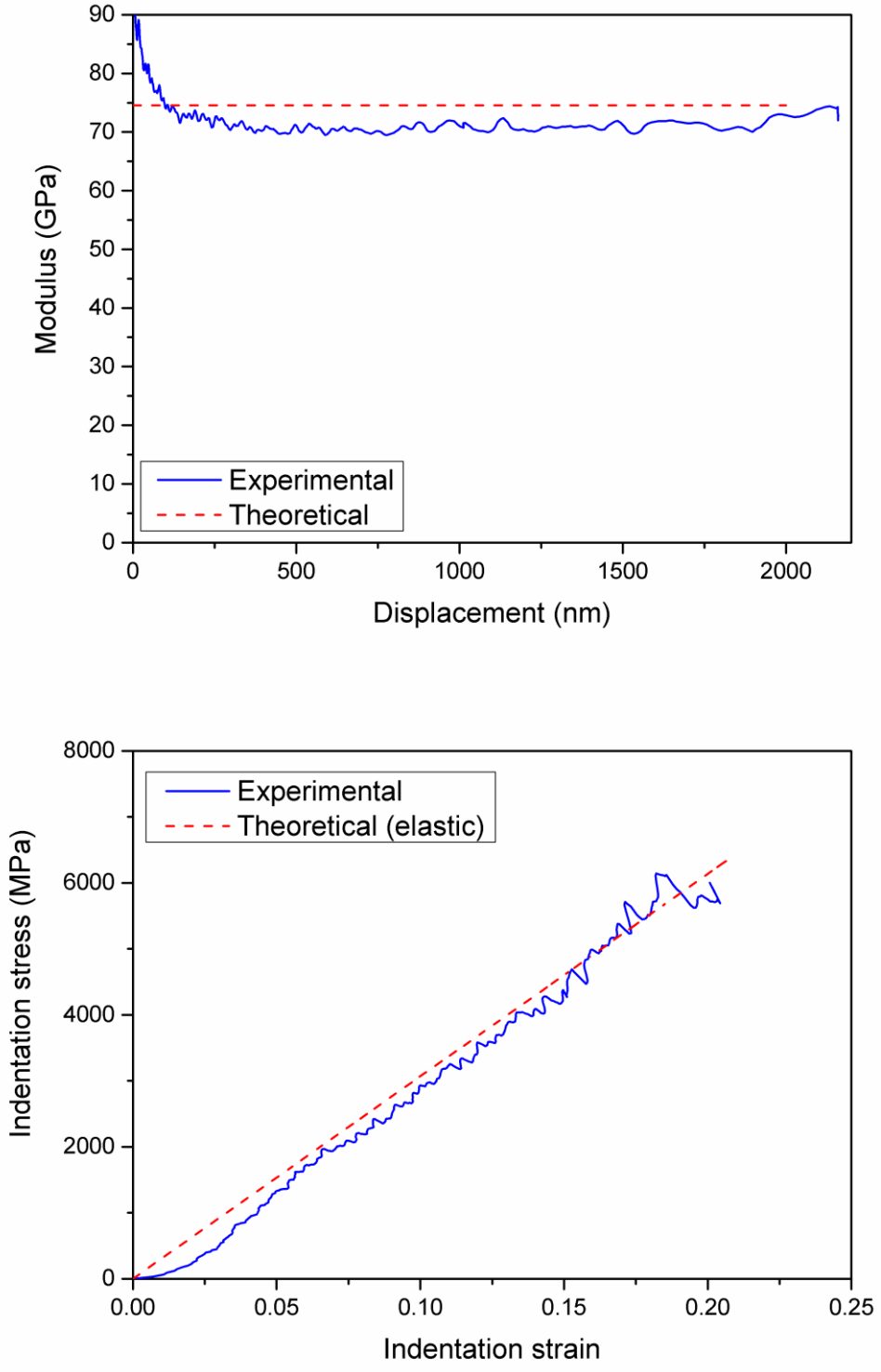

Hardness and indentation stress are equivalent (same definition). The theoretical curve was determined from Hertz theory.

2) Pyrocarbon (E = 23.2 GPa)

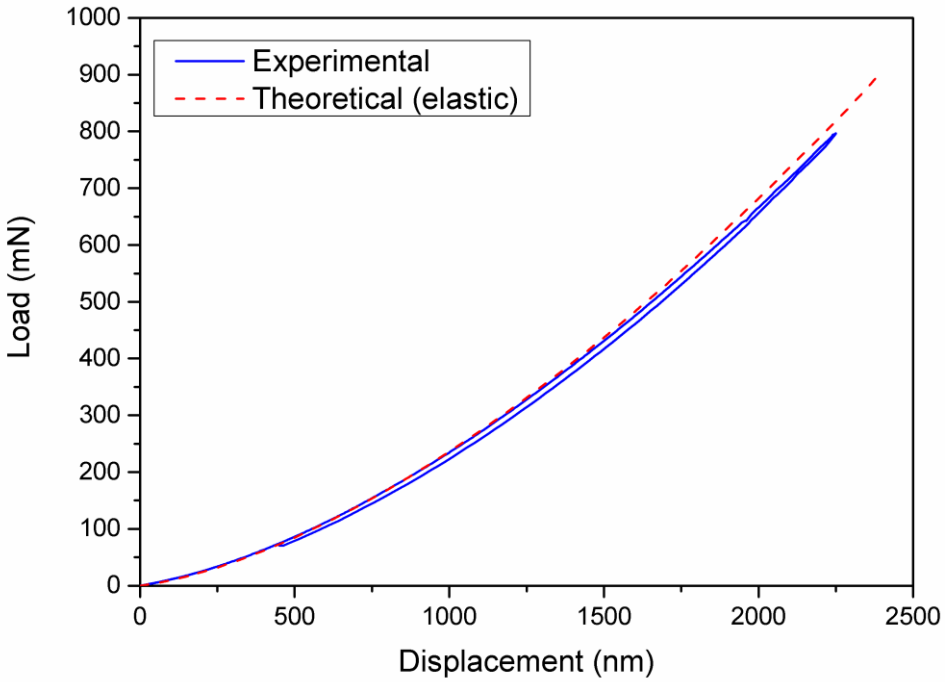

The theoretical curve was determined from Hertz theory.

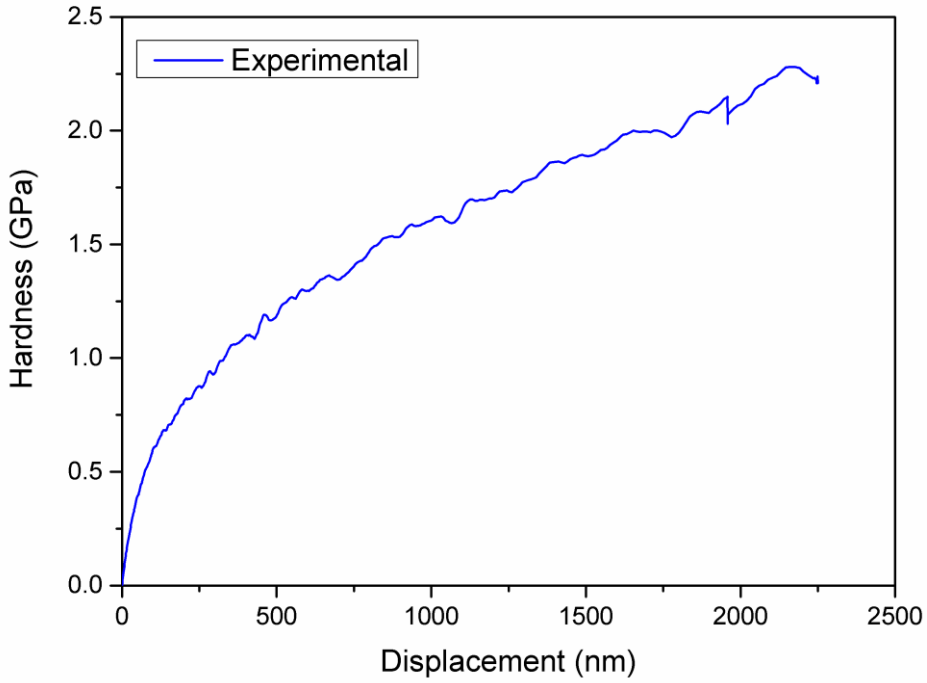

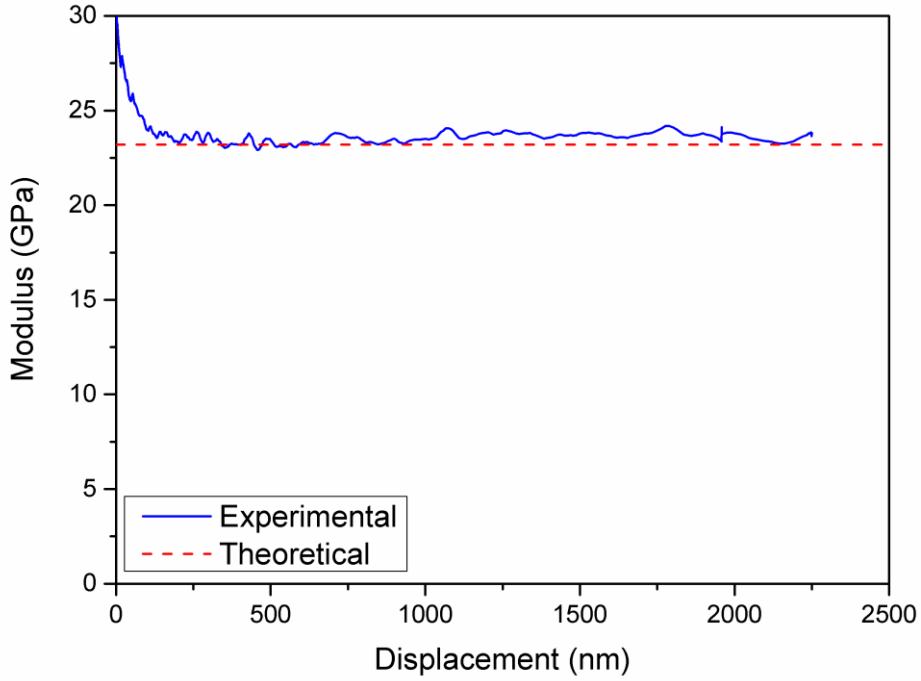

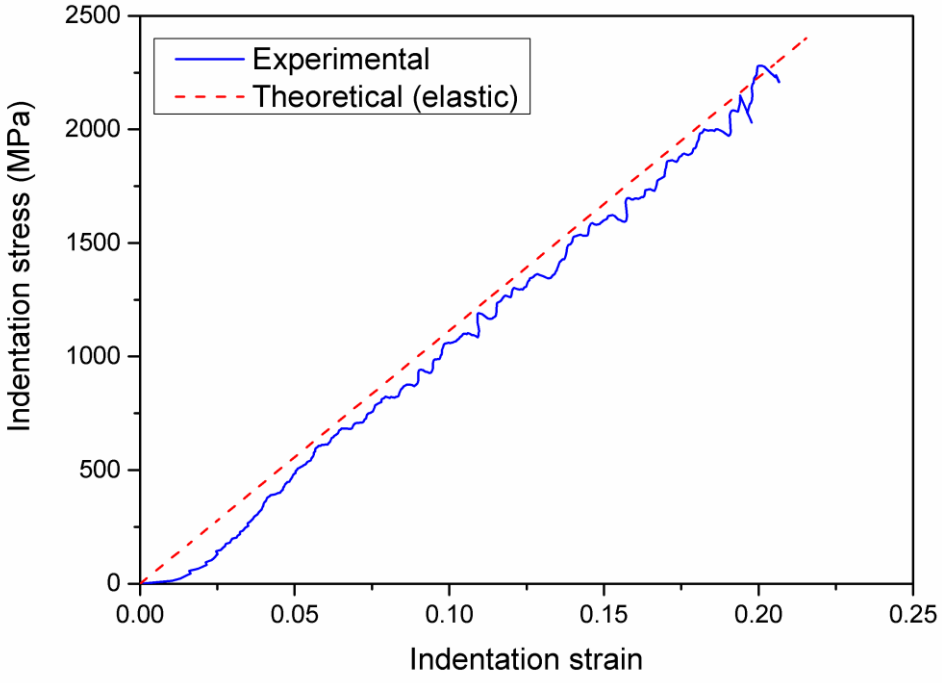

Hardness and indentation stress are equivalent (same definition). The theoretical curve was determined from Hertz theory.

3) Tungsten (E = 405 GPa)

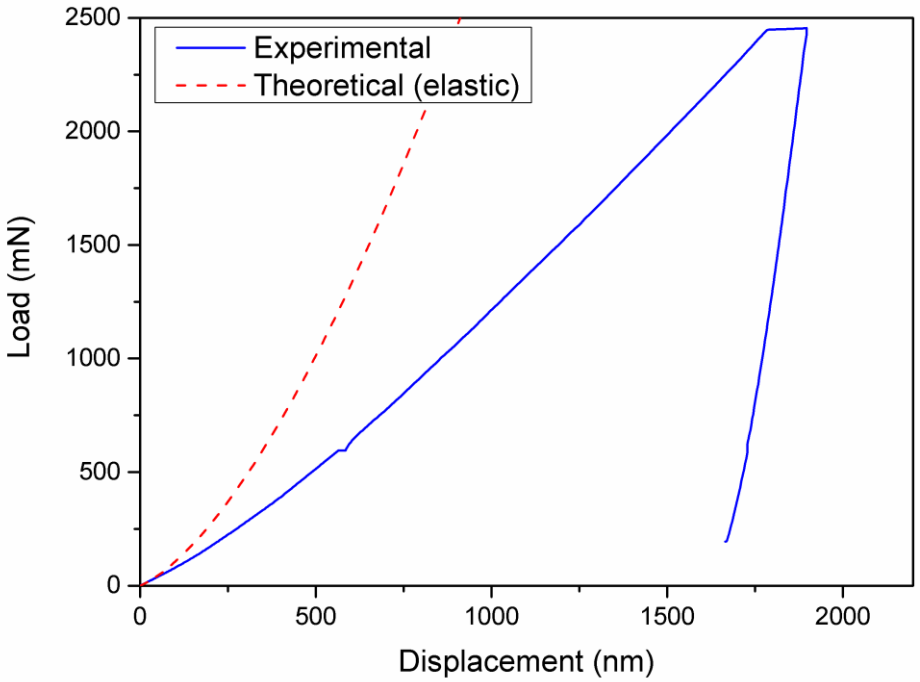

The theoretical curve was determined from Hertz theory. NB: tungsten almost immediately starts to deform plastically.

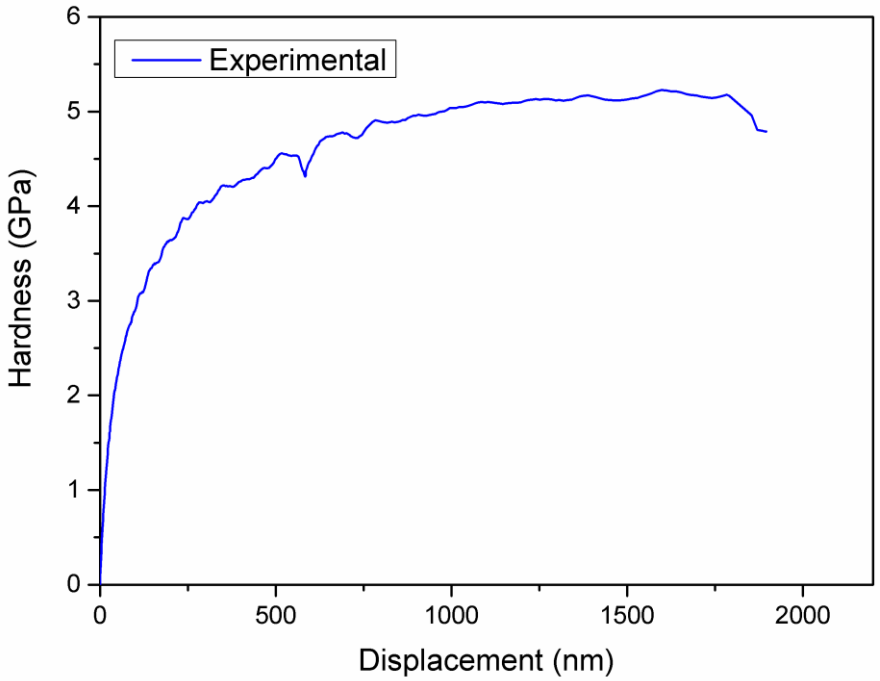

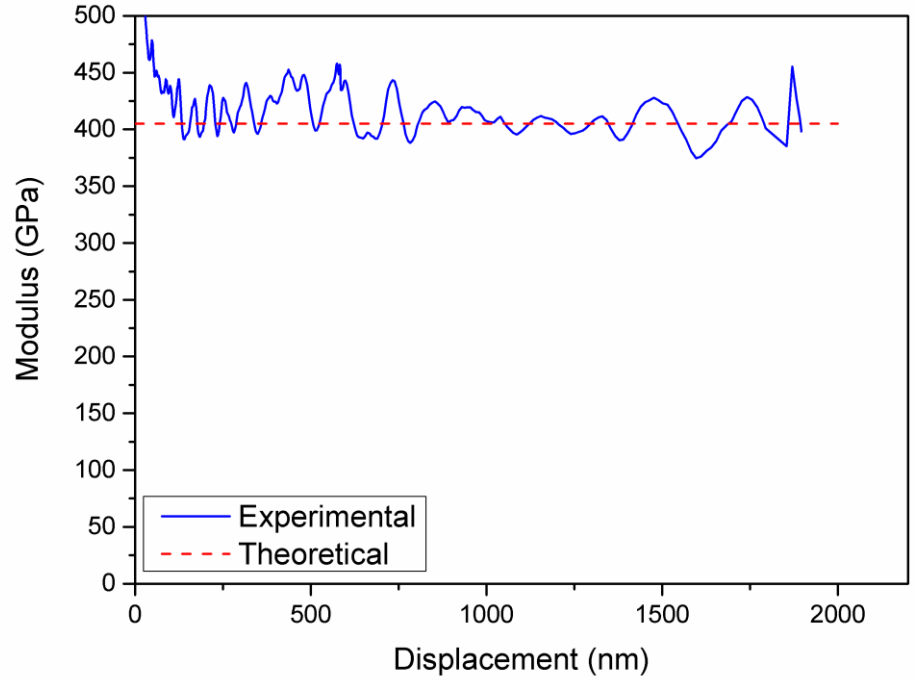

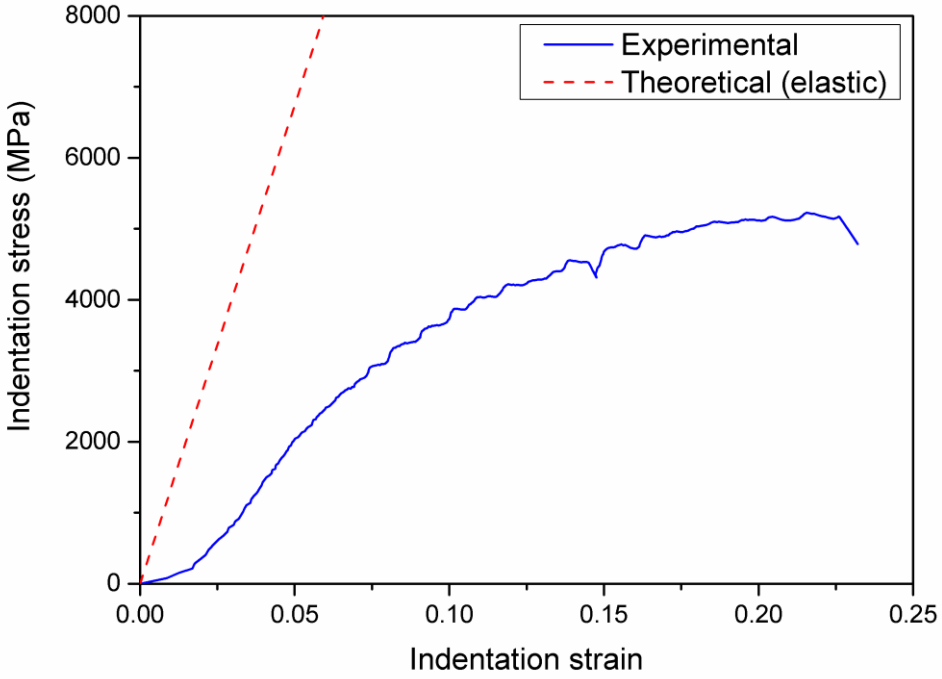

Hardness and indentation stress are equivalent (same definition). The theoretical curve was determined from Hertz theory. NB: tungsten almost immediately starts to deform plastically.

Appendix G. Analytical analysis of spherical nanoindentation data

1) Polished ZTA sample (not etched)

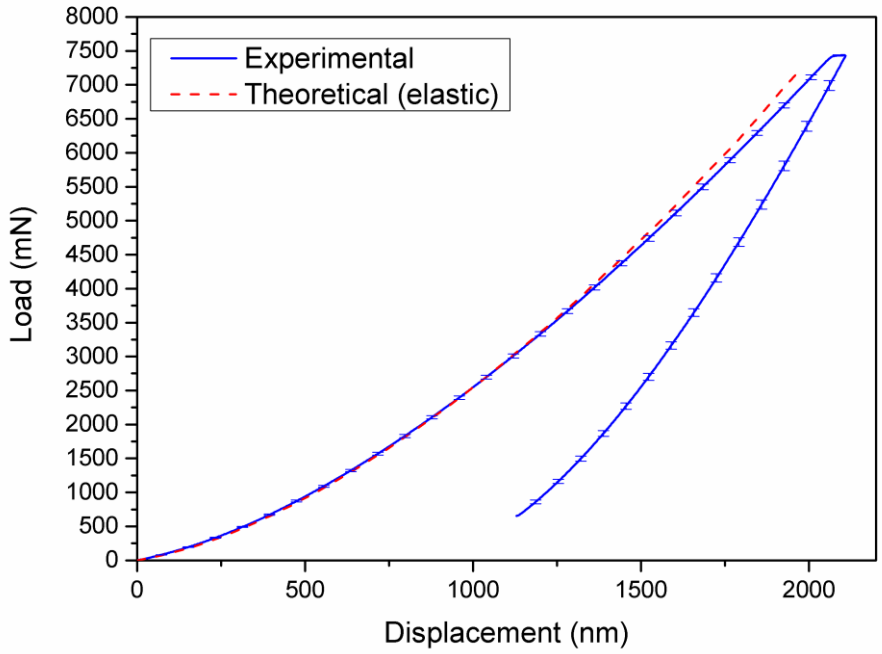

The theoretical curve was determined from Hertz theory.

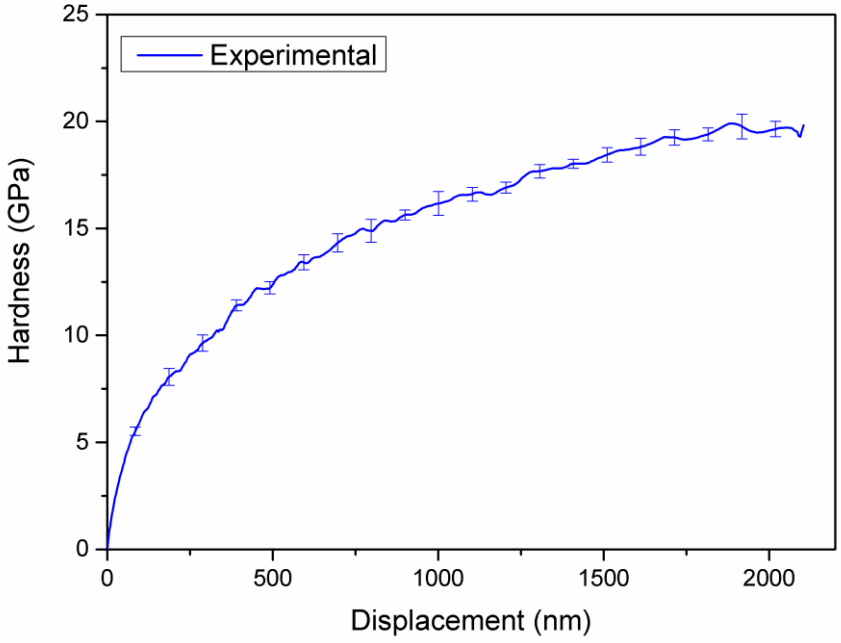

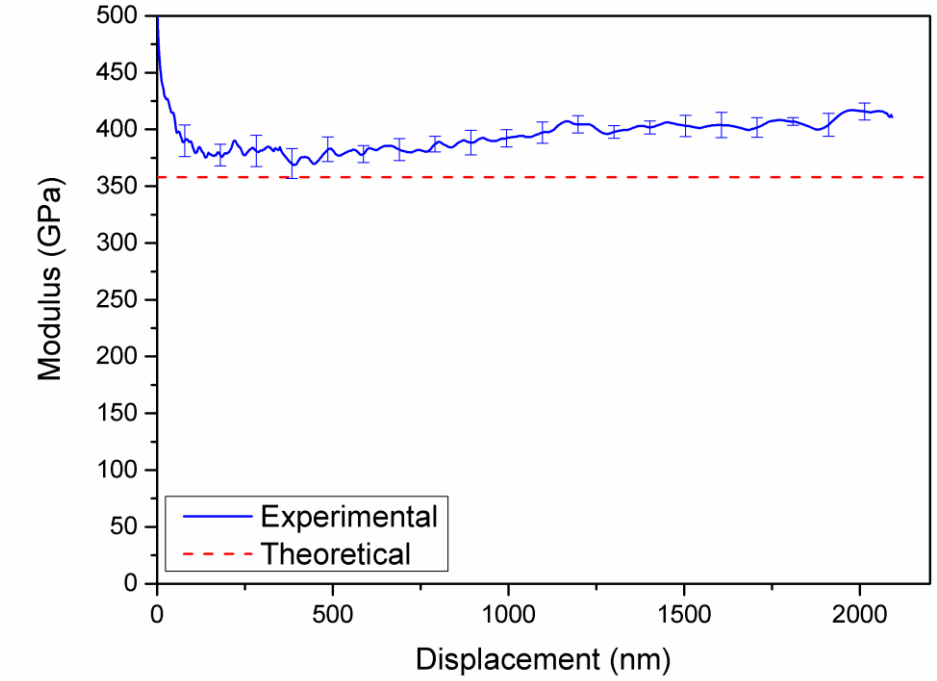

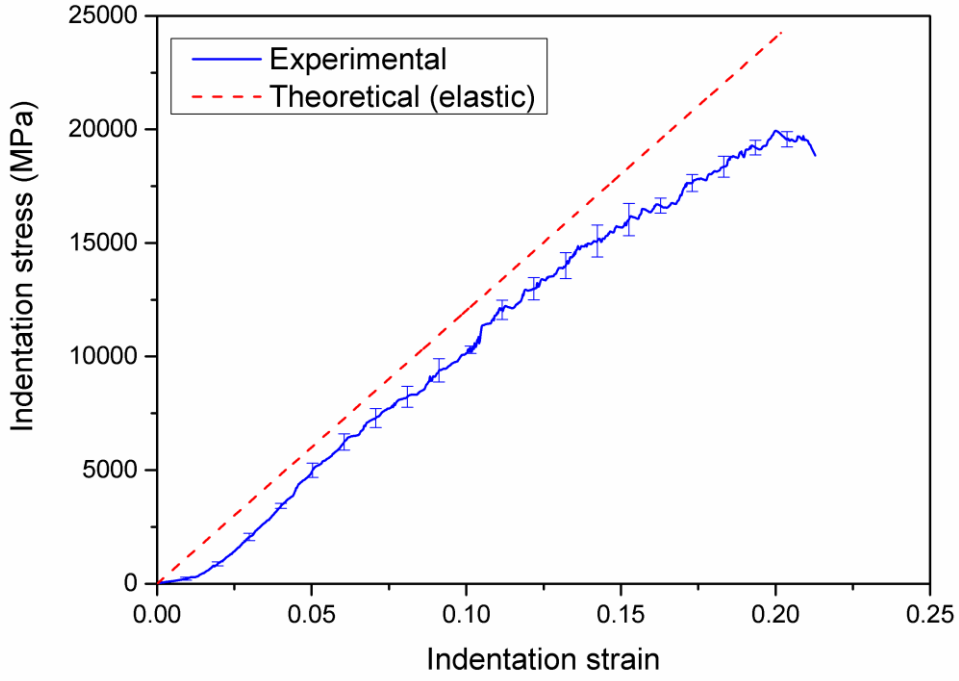

Hardness and indentation stress are equivalent (same definition). The theoretical curve was determined from Hertz theory.

2) Selectively etched ZTA sample (porous layer thickness = 27 µm)

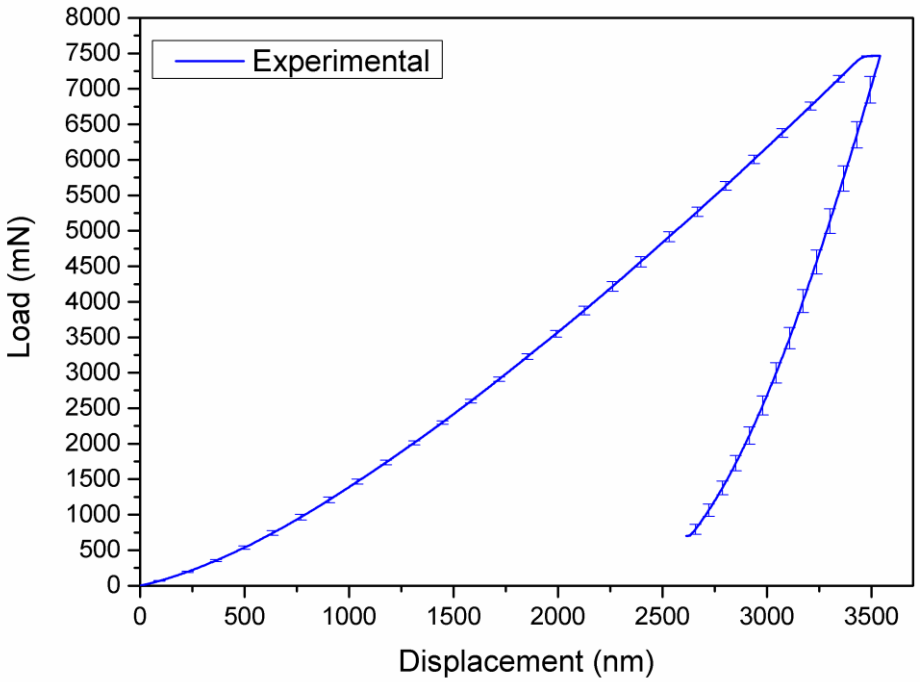

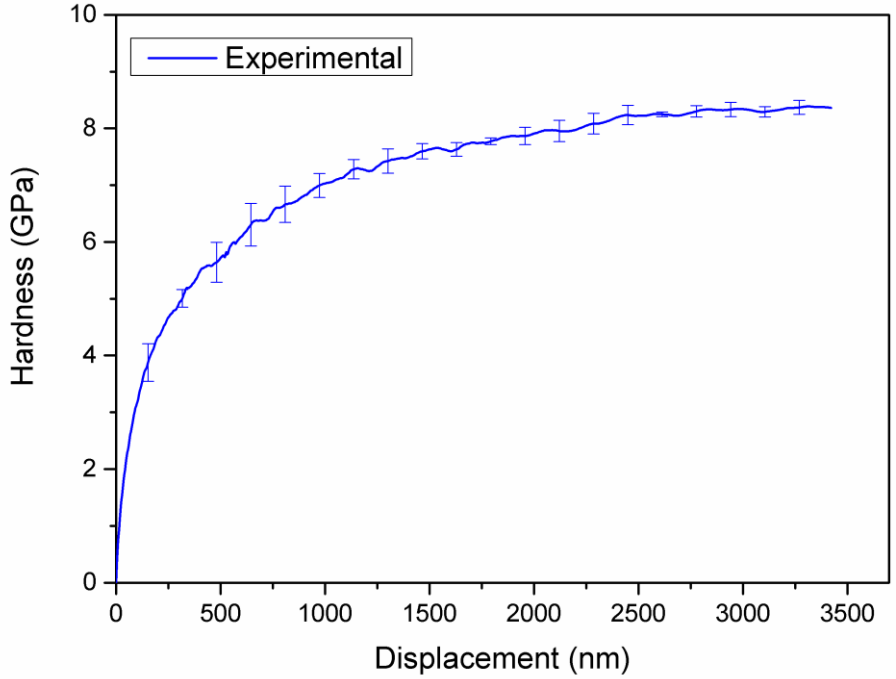

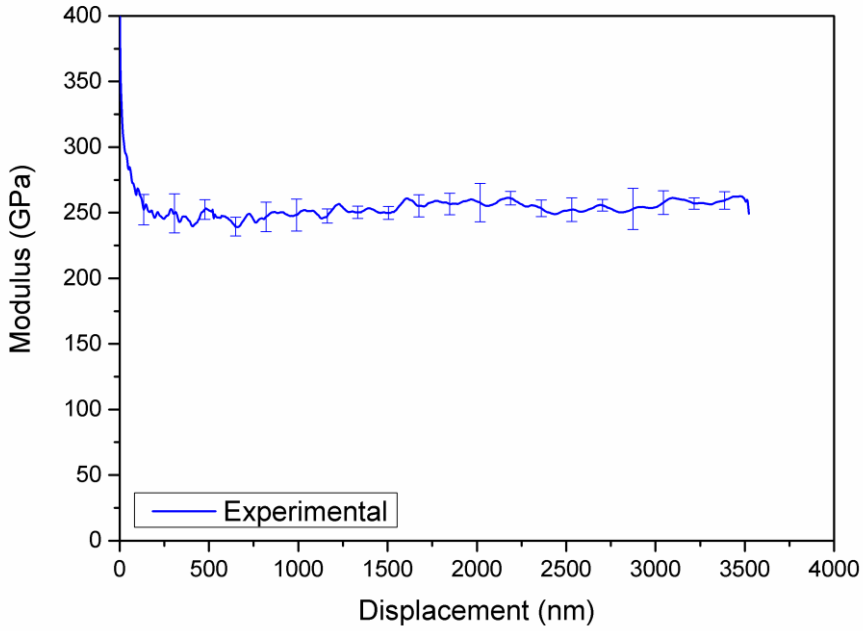

The modulus plotted here is the apparent modulus of the porous layer / ZTA bulk system. Bec *et al.* analytical model (Philos Mag 2006) can be used to compute the elastic modulus of the layer, leading to the following mean value: E_{layer} = *215 GPa.*

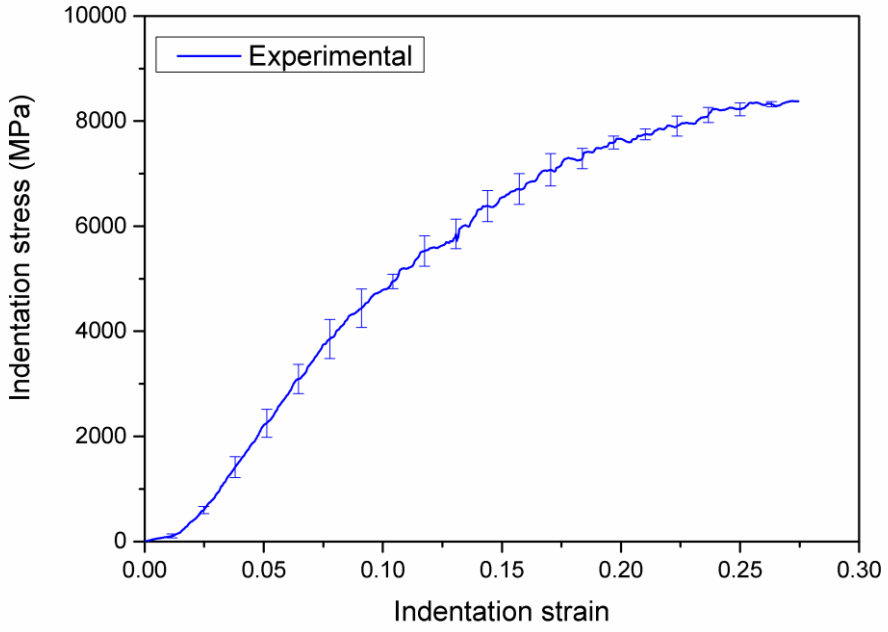

Hardness and indentation stress are equivalent (same definition).